

## **Distribution Agreement**

In presenting this dissertation as a partial fulfillment of the requirements for an advanced degree from Emory University, I hereby grant to Emory University and its agents the nonexclusive license to archive, make accessible, and display my dissertation in whole or in part in all forms of media, now or hereafter known, including display on the world wide web. I understand that I may select some access restrictions as part of the online submission of this dissertation. I retain all ownership rights to the copyright of the dissertation. I also retain the right to use in future works (such as articles or books) all or part of this dissertation.

Signature:

---

Keith A Freel

---

Date

Gas Phase Molecular Spectroscopy: Electronic Spectroscopy of Combustion  
Intermediates, Chlorine Azide Kinetics, and Rovibrational Energy Transfer in  
Acetylene

By

Keith A. Freel  
Doctor of Philosophy

Chemistry

---

Michael C. Heaven, Ph.D.  
Advisor

---

Myron Kaufman, Ph.D.  
Committee Member

---

James Kindt, Ph.D.  
Committee Member

Accepted:

---

Lisa A. Tedesco, Ph.D.  
Dean of the James T. Laney School of Graduate Studies

---

Date

Gas Phase Molecular Spectroscopy: Electronic Spectroscopy of Combustion  
Intermediates, Chlorine Azide kinetics, and Rovibrational Energy Transfer in  
Acetylene

by

Keith A. Freel  
M.Sc., Central Michigan University, 2006  
B.Sc., Michigan State University, 2003

Advisor: Michael C. Heaven, Ph.D.

An abstract of  
A dissertation submitted to the Faculty of the  
James T. Laney School of Graduate Studies of Emory University  
in partial fulfillment of the requirements for the degree of  
Doctor of Philosophy  
in Chemistry  
2012

## Abstract

### Gas Phase Molecular Spectroscopy: Electronic Spectroscopy of Combustion Intermediates, Chlorine Azide kinetics, and Rovibrational Energy Transfer in Acetylene

By Keith A Freel

This dissertation is composed of three sections. The first deals with the electronic spectroscopy of combustion intermediates that are related to the formation of polycyclic aromatic hydrocarbons. Absorption spectra for phenyl, phenoxy, benzyl, and phenyl peroxy radicals were recorded using the technique of cavity ring-down spectroscopy. When possible, molecular constants, vibrational frequencies, and excited state lifetimes for these radicals were derived from these data. The results were supported by theoretical predictions.

The second section presents a study of electron attachment to chlorine azide ( $\text{ClN}_3$ ) using a flowing-afterglow Langmuir-probe apparatus. Electron attachment rates were measured to be  $3.5 \times 10^{-8}$  and  $4.5 \times 10^{-8} \text{ cm}^3 \text{ s}^{-1}$  at 298 and 400 K respectively. The reactions of  $\text{ClN}_3$  with eighteen cations and seventeen anions were characterized. Rate constants were measured using a selected ion flow tube. The ionization energy ( $>9.6 \text{ eV}$ ), proton affinity ( $713 \pm 41 \text{ kJ mol}^{-1}$ ), and electron affinity ( $2.48 \pm 0.2 \text{ eV}$ ) for  $\text{ClN}_3$  were determined from these data.

The third section demonstrates the use of double resonance spectroscopy to observe state-selected rovibrational energy transfer from the first overtone asymmetric stretch of acetylene. The total population removal rate constants from various rotational levels of the  $(1,0,1,0^0,0^0)$  vibrational state were determined to be in the range of  $(9-17) \times 10^{-10} \text{ cm}^3 \text{ s}^{-1}$ . Rotational energy transfer accounted for approximately 90% of the total removal rate from each state. Therefore, the upper limit of vibrational energy transfer from the  $(1,0,1,0^0,0^0)$  state was 10%.

Gas Phase Molecular Spectroscopy: Electronic Spectroscopy of Combustion  
Intermediates, Chlorine Azide kinetics, and Rovibrational Energy Transfer in  
Acetylene

By

Keith A. Freel

M.Sc., Central Michigan University, 2006

B.Sc., Michigan State University, 2003

Advisor: Michael C. Heaven, Ph.D.

A dissertation submitted to the Faculty of the

James T. Laney School of Graduate Studies of Emory University

in partial fulfillment of the requirements for the degree of

Doctor of Philosophy

in Chemistry

2012

## ACKNOWLEDGMENTS

There are a number of people that, without their support, this work would be impossible. First and foremost I would like to thank my advisor, Dr. Michael Heaven. I will always aspire to attain his patience, courage, advice, encouragement, and immense knowledge. I could not imagine a better advisor for my Ph.D. study.

I would also like to thank my committee members Dr. Kindt and Dr. Kaufmann. I thank them for their helpfulness throughout my yearly reports, their thought-provoking questions, and also for their patience and guidance throughout the years.

Thank you to the Heaven and Lin lab members who not only shared their knowledge but also the invaluable lab tips and tricks. I especially thank those who I worked with on various projects: Dr. Joonbum Park, Dr. Rongshun Zhu, Dr. Jeremy Merritt, Dr. Jiande Han, Dr. Humayun Kabir, and Michael Sullivan. It was a blessing to work with the best and the brightest. I will never forget our adventures from stress to success.

My experience at the Air Force Research Lab was invaluable. I am indebted to the “star team”: Dr. Al Viggiano, Dr. Tom Miller, Dr. Nicole Eyt, Dr. Jeffrey Freidman, John Williamson, and Paul Mundis.

I thank my professors, classmates, and the Emory staff. I'd especially like to thank Ann Dasher, Steve Krebs, Patti Barnett, Patrick Morris, Tim

Stevens, and Cody Anderson for always going way beyond the call of duty to help me when I needed it.

Outside of Emory I would first like to thank my wife Rose. This dissertation would be twice as thick if I listed all the ways I was thankful to her. Her love and encouragement allowed me to finish the journey. I will always cherish our time in Atlanta.

A special thanks to Mike and Heather Redden who gave me a home away from home while writing.

I am eternally grateful to my family especially my parents, Paul and Terry Freel. Their love and support is unending and I could not have done this without them. Also my brothers, their families, Andre and Debbie Santangelo – thank you all for your support and encouragement. I would like to dedicate this work to my lost relatives including my grandfather Maj. John Soloc. He was the greatest man of the greatest generation.

Finally, there is only one who makes all of these things possible. *Soli Deo Gloria*. I give thanks to God for revealing His creation: “The heavens declare the glory of God; the skies proclaim the work of his hands.”

## TABLE OF CONTENTS

Section 1: Cavity Ring-down Spectroscopy of Polycyclic Aromatic	
Hydrocarbon Transient Species .....	1
Chapter 1. Introduction to Spectroscopy of Combustion Intermediates.....	1
Bibliography .....	12
Chapter 2. Development and Theory of Cavity Ring-down Spectroscopy ....	15
Bibliography .....	21
Chapter 3. Experimental.....	22
3.1. Cavity Ring-down Spectrometer.....	24
3.2. Electrical Discharge Assembly.....	26
3.3. Gas Expansion and Cooling.....	30
3.4. LabVIEW Programs .....	33
Bibliography .....	36
Chapter 4. Experimental Optimization .....	37
4.1. Iodine.....	38
4.1.1. Introduction.....	38
4.1.2. Experimental .....	39
4.1.3. Results and Discussion.....	40
4.2. C <sub>2</sub> .....	44
4.2.1. Introduction.....	44
4.2.2. Experimental .....	45



4.2.3. Results and Discussion.....	46
4.3. C <sub>6</sub> H.....	48
4.3.1. Introduction.....	48
4.3.2. Experimental.....	49
4.3.3. Results and Discussion.....	49
4.4. N <sub>2</sub> <sup>+</sup> .....	52
4.4.1. Introduction.....	52
4.4.2. Experimental.....	52
4.4.3. Results and Discussion.....	53
4.5. Redesign of the Valve System.....	56
4.5.1. Introduction.....	56
4.5.2. Experimental.....	57
4.5.3. Results and Discussion.....	58
4.6. Dissociation by Pyrolysis.....	59
4.6.1. Introduction.....	59
4.6.2. Experimental.....	61
4.6.3. Results and Discussion.....	62
Bibliography.....	68
Chapter 5. The Phenyl Radical.....	70
5.1. Introduction.....	70
5.2. Experimental.....	73
5.3. Experimental Results.....	75

5.4. Theoretical Calculations and Analysis .....	80
5.5. Discussion and Conclusions .....	92
Bibliography .....	95
Chapter 6. The Phenoxy Radical.....	97
6.1. Introduction.....	97
6.2. Experimental.....	99
6.3. Experimental Results .....	101
6.4. Theoretical Calculations and Analysis .....	103
6.5. Discussion and Conclusions .....	115
Bibliography .....	120
Chapter 7. The Phenylperoxy Radical .....	123
7.1. Introduction.....	123
7.2. Experimental.....	127
7.3. Experimental Results .....	129
7.4. Theoretical Calculations .....	135
7.5. Discussion .....	144
Bibliography .....	150
Section 2: Chlorine Azide – Electron Attachment and Reactions with Ions At the Air Force Research Laboratory.....	152
Chapter 8. Electron Attachment to Chlorine Azide.....	152
8.1. Introduction.....	152
8.2. Experimental.....	155

8.3. Results and Discussion .....	159
8.4. Conclusions.....	165
Bibliography .....	166
Chapter 9. Reactions of Positive and Negative Ions with $\text{ClN}_3$ at 300K .....	168
9.1. Introduction.....	168
9.2. Experimental.....	169
9.3. Results: $\text{ClN}_3$ + Negative Ions .....	171
9.3.1. Negative Ions + $\text{Cl}_2$ .....	173
9.3.2. Negative Ions + $\text{ClN}_3$ .....	175
9.4. Discussion: $\text{ClN}_3$ + Negative Ions .....	178
9.5. Results: $\text{ClN}_3$ + Positive Ions.....	181
9.6. Discussion: $\text{ClN}_3$ + Positive Ions.....	185
Bibliography .....	187
Section 3: Rovibrational Energy Transfer in Acetylene.....	189
Chapter 10. Rotational and Vibrational Energy Transfer From the First Overtone Stretch (10100)00 of Acetylene.....	189
10.1. Introduction.....	189
10.2. Experimental .....	193
10.2.1. Double Resonance Spectroscopy .....	193
10.2.2. Experimental Setup.....	195
10.3. Results and Analysis.....	198
10.3.1. Absorption Spectrum of Acetylene .....	198

10.3.2. Probe Scan Results and Analysis .....	199
10.3.3. Pump Scan Results and Analysis .....	202
10.3.4. Time Delay Scan Results and Analysis .....	207
10.3.5. Quantitative Analysis of Energy Transfer .....	208
10.3.6. Scaling Law .....	212
10.3.7. Vibrational Energy Transfer.....	214
10.4. Discussion and Conclusions.....	214
Bibliography .....	217

## TABLE OF FIGURES

<b>Figure 1.1.</b> Measured and calculated concentration profiles of polycyclic aromatic hydrocarbons in an acetylene-oxygen-argon flame.....	2
<b>Figure 1.2.</b> Select combustion species and reactions including first ring growth from small hydrocarbon radicals, formation of polycyclic aromatic hydrocarbons and soot .....	4
<b>Figure 2.1.</b> Diagram for typical pulsed cavity ring-down spectroscopy experiment.....	17
<b>Figure 2.2.</b> Theoretical detected light intensity from cavity ring-down spectroscopy experiment with empty cavity and with absorption .....	18
<b>Figure 3.1.</b> Experimental setup. The valve and discharge assembly in the dotted box are shown with more detail in Fig. 3.2. ....	23
<b>Figure 3.2.</b> Pulsed valve assembly with slit electrodes. 1. Ground Plate; 2. Phenolic Insulator; 3. High Voltage Jaw .....	23
<b>Figure 3.3.</b> Electrical Circuit built to monitor the current supplied to the discharge. ....	28
<b>Figure 3.4.</b> Temporal profiles for the ballast resistor and PMT voltages showing the relationship between the voltage applied to the electrodes, discharge initiation and the ring-down signal.....	29
<b>Figure 4.1.</b> The 48-0 and 49-0 bands of the $B^3\Pi^+_{0+u} - X^1\Sigma_g^+$ transition of $I_2$ measured at (a) 32 mm (b) 18 mm (c) 8 mm (d) 3 mm from the pinhole source. ....	41
<b>Figure 4.2.</b> Expansion of Figure 4.1 (a) experimental data with (b) calculated spectrum. ....	42

<b>Figure 4.3.</b> Temporal profiles for the ballast resistor and PMT voltages using the Jordan pulsed valve.....	46
<b>Figure 4.4. (a)</b> Theoretical at 130K and <b>(b)</b> experimental spectrum of the 0-0 $d^3\Pi_g - a^3\Pi_u$ transition of $C_2$ acquired using CRDS.....	47
<b>Figure 4.5. (a)</b> Theoretical at 40K and <b>(b)</b> experimental spectrum of the origin band of the $^2\Pi - X^2\Pi$ transition of $C_6H$ acquired by CRDS.....	50
<b>Figure 4.6. (a)</b> Theoretical spectrum of the at the $B^2\Sigma_u^+ - X^2\Sigma_g^+$ transition of $N_2^+$ at 200 K and <b>(b)</b> experimental spectrum of the acquired by CRDS.....	54
<b>Figure 4.7.</b> Visible CRD absorption spectra of products in an expansion of electrically dissociated benzyl chloride (bottom). The calculated spectrum (top) using the molecular constants from Lin et. al. confirms the assignment.....	62
<b>Figure 4.8.</b> Experimental spectra of $v'-v''$ 23-0 band of $I_2$ in a free expansion after passing through a pyrolysis tube at various voltages compared to a simulated spectrum at $T_{ROT} = 40$ K.....	64
<b>Figure 4.9.</b> Absorption of $I_2$ $v'-v'' = 23-0$ R-branch band head at various delays between the gas pulse and CRD laser pulse. The four traces show the time resolved absorption at various pyrolysis voltages corresponding to different pyrolysis temperatures.....	65
<b>Figure 4.10.</b> CRD spectrum taken 3 mm into the expansion of $I_2$ seeded in argon after passing through a pyrolysis tube with (6 V) and without (0 V) heating.....	66
<b>Figure 5.1.</b> Visible CRD absorption spectrum of metastable argon ( $Ar^*$ ), $C_2$ and the phenyl radical in an expansion from electrically dissociated bromobenzene.....	75
<b>Figure 5.2.</b> Rotationally resolved spectrum of the phenyl $1^2B_1 - X^2A_1 (9_0^1)$ transition. <b>a)</b> Experimental spectrum (bottom) and best fit simulation (top). <b>b)</b> Q branch experimental	

spectrum (dashed) compared to fits with (dotted) and without (solid) the Lorentzian contribution to the linewidth.....	77
<b>Figure 5.3.</b> The phenyl radical with atom numbering. ....	81
<b>Figure 5.4.</b> Upper valence molecular orbital diagram for benzene in the ground electronic state ( $X^2A_{1g}$ ) calculated at the RHF/aug-cc-pVDZ level. ....	84
<b>Figure 5.5.</b> Upper valence molecular orbital diagram for phenyl in the ground electronic state ( $X^2A_1$ ) calculated at the ROHF/aug-cc-pVDZ level.....	85
<b>Figure 5.6.</b> TDDFT/cc-pVDZ Franck-Condon calculated spectrum for the phenyl radical (red), compared to Porter and Ward's room temperature gas phase spectrum (green) and jet cooled CRDS spectrum (purple).....	91
<b>Figure 5.7.</b> Displacement vectors for the $\nu_4$ , $\nu_8$ , $\nu_9$ , and $\nu_{10}$ modes of the $1^2B_1$ electronic state of the phenyl radical.....	92
<b>Figure 6.1.</b> Visible CRD absorption spectrum of products in an expansion of electrically dissociated anisole.....	102
<b>Figure 6.2.</b> Upper valence molecular orbital diagram for phenoxy in the ground electronic state ( $X^2B_1$ ) calculated at the ROHF/aug-cc-pVDZ level. ....	105
<b>Figure 6.3.</b> Visible CRD absorption spectrum of products in an expansion of electrically dissociated anisole along with calculated spectrum with (red) and without (green) hot bands. The calculated spectrum was shifted $760\text{ cm}^{-1}$ . ....	111
<b>Figure 6.4.</b> Visible CRD absorption spectrum of products in an expansion of electrically dissociated anisole along with calculated spectrum with (red) and without (green) hot bands. The calculated spectrum was shifted $217\text{ cm}^{-1}$ .....	113
<b>Figure 6.5.</b> Calculated (TDDFT/aug-cc-pVTZ) $\beta$ electron energies in Hartree for the ground electronic state ( $X^2B_1$ ) and second excited electronic states ( $B^2A_2$ ) of phenoxy.	

The orbital symmetries are labeled along with selected orbital numbers. The x-axis has no physical meaning and the orbitals are only staggered for clarity.....	117
<b>Figure 7.1.</b> CRDS absorption spectra of the products in an expansion of electrically dissociated bromobenzene <b>(a)</b> without O <sub>2</sub> and <b>(b)</b> with O <sub>2</sub> compared to <b>(c)</b> a spectrum for phenyl peroxy predicted using molecular properties from a TDDFT/aug-cc-pVTZ calculation.....	130
<b>Figure 7.2.</b> Rotational contour of the phenyl peroxy $\tilde{B}^2A''-X^2A''$ origin band. This figure shows two copies of the experimental data (traces with noise) accompanied by computer simulations.....	134
<b>Figure 7.3.</b> Molecular orbitals involved in the first three electronic transitions of phenyl peroxy calculated at the B3LYP/aug-cc-pVTZ level for $\tilde{X}^2A''$ . Plots were generated with an isodensity value of 0.02 a.u.....	136
<b>Figure 7.4.</b> Equilibrium bond lengths and bond angles for the phenyl peroxy radical calculated at the B3LYP/aug-cc-pVTZ level for <b>(a)</b> $X^2A''$ and <b>(b)</b> by TDDFT/aug-cc-pVTZ for $B^2A''$ .....	136
<b>Figure 7.5.</b> Calculated (TD-DFT/aug-cc-pVTZ) vibrationally-resolved electronic spectrum for the $A^2A'-X^2A''$ transition of phenyl peroxy (solid trace) compared to the experimental (dashed) line positions and estimated relative intensities. The break is where experimental data was not available.....	144
<b>Figure 7.6.</b> Excited state normal modes responsible for the observed progressions in the $\tilde{B}^2A''-\tilde{X}^2A''$ vibronic spectrum of phenyl peroxy. The experimental term values are compared with the harmonic vibrational frequencies calculated by TD-DFT/aug-cc-pVTZ.....	146



<b>Figure 7.7.</b> Calculated vibrationally-resolved electronic spectra for the $\tilde{B}^2A''-\tilde{X}^2A''$ and $\tilde{C}^2A''-\tilde{X}^2A''$ transitions of phenyl peroxy (with aug-cc-pVTZ basis set) compared to the experimental results.....	147
<b>Figure 8.1.</b> Experimental setup. Chlorine azide was produced in the packed bed reactor (left). The absorption from $ClN_3$ was measured with the UV spectrometer. The $ClN_3$ was then sent to the FALP apparatus. Product ions were detected with a mass spectrometer .....	156
<b>Figure 8.2.</b> An example of a UV absorption spectrum of $ClN_3$ (solid line) juxtaposed with the cross section data from Henshaw et al. plotted as absorbance using the same path length (7 cm) and pressure (26.5 Torr) as in the present experiment. The difference in the peak heights at 205 nm implies that the sample used was 54.8% $ClN_3$ (the remainder being unreacted $Cl_2$ ).....	158
<b>Figure 8.3.</b> Electron density data obtained for electron attachment to $ClN_3$ in $3.25 \times 10^{16} \text{ cm}^{-3}$ He (2% Ar) carrier gas.....	160
<b>Figure 8.4.</b> Electron attachment anion spectra at 298 K and 400 K. The $Cl^-$ peak (>99% of the total ion signal) is off scale to allow the minor peaks to be seen. The small mass peak to the right of $N_3^-$ is $NO_2^-$ , a common impurity in afterglows. Another small peak clearly observed at 400 K was assigned to $ClO^-$ .....	163
<b>Figure 8.5.</b> Positive ion spectrum obtained at 400 K from reaction of $Ar^+$ (~5% $He^+$ ) with the $Cl_2$ , $ClN_3$ , and $H_2O$ flowing from the $ClN_3$ synthesis vessel, after 4.5 ms reaction time.....	164
<b>Figure 9.1.</b> Schematic diagram of the selected ion flow tube (SIFT) with the inline synthesis of $ClN_3$ .....	169

<b>Figure 9.2.</b> Semilogarithmic plot of fluoride ion reacting with chlorine azide. The line through the $F^-$ data is a least-squares fit. ....	172
<b>Figure 10.1.</b> Eigenstates involved in IR-UV double resonance experiment includes the initially populated ground state (bottom), intermediate pumped state (next higher), collisionally transferred state (next higher), and electronically excited state (highest)....	193
<b>Figure 10.2.</b> Experimental setup for IR pump, UV probe double resonance spectroscopy .....	196
<b>Figure 10.3.</b> Absorption spectrum of the $X\Sigma_g^+(00000) \rightarrow (10100)$ transition of acetylene by IR absorption. Experimental data is plotted above to be compared with the PGOPHER simulation below.....	198
<b>Figure 10.4.</b> Probe wavelength scans of the (10100) vibrational level 15 ns and 220 ns after pumping $J=6,8,10,12$ or 14. The top spectra are the experimental spectra while the bottom simulation gives a reference for peak positions. ....	200
<b>Figure 10.5.</b> UV scan about $50\text{ cm}^{-1}$ to the blue of the (10100) manifold with 200 ns delay and pumping the (10100) $J=8$ state. The top is the experimental spectrum and the bottom is a PGOPHER simulation of the two assigned transitions .....	201
<b>Figure 10.6.</b> Pump wavelength scan of the (10100) vibrational level 50, 100, 200, and 300 ns prior to probing the $J=8$ level. The y-axis is LIF intensity and the x-axis is the pump wavelength.....	203
<b>Figure 10.7.</b> Pump scan near (10100) region while observing the (11020) $J=5$ state by UV-LIF with a 70 ns delay between the pump and probe laser. ....	205
<b>Figure 10.8.</b> Time delay scans pumping various $J$ states in the (10100) manifold while observing the (10100) $J=0$ state. The data is accompanied by a fit for the LIF from RET as well as background fluorescence.....	207

## TABLE OF TABLES

<b>Table 4.1.</b> Absorption features in region 381-397 nm from CRD spectrum of phenol discharge products. ....	53
<b>Table 5.1.</b> Molecular constants for the phenyl radical. ....	78
<b>Table 5.2.</b> Calculated geometric parameters for the phenyl radical in the ground electronic state ( $X^2A_1$ ) and first excited electronic state ( $1^2B_1$ ). ....	87
<b>Table 5.3.</b> Scaled vibrational frequencies for the $X^2A_1$ and $1^2B_1$ states of phenyl using B3LYP/cc-pVDZ for the $X^2A_1$ state and TDDFT/cc-pVDZ for the $1^2B_1$ state.....	88
<b>Table 6.1.</b> Geometric parameters for phenoxy radical in the ground electronic state ( $X^2B_1$ ) and second excited electronic state ( $B^2A_2$ ).....	107
<b>Table 6.2.</b> Calculated vibrational frequencies for phenoxy radical in the ground electronic state ( $X^2B_1$ ). ....	108
<b>Table 6.3.</b> Calculated vibrational frequencies for phenoxy radical in the second excited electronic state ( $B^2A_2$ ). ....	109
<b>Table 7.1.</b> List of measured band positions and vibrational energies ( $G(v)$ ) compared with scaled harmonic vibrational frequencies ( $\Delta E$ ) from theoretical calculations ( $\text{cm}^{-1}$ units).....	133
<b>Table 7.2.</b> Harmonic Vibrational Constants for the $\tilde{B}^2A''$ state derived from the experimental data. ....	133
<b>Table 7.3.</b> Complete list of bond lengths and bond angles for the phenyl peroxy radical calculated at the B3LYP/aug-cc-pVDZ level (first table) and B3LYP/aug-cc-pVTZ (second table) for $\tilde{X}^2A''$ , and by TD-DFT for the excited electronic states.....	137

<b>Table 7.4.</b> Calculated and scaled normal mode frequencies ( $\text{cm}^{-1}$ ) for the phenyl peroxy radical in the $\tilde{X}^2A''$ and $\tilde{B}^2A''$ electronic states compared with experimental vibrational intervals. The ground state experimental values were reported by Mardyukov and Sander. The calculations are for the aug-cc-pVTZ basis set.....	140
<b>Table 7.5.</b> Calculated and scaled normal mode frequencies for phenyl peroxy radical (TD-DFT/aug-cc-pVTZ) in the $\tilde{A}^2A'$ and $\tilde{C}^2A''$ electronic states compared with experimental term values, $G(v)$ . The $\tilde{A}^2A'$ experimental values were reported by Just et al. (Chem. Phys. Lett. 2006, 417, 378-82).....	141
<b>Table 7.5.</b> Oscillator strength ( $f$ ), vertical excitation energy, adiabatic excitation energy ( $T_e$ ), and electronic transition origin ( $T_{00}$ ) for the first three electronic transition of phenyl peroxy calculated using TD-DFT with the aug-cc-pVDZ and aug-cc-pVTZ basis sets.	143
<b>Table 9.1.</b> Reaction rate constant ( $10^{-10} \text{ cm}^3 \text{ molecule}^{-1} \text{ s}^{-1}$ ), product ion branching ratios, and reaction enthalpies ( $\text{kJ mol}^{-1}$ ) of negative ions with $\text{Cl}_2$ .....	174
<b>Table 9.2.</b> Reaction rate constant ( $10^{-10} \text{ cm}^3 \text{ molecule}^{-1} \text{ s}^{-1}$ ), product ion branching ratios, and reaction enthalpies ( $\text{kJ mol}^{-1}$ ) of negative ions with $\text{ClN}_3$ .....	177
<b>Table 9.3.</b> Reaction rate constants, reaction efficiencies (Eff), and product ion branching distributions measured at 300 K for reactions used to determine the ionization energy of $\text{ClN}_3$ .....	182
<b>Table 9.4.</b> Reaction rate constants, reaction efficiencies (Eff), and product ion branching distributions measured at 300 K for reactions used to determine the electron affinity of $\text{ClN}_3$ .....	183
<b>Table 10.1.</b> The vibrational modes, energies, and symmetries of acetylene in the $X\Sigma_g^+$ and $A^1A_u$ electronic states .....	190

**Table 10.2.** Total removal rate constants for some rotational J states in  $C_2H_2 \ X\Sigma_g^+$  (10100) in units of  $10^{-10} \text{ cm}^3\text{s}^{-1}$ . The measurements at  $T= 295\text{K}$  are given in the 2<sup>nd</sup> column. Given in the 3<sup>rd</sup> column are rate constants measured by Utz et al. using IR-UV double resonance technique. The 4<sup>th</sup> column lists rates deduced by Utz et al. from pressure broadening data. Also listed in the last column are values deduced from our state-to-state RET rate measurements and rebuilt from PEGL fitting reflecting the RET contribution to the total removal rate ..... 209

**Table 10.3.** State-to-state RET rate constants  $k_{i,f}$  in units of  $10^{-10}\text{cm}^3\text{s}^{-1}$ . The top values in each row are the directly measured rate constants as described in the paper. The numbers in parenthesis are standard deviations for the measurements. The lower values in each row are rate constants rebuilt from the parameters used to fit the PEGL to the experimental data. The PEGL fitting parameters are listed in the bottom row. The last column lists the summation of the PEGL predicted rates in each row. .... 212

*Section 1*CAVITY RING-DOWN SPECTROSCOPY OF POLYCYCLIC  
AROMATIC HYDROCARBON TRANSIENT SPECIES**Chapter 1. Introduction to Spectroscopy of Combustion  
Intermediates**

Polycyclic aromatic hydrocarbons (PAHs) are formed by the incomplete combustion of hydrocarbons, usually in fuel-rich conditions.<sup>1</sup> Further growth and aggregation of PAHs leads to soot.<sup>2</sup> This incomplete combustion reduces the efficiency of combustion related energy production. Also, the presence of PAHs in the air, especially in urban regions, has resulted in adverse health effects in humans including cancer<sup>3</sup> and developmental issues such as lowered intelligence in children.<sup>4</sup> In order to limit the production of soot and PAHs in combustion, an accurate model of their formation is crucial as it is a valuable tool for engineers to design more efficient and less polluting combustion systems.

An accurate model of PAH formation requires kinetic and structural information for all of the molecules and reactions involved. The accuracy of the models can be tested by comparing the model predictions to the concentration of observable species in combustions systems. Figure 1.1 shows the measured<sup>5</sup> and calculated<sup>1</sup> profiles of selected PAH's along the length of a premixed acetylene-oxygen-argon flame. Although the trends show promising results, there is still

room for improvement. A more detailed description of the molecules and reactions involved in PAH formation is necessary to make these improvements.

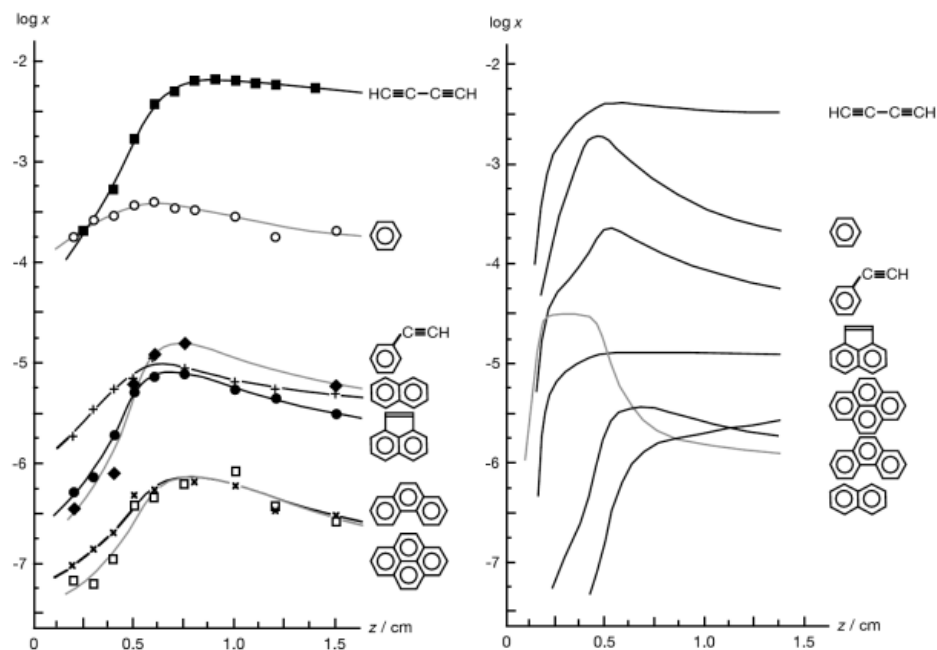


**Figure 1.1.** Measured<sup>5</sup> (left) and calculated<sup>1</sup> (right) concentration profiles of polycyclic aromatic hydrocarbons in an acetylene-oxygen-argon flame. Copied from Reference 1.

The kinetic and structural information for transient species, which define the PAH formation reaction mechanisms, are not completely understood. A transient species is a short lived intermediate in a chemical reaction.<sup>6</sup> They can be thought of as stepping stones between the parent substance and the final product.<sup>7</sup> Transient species include carbenes, carbocations, carbanions, and neutral free radicals. Free radicals are reactive species that contain one unpaired electron. In combustion reactions and PAH formation, free radicals dominate the role as transient species. Large, stable, conjugated radicals are often formed

during combustion due to the stabilization of the unpaired electron by delocalization within the conjugated system.

In hydrocarbon combustion, radicals are formed by high temperature (>1000 K) collisions or hydrogen-abstraction reactions. These types of processes are known as initiation steps because they initiate a variety of radical-radical and radical-molecule reactions. There are three general classifications of radical reactions. The first is chain-propagation. Chain-propagation reactions occur when a radical reacts with a nearby fuel or oxidant molecule to create a new radical. In this case the number of radicals does not increase. The second type of reaction is called chain-branching. In this case, a radical reacts with a nearby stable species to produce two radicals. This type of reaction quickly increases the number of radicals in the combustion system. The third type of combustion reactions, termination reactions, limits the accumulation of radicals in a combustion system. The termination reactions result in a decrease of reactive radicals often by radical-radical reactions. The extent of combustion is related to the relative rates of the chain-propagation, chain-branching, and termination reactions.

The growth of PAHs in fuel rich conditions, including the formation of the first ring, is not completely understood. However, several possible mechanisms have been proposed and are shown in Figure 1.2.



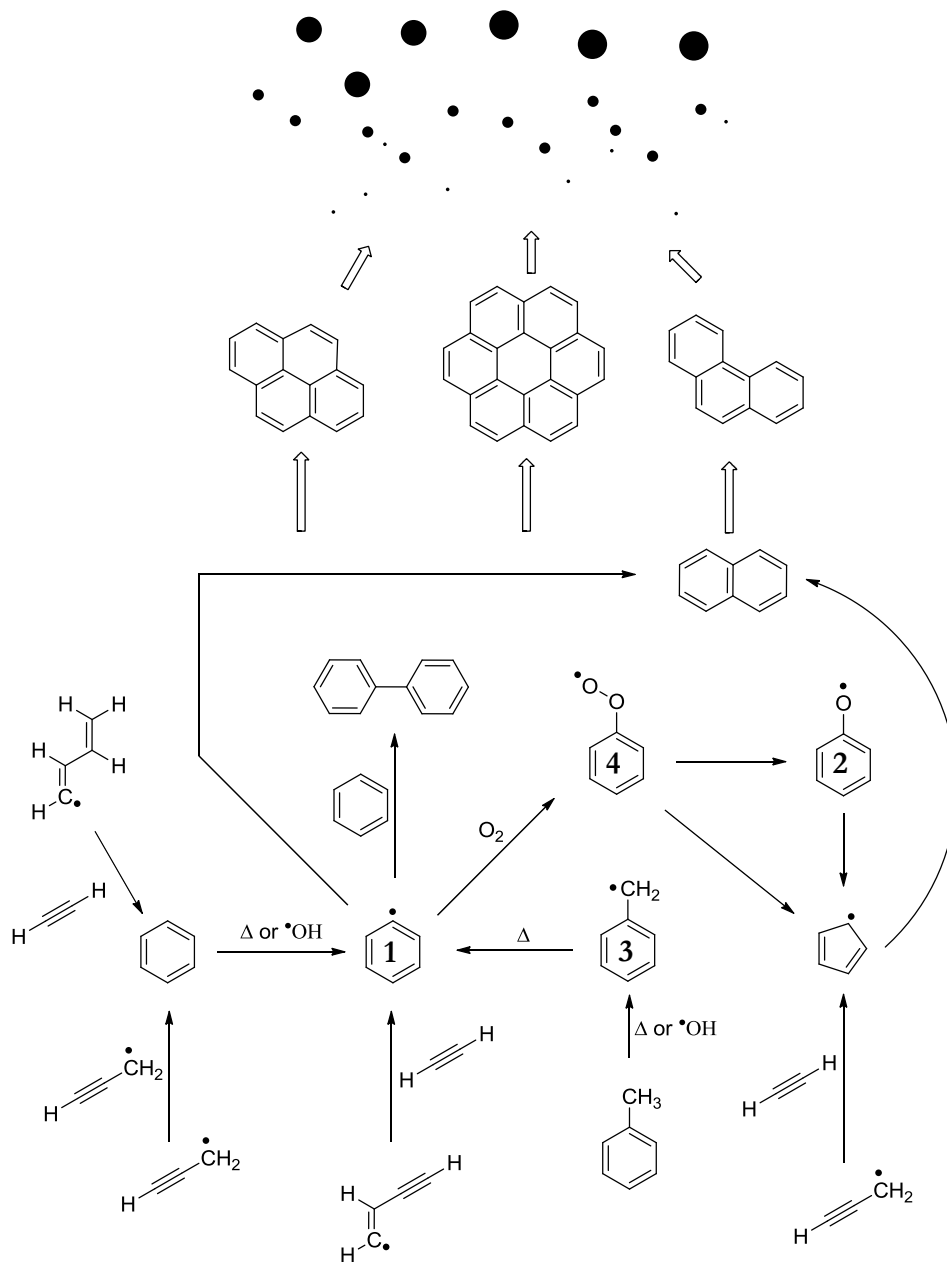


**Figure 1.2.** Select combustion species and reactions including first ring growth from small hydrocarbon radicals, formation of polycyclic aromatic hydrocarbons and soot.

At high temperatures, hydrocarbon fuel dissociates into small fragments including acetylene and hydrocarbon radicals. In incomplete combustion, where the hydrocarbons are not completely converted to  $\text{CO}_2$  and  $\text{H}_2\text{O}$ , the smaller radicals may combine to form ring structures. It has been suggested that two propargyl radicals ( $\text{C}_3\text{H}_3$ ) combine to form a benzene ring ( $\text{C}_6\text{H}_6$ ).<sup>8</sup> Another suggested mechanism involves the addition of acetylene ( $\text{C}_2\text{H}_2$ ) to  $n\text{-C}_4\text{H}_3$  or  $n\text{-C}_4\text{H}_5$  to form the phenyl radical ( $\text{C}_6\text{H}_5$ ) or benzene.<sup>9,10</sup> It may also be possible that propargyl and acetylene combine to form cyclopentadienyl radical ( $\text{C}_5\text{H}_5$ ).<sup>9</sup>

Regardless of the source, once the first ring is present, it will react further to form PAHs and eventually soot. Warnatz et al. lists four general pathways: 1) the alternating H abstraction/ $\text{C}_2\text{H}_2$ -addition (HACA) route<sup>11</sup>, 2) the combination of phenyl with benzene, 3) cyclopentadienyl recombination, and 4) the ring closure reactions of aliphatic hydrocarbons.<sup>1</sup> There have been numerous studies addressing the details of these pathways. Since models for soot formation often consist of thousands of reactions and hundreds of species, only the reactions most relevant to our study, which include the phenyl **(1)**, phenoxy **(2)**, benzyl **(3)**, and phenylperoxy **(4)** radicals (see Figure 1.2) will be discussed here.

At high temperatures a C–H bond of benzene may dissociate, or the H atom may be abstracted, and the phenyl radical is produced. The phenyl radical can then proceed by the HACA route forming PAHs or react with  $\text{O}_2$ .<sup>12</sup> The barrierless addition of  $\text{O}_2$  to phenyl produces the phenylperoxy radical.<sup>13,14</sup>

Several products of the decomposition of phenylperoxy have been suggested yet the more recent computational work and experiments agree that phenoxy ( $C_6H_5O$ ) is the most abundant product.<sup>13-16</sup> Phenoxy then breaks down into cyclopentadienyl which reacts to make naphthalene and ultimately soot.<sup>16,17</sup> Another cyclic radical of importance is the benzyl radical which has been observed in combustion processes. Benzyl, which can be produced from the fuel additive toluene by hydrogen abstraction, can recombine or react with smaller radicals to form PAHs including naphthalene.<sup>18</sup>

Kinetic studies have been completed to study many reactions involving free radicals in combustion systems. Berden and Engeln as well as Friedrichs have compiled large lists of kinetic studies of radicals.<sup>19,20</sup> Notably, kinetic studies have quantified the rate of various chemical reactions involving the phenyl<sup>21-35</sup>, phenoxy<sup>36</sup>, phenylperoxy<sup>37</sup>, and benzyl<sup>38,39</sup> radicals. These kinetic studies often make use of absorption features specific to the molecule of interest. A complete spectroscopic characterization of these radicals is then necessary to complement these studies and will help with the elucidation of reaction mechanisms. The molecular constants measured from the studies will also provide benchmarks for computational work.

One common spectroscopic method is to record the dispersed fluorescence spectrum of flames. This method has supplied a large amount of data for flame profiles of small radicals. However, this method is limited since

flames produce a large amount of emitting species at high temperatures. This combination results in significant spectral overlap and produces a quasi-continuous spectrum. Furthermore, the species with high emission, such as OH or C<sub>2</sub>, dominate most spectral regions. To get more details about specific radicals of interest, it is then advantageous to produce and detect radicals in a more controlled environment where the temperature may be reduced and the total number of species is limited.

Many methods for radical production, cooling and detection have been developed. Radicals can be produced in large concentrations by a number of methods. The most common production methods include pyrolysis, shock tubes, discharge (both microwave and electrical), chemical reaction, and photolysis. Experimental difficulties lie predominately in the detection and characterization of combustion radicals even if radicals are produced in high concentrations. Detection difficulties arise from short lifetimes of the radicals which, after a short amount of time after production, usually results in concentrations too low for detection by traditional means.

Electron paramagnetic resonance (EPR) spectroscopy provides a good starting point for the characterization of radicals. The g-value obtained from the measurement can help to identify the molecular orbital where the lone electron resides.<sup>40</sup> The radical can then be specified as a  $\pi$  or  $\sigma$  type radical if the lone electron resides in a  $\pi$  or  $\sigma$  type orbital. Kinetic measurements have been

achieved in the gas phase using EPR to monitor concentrations of radicals in a flow tube.<sup>41</sup> The experimental difficulties associated with combining EPR with radical production methods has limited its application to only long lived radicals.

The use of mass spectrometry allows the analysis of multiple species, including radicals, in combustion systems. When many species are present, as is the case with combustion systems, mass spectrometry has the advantage of detecting specific species by mass selectivity. One drawback to mass spectrometry methods is that the probe for the mass spectrometer inlet may interfere with the combustion system itself. Also, since only the mass to charge ratio is observed, there is still some uncertainty in the assignment of the species observed since several isomers may share the same mass.<sup>42</sup> Optical methods, which could be combined with mass spectrometry designs or used alone, are essential to obtain reliable structural information. For example, the more recent use of tunable high energy radiation for ionization, e.g. laser vacuum ultraviolet light<sup>43</sup> or synchrotron radiation<sup>44</sup>, in mass spectrometry experiments allows for isomer selectivity in mass spectrometry experiments.

There are several advantages to the use of laser probes to study combustion chemistry. Unlike mass spectrometry, measurements can be made using optical methods without significantly perturbing the combustion system itself. Optical methods alone have been very successful in measuring not only species concentration, but also radical molecular structure information,

vibrational information, electronic information, and/or temperature in combustion systems.<sup>45</sup> Kinetic information can also be obtained by “pump-probe” techniques with up to femtosecond resolution.

Raman spectroscopy is another widely used optical technique used to study combustion chemistry even though nonlinearities limit the accuracy of concentration measurements. Raman spectroscopy makes use of inelastic collision processes between photons and molecules to obtain a Stokes shifted signal. Theoretically, a single laser can be used in Raman experiments to monitor all of the species present. However, spontaneous Raman scattering has a relatively low intensity which limits the number of detected species typically to only one species.<sup>46</sup> The multiphoton coherent anti-stokes Raman scattering (CARS) technique offers improved sensitivity. With this technique, spectra and temperatures can be measured for multiple species simultaneously.<sup>47</sup>

Even higher sensitivity can be achieved with laser induced fluorescence (LIF).<sup>48</sup> With this technique, species can be detected at sub-ppb (part-per-billion) concentrations ( $< 10^9 \text{ cm}^{-3}$ ). In LIF, the molecule of interest is pumped to an excited state using a laser tuned to be in resonance with the excited state transition energy. As the molecule relaxes a photon may be released and observed. As with Raman techniques, spatial as well as temporal concentrations and temperatures can be measured for certain molecules using LIF. LIF has proven to be useful for qualitative and quantitative analysis of PAHs.<sup>49</sup> However,

some PAH intermediates have poor fluorescence quantum yields due to nonradiative decay. This limits the utility of LIF for such species.

A highly sensitive absorption method called cavity ring-down spectroscopy (CRDS) has proven effective in overcoming these difficulties. CRDS incorporates an optical cavity to enhance sensitivity relative to typical absorption. Pulsed laser CRDS experiments can reach sensitivities comparable to LIF. CRDS was first used to study combustion chemistry in a flame in 1994.<sup>50</sup> Since then, several groups have used the technique to identify and study molecules and reactions related to combustion.<sup>19</sup> CRDS has been used for spectroscopic characterization as well as kinetic studies. Contrary to LIF, along with the ability to observe molecules with poor fluorescence quantum yields, CRDS has an advantage with its ability to measure absolute concentrations of selected species in combustion systems.<sup>19</sup> A discussion of CRDS theory is presented in Chapter 2.

The purpose of the experiments presented here was to incorporate CRDS to obtain electronic spectra of single ring radicals which are known to be important for PAH formation. This was done by incorporating radical production, cooling, and detection methods which were versatile enough to detect a wide variety of radicals. The main challenge in this study was to produce single ring radicals, which are typically found in high temperature environments, and study them at low temperatures. This study combined an electrical discharge

to produce radicals, a jet expansion to cool them immediately after production, and CRDS for detection.

The radicals in this study were chosen based on their relevance to combustion chemistry and PAH formation, ease of production, and necessity for spectroscopic analysis. These include the phenyl radical, phenoxy radical, benzyl radical, and phenylperoxy radical.



## BIBLIOGRAPHY

- (1) Warnatz, J.; Maas, U.; Dibble, R. W. *Combustion : physical and chemical fundamentals, modeling and simulation, experiments, pollutant formation*; 4th ed.; Springer: Berlin ; New York, 2006.
- (2) Bockhorn, H. *Soot formation in combustion : mechanisms and models*; Springer-Verlag: Berlin ; New York, 1994.
- (3) Boffetta, P.; Jourenkova, N.; Gustavsson, P. *Cancer Cause Control* **1997**, *8*, 444.
- (4) Edwards, S. C.; Jedrychowski, W.; Butscher, M.; Camann, D.; Kieltyka, A.; Mroz, E.; Flak, E.; Li, Z. G.; Wang, S. A.; Rauh, V.; Perera, F. *Environ Health Persp* **2010**, *118*, 1326.
- (5) Bockhorn, H.; Fetting, F.; Wenz, H. W. *Berichte Der Bunsen-Gesellschaft-Physical Chemistry Chemical Physics* **1983**, *87*, 1067.
- (6) Daintith, J. *A dictionary of chemistry*; 6th ed.; Oxford University Press: New York, 2008.
- (7) Hawley, G. G.; Lewis, R. J. *Hawley's condensed chemical dictionary*; 14th ed.; Wiley: New York, 2002.
- (8) Melius, C. F.; Miller, J. A.; Evleth, E. M. *Symposium (International) on Combustion* **1992**, *24*, 621.
- (9) Frenklach, M. *Physical Chemistry Chemical Physics* **2002**, *4*, 2028.
- (10) Frenklach, M.; Warnatz, J. *Combust Sci Technol* **1987**, *51*, 265.
- (11) Frenklach, M.; Wang, H. *Symposium (International) on Combustion* **1991**, *23*, 1559.
- (12) Shukla, M.; Susa, A.; Miyoshi, A.; Koshi, M. *J Phys Chem A* **2008**, *112*, 2362.
- (13) Tokmakov, I. V.; Kim, G.-S.; Kislov, V. V.; Mebel, A. M.; Lin, M. C. *J Phys. Chem. A* **2005**, *109*, 6114.
- (14) Albert, D. R.; Davis, H. F. *J Phys Chem Lett* **2010**, *1*, 1107.
- (15) Gu, X.; Zhang, F.; Kaiser, R. I. *Chem. Phys. Lett.* **2007**, *448*, 7.
- (16) Frank, P.; Herzler, J.; Just, T.; Wahl, C. *Symposium (International) on Combustion* **1994**, *25*, 833.
- (17) Lin, C. Y.; Lin, M. C. *J Phys Chem-U.S.* **1986**, *90*, 425.
- (18) Zhang, L. D.; Cai, J. G.; Zhang, T. C.; Qi, F. *Combust Flame* **2010**, *157*, 1686.
- (19) Berden, G.; Engeln, R. *Cavity Ring-Down Spectroscopy: Techniques and Applications*; John Wiley & Sons, 2009.
- (20) Friedrichs, G. *Zeitschrift Fur Physikalische Chemie-International Journal of Research in Physical Chemistry & Chemical Physics* **2008**, *222*, 31.
- (21) Choi, Y. M.; Xia, W. S.; Park, J.; Lin, M. C. *J Phys Chem A* **2000**, *104*, 7030.
- (22) Park, J.; Tokmakov, I. V.; Lin, M. C. *J Phys Chem A* **2007**, *111*, 6881.

- (23) Yu, T.; Lin, M. C. *Combust Flame* **1995**, *100*, 169.
- (24) Yu, T.; Lin, M. C. *J Phys Chem-Us* **1995**, *99*, 8599.
- (25) Park, J.; Wang, L. M.; Lin, M. C. *Int J Chem Kinet* **2004**, *36*, 49.
- (26) Park, J.; Gheyas, S.; Lin, M. C. *Int J Chem Kinet* **2001**, *33*, 64.
- (27) Yu, T.; Lin, M. C. *Journal of the American Chemical Society* **1993**, *115*, 4371.
- (28) Park, J.; Lin, M. C. *J Phys Chem A* **1997**, *101*, 14.
- (29) Nam, G.; Tokmakov, I. V.; Park, J.; Lin, M. C. *P Combust Inst* **2007**, *31*, 249.
- (30) Choi, Y. M.; Lin, M. C. *Chemphyschem* **2004**, *5*, 225.
- (31) Choi, Y. M.; Xia, W. S.; Park, J.; Lin, M. C. *Abstr Pap Am Chem S* **2000**, *220*, U226.
- (32) Tokmakov, I. V.; Park, J.; Gheyas, S.; Lin, M. C. *J Phys Chem A* **1999**, *103*, 3636.
- (33) Park, J.; Nam, G. J.; Tokmakov, I. V.; Lin, M. C. *J Phys Chem A* **2006**, *110*, 8729.
- (34) Tanaka, K.; Ando, M.; Sakamoto, Y.; Tonokura, K. *Int J Chem Kinet* **2012**, *44*, 41.
- (35) Tonokura, K.; Norikane, Y.; Koshi, M.; Nakano, Y.; Nakamichi, S.; Goto, M.; Hashimoto, S.; Kawasaki, M.; Andersen, M. P. S.; Hurley, M. D.; Wallington, T. J. *J Phys Chem A* **2002**, *106*, 5908.
- (36) Tonokura, K.; Ogura, T.; Koshi, M. *J Phys Chem A* **2004**, *108*, 7801.
- (37) Alfassi, Z. B.; Khaikin, G. I.; Neta, P. *J. Phys. Chem.* **1995**, *99*, 265.
- (38) Tonokura, K.; Koshi, M. *J Phys Chem A* **2003**, *107*, 4457.
- (39) Matsugi, A.; Miyoshi, A. *Chemical Physics Letters* **2012**, *521*, 26.
- (40) Gerson, F.; Huber, W. *Electron Spin Resonance Spectroscopy of Organic Radicals*; John Wiley & Sons, 2006.
- (41) Westenbe.Aa *Science* **1969**, *164*, 381.
- (42) Platz, M.; Moss, R. A.; Jones, M. *Reviews of reactive intermediate chemistry*; Wiley-Interscience: Hoboken, N.J., 2007.
- (43) Baeza-Romero, M. T.; Blitz, M. A.; Goddard, A.; Seakins, P. W. *Int J Chem Kinet* **2012**, *44*, 532.
- (44) Qi, F. *P Combust Inst* **2013**, *34*, 33.
- (45) Hayes, C. J.; Merle, J. K.; Hadad, C. M. In *Advances in Physical Organic Chemistry*; Richard, J. P., Ed.; Academic Press: 2009; Vol. Volume 43, p 79.
- (46) Eckbreth, A. C. *Laser Diagnostics for Combustion Temperature and Species*; Taylor & Francis, 1996.
- (47) Attal-Trétout, B.; Bouchardy, P.; Magre, P.; Péalat, M.; Taran, J. P. *Applied Physics B: Lasers and Optics* **1990**, *51*, 17.
- (48) Leipertz, A.; Braeuer, A.; Kiefer, J.; Dreizler, A.; Heeger, C. In *Handbook of Combustion*; Wiley-VCH Verlag GmbH & Co. KGaA: 2010.
- (49) Sun, R.; Zobel, N.; Neubauer, Y.; Cardenas Chavez, C.; Behrendt, F. *Optics and Lasers in Engineering* **2010**, *48*, 1231.

(50) Meijer, G.; Boogaarts, M. G. H.; Jongma, R. T.; Parker, D. H.; Wodtke, A. M. *Chemical Physics Letters* **1994**, *217*, 112.

## Chapter 2. Development and Theory of Cavity Ring-down Spectroscopy

In 1980, J.M. Herblin et al. proposed the use of an optical cavity for measuring the reflectance of mirror coatings.<sup>1</sup> In an optical cavity, the incoming light reflects back and forth off of two mirrors. Each time the light reflects off of a mirror a small amount passes through while the rest is reflected and remains in the cavity. After some time all of the light is lost from the cavity. Absorption and scattering losses reduce the residence time of the light inside the cavity. Herblin et al. measured the mirror reflectance by passing a continuous wave laser through the cavity and measured the output while the intensity of the laser light was varied. This method led D.Z. Anderson et al. to report the first ring-down measurement in 1984.<sup>2</sup> They simply switched the laser light off and recorded the exponential decay of light intensity that escaped the cavity over time. This decay is called ring-down and is the fundamental measurement of cavity ring-down spectroscopy.

Cavity ring-down spectroscopy (CRDS) is an absorption spectroscopy technique particularly for the spectroscopy of gasses. It has several advantages and few limitations when compared to traditional absorption experiments. These will be discussed later but the most important advantage is that CRDS results in high sensitivity.

In a traditional absorption experiment, light is passed through a liquid, solid, or gas sample. The intensity of the light before passing through the sample

( $I_0$ ) is compared to the intensity of the light after leaving the sample ( $I$ ). Some of the light may be absorbed by the sample and results in a decrease in intensity. If a broadband light source is used the transmitted light can be dispersed to produce an absorption spectrum. Alternatively, if a monochromatic light source is used, a spectrum can be recorded by measuring the decrease in light intensity as a function of wavelength. The comparison of the light intensities can also be used to calculate the concentration of the absorbing species in the sample using Beers law.

$$\frac{I}{I_0} = 10^{-\alpha l c} \quad (2.1)$$

In this equation  $\alpha$  is the molar absorptivity and  $l$  is the length that the light passes through the sample. With these values known, the concentration ( $c$ ) of the absorbing species can be calculated.

In CRDS the path length is increased by incorporating an optical cavity. The absorbing material is placed in the path of the reflected laser inside the cavity. The use of highly reflective mirrors can increase the path length from centimeters to several kilometers. The light that is emitted can be measured and used to construct a high sensitivity absorption spectrum.

As discussed earlier, the CRDS experiment requires a light source and a cavity with highly reflective mirrors. Also included in the experiment is a detector for the light exiting the cavity and a computer to read and store the signal from

the detector. Each of these components can be tailored for a specific experiment. Many variations of CRDS exist and each has their own strengths and weaknesses. The standard pulsed laser configuration is presented here. An illustration of the experimental setup of a typical pulsed laser CRDS experiment is shown in Figure 2.1.

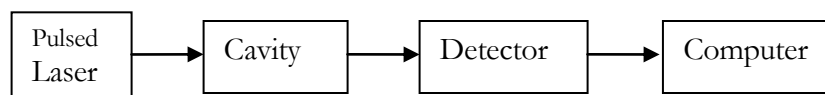


**Figure 2.1.** Diagram for typical pulsed cavity ring-down spectroscopy experiment.

Books edited by Busch & Busch<sup>3</sup> and Berden & Engeln<sup>4</sup> include excellent introductions to CRDS, optical cavity theory, and CRDS applications. The theory begins by discussing Beers law which has already been discussed above. Of course, the optical cavity is the most distinguishing component of CRDS. The two mirrors reflect the incoming laser beam. With each reflection a small percentage (and same percentage throughout) leaks through the mirror to the detector. In the case of an empty cavity with mirrors of reflectivity  $R$ , and cavity length  $L$  the intensity of light detected is described as a function of time by:

$$I(t) = I_o \exp\left[-(1-R)\frac{tc}{L}\right] \quad (2.2)$$

This equation shows that the detected light (light exiting the cavity) decays exponentially with a rate which depends on the mirror loss per reflection  $(1-R)$  and the number of round trips after time  $t$   $(tc/2L)$  where  $c$  is the speed of the

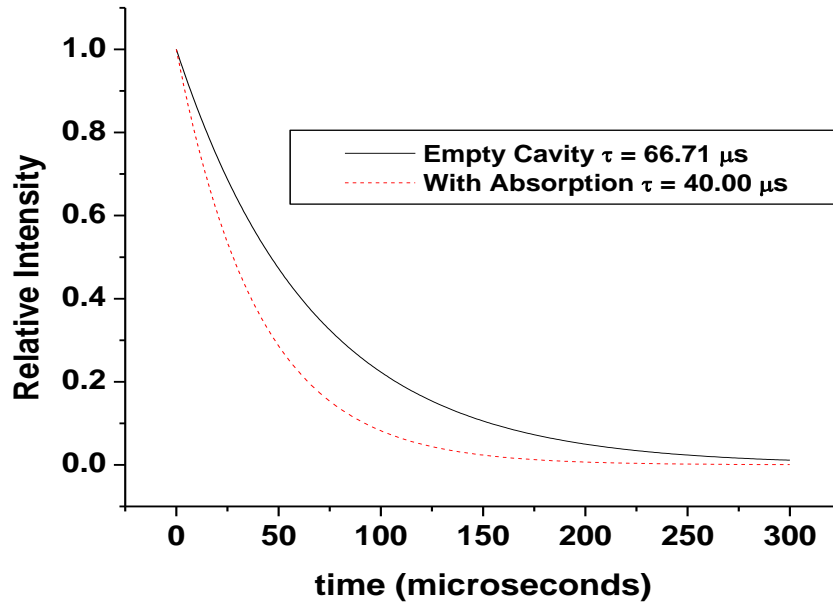


**Figure 2.2.** Theoretical detected light intensity from cavity ring-down spectroscopy experiment with empty cavity (solid) and with absorption (dashed).

light in the cavity. For example, with mirrors of 99.995% reflectivity in a cavity of 1.0 m length, the ring-down pattern produced by a laser pulsed injected into the cavity is shown in Figure 2.2 (solid line). The initial intensity was set at 100 arbitrary units. The time constant ( $\tau$ ) for this decay is defined as the time when  $I(t) = I_0 e^{-1}$ . In this case  $I(\tau) = 36.8$  where  $\tau \sim 66.71 \mu\text{s}$ .

Next, the absorption by a sample inside the cavity can be considered. The absorption of a sample is described quantitatively by the absorption coefficient as defined in Beers law (Equation 2.1). The absorption loss in the cavity is equal to the loss per round trip multiplied by the number of round trips.

$$\text{Loss} = (2\alpha L)(tc/2L) \quad (2.3)$$

Now the total loss can be found by adding the loss in the empty cavity to the absorption loss. The total loss is defined as:

$$\text{Total loss} = [(1-R) + \alpha L] tc/L \quad (2.4)$$

Now the detected intensity decay curve must contain this term to include the loss from the absorption. So equation 2.2 can be rewritten as:

$$I(t) = I_o \exp\left[-[(1-R) + \alpha L] \frac{tc}{L}\right] \quad (2.5)$$

To continue with the example, if the absorption coefficient is  $\alpha = 3.34 \times 10^9 \text{ m}^{-1}$  the detected curve is illustrated in Figure 2.2 (dashed line). This figure compares the curve from an empty cavity to a curve with the absorbing sample. Note that the added loss from absorption increases the decay constant. A spectrum can be made by comparing the ring-down time of the empty cavity ( $\tau_1$ ) with the ring-down time with the absorption ( $\tau_2$ ). More specifically, the absorption coefficient can be found by using the following equation:

$$\alpha = \frac{1}{c} \left( \frac{1}{\tau_1} - \frac{1}{\tau_2} \right) \quad (2.6)$$

If the absorption coefficient is measured at various wavelengths ( $\lambda$ ), the spectrum ( $\alpha$  vs.  $\lambda$ ) for any absorbing species can be constructed. For accurate measurements it is required to measure  $\tau_1$  for each wavelength to account for variations in R with wavelength.



One advantage of CRDS is that the results are not distorted by shot-to-shot fluctuations in laser intensity. This is proven by examining equation 2.6. The ring-down times are dependent only on the time dependence of the signal given by equation 2.5. This allows for accurate signal averaging and a relatively quantitative spectrum.

Another main advantage to CRDS, as previously mentioned, is the increased sensitivity due to the dramatically increased effective path length. Continuing with the example above for a 1.0 m cavity with a 66.71  $\mu\text{s}$  ring-down time, the cavity enhancement will increase the effective path length from 1.0 m to  $L_{\text{eff}} = c\tau = 20$  km. At best, designs may incorporate mirrors with reflectivities of 99.999% giving a ring-down time of 333.6  $\mu\text{s}$  for a 1.0 m cavity. In this case  $L_{\text{eff}} \approx 100$  km, the equivalent to an absorption cell stretching from Emory University (Atlanta, GA) to the University of Georgia (Athens, GA). A statistical description of a CRDS instrument can be used to determine the minimum absorption coefficient. This description will be applied in the experimental section. However, the sensitivity can be approximated as follows. A typical ring-down measurement is  $\sim 40$   $\mu\text{s}$ . The error in this measurement is about 1% or 0.4  $\mu\text{s}$ . The ring-down time must then be reduced by absorption to a value beyond the error of the measurement, therefore below 39.6  $\mu\text{s}$ . Using equation 2.6, the minimum absorption ( $\alpha L$ ) which can be detected is then  $\sim 10^{-10}$  per pass.

## BIBLIOGRAPHY

- (1)Herbelin, J. M.; Mckay, J. A.; Kwok, M. A.; Ueunten, R. H.; Urevig, D. S.; Spencer, D. J.; Benard, D. J. *Appl Optics* **1980**, *19*, 144.
- (2)Anderson, D. Z.; Frisch, J. C.; Masser, C. S. *Appl Optics* **1984**, *23*, 1238.
- (3)Busch, K. W.; Busch, M. A. *Cavity-ringdown spectroscopy: an ultratrace-absorption measurement technique*; American Chemical Society, 1999.
- (4)Berden, G.; Engeln, R. *Cavity Ring-Down Spectroscopy: Techniques and Applications*; John Wiley & Sons, 2009.

### Chapter 3. Experimental

The apparatus used to measure the spectra of jet cooled combustion radicals utilized the high sensitivity of a cavity ring-down spectrometer. An electrical discharge was used to produce the radicals. The hot radicals produced in the discharge were then cooled by free expansion into a vacuum chamber prior to cavity ring-down absorption measurements. Various discharge/expansion nozzle configurations were tested in order to optimize the production of the radicals. The initial testing and continuous improvement of the experimental design will be presented in Chapter 4. Here, the optimal design will be described.

This system closely resembles the discharge-jet / cavity ring-down instruments reported by Linnartz et al. <sup>1</sup> and Wu et al. <sup>2</sup> The key elements are shown in Figure 3.1, and a more detailed illustration of the optimal pulsed valve and electrical discharge system is shown in Figure 3.2.

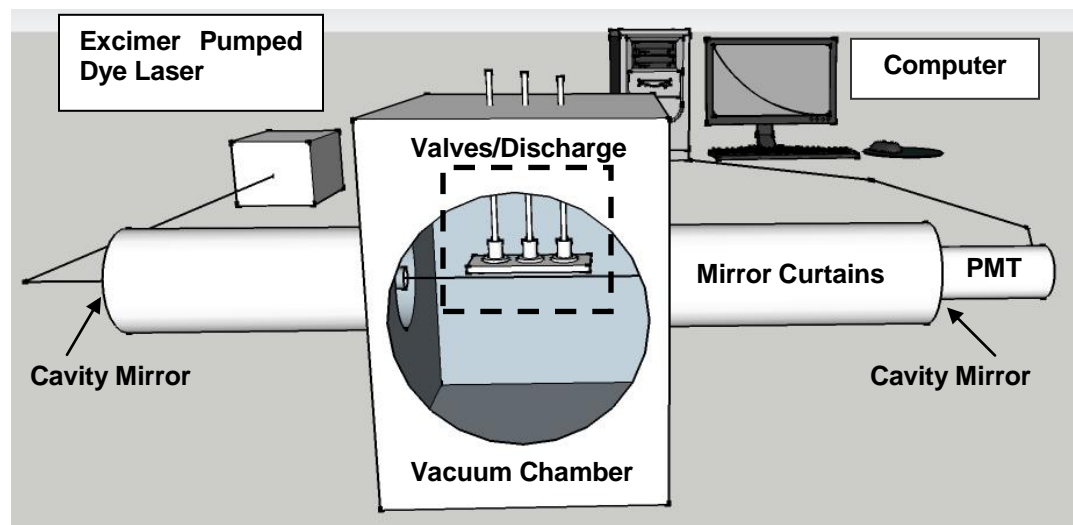


**Figure 3.1.** Experimental setup. The valve and discharge assembly in the dotted box are shown with more detail in Fig. 3.2.

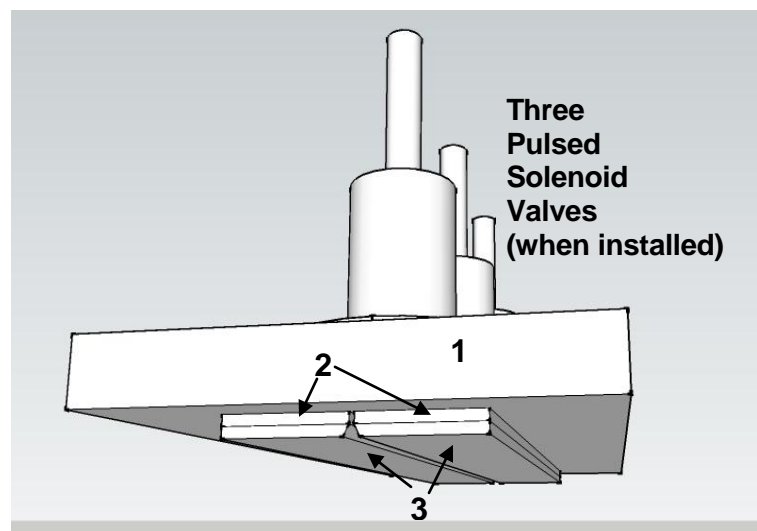


**Figure 3.2.** Pulsed valve assembly with slit electrodes. 1. Ground Plate; 2. Phenolic Insulator; 3. High Voltage Jaw

### 3.1. Cavity Ring-down Spectrometer

The 6-way cross vacuum chamber (MDC Vacuum Corp.) used in these experiments was equipped with precision optical mounts that held the mirrors used to form the optical cavity. The mirrors were mounted at the ends of two baffle arms, such that they were separated by a distance of 1.0 m (see Fig. 3.1). The mirrors were rated for 99.990 -99.999 % reflection, with a 6 m radius of curvature to correct for beam divergence. In order to protect the mirrors from the deposit of the radical precursor and discharge products, a slow flow of inert gas (usually He or Ar) was introduced near the end of each baffle arm. Inside the baffle arms, metal washers were used to further limit the ability of the radical precursor discharge products to reach the mirrors. These precautions allowed for several months of measurements without the need to clean the cavity ring-down optics. The chamber was evacuated by a 500 CFM Roots blower (Leybold, WSU 1001). The pressure in the vacuum chamber was 5 mTorr with the Roots blower operating. The pressure equilibrated to 15-60 mTorr with the mirror protection gas flowing. With the system under typical experimental conditions, ring-down times up to 200  $\mu$ s were observed.

A tunable pulsed dye laser (Lambda Physik, FL3002) pumped by a XeCl excimer laser (Lambda Physik, EMG201) was used for the ring-down experiments. The pulse duration was nominally 10 ns and the laser was operated at a repetition frequency of 10 Hz. The excimer pump laser power varied

between 60-250 mJ/pulse. The dye laser, operated with or without an intracavity etalon, had linewidths of 0.05 and 0.30  $\text{cm}^{-1}$  full width at half maximum (FWHM), respectively. Even for the latter, the linewidth was an order of magnitude greater than the free spectral range of the ring-down cavity ( $\sim 0.005 \text{ cm}^{-1}$  or 150 MHz). The output of the dye laser varied between 0.1-1.0 mJ/pulse.

Light exiting the optical cavity was detected by a photomultiplier tube (PMT). The output from the tube was captured by a 16 bit, 10MS/s GageScope A/D card which was installed in a personal computer. A LabVIEW program was used to control the experiment and extract ring-down decay rates from the time resolved signals. This program will be described in section 3.4. In general, to remove some of the noise from the pulsed discharge, the program was set to reject pulses for conditions where the discharge pulse failed to develop or was subject to localized arching.

10-15 pulses were averaged per wavelength point. This was usually sufficient to reduce the error in the ring-down decay rate to approximately 1%. Further noise reduction was achieved by co-adding multiple scans. This also helped to reduce the effects of signal drift resulting from soot buildup at the discharge, small alignment changes due to vibrations, and damage to the pulsed valve poppets, among other causes. Long survey scans averaging more than 15 pulses per wavelength point were not optimal because of drift. For longer survey scans the step size was normally 0.40  $\text{cm}^{-1}$ . Averaging of up to 100 pulses per

point were used for short scans over specific absorption features of interest in the survey scans. For these short scans the laser step size was normally set to  $0.04 \text{ cm}^{-1}$  ( $0.001 \text{ nm}$ ) for scans without the dye laser etalon, and  $0.008 \text{ cm}^{-1}$  ( $0.0002 \text{ nm}$ ) with the etalon installed.

### **3.2. Electrical Discharge Assembly**

Several designs for the electrical discharge followed by a jet expansion have proven effective for radical production. Our design mostly resembled that of Motylewski and Linnartz<sup>3</sup> and is shown in Figure 3.2. Three pulsed pin-hole valves (Parker-Hannifin, Series 9) were attached to the face of a 1.0 cm thick aluminum plate. Three 0.8 mm diameter holes were drilled through the plate to provide channels for the gas pulses. Flow rates from the pulsed valves varied from day to day, and sometimes hour to hour, resulting in variations in the discharge, gas concentrations, and ultimately resulting in large signal amplitude variations. Alternatively, the pulsed valves could be removed for continuous flow operation. Continuous flow resulted in high chamber pressures which lowered the cooling efficiency of the expansion. For this reason the pinholes were narrowed to 0.5 mm diameter holes for continuous operation to help reduce the gas loading. Although cooling was more efficient with the pulsed configuration, the continuous flow was advantageous because the flow rates were more stable over time.

The valve mounting plate and valve bodies were electrically grounded. Metal strip electrodes were mounted on the exit side of the plate. The electrodes were insulated from the grounded block by phenolic plates and attached to the grounded plate using non-conducting nylon or ceramic screws. The spacing between the edges of the plates was adjusted to form a slit that was 80 mm long and 0.8 mm wide. The slit formed the exit plane for a supersonic nozzle.

A large potential difference was applied across the first few millimeters of the gas expansion. The potential was applied by the outer negatively charged electrodes and the ground plate. Breakdown occurred and current flowed only when the gas density in the slit was high enough for conduction. The gas density was controlled by varying the backing pressure and/or opening time of the pulsed valves. The electrical current in the discharge was calculated using the voltage drop measurement across a ballast resistor. For this measurement, 1000:1 voltage dividers were placed before and after the ballast resistor. The circuit diagram is shown in Figure 3.3. The ballast resistance could be varied from 500  $\Omega$  to 100 k $\Omega$  to limit the current across the discharge and the high voltage of -300 to -1300 V was supplied by a Stanford Research Systems high voltage power supply (Model: VS325).



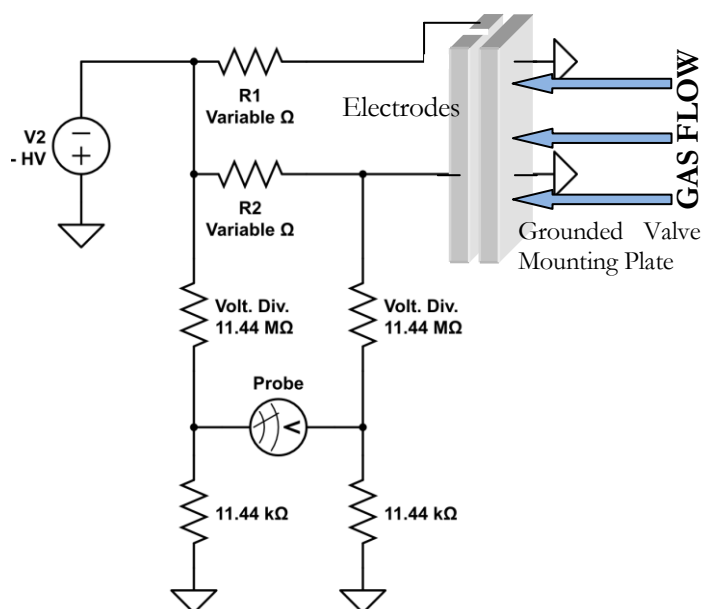


**Figure 3.3.** Electrical Circuit built to monitor the current supplied to the discharge.

The “probe” voltage at the voltage divider was recorded with the difference input of the GageScope A/D card. The discharge pulse was timed to coincide with the gas pulse to help reduce arcing and limit the current drawn. The discharge pulse started prior to the laser pulse. This was accomplished using a PVX-4140 Pulse Generator (Directed Energy, Inc) with the gate controlled by the delay generator also used to control the laser and pulsed valves. This allowed precise control of the relative timings between the laser, electrical discharge, and gas valves.

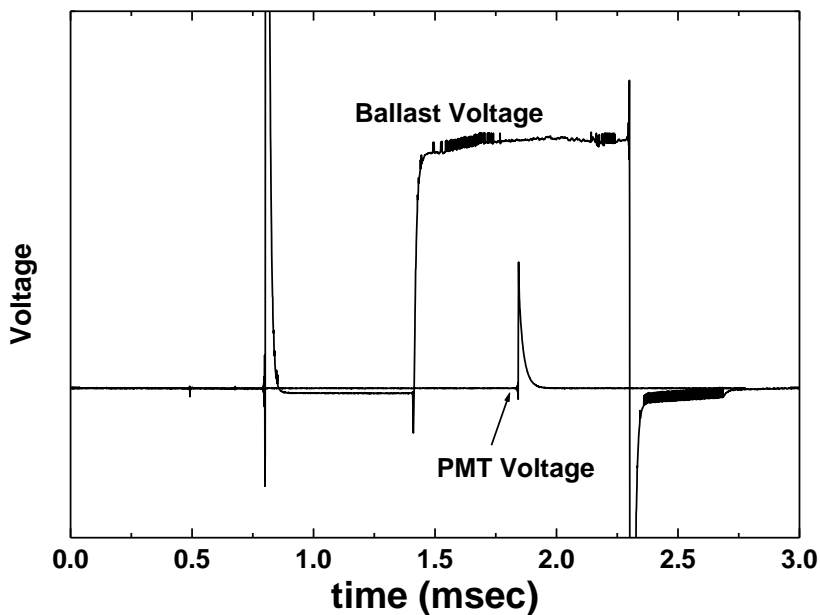


**Figure 3.4.** Temporal profiles for the ballast resistor and PMT voltages showing the relationship between the voltage applied to the electrodes, discharge initiation and the ring-down signal.

Figure 3.4 shows a typical timing sequence. First, the outer electrodes were charged with a high voltage. When sufficient gas densities flowed past the discharge plates, breakdown occurred and a voltage drop was observed across the ballast resistor. The ring-down measurement was taken after allowing adequate time for the discharge to stabilize ( $\sim 300 - 1000 \mu\text{s}$ ). Finally, after the ring-down measurement was taken, the power supply for the high voltage discharge was switched off. Previous studies<sup>4</sup> showed that a positive high voltage applied to the biased electrode produced a less stable discharge than a negative voltage and lower radical production rates were observed. At typical voltages ( $\sim 1000 \text{ V}$ ) the

discharge current was as high as 1.0 A while the discharge was on. The radical production efficiency and discharge stability depended on the ballast resistance, gas density, gas conductivity, precursor concentration, slit width, and applied voltage. Each was varied to optimize radical production.

The radical production in the discharge also depended on the choice of precursor molecule. The appropriate radical precursor was chosen so that the homolytic dissociation of the weakest bond would form the radical of interest. For example, the phenyl radical was formed from the precursor bromobenzene since the C-Br bond is the weakest bond in the molecule. The vapor phase precursor was seeded into a rare gas carrier flow by passing the gas over the surface of the liquid or through the liquid in a bubbler. The sample and gas lines could be heated to increase the partial pressure of the precursor.

### **3.3. Gas Expansion and Cooling**

Immediately after passing the electric discharge plates, the gas was expanded into a vacuum to cool the hot radicals. Cooling the radicals was necessary so that the majority populated low vibrational and rotational states. The shift of the population from a wide distribution of states to a smaller number of low energy states resulted in increased absorption for transitions from the low energy states. This also resulted in simplified spectra since the absorption from high vibrational and rotational states was removed. The valve opening duration was typically set to 700  $\mu\text{s}$  for the pulsed valve configuration. However, the

transit of the gas through the discharge assembly lengthened the gas pulse arriving in the chamber to nearly three times the width.

The use of an expansion to cool radicals produced in a discharge was first reported in the mid 1980's by Engelking<sup>5</sup>. With a pinhole source the density of the expanding gas decreased along the expansion length ( $x$ ) by  $\sim 1/x^2$ . Slit expansions were developed<sup>6</sup> next as an alternative, with the advantage that the expanding gas density decreased by  $1/x$ . This design used a pinhole expansion which was then confined into a slit discharge. The assembly produced a gas flow pattern that resembled a pulsed slit valve by confining the pinhole expansion into the slit discharge. However, a pinhole description was used here to determine the minimum detectable absorption coefficient as a function of distance from the nozzle since the confinement of the expansion to a slit would only improve the sensitivity. Michael Morse has published an excellent review<sup>7</sup> of this theory. The basics are described here and applied to our system.

In an adiabatic pinhole expansion, the average velocity along the expansion length,  $u(x)$ , approaches the maximum average velocity as internal energy and random translational motion is converted into directed mass flow within the expansion. The maximum average velocity of the gas (mostly He or Ar) can be determined by equating the enthalpy ( $5kT/2$ ) and the gas kinetic energy ( $mv^2/2$ ). For helium and argon the maximum average velocities are 1760

and 557 m/s respectively. The adiabatic cooling for a monatomic gas can be described by the difference in initial pressure ( $P_0$ ) and the final pressure ( $P_1$ ) by:

$$\frac{T_1}{T_0} = \left(\frac{P_1}{P_0}\right)^{\frac{2}{5}} \quad (3.1)$$

where  $T_1$  and  $T_0$  are the final and initial temperatures respectively. This equation shows that rapid cooling takes place and is dependent on the pressure ratio of the vacuum chamber pressure ( $P_1$ ) and the backing pressure ( $P_0$ ).

Since the speed of sound,  $a(T)$ , is dependent on  $T$ , the expansion velocity conditions along the expansion length ( $x$ ) are often described using the mach number,  $M(x) = \frac{u(x)}{a(x)}$ . Since the propagation of sound in a gas is also an adiabatic process, the mach number along the expansion can be approximated using:

$$M(x) = 3.26 \left(\frac{x}{D}\right)^{\frac{2}{3}} \quad (3.2)$$

for a monatomic gas where  $D$  is the diameter of the pinhole. From this value, the temperature (and the pressure and density using the ideal gas law) can finally be estimated along the expansion length:

$$T_1(x) = T_0 \left[1 + \frac{M(x)^2}{3}\right]^{-1} \quad (3.3)$$

The above equations can be used to approximate the conditions of the expansion in this study since most of the expanding gas was monatomic. For example, during a typical experiment a precursor with a vapor pressure of 7.6

Torr was seeded in 760 Torr of room temperature argon (99% monatomic gas). At 5 mm from the 0.46 mm pinhole the Mach number was  $M=15.9$ . If there were no discharge and the expansion were completely adiabatic, the expected temperature at 5 mm would be 3.5K. With 10% radical production efficiency from the discharge, which is reasonable based on halide dissociation efficiencies reported in a similar discharge source<sup>8</sup>, a radical density of  $3.7 \times 10^{11} \text{ cm}^{-3}$  (11  $\mu\text{Torr}$ ) would be present 5 mm from the pinhole. Using equations 2.1 and 2.5, the experiment would require an absorption cross section of  $5.0 \times 10^{-19} \text{ cm}^2$  to provide a 1.8 % change in a 40  $\mu\text{s}$  ring-down time (path length = 10 cm). This is just above the 1% relative error of our measurement and near the limit of the spectrometer. The minimum detectable absorption cross section for a typical experiment using this spectrometer is then  $\sigma_{\text{min}} \sim 5.0 \times 10^{-19} \text{ cm}^2$ . This minimum absorption cross section could be decreased by extended averaging, heating the precursor, using a larger pinhole, detecting radicals closer to the pinhole source, and/or adjusting the discharge parameters to increase radical production efficiency.

### 3.4. LabVIEW Programs

LabVIEW programs were used to process and store data recorded by a Gage Applied Technologies A/D card. The programs recorded two sets of data simultaneously. The first was the transient voltage difference reading labeled

“probe” in Figure 3.3. The second was the transient voltage from the photomultiplier tube. This was used to calculate the ring-down time.

The natural log of the ring-down trace was plotted and the ring-down time was calculated from the measured slope. Consecutive measurements at each wavelength were acquired for signal averaging. The shot-to-shot  $R^2$  value for the linear fit was also recorded. Any outliers were removed by setting a threshold for both the  $R^2$  value (usually a few standard deviations). Outliers in the ring-down averaging were common for a variety of reasons including arching in the discharge, the laser beam being blocked, etc, and resulted in large error if the ring-down mean was calculated without their removal. The program also recorded the mean discharge current from the discharge probe reading by averaging the probe voltage for a specified range.

During a typical scan the program recorded the ring-down time and current, sent a signal to the laser to change wavelength, and repeated until the ring-down time measurements were completed for a specified range. If an outlier was removed a new measurement would replace the outlier. This assured a consistent noise level for the baseline. When necessary, a calibration spectrum (i.e.,  $I_2$ ) could be acquired simultaneously.

After the scan was completed a file was created to store the average ring-down time, average discharge current, and calibration intensity for each

wavelength point. A separate text file was created which stored important parameter and values of the controls for the experiment.

Spectral subtraction was also possible if the laser pulsed at 10 Hz while the discharge pulsed at 5 Hz. Equation 2.6 shows that two ring-down measurement were needed to calculate the absorption coefficient of a species; one with the species present, and another with the species absent. In this case, the ring-down time was measured with the discharge on and with the discharge off.



## BIBLIOGRAPHY

- (1) Linnartz, H.; Vaizert, O.; Cias, P.; Gruter, L.; Maier, J. P. *Chemical Physics Letters* **2001**, *345*, 89.
- (2) Wu, S.; Dupre, P.; Rupper, P.; Miller, T. A. J. *Chem. Phys. FIELD Full Journal Title: Journal of Chemical Physics* **2007**, *127*, 224305/1.
- (3) Motylewski, T.; Linnartz, H. *Rev Sci Instrum* **1999**, *70*, 1305.
- (4) Davis, S.; Anderson, D. T.; Duxbury, G.; Nesbitt, D. J. *Journal of Chemical Physics* **1997**, *107*, 5661.
- (5) Engelking, P. C. *Rev Sci Instrum* **1986**, *57*, 2274.
- (6) Lovejoy, C. M.; Nesbitt, D. J. *Rev Sci Instrum* **1987**, *58*, 807.
- (7) Morse, M. D. In *Experimental Methods in the Physical Sciences*; Dunning, F. B., Randall, G. H., Eds.; Academic Press: 1996; Vol. Volume 29, Part B, p 21.
- (8) Davis, S.; Uy, D.; Nesbitt, D. J. *J Chem Phys* **2000**, *112*, 1823.

## Chapter 4. Experimental Optimization

Many experimental parameters influenced the performance of the radical production and cooling efficiency within the expansion. A few examples were precursor concentration, pinhole size, and discharge voltage. A large amount of effort was taken to determine what experimental parameters were most important. The experimental design was often modified to optimize an important experimental parameter.

Parameters were optimized by changing the parameter and observing the result that the change made. For example, the discharge voltage varied between -300 to -1300 V. Eleven spectra were then taken at 100 V increments to observe the radical production efficiency vs. voltage. This is an example of a 1-dimensional effect. If a different parameter was changed, such as the discharge slit width, the voltage effect on radical production efficiency was different. Therefore a 2-dimensional study was designed. In this case the same eleven voltages were used for say four or five slit widths. Of course, each experiment took time and the 2-dimensional experiment took 50 times as much time as the 1-dimensional experiment.

Since the experiment had tens of parameters that affected performance, a systematic multidimensional approach was not possible. Instead a series of 1- or 2-dimensional experiments were performed to test the radical production efficiency and explore the properties of the discharge. The results from these

studies were useful to optimize the parameters and make changes and improvements to the experimental design in order to optimize the production of radicals. The following sections show the results of these studies from the first cavity ring-down spectra and ends with the detection of the phenyl radical. Several experimental design improvements were made along the way. Attempts to produce radicals by pyrolysis were also attempted and the results are reported in the last section.

## 4.1. Iodine

### 4.1.1. Introduction

Due to its strong absorption strength in the visible region of the electromagnetic spectrum, iodine ( $I_2$ ) is one of the most studied species in gas phase spectroscopy. The line positions and intensities for the  $B^3\Pi^+_{0+u} - X^1\Sigma_g^+$  electronic transition are well known<sup>1</sup> and are often used for a wavelength calibration. In this experiment, spectra of jet cooled  $I_2$  were recorded in order to test the functionality of the newly constructed pulsed nozzle, electrical discharge, and cavity ring-down spectrometer. The results gave important information about the sensitivity of the spectrometer as well as the cooling efficiency of the jet expansion.

#### 4.1.2. *Experimental*

This experiment used the initial design. The differences between the initial design and the optimum design described in Chapter 3 are described here. First, a different pulsed valve was used than the valve described in Chapter 3. For the I<sub>2</sub> experiments, a PSV pulsed supersonic valve (Jordan TOF Products, Inc.) was used. The valve was open for a fixed duration of approximately 60 μs. This valve produced pulsed gas flow through a 0.5 mm pinhole. An adaptor with microchannels was used to direct the gas from the valve pinhole to two 1.0 mm pinholes that were above and in line with the laser probe beam. Another difference was the use of a diffusion pump instead of the Roots blower to evacuate the chamber. This produced a lower ultimate chamber pressure (~2 μTorr), but the pumping speed was much slower. The chamber pressure increased to 50-100 μTorr when the pulsed valve was operating. The pressure was measured using an ion gauge. The discharge setup was comparable to the design in section 3.2.

The 1.0 inch diameter mirrors were purchased from Los Gatos Research Inc. and had a maximum reflectivity of 99.995% at 500 nm. With a cavity length of 1.0 m, the optimum ring-down time was 67 μs. The reflectivity then decreased exponentially with wavelength from 500 nm. At 522 nm, the reflectivity dropped to 99.990 %.

I<sub>2</sub> was seeded into the helium carrier gas by passing the He at 760 Torr over the solid I<sub>2</sub> in a glass bubbler. The gas entering the nozzle was then 0.05% I<sub>2</sub> in He since the vapor pressure of I<sub>2</sub> at room temp (23 C) is 0.3843 Torr.<sup>2</sup> Ten ring-down time measurements were averaged at 0.001 nm (0.04 cm<sup>-1</sup>) increments. After a few days of pulsing the gas the mirrors were dirtied by the I<sub>2</sub> resulting in reflectivity loss. This prompted the addition of the mirror curtains described in Chapter 3. In these experiments, N<sub>2</sub> was used to purge the mirrors.

#### 4.1.3 Results and Discussion

Figure 4.1 shows selected cavity ring-down absorption spectra. The relative intensities of spectra (b)-(d) are plotted to the same scale as spectrum (a) but are shifted on the y-axis for comparison. These are some of the first spectra recorded with this spectrometer. The ring-down time without I<sub>2</sub> present was ~ 40 μs in this region. The absorption coefficient for each wavelength measurement was then calculated using the equation:

$$\alpha = \frac{L}{lc} \left( \frac{1}{\tau_1} - \frac{1}{\tau_2} \right) \quad (4.1)$$

which is a modification of equation 2.6 to account for the difference between the absorption path length per pass ( $l = 5$  cm) and the cavity length ( $L = 100$  cm).

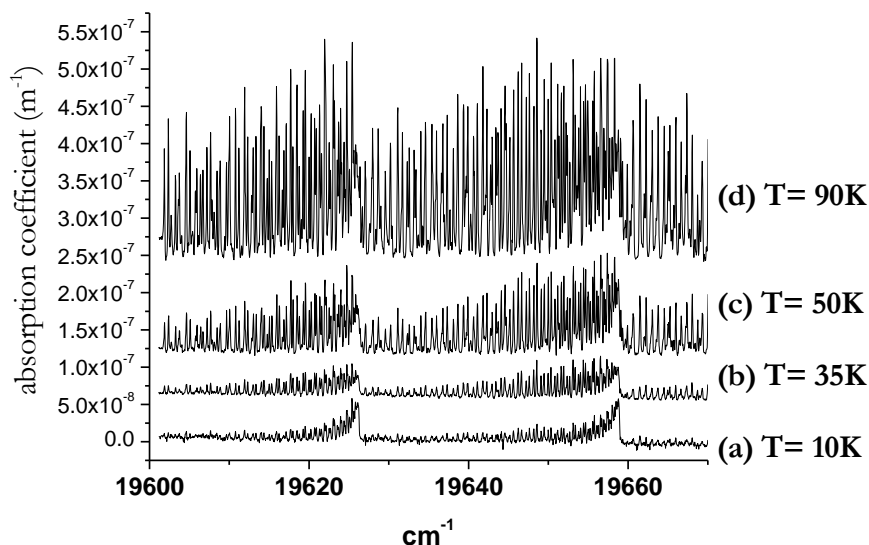


**Figure 4.1.** The 48-0 and 49-0 bands of the  $B^3\Pi^+_{0+u} - X^1\Sigma_g^+$  transition of  $I_2$  measured at (a) 32 mm (b) 18 mm (c) 8 mm (d) 3 mm from the pinhole source.

The four traces shown in Figure 4.1 are the absorption spectra for  $I_2$  at various distances from the nozzle pinhole, increasing in distance from top to bottom. As predicted by the description of the gas expansion in section 3.3, there was a decrease in both the temperature and density as the gas expanded away from the pinholes. As seen in at 10K, only the low J states with transitions near the band origin were populated at low temperatures. The temperatures listed in the figure are the rotational temperatures obtained by comparing the experimental spectra to simulations with various rotational temperatures. PGOPHER software<sup>3</sup> produced the simulations and has stored  $I_2$  lines<sup>4</sup> as a calibration option in the program. The software has the added option to broaden lines with a specified Gaussian and/or Lorentzian linewidth. Relative line

intensities were determined based on a defined rotational temperature using a Boltzmann distribution.

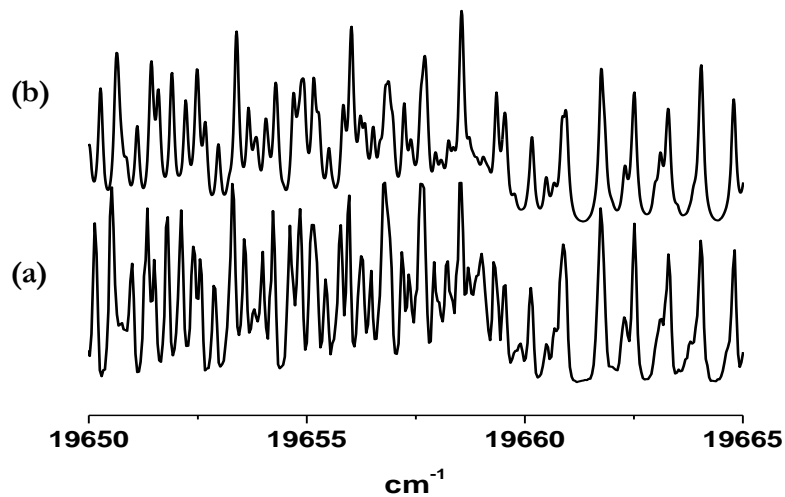


**Figure 4.2.** Expansion of Figure 4.1 (a) experimental data with (b) calculated spectrum.

Figure 4.2 compares the experimental spectrum to the simulated spectrum for a portion of the spectrum in Figure 4.1d. The relative line intensities of the simulated spectrum had the best agreement with the experimental spectrum at 90 K using a Gaussian linewidth of  $0.13 \text{ cm}^{-1}$ .

Slightly warmer temperatures were measured than were expected. Using the equations from section 3.3, we expected temperatures of 1, 2, 5, and 18 K for the distances listed in Figure 4.1. The most probable reason for the discrepancy was the effect of the microchannel adaptor that channeled the flowing gas out through two pinholes. This produced a drop in backing pressure prior to the final expansion. The pressure drop decreased the cooling efficiency since the

cooling efficiency is dependent on the pressure ratio  $P_1/P_0$  (see equation 3.1). Another possibility was the presence of the discharge assembly - a smaller version of the assembly described in Chapter 3. This confined the expansion within the electrodes thereby increasing the number of collisions. To test this effect the microchannel adaptor and discharge assembly were removed. The cooling efficiency was improved and a temperature of 5 K was measured for  $I_2$  at a distance of 14 mm from the pinhole source. The predicted temperature was 2.5 K.

The iodine experiments also give information about the instrumental sensitivity and whether the spectrometer had the ability to observe small cyclic radicals. The baseline noise level of the absorption coefficient (y-axis) in Figure 4.1a was  $\sim 1.0 \times 10^{-8} \text{ m}^{-1}$  which corresponded to about 1% error in the ring-down time measurement (Eq. 2.6). The main impetus for this study was to observe small cyclic radicals such as the phenyl radical ( $\sigma_{504.8 \text{ nm}} \sim 5.0 \times 10^{19} \text{ cm}^2$ )<sup>5</sup>. Using the equations from Section 3.3 it was expected that the phenyl radical would produce a 6% change in ring-down time under the following conditions: 1% precursor (such as bromobenzene @ 70C)<sup>6</sup>, two 1 mm pinholes with a 4 cm path length, 10% radical production efficiency, and a 5 mm detection distance. This was well within the sensitivity of the spectrometer.

Finally, the effect of the discharge was tested. The appearance of the discharge was a bluish-white plasma due to emission from the excited electronic



states of Helium. The intensity of emission was strongest near the discharge source and decreased in intensity along the distance of the expansion. Visible emission was observed for several centimeters in the expansion. Breakdown within the gas occurred at -500 to -600 V.  $I_2$  was still observed in the spectrum with a discharge voltage of -600 V. When the voltage was changed to -800 V, the  $I_2$  intensity decreased  $\sim 60\%$ . At -1000 V,  $I_2$  was not observed in the spectrum and was assumed to be dissociated to atomic I.

The experiments for  $I_2$  showed that sufficient cooling was achieved by gas expansion. As expected, the gas temperature decreased with distance in the expansion and the spectra of  $I_2$  was greatly simplified at low temperatures due to the population of only low J states. However, the concentration of  $I_2$  also decreased with distance. Therefore, when optimizing the detection distance, a compromise between concentration and temperature was necessary. We also found that the electrical discharge could dissociate  $I_2$  which has a bond dissociation energy of 36 kcal/mol<sup>7</sup>.

## 4.2. $C_2$

### 4.2.1. Introduction

Since the discharge proved to dissociate molecular iodine, the precursor was then switched to benzene or benzene halides with the hopes of producing and detecting the phenyl radical. Many experimental parameters were tested to

optimize radical production including discharge voltage, ballast resistance, backing pressure, and discharge equilibration time. Although the phenyl radical was not observed,  $C_2$  was produced and spectra were acquired. The results gave more information about the nature of the discharge.

#### *4.2.2. Experimental*

The spectrometer and electrical discharge for these experiments were similar to that described in section 4.1.2. The region 498-508 nm was scanned in hopes of observing the phenyl absorption reported at room temperature by Tonokura et.al.<sup>5</sup> Various precursors were used such as benzene halides and nitrosobenzene that have lower dissociation energies and therefore might be more likely to produce phenyl. Helium was used as the carrier gas. The voltages were varied from -500 to -1500 V. Figure 4.3 shows a typical timing sequence with the experimental setup described above.

The gas flow rate and discharge did not have time to equilibrate (compare to that of the optimal setup in Figure 3.4). The rise and fall of the ballast voltage indicates that valve was not open long enough to reach a maximum steady-state flow. The expected 60  $\mu$ s gas pulse was also spread out to nearly 250  $\mu$ s. This was due to gas spreading out in the microchannels prior to the free expansion.

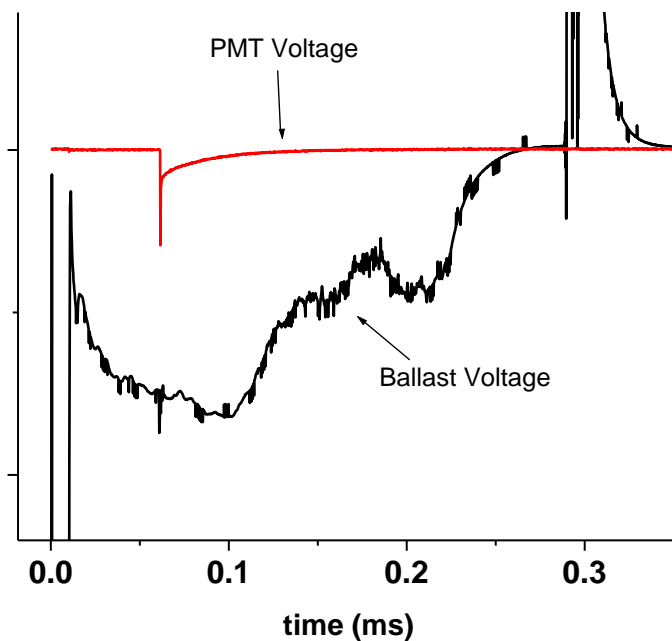


**Figure 4.3.** Temporal profiles for the ballast resistor and PMT voltages using the Jordan pulsed valve.

#### 4.2.3. Results and Discussion

Several spectra were acquired after expanding 0.5 % bromobenzene in He into the pulsed slit discharge. There were several absorption bands and peaks observed from 498 to 508 nm. The relatively large rotational splitting ( $B \sim 1.6 \text{ cm}^{-1}$ ) in one band was comparable to that of first and second row diatomic molecules.

Molecular constants for several candidates (CH, C<sub>2</sub>, H<sub>2</sub>, CN, etc.) were collected and compared to the observed data. The simulated spectra for C<sub>2</sub> matched the experimental data well. Absorption spectra of C<sub>2</sub> are well known

and the molecular constants<sup>8</sup> were used to reconstruct a theoretical spectrum using the PGOPHER software. The rotational temperature was determined by varying its value in the simulation until the relative peak intensities agreed with the experiment. A comparison of the theoretical and acquired spectra led to a confident assignment of the  $d^3\Pi_g - a^3\Pi_u$  ( $v'-v''=3-3$ ) transition (Swan band) of  $C_2$ .

To verify the assignment, a spectrum recorded with identical discharge conditions over the range 515-517 nm ( $19340-19420\text{ cm}^{-1}$ ) gave rise to large absorption bands corresponding to the 0-0 transition of the Swan band system. Figure 4.4 shows the recorded spectrum of this band with the corresponding theoretical spectrum at 130 K. The high temperature could be due to inefficient expansion or from the harsh conditions of the discharge itself.

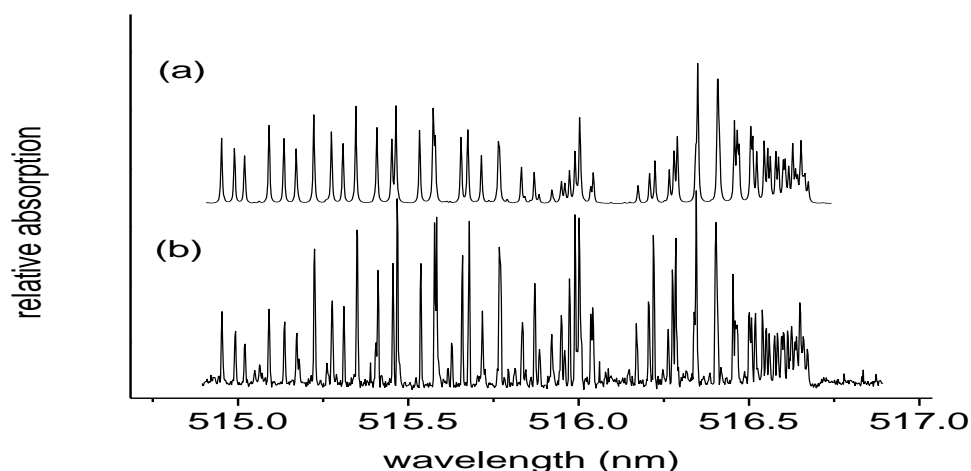


**Figure 4.4.** (a) Theoretical at 130K and (b) experimental spectrum of the 0-0  $d^3\Pi_g - a^3\Pi_u$  transition of  $C_2$  acquired using CRDS

The results indicated that the discharge supplied enough energy to break apart bromobenzene into small fragments. Higher energy discharges resulted in

more  $C_2$  production. This was the first indication that more energy was supplied by the discharge than was needed to remove only the Br atom from bromobenzene to produce phenyl. A wide variety of experimental parameters were varied in order to produce less destructive discharge conditions. There was no evidence of softer fragmentation in these studies. Absorption peaks for the phenyl radical were not observed.

### 4.3. $C_6H$

#### 4.3.1. *Introduction*

Since the phenyl radical was not detected, we next explored the extent of collision and chemistry in the gas expansion. It was possible that the yield of phenyl radical produced too little concentration for detection. However, it was also likely that the phenyl radicals recombined to larger cyclic molecules such as biphenyl.

The work of Motylewski and Linnartz<sup>9</sup> was reproduced to explore the possibility of chemistry in the gas expansion. They reported the rotationally resolved spin-orbit components of the origin band of the  ${}^2\Pi - X^2\Pi$  electronic transition of  $C_6H$  at 10 K. Their measurement was taken in a supersonic slit jet plasma by cavity ring-down detection. The  $C_6H$  radical was produced by seeding  $C_2H_2$  in He, and passing the gas through the discharge before free expansion. The formation of  $C_6H$  from  $C_2H_2$  requires complex chemistry and multiple

reactive collisions. A reproduction of this chemistry in our system would suggest that collisions were frequent in the free jet expansion. If this was the case, phenyl may have been lost due to recombination reactions.

#### *4.3.2. Experimental*

Premixed 0.1% C<sub>2</sub>H<sub>2</sub> in He was used as the precursor for the C<sub>6</sub>H production. The spectrometer and electrical discharge for these experiments were similar to that described in sections 4.1.2. The Jordan pulsed valve was used and an adaptor channeled the flowing gas out through two 1.0 mm pinholes. The discharge voltages were varied from -500 to -1200 V. The region 526-528 nm was scanned in hopes of observing the C<sub>6</sub>H absorption reported by Motylewski and Linnartz<sup>9</sup>. Typical ring-down times were  $\sim 30 \mu\text{s}$ .

#### *4.3.3. Results and Discussion*

After systematically varying the discharge and detection conditions, the absorption spectrum of C<sub>6</sub>H was successfully reproduced. Figure 4.5 shows the recorded spectrum (b) along with the theoretical spectrum (a) at 40 K. C<sub>6</sub>H has an inverted <sup>2</sup>Π ground state.

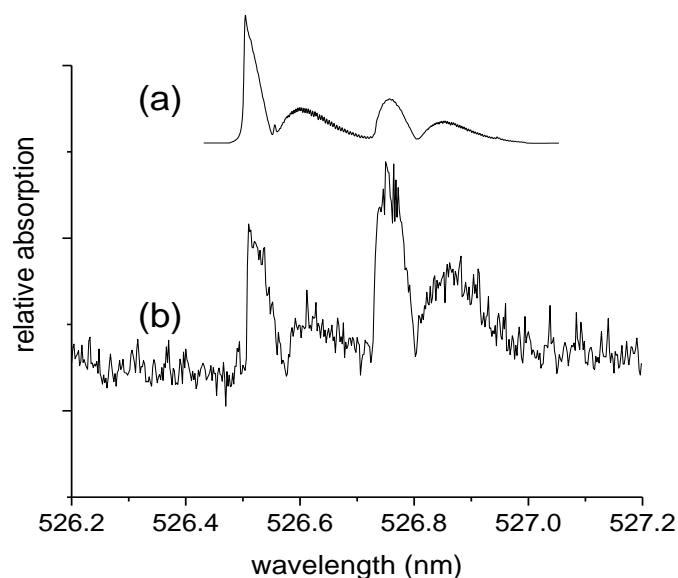


**Figure 4.5.** (a) Theoretical at 40K and (b) experimental spectrum of the origin band of the  ${}^2\Pi - X^2\Pi$  transition of  $C_6H$  acquired by CRDS.

Both the  $\Omega = 3/2$  and  $1/2$  components were observed in the spectrum and were separated by the difference of the spin-orbit constants ( $8.8\text{ cm}^{-1}$ ). Further experiments were completed to examine the cooling efficiency along the length of the gas expansion. The  $C_6H$  spectrum was acquired at varying distances from the discharge in the expansion. The radical was observed within the first 2 mm of the expansion. At this point the high gas densities and large amounts of collisions resulted in rotational temperatures of  $\sim 100\text{ K}$ . As the jet expanded, the sensitivity decreased and the temperature was quickly lowered to less than 30 K.

The results of this experiment have two important implications. First, radicals can be produced and react via collisions in the jet expansion. This is shown just by the detection of  $C_6H$  in the jet expansion. The second implication, which is more important for radical production and detection, was that there may have been large amounts of reactive collisions within the first few mm of the jet expansion. Motylewski and Linnartz<sup>9</sup> saw a rise in  $C_6H$  absorption with increased distance in the expansion suggesting its production by reactive collisions within the expansion. Also, previous studies have concluded that the residence time in the discharge is too short for  $C_6H$  producing radical-radical reactions to occur.<sup>10</sup> Therefore, the carbon chains must have been formed in the expanding plasma. This behavior can easily inhibit the detection of phenyl radical due to reactions before detection. Furthermore, if the radical must be detected near the discharge, a wide range of states are populated which may complicate and reduce the intensity of acquired spectra. Low concentrations of precursor may help to reduce unwanted radical-radical or radical-precursor collisions during the initial stages of the jet expansion.



## 4.4. $\text{N}_2^+$

### 4.4.1. *Introduction*

Considering the results of the previous experiments, if the phenyl radical was being produced in the discharge, the best chance for observing the radicals was in the initial few mm of the expansion even though they would still be at high temperatures. The focus was next shifted to a different cyclic radical.

The other option was to measure absorption spectra for the phenoxy radical. It is also important in PAH formation but has a larger absorption cross-section than phenyl. The  $\text{C}^2\text{B}_1\text{-X}^2\text{B}_1$  origin band of phenoxy (near 390 nm) has an absorption cross section that is a ten times larger than phenyl at  $3 \times 10^{-18} \text{ cm}^2$ .<sup>11</sup> Detection of phenoxy would indicate that the phenyl radical may have been produced but the concentrations were too low to detect it.

### 4.4.2. *Experimental*

The spectrometer and electrical discharge for these experiments were similar to that described in sections 4.1.2. The Jordan pulsed valve was used and an adaptor channeled the flowing gas out through two 1.0 mm pinholes. The discharge voltages were varied from -500 to -1200 V. Several precursors were chosen to try to produce phenoxy in a slit jet discharge including phenol, ethyl phenyl ether, and methyl phenyl ether. A wide variety of experimental conditions (discharge voltage, detection distance, etc.) were tested in attempts to detect the phenoxy radical.

#### 4.4.3. Results and Discussion

Even with the detection beam directly at the orifice of the expansion, the selected precursors and various experimental conditions did not lead to any phenoxy absorption. However, the experiments did lead to some interesting results.

Peak (nm)	Species	Transition
382.08	He I	$1s2p - 1s6d$ ( $^3P^o - ^3D$ )
383.47	He I	$1s2p - 1s10d$ ( $^1P^o - ^1D$ )
387.28	He I	$1s2p - 1s9d$ ( $^1P^o - ^1D$ )
386-388	CN	$B^2\Sigma^+ - X^2\Sigma^+$ (0-0 and 1-1)
388.97	He I	$1s2s - 1s3p$ ( $^3S - ^3P^o$ )
389-392	$N_2^+$	$B^2\Sigma_u^+ - X^2\Sigma_g^+$
392.77	He I	$1s2p - 1s8d$ ( $^1P^o - ^1D$ )
396.58	He I	$1s2s - 1s4p$ ( $^1S - ^1P^o$ )

**Table 4.1.** Absorption features in region 381-397 nm from CRD spectrum of phenol discharge products.

Table 4.1 lists the observed absorptions of a long range wavelength scan for the discharge products of 0.05% phenol seeded in He. The single peaks correspond to the assigned He (carrier gas) atomic absorptions. The most intense molecular band feature was observed around 391 nm. The experimental spectrum is shown in Figure 4.6b. The relatively large rotational spacing ( $2.0 \text{ cm}^{-1}$ ) indicates small atomic masses, probably 2<sup>nd</sup> or 3<sup>rd</sup> row elements. The alternating intensities show the characteristic pattern of nuclear spin effects. For two bosons of  $I=1$  and  $m_I = -1, 0, 1$  there are nine possible combinations of the three values of  $m_I$ . There are nine nuclear spin wavefunctions associated with

those combinations. Six of them are symmetric to nuclear exchange and three are antisymmetric. When the nuclear spin statistics are considered, the result is an intensity alternation of 6:3 for  $J$  even:odd. The only boson in the chamber was N (from the mirror purge – see section 4.1.2). However,  $N_2$  does not have any electronic transitions in this region.

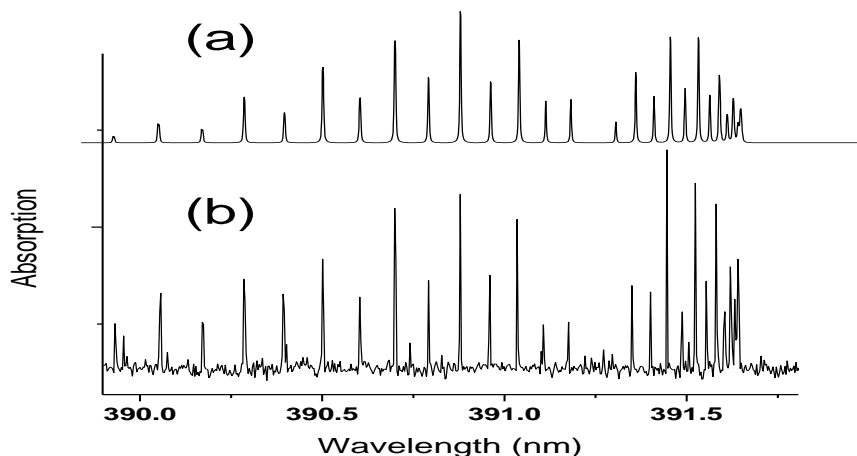


**Figure 4.6.** (a) Theoretical spectrum of the at the  $B^2\Sigma_u^+ - X^2\Sigma_g^+$  transition of  $N_2^+$  at 200 K and (b) experimental spectrum of the acquired by CRDS.

A weaker band to the blue of the large molecular band was also observed. However, it did not exhibit the same nuclear spin effects. The rotational splitting for that band indicated the presence of CN with a rotational constant of  $1.9\text{ cm}^{-1}$ . A PGopher simulation confirmed that the bands were in fact the well known  $v'-v'' = 0,0$  and  $1-1$  transitions of the  $B^2\Sigma_u^+ - X^2\Sigma_g^+$  CN electronic band.

Armed with this knowledge and the nuclear spin effects, it became clear that the larger band at 391.2 nm was the ion  $\text{N}_2^+$ . This was recognized by the fact that isoelectronic species, such as CN and  $\text{N}_2^+$ , have electronic bands in the same region on the electromagnetic spectrum. Also, CN and  $\text{N}_2$  have comparable moments of inertia due to the similar size of contributing elements. Therefore, they have similar rotational constants as observed in the spectrum. This was confirmed by comparing the band origin and rotational constant with previously observed values<sup>12</sup>. The theoretical spectrum (see Figure 4.6a - calculated using PGOPHER) of the  $B^2\Sigma_u^+ - X^2\Sigma_g^+$  transition of  $\text{N}_2^+$  at 200 K confirmed the assignment.

The detection of  $\text{N}_2^+$  was interesting because  $\text{N}_2$  gas was used only for mirror curtains and was not emitted into the discharge through the supersonic expansion. Therefore,  $\text{N}_2$  was being ionized by a different mechanism. This mechanism was believed to be through Penning ionization. Penning ionization is the removal of an electron from a molecule by the absorption of energy through a collision with an excited atom or molecule. In this case,  $\text{N}_2$  was ionized by metastable He atoms in the gas expansion.

Metastable He has enough energy to allow Penning ionization to be a plausible mechanism. The first ionization energy of  $\text{N}_2$  is 86.0 kcal/mol.<sup>13</sup> The lowest energy transition from the ground state of helium, the 1s to 2s transition, is 109 kcal/mol.<sup>14</sup> Since many transitions from even higher states were observed,

it is certain that electronically excited He in the expanding plasma carries more than enough energy to ionize  $N_2$ .

This mechanism was of interest because the harsh discharge conditions tended to obliterate precursor molecules when only a fraction of that energy was needed to dissociate a hydrogen or halide. Ne or Ar would be more suitable as a carrier gas since they carry less energy in their metastable states and would be less destructive. Also, the detection of CN indicated that Penning dissociation broke apart  $N_2$  which then combined with C atoms from the precursor fragments expanded from the discharge. The collision of metastable atoms with cooled precursor molecules (not sent through a discharge) could be an alternative, less destructive method to produce the radicals.

## **4.5. Redesign of the Valve System**

### *4.5.1. Introduction*

The initial tests of our experiment found that the jet expansion was capable of cooling molecules to low rotational temperatures. Phenyl and phenoxy radicals were not observed but free radicals, specifically  $C_2$ , were observed in the gas expansion. The presence of smaller radicals suggested that the discharge in our setup was too destructive for efficient selective dissociation of a single bond. Furthermore, the limited valve opening duration did not allow sufficient time for the discharge to equilibrate.  $C_2$  production was reduced by decreasing the discharge voltage but larger radicals such as phenyl or phenoxy

were not observed under these softer discharge conditions. The radical density was too low to detect larger radicals if they were produced in low yields under softer discharge conditions.

The next step was to redesign the valve system to produce a more stable, equilibrated discharge pulse with larger column densities and a longer path length. This would improve the ability to detect any larger radicals produced in the discharge even if the production efficiency was low.

#### *4.5.2. Experimental*

Several previously reported designs including those from Sharp et al.<sup>15</sup>, Sharpe et al.<sup>16</sup>, Miller et al.<sup>17</sup>, and Saykally et al.<sup>18</sup> provided a template for the redesign. The aim was to produce higher column densities in the jet expansion and a longer slit discharge. The Jordan valve was replaced with three collinear solenoid pinhole valves. The optimized design for this configuration was described in detail in Chapter 3. This new design, described briefly here, had three independently controlled 0.5 or 0.8 mm pinhole valves. The three pinhole valve configuration had three main advantages. First, the opening time for the pinhole solenoid valves could be controlled. This increased the gas flow rate per pinhole by allowing sufficient time for the gas flow to reach the maximum steady-state flow. Another advantage was that the longer valve opening time allowed for the discharge to equilibrate resulting in less variability in the experimental results.

The final advantage was the increased path length decreased the minimum detectable absorption cross section.

#### *4.5.3. Results and Discussion*

The effects of the increased gas density and path length were quickly apparent. The ring-down time decreased slightly ( $< 5\%$ ) when the gas pulses were on compared to an empty cavity. This effect was more prominent when the beam was aligned close to the nozzle where the gas density was the highest. A decrease in the ring-down time might indicate scattering losses.

When the discharge was turned on, the ring-down time always decreased significantly (1-50 %). A portion of the losses may have been due to scattering. The losses may also be attributed to broadband absorption from a wide variety of possible molecules and ions.

The most important observation was the measurable absorption of the phenyl radical using the multiple pinhole configuration. The spectroscopic characterization of the phenyl radical and other small cyclic PAH precursor radicals will be the focus of the following chapters. The increase in phenyl production and absorption was due to several factors.

The main benefit was the increased absorption path length. Absorption assigned to the phenyl radical was observed even when only two of the three pinhole valves were operating. The addition of a third pinhole not only increased the phenyl absorption more than expected but also decreased the absorption of

C<sub>2</sub>. This observation suggests that as more pinholes were added, the discharge conditions became softer and more efficient for phenyl production.

It is possible that metastable noble gas atoms produced the phenyl radical by collisional dissociation of bromobenzene. This mechanism is supported by the previous observation of Penning ionization of N<sub>2</sub>. An increase in phenyl absorption and decrease in metastable noble gas atoms as the expansion distance increased was also observed. The source of the metastable noble gas atoms was from high energy electron collisions with the noble gas atom. The excited state atom then collided with bromobenzene in the jet expansion to form the phenyl radical. The increased gas density would result in increased metastable noble gas atoms which would produce more phenyl radical in the expansion.

Various experimental parameters were varied to optimize the production of each radical studied. The details of the optimization studies will be presented in the experimental section for each radical of interest in the following chapters. In general the three pinhole configuration was the best for producing and detecting radicals.

## **4.6. Dissociation by Pyrolysis**

### *4.6.1. Introduction*

Pyrolysis is the thermal decomposition of a molecule. Radicals can be produced by pyrolysis through homolytic bond dissociation. A pyrolysis source



was constructed for this study based on the design reported by Kohn et al.<sup>19</sup> With this method, radicals might be produced more efficiently than with the more destructive electrical discharge source. After its construction, the pyrolysis source was tested with I<sub>2</sub> dissociation experiments. Although there was evidence of I<sub>2</sub> dissociation, attempts to observe single ring radicals by pyrolysis were unsuccessful.

The benzyl radical (C<sub>6</sub>H<sub>5</sub>CH<sub>2</sub>), among others, has been observed in previous pyrolysis studies. It can be produced by dissociation of the Cl-C bond in benzyl chloride. Benzyl recombination and the reactions of benzyl with other hydrocarbon radicals are important for combustion chemistry, especially in the formation of PAH's. Benzyl can be formed by the hydrogen abstraction at the methyl group of toluene by an OH radical. A radical-radical pathway to the formation of naphthalene may be by photoexcitation and H-atom loss of C<sub>10</sub>H<sub>10</sub> isomers produced by combination of benzyl with propargyl (C<sub>3</sub>H<sub>3</sub>).<sup>20</sup>

Contrary to the other radicals presented in the following chapters, the benzyl radical has been observed in fluorescence studies. Because of this, the visible spectrum of the benzyl radical has been well characterized. The visible spectrum of benzyl, with its origin at 22,002 cm<sup>-1</sup><sup>21</sup>, involves the excitation from the ground 1<sup>2</sup>B<sub>2</sub> state to the vibronically mixed 1<sup>2</sup>A<sub>2</sub>-2<sup>2</sup>B<sub>2</sub> excited states. Spectra in this region have been recorded at high resolution and have been definitively assigned.

#### 4.6.2. *Experimental*

The jet cooled benzyl radical was produced in an electrical discharge prior to pyrolysis experiments. This was done to provide a wavelength calibration intended to minimize the wavelength range scanned during the pyrolysis experiments. Two 0.8 mm pinholes spaced two inches apart provided continuously flowing benzyl chloride (2%) seeded in argon through the pulsed electrical discharge with a voltage of -900 V ( $\sim 100$  mA when the discharge was on). A ballast resistance of  $1000 \Omega$  was used. The backing pressure was 0.6 atm. The discharge slit was aligned 1.0 cm above the ring-down beam.

The pyrolysis source was based on a design reported by Kohn<sup>19</sup>. Two 0.8 mm ID nonporous high-alumina ceramic tubes (McMaster-Carr) rated for 3075° F were resistively heated using tungsten wire which was coiled around the tubes. The seeded gas flowed through the heated tubes. The tubes were mounted on a 0.8 cm thick aluminum block which also had pulsed valves mounted opposite the pyrolysis tubes. 0.8 mm diameter microchannels through the aluminum block connected the output of the pulsed valves to the pyrolysis tubes.

Ceramic and Plexiglass insulation was wrapped around the coils to reduce glow. Current was supplied to the coil by a variable autotransformer (Variac). The gas was either pulsed or flowed continuously through the heated tubes

before expansion into the vacuum chamber. The tubes were aligned 3-10 mm above the CRD detection beam.

#### 4.6.3. Results and Discussion

A cavity ring-down spectrum for jet-cooled benzyl chloride discharge products is shown in Figure 4.7 (bottom) along with the PGOPHER simulated spectrum (top) that was based on molecular constants from LIF studies. The rovibronic bands were assigned to the excitation from the ground  $1^2B_2$  state to the vibronically mixed  $1^2A_2$ - $2^2B_2$  excited states of the benzyl radical. The band at  $22,326\text{ cm}^{-1}$  is the known  $A^1$  band. The band at  $22,432\text{ cm}^{-1}$  is the known  $6a_0^1$  band. The  $A^2$  band was also observed.

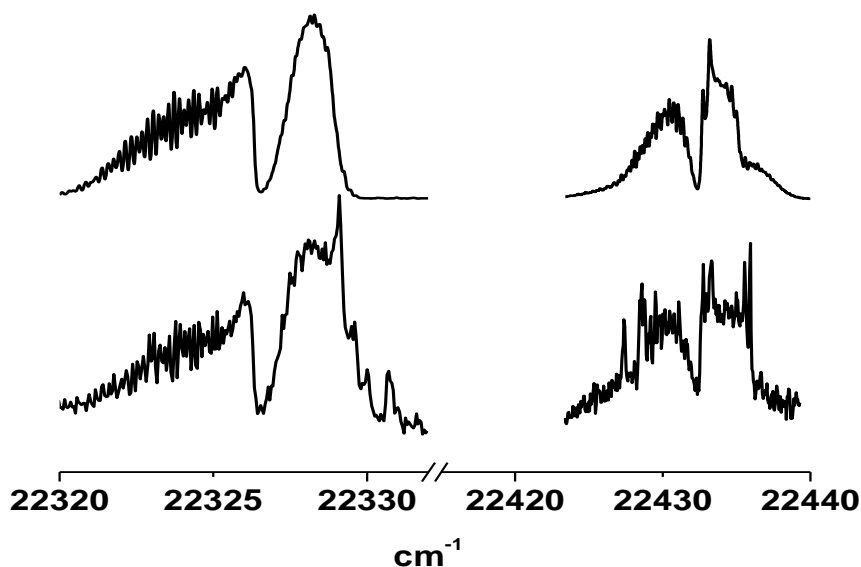


**Figure 4.7.** Visible CRD absorption spectra of products in an expansion of electrically dissociated benzyl chloride (bottom). The calculated spectrum (top) using the molecular constants from Lin et. al.<sup>22</sup> confirms the assignment.

There are some additional absorption features that overlap with the assigned bands. Weak absorption features were present across the entire 22,272-22472  $\text{cm}^{-1}$  region. The anomalous peak in the 22,326  $\text{cm}^{-1}$   $A^1$  band was 2.7  $\text{cm}^{-1}$  from the band origin. A similar feature was also observed in the  $A^2$  band and was also 2.7  $\text{cm}^{-1}$  from the band origin. This indicates that these features are associated with the benzyl radical. A hot band such as  $A^1 \nu_1^0$  would appear to the red of the origin. However, a hot band from  $A^1 \nu_1^1$  would appear to the blue if the energy of the mode  $\nu$  is larger in the excited electronic state than in the ground electronic state.

The results show that the benzyl radical could be produced in the electrical discharge using the benzyl chloride precursor. The sensitivity was high enough to characterize the spectrum and would provide a good reference for pyrolysis experiments.

Pyrolysis of  $\text{I}_2$  was explored before attempting to observe the benzyl radical with the pyrolysis source. As shown in section 4.1, the cavity ring-down spectrometer had adequate sensitivity to measure absorption spectra for jet cooled  $\text{I}_2$ . Preliminary studies showed that the addition of the unheated pyrolysis tube to a pinhole expansion had little effect on the expansion cooling efficiency.

Next,  $\text{I}_2$  spectra were recorded after heating the tube at various voltage increments. Voltage is used here to indicate temperature because the pyrolysis temperature was not directly measured. The voltage listed was the voltage drop

across the heating coil supplied by the Variac. A higher voltage corresponds to higher temperature. Figure 4.8 shows the spectra of jet cooled  $I_2$  at various heater voltages measured in the expansion 3 mm from the end of the pyrolysis tube. The pulsed valves were used and the solenoid voltage pulse duration was set so that the valves were open for 4 ms. The ring-down laser was fired 1.5 ms into the gas pulse. The results show an increase in the rotational temperature of  $I_2$  in the expansion as the voltage (pyrolysis temperature) increased.

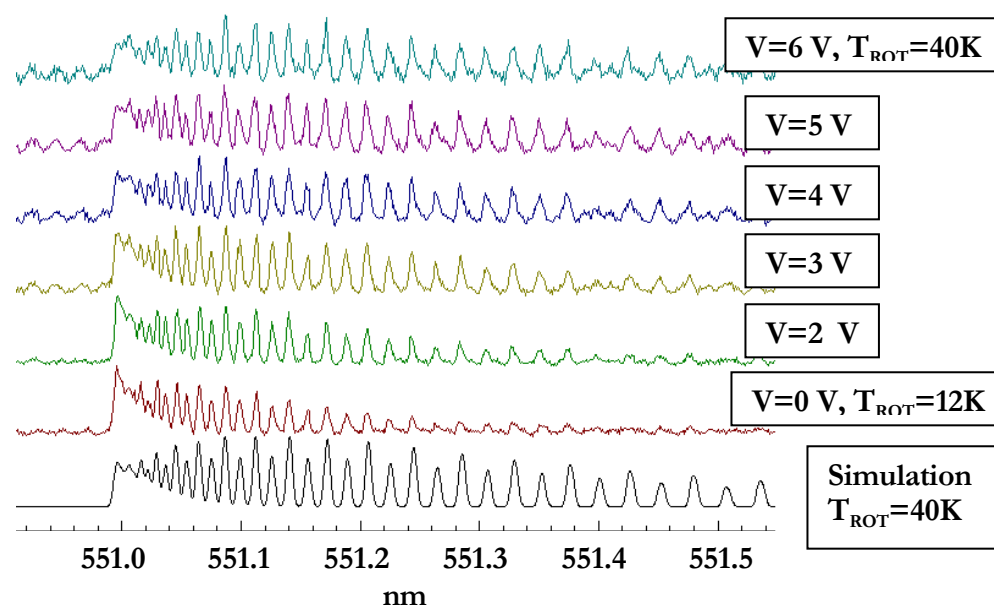


**Figure 4.8.** Experimental spectra of  $v'-v''$  23-0 band of  $I_2$  in a free expansion after passing through a pyrolysis tube at various voltages compared to a simulated spectrum at  $T_{\text{ROT}} = 40$  K.

The rotational temperature of  $I_2$  in the expansion increased from 12 K (with the source at ambient temperature,  $V = 0$  V) to 40 K at  $V = 6$  V. Also, the noise increased as the voltage was raised due to the PMT detecting the glow from the heating coil. Beyond  $V = 6$  V the PMT became saturated and a ring-down time could not be measured.

Next the absorption was measured while varying the delay between the gas pulse and the laser pulse. This time resolved study was done to examine the time dependence of the  $I_2$  absorption through the duration of the gas pulse. First, the CRD laser wavelength was set to the  $I_2$  23-0 R-branch band head. The delay was then varied while measuring the absorption at various delay times. The results for various voltages are shown in Figure 4.9.

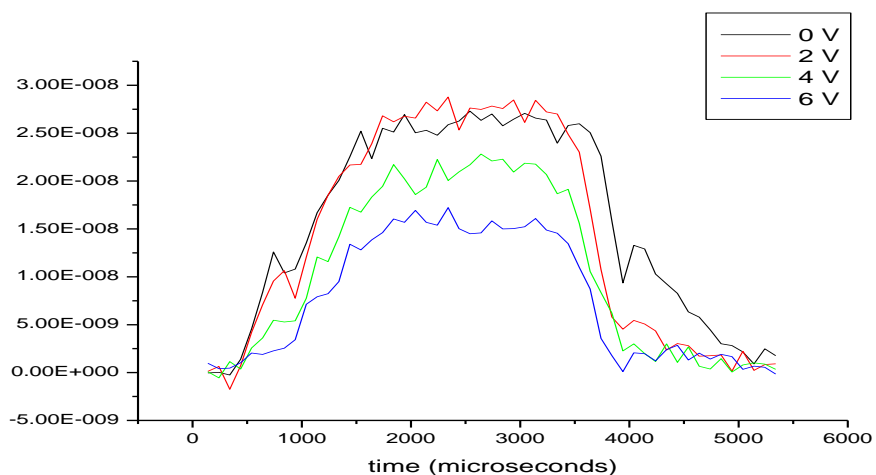


**Figure 4.9.** Absorption of  $I_2$   $v'-v'' = 23-0$  R-branch band head at various delays between the gas pulse and CRD laser pulse. The four traces show the time resolved absorption at various pyrolysis voltages corresponding to different pyrolysis temperatures.

As observed in Figures 4.8 and 4.9, the intensity of the R-branch band head at  $1200 \mu\text{s}$  was reduced by 50% when the voltage was changed from  $V=0 \text{ V}$  to  $V=6 \text{ V}$ . The main cause of the reduction was attributed to the redistribution of the population to higher energy rotational states, not dissociation. This trend was true for the majority of the gas pulse duration. However, there was a  $> 50\%$  reduction in  $\text{I}_2$  absorption at the beginning  $800 \mu\text{s}$  and last  $200 \mu\text{s}$  of the gas pulse. This indicates that dissociation might have occurred in this time range. To further investigate this observation, the full  $\text{I}_2$  spectrum was measured with a  $700 \mu\text{s}$  time delay between the start of the gas pulse and the CRD laser measurement with and without pyrolysis ( $V = 0 \text{ V}$  and  $V = 6 \text{ V}$ ). This allowed enough time for ample gas density but was short enough to remain in the delay range where the R-branch absorption was significantly decreased due to pyrolysis.

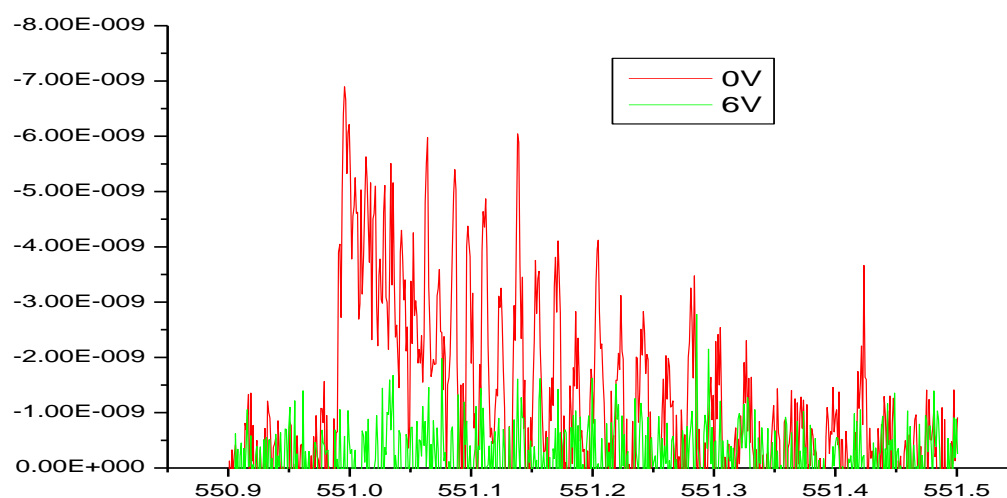


**Figure 4.10.** CRD spectrum taken 3 mm into the expansion of  $\text{I}_2$  seeded in argon after passing through a pyrolysis tube with (6 V) and without (0 V) heating.

As shown in Figure 4.10, the concentration of  $I_2$  was decreased beyond the detection limits after pyrolysis using  $V = 6$  V. This is evidence that dissociation was occurring at the beginning millisecond of the gas pulse. As gas flow continued beyond this time period the pyrolysis tube temperature decreased due to heat loss by convection and dissociation no longer occurred. A larger voltage (higher T) would have extended this dissociation period into the region of the gas pulse where there were higher densities. Attempts to increase the voltage beyond  $V = 6$  V resulted in failure of the pyrolysis heating element, PMT saturation, and/or cracking of the ceramic pyrolysis tube.

The next step was then to produce benzyl by pyrolysis and detect the radical by CRDS. Unfortunately benzyl was not detected using various voltages and delay times.



## BIBLIOGRAPHY

- (1) Gerstenkorn, S.; Luc, P. *Atlas du spectre d'absorption de la molécule d'iode, 14800-20000 cm<sup>-1</sup>*; Centre national de la recherche scientifique: Paris, 1978.
- (2) Yaws, C. L. *Handbook of vapor pressure*; Gulf Pub. Co.: Houston, 1994.
- (3) C.M. Western, P., a program for simulating rotational structure, University of Bristol, 2007.
- (4) Martin, F.; Bacis, R.; Churassy, S.; Verges, J. *J Mol Spectrosc* **1986**, *116*, 71.
- (5) Tonokura, K.; Norikane, Y.; Koshi, M.; Nakano, Y.; Nakamichi, S.; Goto, M.; Hashimoto, S.; Kawasaki, M.; Andersen, M. P. S.; Hurley, M. D.; Wallington, T. J. *J. Phys. Chem. A* **2002**, *106*, 5908.
- (6) Ashcroft, S. J. *Journal of Chemical & Engineering Data* **1976**, *21*, 397.
- (7) Sanderson, R. T. *Chemical bonds and bond energy*; 2d ed.; Academic Press: New York, 1976.
- (8) K.P. Huber, G. H. C. o. D. M. d. p. b. J. W. G. a. R. D. J., III) in NIST Chemistry WebBook, NIST Standard Reference Database Number 69, Eds. P.J. Linstrom and W.G. Mallard, June 2005, National Institute of Standards and Technology, Gaithersburg MD, 20899 (<http://webbook.nist.gov>). .
- (9) Motylewski, T.; Linnartz, H. *Rev Sci Instrum* **1999**, *70*, 1305.
- (10) Davis, S.; Anderson, D. T.; Duxbury, G.; Nesbitt, D. J. *J Chem Phys* **1997**, *107*, 5661.
- (11) Platz, J.; Nielsen, O. J.; Wallington, T. J.; Ball, J. C.; Hurley, M. D.; Straccia, A. M.; Schneider, W. F.; Sehested, J. *J Phys Chem A* **1998**, *102*, 7964.
- (12) Lofthus, A.; Krupenie, P. H. *J Phys Chem Ref Data* **1977**, *6*, 113.
- (13) Peters, D. *J Chem Phys* **1966**, *45*, 3474.
- (14) Ralchenko, Y., Kramida, A.E., Reader, J. and NIST ASD Team (2008). NIST Atomic Spectra Database (version 3.1.5), [Online]. Available: <http://physics.nist.gov/asd3>. National Institute of Standards and Technology, Gaithersburg, MD.
- (15) Sharp, E. N.; Roberts, M. A.; Nesbitt, D. J. *Physical Chemistry Chemical Physics* **2008**, *10*, 6592.
- (16) Sharpe, S. W.; Sheeks, R.; Wittig, C.; Beaudet, R. A. *Chemical Physics Letters* **1988**, *151*, 267.
- (17) Wu, S. H.; Dupre, P.; Miller, T. A. *Physical Chemistry Chemical Physics* **2006**, *8*, 1682.
- (18) Liu, K.; Fellers, R. S.; Viant, M. R.; McLaughlin, R. P.; Brown, M. G.; Saykally, R. J. *Rev Sci Instrum* **1996**, *67*, 410.
- (19) Kohn, D. W.; Clauberg, H.; Chen, P. *Rev Sci Instrum* **1992**, *63*, 4003.
- (20) Sebree, J. A.; Kidwell, N. M.; Selby, T. M.; Amberger, B. K.; McMahan, R. J.; Zwier, T. S. *Journal of the American Chemical Society* **2012**, *134*, 1153.
- (21) Porter, G.; Ward, B. *J Chim Phys* **1964**, *61*, 1517.

(22) Lin, T. Y. D.; Tan, X. Q.; Cerny, T. M.; Williamson, J. M.; Cullin, D. W.; Miller, T. A. *Chemical Physics* **1992**, *167*, 203.

## Chapter 5. The Phenyl Radical

### 5.1. Introduction

The phenyl radical ( $C_6H_5$ ) is a prototypical aromatic reaction intermediate. The properties of phenyl in the gas phase are relevant to astrochemistry<sup>1-3</sup> and hydrocarbon combustion<sup>4-6</sup>. For the latter, phenyl is thought to play a critical role in the formation of soot. The path involves a sequence of hydrogen abstraction and hydrocarbon addition steps that yield polycyclic aromatic hydrocarbons<sup>4,5</sup>.

Spectroscopic studies of phenyl date back to the first observation of the visible absorption bands (440-530 nm) by Porter and Ward<sup>7</sup>. This band system was identified as the  $1^2B_1-X^2A_1$  transition resulting from an  $n\leftarrow\pi$  electron promotion. Electron spin resonance studies of matrix isolated phenyl confirmed that the ground state has  $C_{2v}$  symmetry with the unpaired electron in a non-bonding carbon  $\sigma$ -orbital<sup>8-10</sup>. Matrix isolation techniques have also been used to examine the IR and UV/visible transitions of phenyl<sup>11-16</sup>. Friderichsen et al.<sup>16</sup> recorded extensive IR spectra for six isotopomers (deuterium substitutions) using Ar as the matrix host. Frequencies for twenty-four vibrational modes were reported and linear dichroism measurements were used to determine the orientations of the transition moments. Absorption spectra for phenyl in Ar were examined over the range from 4000 to 52000  $cm^{-1}$  by Radziszewski et al.<sup>13,14</sup> Transitions to the  $1^2B_1$ ,  $2^2A_1$  and  $1^2B_2$  excited states were identified. Vibrational

structure was observed in these spectra but not analyzed, as the focus was on symmetry assignment through linear dichroism measurements.

Recent gas phase studies of phenyl include the observation of the pure rotational spectrum<sup>2</sup> and a rotationally resolved IR spectrum for the 3071.89 cm<sup>-1</sup> fundamental of the  $\nu_{19}$  vibrational mode<sup>3</sup> (Wilson numbering). Both of these studies used supersonic jet-cooling with electrical discharge generation of the radical. Accurate geometrical parameters were derived from the rotational constants. The electronic band systems of phenyl at room temperature have also been revisited using the technique of cavity ring-down spectroscopy (CRDS). Lin, Park and co-workers<sup>6,17-19</sup> pioneered the use of CRDS as a means to follow the reaction kinetics of C<sub>6</sub>H<sub>5</sub>. Subsequently, Tonokura<sup>20</sup> et al. examined the  $1^2B_1-X^2A_1$  transition over the range from 18700-20500 cm<sup>-1</sup>. Rotational contours were recorded for the origin band and a hot band near 19630 cm<sup>-1</sup>. These contours were simulated using rotational constants derived from density functional theory (DFT) calculations. The electronic symmetry of the excited state was confirmed by the band contour analyses, but no attempt was made to refine the rotational constants. Vibrational constants for three of the twenty-seven vibrational modes of the excited state were determined.

Emission spectra have not been reported for phenyl and it is likely that the excited state quantum yields are low due to rapid internal conversion processes. In simulating the rotational contours of their room temperature

spectra, Tonokura et al.<sup>20</sup> assumed a Lorentzian lineshape with a width of  $0.5 \text{ cm}^{-1}$ , corresponding to an excited state lifetime of 11 ps.

Electronic structure calculations have been carried out for the ground and excited states of phenyl. Recent work includes Mattar's<sup>21</sup> study of the ground state geometry, magnetic properties and vertical transition energies using DFT methods, Kim et al.'s<sup>22</sup> calculations of vibronic spectra for transitions from the ground state to the states in the  $17000\text{-}44000 \text{ cm}^{-1}$  energy range using the multi-reference configuration interaction technique, and Biczysko et al.'s<sup>23</sup> prediction of the vibronic band structure of the  $1^2B_1\text{-}X^2A_1$  transition.

In the experimental work conducted to date, the relatively low resolution achieved has limited the accuracy with which the electronically excited states could be characterized. Rotationally resolved data have not been obtained for any of the excited states. In part, the inability to observe resolved rotational structure is a consequence of the spectral congestion resulting from the population of a large number of rotational levels at room temperature. This problem can be mitigated by applying the jet-cooling techniques that were used successfully to obtain microwave<sup>2</sup> and IR spectra<sup>3</sup>. Here the cavity ring-down spectra are reported for the  $1^2B_1\text{-}X^2A_1$  transition of jet-cooled phenyl. Partially resolved rotational structure was observed. Homogeneous line broadening was detected and the Lorentzian linewidth was used to determine the lifetime of the excited state. The vibrational mode numbering used for the  $1^2B_1$  state is that of

Tonokura et al.<sup>20</sup> Transitions to  $9^1$  and  $10^1$  were characterized. These are both in-plane carbon ring vibrations of  $a_1$  symmetry.

## 5.2. Experimental

The experiment was comprised of a cavity ring-down spectrometer, pulsed valve system and an electrical discharge. The experimental setup was described in detail in Chapter 3. Presented here are the details related to the optimization of the experiment for the production and detection of the phenyl radical.

Typical ring-down decay lifetimes were close to 40  $\mu$ s with an error less than 1% when averaging 10 shots per wavelength measurement. The laser step size was normally set to 0.001-0.003 nm ( $\sim 0.04$   $\text{cm}^{-1}$  at 500 nm). This step size was less than the laser bandwidth of  $\sim 0.15$   $\text{cm}^{-1}$ . An etalon was installed in the dye laser oscillator for higher resolution scans with a bandwidth of 0.04  $\text{cm}^{-1}$ . The spectral range of 500 - 530 nm for  $\text{C}_6\text{H}_5$  was chosen by considering our mirror range, dye laser spectral range, and previous data from the literature. The frequency of the laser was calibrated for each scan using absorption lines from metastable noble gas atoms present in the discharge or by simultaneously recording a LIF spectrum of  $\text{I}_2$ .

Approximately 1-4% bromobenzene 99+% (Aldrich Chemical Company, Inc, Milwaukee Wisconsin) or chlorobenzene 99.9% (Sigma-Aldrich, Milwaukee

Wisconsin) was seeded in argon or first run neon (Specialty Gases Southeast, Suwanee, GA). The precursor was added by flowing the carrier gas over the liquid precursor prior to reaching the pulsed valves. The concentration of bromobenzene was raised by heating the sample holder and gas lines up to 70 °C. The gas mixture was pulsed through two pinhole orifices using the Parker series 9 general valves.

The voltage applied to the outer electrodes of the discharge ranged from -550 to -900 V. Higher voltages often resulted in higher radical production efficiencies. The current varied between 100-500 mA when the discharge was on. Optimal conditions included argon carrier gas, high backing pressures (2-3 atm), high precursor concentration (4%), 0.8 mm slit width, and 200-300 mA of drawn current. The HV discharge plates were isolated from the mounting plate with the phenolic insulator. Close to the discharge (<5mm) sensitivity was high due to large concentrations. However, rotational temperatures at this position were often tens of Kelvin. A few centimeters downstream in the expansion the rotational temperature dropped to less than 10 K but sensitivity was lost due to lower radical concentrations at the beam path. A compromise put our measurements around 1.0 cm from the nozzle. Subsequent studies showed that the phenyl radical could be produced efficiently at cold temperatures with the continuous expansion configuration. However, only results from the pulsed expansion are presented here.

### 5.3. Experimental Results

A typical CRD spectrum (18888 – 19845  $\text{cm}^{-1}$  or 504 – 530 nm) for jet-cooled bromobenzene discharge products is shown in Figure 5.1. Features originating from  $\text{Ar}^*$ ,  $\text{C}_2$ , and the phenyl radical are indicated. Broadband absorption and/or scattering losses were present across the entire range of the spectrum. The ring-down time also changed with wavelength due to changes in mirror reflectivity. The absorption coefficient was calculated at each wavelength measurement using equation 4.1. The background ring-down time,  $\tau_2$ , was found by fitting to the spectrum baseline at small increments ( $<10 \text{ cm}^{-1}$ ).

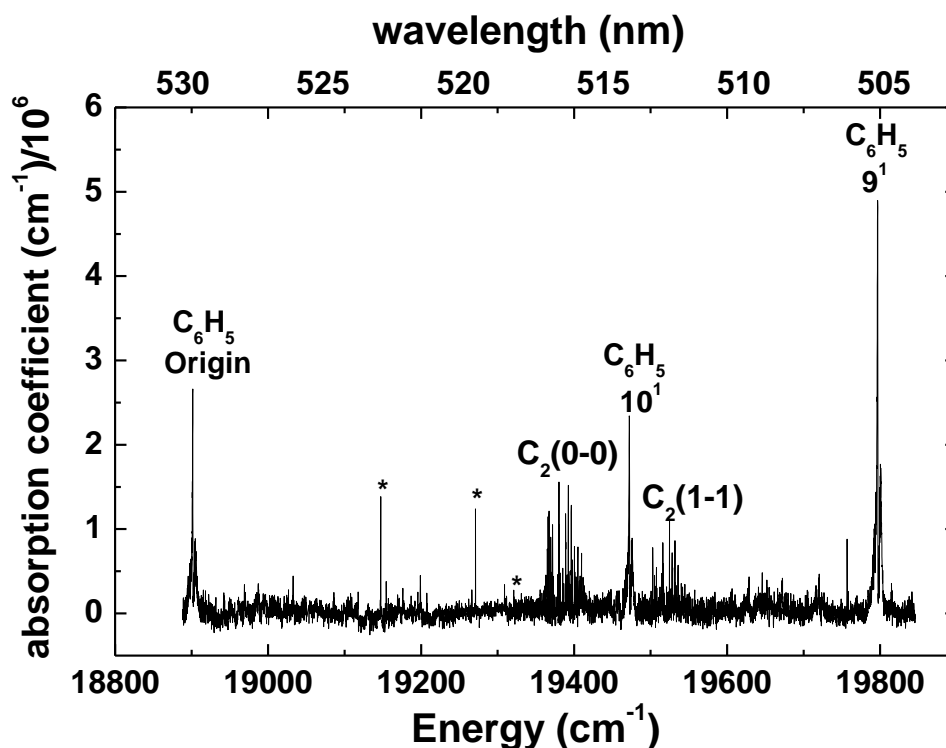


**Figure 5.1.** Visible CRD absorption spectrum of metastable argon ( $\text{Ar}^*$ ),  $\text{C}_2$  and the phenyl radical in an expansion from electrically dissociated bromobenzene.



The bands in Figure 5.1 near  $19380\text{ cm}^{-1}$  and  $19520\text{ cm}^{-1}$  were assigned to the well known (0-0) and (1-1) Swan bands of  $\text{C}_2$ . A comparison of the relative intensities of the lines in the 0-0 band with a simulation was consistent with  $T_{\text{rot}} \approx 30\text{ K}$ . Similarly, a comparison of intensities of the 0-0 band with the 1-1 band was consistent with  $T_{\text{vib}} \approx 5000\text{ K}$ . The low rotational temperature and high vibrational temperature was expected since the low energy collisions in the expansion transfer energy more efficiently with the nearly resonant rotational energy transitions rather than the relatively higher energy vibrational transitions. Other sharp peaks in Figure 5.1 were assigned to transitions originating from the  $3s^23p^5(^2P^{\circ}_{3/2})4p$  state of Ar.

As described below, the component of line broadening due to upper state decay processes for the phenyl radical was determined from the band contours. It was therefore important to characterize the lineshapes for transitions that were not lifetime broadened, in order to define the instrumental effects. This was accomplished by recording spectra for isolated lines of  $\text{Ar}^*$  and  $\text{C}_2$ . These data were consistent with a Gaussian lineshape with a FWHM of  $0.05\text{ cm}^{-1}$ , indicating that the Doppler broadening from the expansion was below the laser linewidth.

The absorption bands of phenyl were identified based on the results from previous studies. The measured transition energies are collected in Table 5.1. Rotationally resolved spectra were recorded for the origin band and the  $9_0^1$  and  $10_0^1$  fundamentals as assigned by Tonokura<sup>20</sup>. Examples of the higher resolution

spectra are shown in Figure 5.2. Note that the sharp, intense peak in the R branch of Figure 5.2 is the  $3s^23p^5(^2P^{\circ}_{3/2})4p - 3s^23p^5(2P^{\circ}_{3/2})8s$  transition of  $\text{Ar}^*$  at  $19801.12 \text{ cm}^{-1}$ .

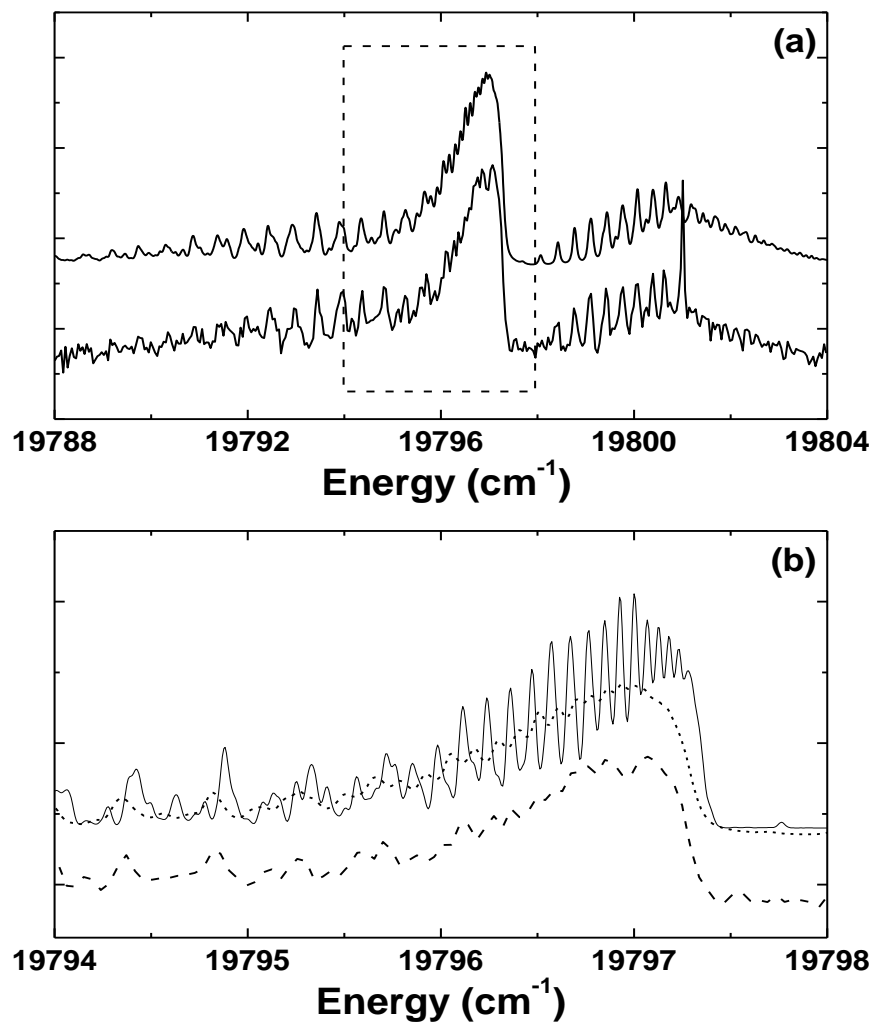


**Figure 5.2.** Rotationally resolved spectrum of the phenyl  $1^2B_1 - X^2A_1 (9_0^1)$  transition. **a)** Experimental spectrum (bottom) and best fit simulation (top). **b)** Q branch experimental spectrum (dashed) compared to fits with (dotted) and without (solid) the Lorentzian contribution to the linewidth.

Transition	Band origin (cm <sup>-1</sup> )	G(v')(cm <sup>-1</sup> )	A'(cm <sup>-1</sup> )	B'(cm <sup>-1</sup> )	C'(cm <sup>-1</sup> )	Excited state lifetime(ns)
0 <sub>0</sub> <sup>0</sup>	18901.29(3)	0	0.198(1)	0.185(1)	0.0957(5)	>0.3
10 <sub>0</sub> <sup>1</sup>	19472.45(3)	571.16(6)	0.197(1)	0.185(1)	0.0959(5)	>0.3
9 <sub>0</sub> <sup>1</sup>	19797.41(3)	896.12(6)	0.197(1)	0.185(1)	0.0957(5)	0.10(3)

1- $\sigma$  errors are given in parenthesis.

**Table 5.1.** Molecular constants for the phenyl radical.

Excited state rotational constants, rotational temperatures, and excited state lifetimes were determined by fitting simulated spectra to the experimental data. The program PGOPHER<sup>24</sup> was used for this analysis. The rotational constants for the ground state were fixed at the values determined from microwave spectra by McMahon et al.<sup>2</sup> ( $A''=0.20947$ ,  $B''=0.18679$ ,  $C''=0.09872$  cm<sup>-1</sup>). Centrifugal distortion and spin-rotation interaction parameters were not included in the model as the energy corrections associated with these terms are far below the present resolution. As a starting point for the simulations, we used the excited state rotational constants of Tonokura<sup>20</sup> et al., which were derived from a hybrid DFT calculation ( $A'=0.1964$ ,  $B'=0.1846$ ,  $C'=0.0952$  cm<sup>-1</sup>). The  $1^2B_1-X^2A_1$  transitions examined were from the zero-point level of the ground state to upper levels of  $b_1$  vibronic symmetry, and were therefore governed by C-type rotational selection rules. Preliminary spectral simulations with the above

parameters were quite close to the observed spectra, permitting assignment of the resolved structure and determination of the rotational temperatures. The latter were typically around 20 K. The final excited state band origins and rotational constants were obtained using the least squares fitting capabilities of PGOPHER<sup>24</sup>. The constants resulting from these fits are listed in Table 5.1. Comparisons of the observed and calculated spectra are presented in Figure 5.2.

Simulations that employed the instrumental linewidth of  $0.05\text{ cm}^{-1}$  were markedly more resolved than the observed spectra. As an example, Figure 5.2b shows the experimental and simulated data for the Q-branch region of the  $9_0^1$  band. Partial resolution of the Q-branch was predicted for the instrumental linewidth. Agreement with the experimental data was achieved by convoluting the instrumental lineshape with a Lorentzian function of  $0.055\text{ cm}^{-1}$  FWHM. This width corresponds to an upper state lifetime of 96 ps. The contours for the  $0_0^0$  and  $10_0^1$  bands were consistent with the instrumental linewidth, and the differences were less than the measurement errors (c.f., Table 5.1). With the present resolution it was possible to detect Lorentzian contributions of  $0.015\text{ cm}^{-1}$  or greater. Based on this upper bound, the lifetimes of the  $0^0$  and  $10^1$  vibronic states must be greater than 0.35ns.

#### 5.4. Theoretical Calculations and Analysis

The change in rotational constants gives some indications about the change in geometry upon excitation from the ground to the first excited electronic state. The results showed a slight decrease in all three rotational constants. A decrease in the rotational constants indicates an increase in the moment of inertia. This result suggests that the ring expands slightly upon excitation, consistent with a  $n \leftarrow \pi$  transition where an electron is promoted from the stabilizing  $\pi$  network.

A program was written using Mathematica 7 to estimate the extent of the increase in the ring. The program changed the C-C bond lengths in the ground state geometry by a factor ranging from 0.95 to 1.05. At each increment (0.0001) the rotational constants, A, B, and C were calculated. The calculated rotational constants were then compared to the excited state rotational constants measured in the experiment. A comparative parameter was defined as  $\delta = |A'-A''| + |B'B''| + |C'-C''|$ .  $\delta$  was minimized ( $\delta < 0.003 \text{ cm}^{-1}$ ) at a factor of 1.02. This result estimated a 2 % increase in the C-C bonds upon excitation.

Given three rotational constants, there is not enough information to predict a unique geometry since numerous molecular geometries share the same rotational constants within the experimental error. To demonstrate this, a program was written using Mathematica 7 to randomly search for geometries that have rotational constants equal to the experimental values.

The program first defined coordinates for each atom in the planar structure for phenyl as shown in Figure 5.3. The geometry in this figure was the optimized geometry calculated with a hybrid density functional theory B3LYP, based on Becke's three-grid integrations and exchange functional<sup>25-27</sup> and the correlation functional of Lee, Yan, and Parr<sup>28</sup>. Dunning's correction consistent aug-cc-pvdz basis set<sup>29</sup> was used. Millions of random geometries were sampled by randomly moving the atoms 0 - 0.20 Å from the initial geometry.  $C_{2v}$  symmetry was conserved by keeping  $C_1$ ,  $C_4$ , and  $H_9$  on the  $C_2$  axis (the  $z$ -axis), preserving the  $\sigma_v$  plane of symmetry, and retaining a planar molecule for each move. Rotational constants were calculated for each random geometry and compared with the experimental values.

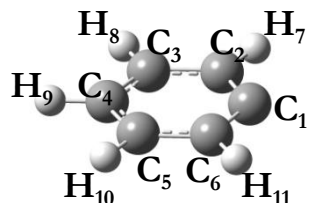


**Figure 5.3.** The phenyl radical with atom numbering.

The program was used in this way to predict possible geometries for the  $1^2B_1$  state of phenyl. The rotational constants for 100 million random geometries were compared to the measured rotational constants. There were 483,416 geometries with rotational constants within the experimental error. There was a

wide distribution of bond lengths and angles within these selected geometries. Of the 483,416 geometries, the mean and median  $C_2C_3$  bond length was longer than the initial geometry suggesting that the geometry may lengthen along the z axis upon excitation. Overall however, the results from the random geometry searching show that the experimentally determined rotational constants do not provide enough information to make definitive conclusions about the excited electronic state molecular geometry.

The random structure searching method might be more useful given results from higher resolution experiments such as molecular constants from microwave spectroscopy experiments. The rotational constants for 200 million random geometries were compared with the ground state rotational constants reported in McMahon's microwave spectroscopy study for the ground electronic state. The total computational time was 37 hours using a single 1.7 MHz processor. Out of the 200 million random geometries, only 126 geometries were found that matched the experimental rotational constants within the experimental error. Each geometry was distinct and only one of the 126 geometries was similar to the optimized geometry predicted using density functional theory.

Further computational work was completed to help characterize the observed electronic spectrum. The ground state optimized geometry, electronic structure, and vibrational frequencies were calculated at the UB3LYP/cc-pVDZ level. A separate calculation used restricted open-shell Hartree-Fock (ROHF)<sup>30</sup>

theory with the aug-cc-pVDZ basis set. For comparison, the molecular orbital energies were also calculated for the ground state of benzene at the RHF/aug-cc-pVDZ level. Time-dependent density functional theory (TDDFT)<sup>31,32</sup> was used to calculate the optimized geometry, electronic structure, and vibrational frequencies for the first excited electronic state of the phenyl radical with the cc-pVDZ basis set. The vertical excitation energy,  $T_0$ , and oscillator strength were also calculated for the  $1^2B_1 \leftarrow X^2A_1$  transition. All calculations were performed with the Gaussian 09 computational package<sup>33</sup>. The phenyl radical is known to have  $C_{2v}$  symmetry in both the ground and excited electronic states. The planar molecule was oriented on the  $y\bar{z}$  plane with the  $C_2$  axis along  $\bar{z}$ . The  $\sigma_v$  plane is the  $x\bar{z}$  plane. Tight convergence criteria was used for geometry optimizations.

The upper valence molecular orbital diagrams for benzene and the phenyl radical calculated at the ROHF/aug-cc-pVDZ level (RHF for benzene) are shown in Figures 5.4 and 5.5. The highest occupied molecular orbitals (HOMOs) for benzene are the well known doubly degenerate  $\pi_z$  orbitals labeled MO 20 and MO 21 in Figure 5.4 that have  $E_{1g}$  symmetry. Note that by convention the  $\bar{z}$ -axis is out of plane for benzene and the  $x$ -axis is out of plane for phenyl. The UV electronic transitions of benzene are characterized by the promotion of an electron from these  $\pi_z$  orbitals to higher energy virtual orbitals.



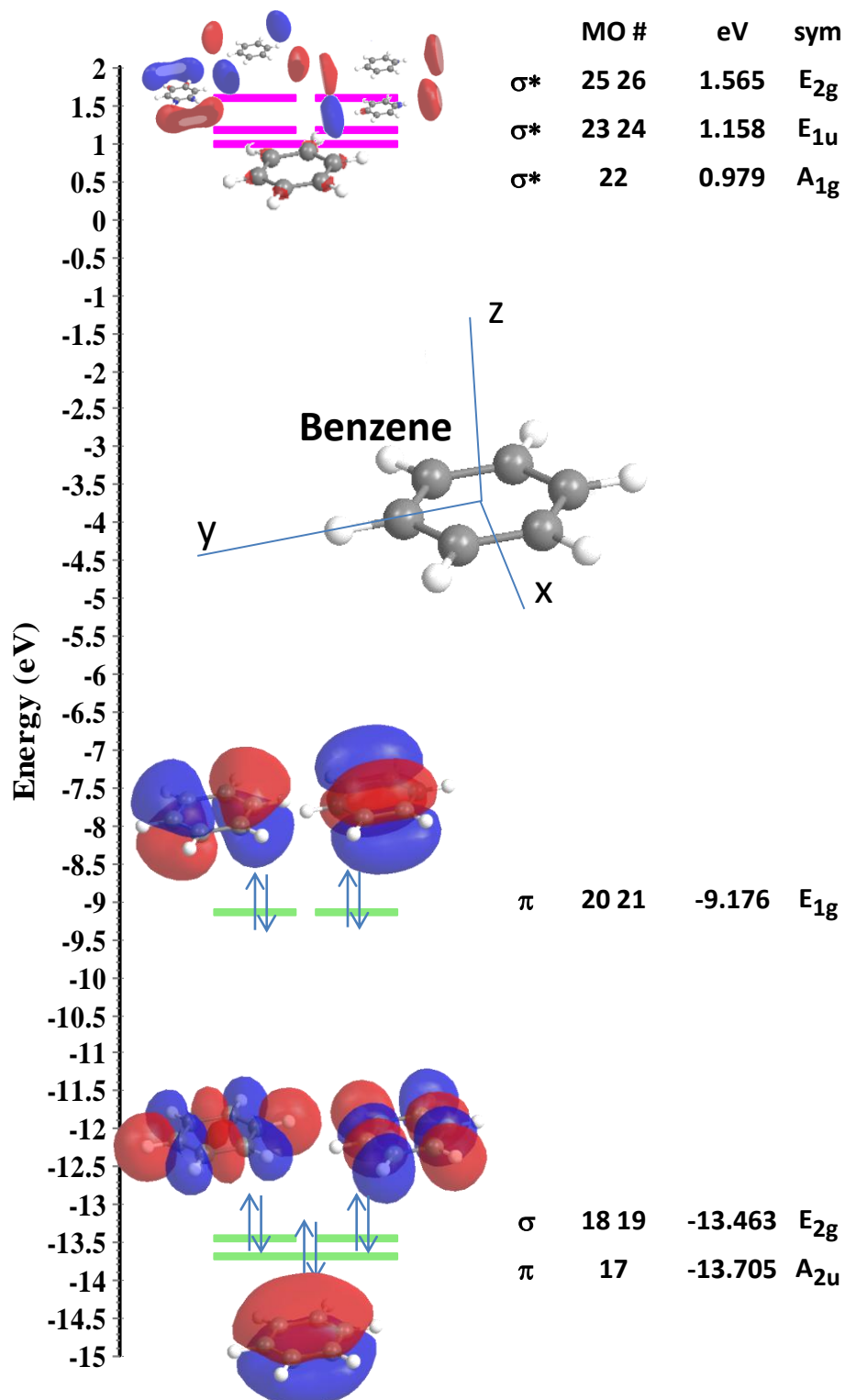


Figure 5.4. Upper valence molecular orbital diagram for benzene in the ground electronic state ( $X^1A_{1g}$ ) calculated at the RHF/aug-cc-pVDZ level.

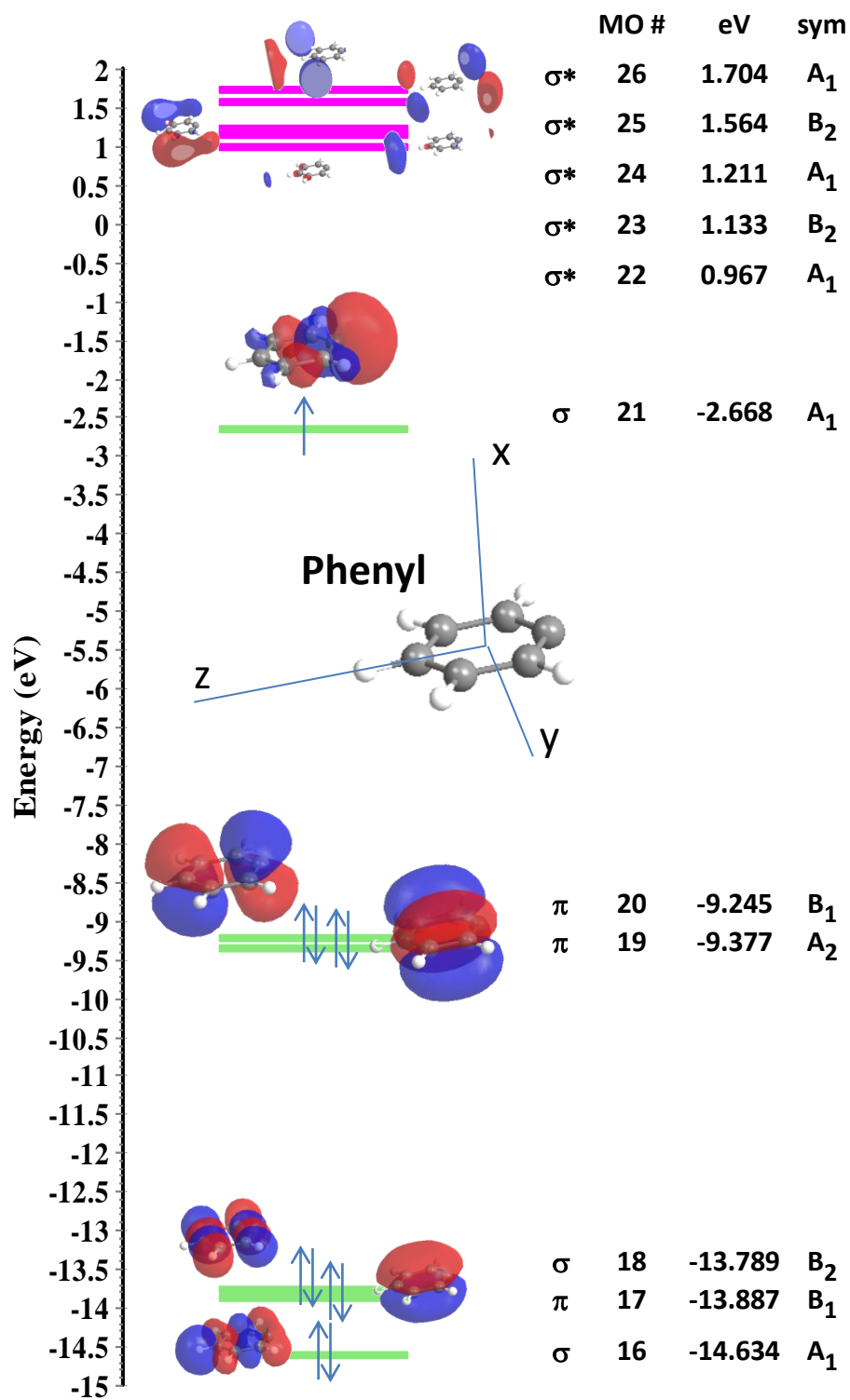


Figure 5.5. Upper valence molecular orbital diagram for phenyl in the ground electronic state ( $X^2A_1$ ) calculated at the ROHF/aug-cc-pVDZ level.

The phenyl radical is produced from benzene by the homolytic dissociation of a hydrogen atom. As a result the symmetry is reduced from  $D_{6h}$  to  $C_{2v}$ . This lifts the degeneracy of MOs 20 and 21 of benzene to produce the non-degenerate MOs 19 and 20 of the phenyl radical in Figure 5.5 which have  $A_2$  and  $B_1$  symmetry respectively. The degenerate  $\sigma$  orbitals of benzene (MOs 18 and 19) are also split to form MOs 18 and 21 of the phenyl radical which have  $B_2$  and  $A_1$  symmetry respectively. MO 18 of benzene has CH  $\sigma$ -type bonding for all six CH bonds. The breaking of the CH bond to form phenyl largely destabilizes this orbital resulting in the non-bonding type MO 21 of phenyl at higher energy.

The CRD spectrum in Figure 5.1 is most likely the promotion of an electron from MO 20 to MO 21 in the phenyl radical. DFT calculations were completed to test this interpretation and provide more details about the ground and excited states.

Ground state calculations were done at the UB3LYP/cc-pVDZ level. With the axis orientation in Figure 5.5, the doublet ground electronic state had  $A_1$  symmetry since the unpaired electron existed in the MO 21 which has  $A_1$  symmetry. This singly occupied molecular orbital (SOMO) can be described as a  $\sigma$  non-bonding orbital centered on  $C_1$ . The ground state geometry is described in Table 5.2. The carbon-carbon bonds  $C_1C_2$ ,  $C_2C_3$ , and  $C_3C_4$  were 1.381, 1.407, and 1.399 Å respectively. The rotational constants for the optimized ground state

geometry were  $A''= 0.20842$ ,  $B''= 0.18600$ , and  $C''= 0.09829 \text{ cm}^{-1}$ . The calculated (scaled) harmonic vibrational frequencies for the  $X^2A_1$  electronic state are listed in Table 5.3 and assigned using Wilson's<sup>34</sup> numbering. A scaling factor of 0.967 was recommended for small cyclic aromatic radicals.<sup>35</sup>

<b>Level</b>	<b>UB3LYP</b>	<b>TDDFT</b>
<b>Basis Set</b>	<b>cc-pvdz</b>	<b>cc-pvdz</b>
<b>Electronic State</b>	<b><math>X^2A_1</math></b>	<b><math>1^2B_1</math></b>
<b>r C<sub>1</sub>C<sub>2</sub></b>	1.381	1.466
<b>r C<sub>2</sub>C<sub>3</sub></b>	1.407	1.381
<b>r C<sub>3</sub>C<sub>4</sub></b>	1.399	1.415
<b>r C<sub>2</sub>H<sub>7</sub></b>	1.093	1.097
<b>r C<sub>3</sub>H<sub>8</sub></b>	1.093	1.094
<b>r C<sub>4</sub>H<sub>9</sub></b>	1.092	1.094
<b>a C<sub>6</sub>C<sub>1</sub>C<sub>2</sub></b>	125.8	111.8
<b>a C<sub>1</sub>C<sub>2</sub>C<sub>3</sub></b>	116.6	124.8
<b>a C<sub>2</sub>C<sub>3</sub>C<sub>4</sub></b>	120.2	119.0
<b>a C<sub>1</sub>C<sub>2</sub>H<sub>7</sub></b>	122.4	117.3
<b>a C<sub>4</sub>C<sub>3</sub>H<sub>8</sub></b>	120.2	119.4

**Table 5.2.** Calculated geometric parameters for the phenyl radical in the ground electronic state ( $X^2A_1$ ) and first excited electronic state ( $1^2B_1$ ).

Mode	$X^2A_1$			$1^2B_1$		
	Assignment	Sym	$\omega$	$\omega$	Sym	Assignment
1	$v_2$	$A_1$	<b>3092</b>	<b>3086</b>	$A_1$	$0.93v_2$
2	$v_{20a}$	$A_1$	<b>3078</b>	<b>3060</b>	$A_1$	$0.53v_{7b}+0.43v_{20a}$
3	$v_{7b}$	$A_1$	<b>3060</b>	<b>3033</b>	$A_1$	$0.50v_{20a}+0.47v_{7b}$
4	$v_{8a}$	$A_1$	<b>1531</b>	<b>1588</b>	$A_1$	$0.97v_{8a}$
5	$v_{19a}$	$A_1$	<b>1417</b>	<b>1387</b>	$A_1$	$0.94v_{19a}$
6	$v_{CH}$ scissor	$A_1$	<b>1125</b>	<b>1166</b>	$A_1$	$0.96v_{CH}$ scissor
7	$v_{18a}$	$A_1$	<b>1013</b>	<b>989</b>	$A_1$	$0.62v_1+0.33v_{18a}$
8	$v_1$	$A_1$	<b>988</b>	<b>966</b>	$A_1$	$0.73v_{12}+0.14v_{18a}+0.12v_1$
9	$v_{12}$	$A_1$	<b>949</b>	<b>897</b>	$A_1$	$0.47v_{18a}+0.26v_{12}+0.23v_1$
10	$v_{6b}$	$A_1$	<b>594</b>	<b>573</b>	$A_1$	$0.99v_{6b}$
11	$v_{17a}$	$A_2$	<b>935</b>	<b>965</b>	$A_2$	$1.00v_{17a}$
12	$v_{10a}$	$A_2$	<b>787</b>	<b>762</b>	$A_2$	$0.99v_{10a}$
13	$v_{16a}$	$A_2$	<b>388</b>	<b>291</b>	$A_2$	$1.00v_{16a}$
14	$v_{17b}$	$B_1$	<b>966</b>	<b>994</b>	$B_1$	$0.85v_{17b}+0.15v_{10b}$
15	$v_{10b}$	$B_1$	<b>864</b>	<b>935</b>	$B_1$	$0.83v_{10b}+0.14v_{17b}$
16	$v_{11}$	$B_1$	<b>697</b>	<b>747</b>	$B_1$	$0.50v_4+0.47v_{11}$
17	$v_4$	$B_1$	<b>651</b>	<b>663</b>	$B_1$	$0.52v_{11}+0.41v_4$
18	$v_{16b}$	$B_1$	<b>412</b>	<b>349</b>	$B_1$	$0.92v_{16b}$
19	$v_{20b}$	$B_2$	<b>3081</b>	<b>3066</b>	$B_2$	$0.59v_{20b}+0.41v_{7a}$
20	$v_{7a}$	$B_2$	<b>3066</b>	<b>3033</b>	$B_2$	$0.59v_{7a}+0.41v_{20b}$
21	$v_{8b}$	$B_2$	<b>1585</b>	<b>1473</b>	$B_2$	$0.55v_3+0.33v_{8b}$
22	$v_3$	$B_2$	<b>1409</b>	<b>1344</b>	$B_2$	$0.42v_{14}+0.29v_{8b}+0.15v_{9b}...$
23	$v_{14}$	$B_2$	<b>1296</b>	<b>1306</b>	$B_2$	$0.51v_{9b}+0.29v_{14}+0.16v_3...$
24	$v_{9b}$	$B_2$	<b>1250</b>	<b>1191</b>	$B_2$	$0.30v_{15}+0.22v_{18b}+0.15v_{9b}...$
25	$v_{15}$	$B_2$	<b>1126</b>	<b>1082</b>	$B_2$	$0.66v_{15}+0.14v_{18b}+0.11v_{8b}...$
26	$v_{18b}$	$B_2$	<b>1035</b>	<b>1014</b>	$B_2$	$0.60v_{18b}+0.15v_{14}+0.11v_{8b}...$
27	$v_{6a}$	$B_2$	<b>577</b>	<b>514</b>	$B_2$	$0.96v_{6a}$

**Table 5.3.** Scaled vibrational frequencies for the  $X^2A_1$  and  $1^2B_1$  states of phenyl using B3LYP/cc-pVDZ for the  $X^2A_1$  state and TDDFT/cc-pVDZ for the  $1^2B_1$  state.

TDDFT calculations confirmed that the first excited electronic state was a doublet with  $B_1$  symmetry. The electronic transition involved the promotion of one electron from the highest lying doubly occupied  $B_1$  molecular orbital (MO 20) to the SOMO mentioned above (MO 21). The calculated vertical excitation energy (TDDFT/cc-pVDZ) for  $1^2B_1 \leftarrow X^2A_1$  was 2.8898 eV (429.03 nm or 23,308.39  $\text{cm}^{-1}$ ) with a very weak oscillator strength ( $f=0.0007$ ). The  $B_1$  orbital, MO 20 in Figure 5.5, can be described as a bonding  $\pi_x$  molecular orbital with population over the  $C_6C_1C_2$  carbons and the  $C_3C_4C_5$  carbons with nodes between the  $C_2C_3$  bond and  $C_5C_6$  bond. The optimized excited state geometry was compared with the optimized ground state geometry in Table 5.2. The carbon-carbon bonds  $C_1C_2$ ,  $C_2C_3$ , and  $C_3C_4$  were 1.466, 1.381, and 1.415 Å respectively. The rotational constants for the optimized excited state geometry were  $A'=0.19622$ ,  $B'=0.18596$ , and  $C'=0.09548$  which agree well with the experimentally determined values. The largest change in carbon-carbon bond distances was the increase in the  $C_1C_2$  and  $C_6C_1$  bonds compared to the ground electronic state. There was a large decrease in the  $C_6C_1C_2$  angle and an increase in the  $C_3C_4C_5$  and  $C_5C_6C_1$  angles. The calculated (and scaled) harmonic vibrational frequencies for the  $1^2B_1$  electronic state are listed in Table 5.3. The assignments for the excited state are linear combinations of the ground state

normal modes with coefficients corresponding to the dominant squared elements of the Duschinsky matrix ( $J_{ik}^2$ ).<sup>36</sup>

The  $1^2B_1 \leftarrow X^2A_1$  vibronic spectrum of phenyl was calculated using the Franck-Condon principle to determine intensities of transitions between the two states. The optimized geometries and frequencies for the ground and excited states described above were used, along with the built in function<sup>36</sup> in Gaussian 09, to calculate the vibrationally-resolved electronic spectrum shown in Figure 5.6 (red). The stick spectrum was simulated using the 0.967 scaling factor for excited state frequencies. There were no hot bands included in the simulation. The main progressions agree remarkably well with Porter's and Ward's<sup>37</sup> room temperature gas phase spectrum (green) and with our jet cooled spectrum (purple).

TDDFT with the cc-pVDZ basis set predicted the transition band origin ( $T_0$ ), to be  $18436.80 \text{ cm}^{-1}$  (542.39 nm or 2.286 eV). Experimentally, the origin ( $T_0$ ) was measured at  $18901.29 \text{ cm}^{-1}$ , a difference of  $464.49 \text{ cm}^{-1}$ . This difference is not beyond the typical error for this level of theory for similar molecules.<sup>38</sup> The calculated spectrum was shifted  $464.49 \text{ cm}^{-1}$  in Figure 5.6 to compare the calculated vibrational band positions with our experimental spectrum and with Porter and Ward's<sup>37</sup> data. The main progressions, those from the  $\nu_{10}$  and  $\nu_9$  modes, show excellent agreement in both line position and intensity.

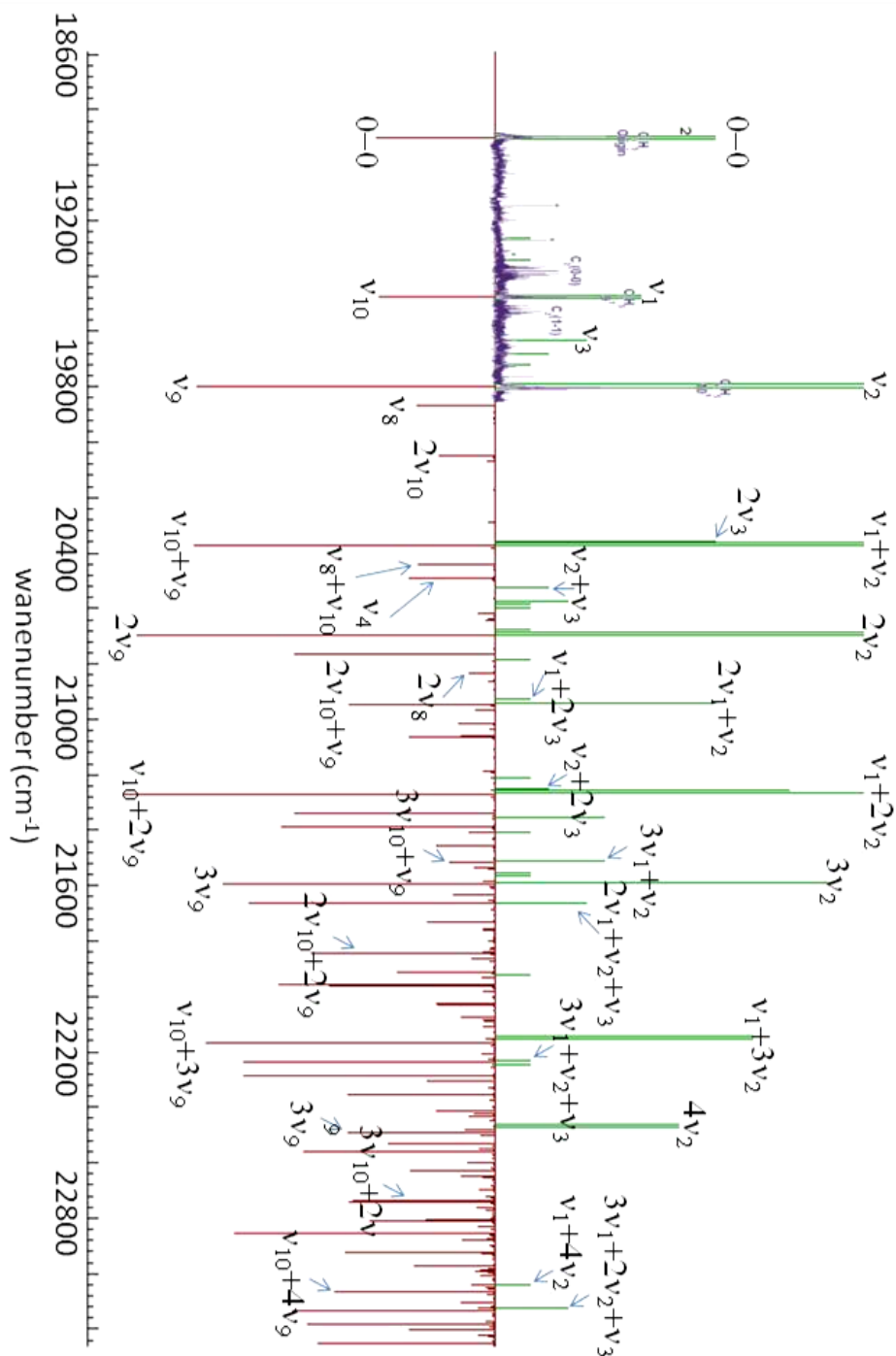


**Figure 5.6.** TDDFT/cc-pVDZ Franck-Condon calculated spectrum for the phenyl radical (red), compared to Porter and Ward's<sup>37</sup> room temperature gas phase spectrum (green) and jet cooled CRDS spectrum (purple).



The majority of the calculated spectrum was dominated by four modes:  $\nu_4$ ,  $\nu_8$ ,  $\nu_9$ , and  $\nu_{10}$ . All of these modes have  $a_1$  symmetry. The excited state modes  $\nu_9$  and  $\nu_8$  are described as linear combinations of the ground state  $\nu_7$ ,  $\nu_8$ , and  $\nu_9$  modes (see Table 5.3) due to the mode mixing of these states. Neither excited state modes  $\nu_4$  nor  $\nu_{10}$  have significant mode mixing. The displacement vectors for the  $\nu_4$ ,  $\nu_8$ ,  $\nu_9$ , and  $\nu_{10}$  modes are shown in Figure 5.7. These modes are all associated with the in-plane ring bending and stretching modes of  $a_1$  symmetry. These modes have large Franck-Conon factors because they coincide with the change in geometry associated with the  $n \leftarrow \pi$  electronic transition.

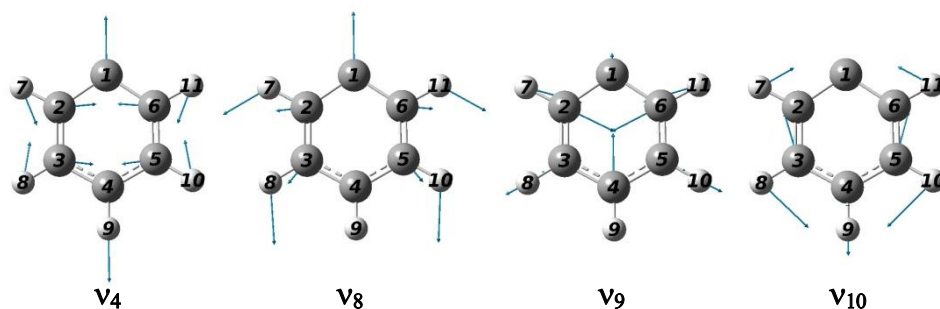


**Figure 5.7.** Displacement vectors for the  $\nu_4$ ,  $\nu_8$ ,  $\nu_9$ , and  $\nu_{10}$  modes of the  $1^2B_1$  electronic state of the phenyl radical.

## 5.5. Discussion and Conclusions

The measurements of jet-cooled phenyl radicals provide improved values for the band origins of the  $0_0^0$ ,  $9_0^1$  and  $10_0^1$  transitions. The band positions listed in the original work of Porter and Ward<sup>7</sup> appear to be R-branch band heads, and

they are displaced about  $8\text{ cm}^{-1}$  to the high-frequency side of the origins given in Table 5.1. From their rotational contour fit of the  $0_0^0$  band, Tonokura<sup>20</sup> et al. reported a band origin of  $18900 \pm 2\text{ cm}^{-1}$ , which is in good agreement with the present results. The vibrational intervals given in Table 5.1 are also in agreement with earlier measurements, while slightly improving the accuracy.

Theoretical calculations for the  $1^2B_7$  state predict a planar structure<sup>20-23</sup> and the fitted rotational constants are consistent with this geometry (i.e., the inertial defect is below the error limits). The constants are very close to the values predicted for the  $1^2B_7$  equilibrium structure by the hybrid DFT calculations of Tonokura<sup>20</sup> et al. (B3LYP with the cc-pVDZ basis set, values given above) and with the TDDFT/cc-pVDZ results from this study. Both the measured and calculated constants are smaller than those of the ground state zero-point level. This fits with the  $n\leftarrow\pi$  character of the transition, which leads to a weakening of the  $\pi$ -bonding network and an expansion of the carbon ring.

The upper state linewidths were found to be far smaller than the estimate of  $0.5\text{ cm}^{-1}$  provided by Tonokura<sup>20</sup> et al.. Homogenous broadening of the  $0^0$  and  $10^1$  levels was not detected, but the fact that fluorescence spectra have not been reported for phenyl indicates that the fluorescence quantum yield may be low due to the presence of non-radiative decay channels. TDDFT predicted an oscillator strength of 0.0007 for the  $1^2B_1\text{-X}^2A_1$  transition, which corresponds to a radiative lifetime for  $1^2B_7$  of  $6.0\text{ }\mu\text{s}$ . If the lifetimes of the  $0^0$  and  $10^1$  levels are just above

the 0.35 ns lower bound, the fluorescence quantum yield could be as low as  $6 \times 10^{-5}$ . The 96 ps lifetime for  $9^1$  results in a quantum yield of  $1.6 \times 10^{-5}$ . Internal conversion to the ground state is the only non-radiative decay channel open for the  $0^0$ ,  $10^1$  and  $9^1$  levels, and the observation of the fastest decay rate for the highest energy level may reflect the increasing density of available final states. Channels that lead to ring opening or the elimination of a hydrogen atom to form benzyne were not energetically accessible<sup>39,40</sup>. The calculations of Madden et al.<sup>39</sup> predict that these channels will open for photon energies of  $21,000 \text{ cm}^{-1}$  (ring opening) and  $26,600 \text{ cm}^{-1}$  (H atom loss).

## BIBLIOGRAPHY

- (1)Herbst, E. *Annu. Rev. Phys. Chem.* **1995**, *46*, 27.
- (2)McMahon, R. J.; McCarthy, M. C.; Gottlieb, C. A.; Dudek, J. B.; Stanton, J. F.; Thaddeus, P. *Astrophys. J.* **2003**, *590*, L61.
- (3)Sharp, E. N.; Roberts, M. A.; Nesbitt, D. J. *Physical Chemistry Chemical Physics* **2008**, *10*, 6592.
- (4)Glassman, I.; Editor *Combustion, Third Edition*, 1996.
- (5)Frenklach, M.; Warnatz, J. *Combustion Science and Technology* **1987**, *51*, 265.
- (6)Park, J.; Lin, M. C. *ACS Symp. Ser.* **1999**, *720*, 196.
- (7)Porter, G.; Ward, B. *Proceedings of the Chemical Society, London* **1964**, 288.
- (8)Bennett, J. E.; Mile, B.; Thomas, A. *Chemical Communications (London)* **1965**, 265.
- (9)Bennett, J. E.; Mile, B.; Thomas, A. *Proceedings of the Royal Society of London, Series A: Mathematical, Physical and Engineering Sciences* **1966**, *293*, 246.
- (10)Kasai, P. H.; Hedaya, E.; Whipple, E. B. *J. Amer. Chem. Soc.* **1969**, *91*, 4364.
- (11)Pacansky, J.; Bargon, J. *Journal of the American Chemical Society* **1975**, *97*, 6896.
- (12)Miller, J. H.; Andrews, L.; Lund, P. A.; Schatz, P. N. *J. Chem. Phys.* **1980**, *73*, 4932.
- (13)Radziszewski, J. G. *Chemical Physics Letters* **1999**, *301*, 565.
- (14)Radziszewski, J. G.; Gil, M.; Gorski, A.; Spanget-Larsen, J.; Waluk, J.; Mroz, B. *Journal of Chemical Physics* **2001**, *115*, 9733.
- (15)Engert, J. M.; Dick, B. *Appl. Phys. B Lasers Opt.* **1996**, *63*, 531.
- (16)Friderichsen, A. V.; Radziszewski, J. G.; Nimlos, M. R.; Winter, P. R.; Dayton, D. C.; David, D. E.; Ellison, G. B. *Journal of the American Chemical Society* **2001**, *123*, 1977.
- (17)Park, J.; Burova, S.; Rodgers, A. S.; Lin, M. C. *Chemical and Physical Processes in Combustion* **1999**, 308.
- (18)Park, J.; Chakraborty, D.; Bhusari, D. M.; Lin, M. C. *J. Phys. Chem. A* **1999**, *103*, 4002.
- (19)Park, J.; Nam, G. J.; Tokmakov, I. V.; Lin, M. C. *J. Phys. Chem. A* **2006**, *110*, 8729.
- (20)Tonokura, K.; Norikane, Y.; Koshi, M.; Nakano, Y.; Nakamichi, S.; Goto, M.; Hashimoto, S.; Kawasaki, M.; Andersen, M. P. S.; Hurley, M. D.; Wallington, T. J. *J. Phys. Chem. A* **2002**, *106*, 5908.
- (21)Mattar, S. M. *J. Phys. Chem. A* **2007**, *111*, 251.
- (22)Kim, G.-S.; Mebel, A. M.; Lin, S. H. *Chem. Phys. Lett.* **2002**, *361*, 421.
- (23)Biczysko, M.; Bloino, J.; Barone, V. *Chem. Phys. Lett.* **2009**, *471*, 143.
- (24)Western, C. M.; University of Bristol: 2007.
- (25)Becke, A. D. *J Chem Phys* **1993**, *98*, 5648.

- (26) Becke, A. D. *J Chem Phys* **1992**, *97*, 9173.
- (27) Becke, A. D. *J Chem Phys* **1992**, *96*, 2155.
- (28) Lee, C. T.; Yang, W. T.; Parr, R. G. *Phys Rev B* **1988**, *37*, 785.
- (29) Dunning, T. H. *J Chem Phys* **1989**, *90*, 1007.
- (30) Roothaan, C. C. J. *Rev Mod Phys* **1960**, *32*, 179.
- (31) Furche, F.; Ahlrichs, R. *J Chem Phys* **2002**, *117*, 7433.
- (32) Scalmani, G.; Frisch, M. J.; Mennucci, B.; Tomasi, J.; Cammi, R.; Barone, V. *J Chem Phys* **2006**, *124*.
- (33) Frisch, M. J. **2009**.
- (34) Wilson, E. B., Jr. *Phys Rev* **1934**, *45*, 706.
- (35) Cheng, C. W.; Lee, Y. P.; Witek, H. A. *J Phys Chem A* **2008**, *112*, 2648.
- (36) Bloino, J.; Biczysko, M.; Santoro, F.; Barone, V. *J Chem Theory Comput* **2010**, *6*, 1256.
- (37) Porter, G.; Ward, B. *P Chem Soc London* **1964**, 288.
- (38) Dierksen, M.; Grimme, S. *J Chem Phys* **2004**, *120*, 3544.
- (39) Madden, L. K.; Moskaleva, L. V.; Kristyan, S.; Lin, M. C. *J. Phys. Chem. A* **1997**, *101*, 6790.
- (40) Negru, B.; Goncher, S. J.; Brunsvold, A. L.; Just, G. M. P.; Park, D.; Neumark, D. M. *J. Chem. Phys.* **2010**, *133*, 074302/1.

## Chapter 6. The Phenoxy Radical

### 6.1. Introduction

The phenoxy radical has an important role in combustion chemistry. It is an intermediate in the oxidation of small aromatic hydrocarbons. The presence of phenoxy in combustion is likely to contribute to the formation of polycyclic aromatic hydrocarbons, the precursors to soot.<sup>1</sup> Kinetic studies, involving the phenoxy radical, are therefore numerous.<sup>2-13</sup> These kinetic studies often use absorption methods to determine the transient concentrations of the species involved. Ample spectroscopic data for the phenoxy radical are then necessary to carry out these studies.

Like many combustion intermediates, phenoxy is a free radical with very high reactivity. Intricate experimental methods are then required to produce high radical concentrations and detect them quickly after production. Despite this difficulty, phenoxy has been produced and detected by a variety of methods. Production methods include photolysis<sup>3-5,10,14-22</sup>, pyrolysis<sup>1,23,24</sup>, photodetachment of phenoxide<sup>25</sup>, decomposition of phenyl peroxide<sup>2</sup>, and pulsed radiolysis<sup>9,26,27</sup>.

Porter and Wright<sup>28</sup> first observed phenoxy in the gas phase by UV spectroscopy of photodissociated anisole and phenol. Other spectroscopic studies followed including electron spin resonance spectroscopy (ESR)<sup>27,29-32</sup>, Raman spectroscopy<sup>18,33-36</sup>, IR spectroscopy<sup>1,14,23,37</sup> and UV-Vis spectroscopy<sup>14,17,37</sup> of matrix isolated phenoxy, gas phase photoelectron spectroscopy<sup>25,38</sup>, electronic

absorption spectroscopy<sup>4-6,9,10,12,14-17,19-21,26,28,39</sup>, cavity ring-down spectroscopy<sup>3,4</sup>, anion photodetachment spectroscopy<sup>40</sup>, and mass spectrometry<sup>1,2,23,24</sup>. Microwave spectra are not yet available for this radical.

The phenoxy radical provides a great example of the collaboration between experimental and computational chemistry to assign spectra and determine molecular and electronic structure. The large number of normal modes made assignment of IR and Raman spectra difficult without the aid of *ab initio* calculations. However by 2001, a combination of experimental<sup>1,7,14,18,33-38</sup> and theoretical<sup>7,14,15,33,38,41,42</sup> studies resulted in the assignment of all but one of the vibrational normal modes. The assignment of the electronic absorption spectra was also a difficult task. There were many disagreements in assigning the UV and visible transitions<sup>9,10,13,15-17,19-21,26,28,37,38,40-45</sup> until they were definitively assigned by combined UV-Vis and IR polarization spectroscopy<sup>6</sup> and high level theoretical studies<sup>4,43,44,46-48</sup>.

Kinetic studies of combustion intermediates often utilize the lower energy electronic transitions in the visible region. These lower energy transitions are used because they are often more narrow and less likely to overlap with absorption from other molecules. For phenoxy, the  $B^2A_2-X^2B_1$  transition has been shown to exhibit vibrational structure in the visible region.<sup>6,12,15,17,19</sup> However, the features of the  $500\text{ cm}^{-1}$  progression in this region are still quite broad at room temperature. Although excited state calculations<sup>47</sup> predict the

contour of this transition well, it would be beneficial to examine the excited state more closely.

The previous section detailed the successful observation of the first electronic transition of the rotationally cold phenyl radical by cavity ring-down spectroscopy in a jet expansion.<sup>49</sup> The absorption spectrum of the cold radical both increased in intensity and was greatly simplified due to the radical population being restricted to low rotational states. In this experiment the phenoxy radical was produced in an electrical discharge, cooled in a jet expansion, and the  $B^2A_2-X^2B_1$  transition was recorded by cavity ring-down spectroscopy. The spectrum of the cold radical, combined with computational results, provided more details about the  $B^2A_2$  electronic state.

## 6.2. Experimental

The experimental setup was similar to the phenyl experiments in Chapter 5 but with some minor changes. First, an insulator and grounding plate was added between the high voltage plates and the mounting plate. This helped to reduce soot buildup at the expansion site. Even with less soot, the radical production efficiency varied greatly from day to day. This was attributed to the variation in flow rates of the pulsed solenoid valves. The internal plastic poppets which seal the pinhole would easily deform during operation which altered the valve operation.



Eventually, a continuous pinhole flow system was constructed and used in place of the pulsed valves. All interior valve components were removed for continuous flow measurements so that gas could freely flow into the vacuum chamber. The gas flowed through the open valve and entered the slit discharge through a 0.8 mm channel in a 1.0 cm thick aluminum plate. Flow rates were controlled by varying the backing pressure and could not surpass 20 psia. Two pinholes were used for the continuous flow and pulsed valve experiments.

Two pairs of ring-down mirrors and two laser dyes were used to span the necessary wavelength range for this experiment. One pair of mirrors was centered at 570 nm with a maximum reflectance of 99.995% and a bandwidth of 40 nm. Typical ring-down time measurements were 30-40  $\mu$ s with these mirrors. The other pair had a higher reflectivity of 99.9985% at their center (620 nm) and had a 30 nm bandwidth. Ring-down times up to 180  $\mu$ s were observed with an empty cavity.

Phenoxy was observed in the jet expansion after passing phenol or anisole through the electrical discharge. Anisole produced higher radical concentrations likely due to its higher vapor pressure. The precursor was seeded in argon. A low ballast resistance (1 k $\Omega$ ) and high voltage (1 kV), which produced  $\approx$  220 mA current when the discharge was on resulted in the highest phenoxy detection sensitivity. The probe beam detection distance was 6 mm from the exit of the nozzle. Rotational temperatures were  $\approx$  20K for the pulsed

valves and  $\approx 45$  K with the continuous expansion. Spectral calibrations were obtained using both metastable argon and  $C_2$  absorption features.

### 6.3. Experimental Results

A cavity ring-down spectrum ( $15785$ – $17513$   $\text{cm}^{-1}$  or  $571$ – $633.5$  nm) for jet-cooled anisole discharge products is shown in Figure 6.1. The absorption coefficient was calculated using equation 4.1 where  $\tau_1$  was the ring-down time with the discharge on and  $\tau_2$  was the ring-down time with the discharge off. The broad absorption peaks are assigned to the  $B^2A_2$ - $X^2B_1$  transition of the phenoxy radical. The suspected weak origin band is centered at  $15860$   $\text{cm}^{-1}$ . A  $516$   $\text{cm}^{-1}$  progression of three additional peaks was observed to the blue of the origin band. Shoulder peaks arise about  $60$   $\text{cm}^{-1}$  to the red of the peaks in the progression. The continuous expansion source was used in the region  $15785$ – $16600$   $\text{cm}^{-1}$ . The pulsed valve source was used in the region  $16600$ – $17513$   $\text{cm}^{-1}$ . Without computational results, no immediate assignments could be made because of the diffuse nature of the vibronic spectrum. Further analysis will be presented in Section 6.4.

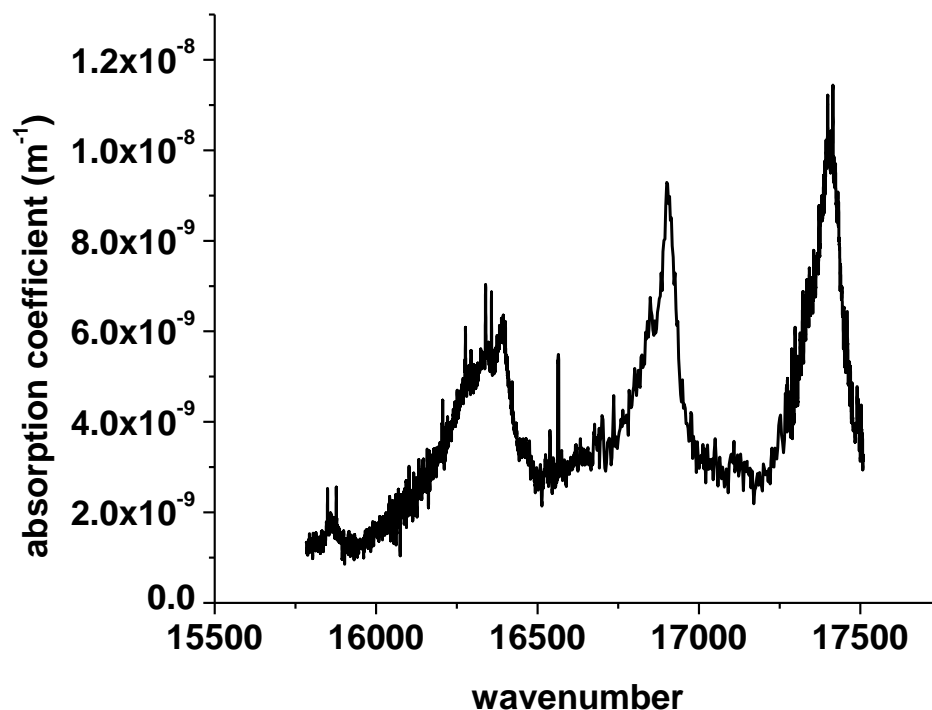


**Figure 6.1.** Visible CRD absorption spectrum of products in an expansion of electrically dissociated anisole.

Sharp features originating from Ar\* were present near the origin band and provided convenient calibration lines. Broadband absorption and/or scattering losses were present across the entire range of the spectrum, even near the origin band. The ring-down time also changed with wavelength due to changes in mirror reflectivity as described in the experimental section.

Several of the sharp peaks in Figure 6.1 were assigned to the well known Swan bands of C<sub>2</sub>. These peaks, along with the phenoxy absorption, grew in intensity as the discharge voltage was increased. At high voltage, a comparison of the relative intensities of the lines of the C<sub>2</sub> 0-0 band with a simulation was

consistent with  $T_{\text{rot}} \approx 30$  K when the pulsed valves were used. To estimate the cooling efficiency using the continuous expansion the partially resolved rovibrational contour of the phenyl radical at 505.1 nm was fit to a PGopher simulation. With bromobenzene as a precursor, phenyl was produced in the continuous expansion at  $T_{\text{rot}} \approx 45$  K. Vibrational cooling was not as efficient and  $C_2$  often had vibrational temperatures approaching 5,000 K. The vibrational cooling efficiency for larger molecules could not be determined. Other sharp peaks in Figure 6.1 were assigned to transitions originating from the  $3s^23p^5(^2P^{\circ}_{3/2})4p$  and  $3s^23p^5(^2P^{\circ}_{1/2})4p$  states of Ar.

#### 6.4 Theoretical Calculations and Analysis

Theoretical descriptions of the  $X^2B_1$  and  $B^2A_2$  electronic states of phenoxy were needed in order to simulate the spectrum to support the assignment. The ground state optimized geometry, electronic structure, and vibrational frequencies were calculated at the UB3LYP/cc-pVDZ and UB3LYP/aug-cc-pVTZ levels. The upper valence molecular orbital diagram was constructed from ROHF/aug-cc-pVDZ calculations to explore the nature of the electronic transitions and for comparison with the phenyl radical. Time-dependent density functional theory (TDDFT) was used to calculate the optimized geometry, electronic structure, and vibrational frequencies for the second excited electronic state of the phenoxy radical with the cc-pVDZ and aug-cc-pVTZ basis sets. The

vertical excitation energy, transition band origin ( $T_0$ ), and oscillator strength were also calculated for the  $B^2A_2 \leftarrow X^2B_1$  transition. All calculations were performed with the Gaussian 09 computational package<sup>50</sup>. The phenoxy radical is known to have  $C_{2v}$  symmetry in both the ground and excited electronic states. The planar molecule was oriented on the  $y\zeta$  plane with the  $C_2$  axis as the  $\zeta$ -axis. The  $\sigma_v$  plane was the  $x\zeta$  plane. Tight convergence criteria were used for geometry optimizations.

The upper valence molecular orbital diagram for the phenoxy radical, calculated at the ROHF/aug-cc-pVDZ level, is shown in Figure 6.2. The molecular orbitals of phenoxy can be viewed as a combination of the phenyl orbitals (see Figure 5.5) with the p atomic orbitals of the oxygen atom. For example, the SOMO of phenoxy (MO 25) is the antibonding combination of MO 20 of phenyl with the  $p_x$  orbital of O. MO 22 of phenoxy is the bonding combination of those two orbitals. Likewise MOs 23 and 21 are the antibonding and bonding combinations involving MO18 of phenyl and O  $p_y$  orbitals. MO 20 of phenoxy has a small amount of O  $p_z$  character mixed with the  $\sigma$  orbital 16 of phenyl.

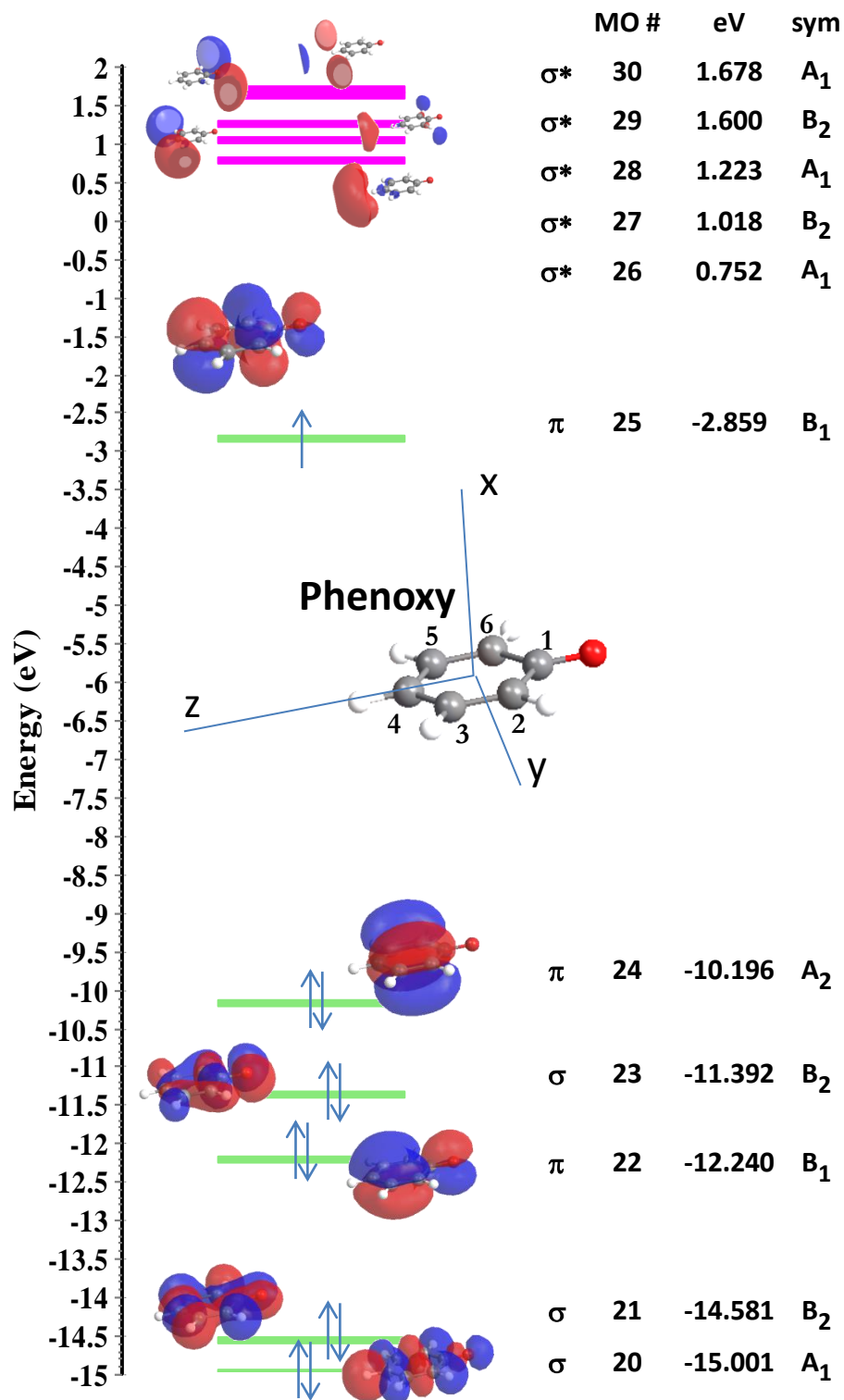


Figure 6.2. Upper valence molecular orbital diagram for phenoxy in the ground electronic state ( $X^2B_1$ ) calculated at the ROHF/aug-cc-pVDZ level.

The first optically allowed transition involves the promotion of an electron from MO 24 to MO 25. The spectrum in Figure 6.1 is characterized by this electronic transition. DFT calculations were completed to support this assignment and provide more details about the ground and excited states.

With the orientation in Figure 6.2, the doublet ground electronic state has  $B_1$  symmetry since the lone electron in the SOMO has  $B_1$  symmetry. This singly occupied molecular orbital (SOMO) is described as a delocalized  $\pi_x$  molecular orbital with nodes at the  $C_1=O$  bond, and between the  $C_2C_3$  and  $C_5C_6$  bonds and with bonding character at the  $C_3C_4C_5$  and  $C_6C_1C_2$  regions. The calculated ground state geometric parameters are listed in Table 6.1. The C=O bond length of 1.252 Å is close to known lengths for CO double bonds. The carbon-carbon bonds  $C_1C_2$ ,  $C_2C_3$ , and  $C_3C_4$  were 1.448, 1.371, and 1.405 Å respectively at the aug-cc-pVTZ level. The calculated harmonic vibrational frequencies for the  $X^2B_1$  electronic state are listed in Table 6.2. The same mode labeling and scaling factor (0.967) as Cheng et al.<sup>46</sup> was used for comparison and the results agreed well for the ground electronic state.

Level	UB3LYP	UB3LYP	TDDFT	TDDFT
Basis Set	cc-pvdz	aug-cc-pvtz	cc-pvdz	aug-cc-pvtz
Electronic State	$X^2B_1$	$X^2B_1$	$B^2A_2$	$B^2A_2$
r CO	1.256	1.252	1.244	1.244
r C <sub>1</sub> C <sub>2</sub>	1.455	1.448	1.451	1.440
r C <sub>2</sub> C <sub>3</sub>	1.380	1.371	1.439	1.433
r C <sub>3</sub> C <sub>4</sub>	1.412	1.405	1.394	1.385
r C <sub>2</sub> H <sub>1</sub>	1.092	1.081	1.093	1.082
r C <sub>3</sub> H <sub>2</sub>	1.093	1.082	1.094	1.083
r C <sub>4</sub> H <sub>3</sub>	1.092	1.081	1.089	1.078
a C <sub>6</sub> C <sub>1</sub> C <sub>2</sub>	117.0	117.1	111.7	112.1
a C <sub>1</sub> C <sub>2</sub> C <sub>3</sub>	121.0	120.8	123.6	123.3
a C <sub>2</sub> C <sub>3</sub> C <sub>4</sub>	120.2	120.3	122.4	122.4
a C <sub>1</sub> C <sub>2</sub> H <sub>1</sub>	116.9	117.1	117.3	117.7
a C <sub>4</sub> C <sub>3</sub> H <sub>2</sub>	119.5	119.4	119.7	119.7

Table 6.1. Geometric parameters for phenoxy radical in the ground electronic state ( $X^2B_1$ ) and second excited electronic state ( $B^2A_2$ ).

Mode	Sym	B3LYP cc-pVDZ		B3LYP aug-cc-pVTZ	
		$X^2B_1$	x0.967	$X^2B_1$	x0.967
v <sub>1</sub>	a <sub>1</sub>	3207.8	<b>3102</b>	3199.2	<b>3094</b>
v <sub>2</sub>	a <sub>1</sub>	3196.5	<b>3091</b>	3188.9	<b>3084</b>
v <sub>3</sub>	a <sub>1</sub>	3174.9	<b>3070</b>	3167.2	<b>3063</b>
v <sub>4</sub>	a <sub>1</sub>	1594.6	<b>1542</b>	1586.5	<b>1534</b>
v <sub>5</sub>	a <sub>1</sub>	1486.0	<b>1437</b>	1481.1	<b>1432</b>
v <sub>6</sub>	a <sub>1</sub>	1414.2	<b>1367</b>	1420.1	<b>1373</b>
v <sub>7</sub>	a <sub>1</sub>	1152.0	<b>1114</b>	1166.6	<b>1128</b>
v <sub>8</sub>	a <sub>1</sub>	1011.5	<b>978</b>	1010.4	<b>977</b>
v <sub>9</sub>	a <sub>1</sub>	978.3	<b>946</b>	989.9	<b>957</b>
v <sub>10</sub>	a <sub>1</sub>	808.9	<b>782</b>	806.8	<b>780</b>
v <sub>11</sub>	a <sub>1</sub>	528.3	<b>511</b>	531.4	<b>514</b>



v <sub>12</sub>	<b>a<sub>2</sub></b>	990.2	<b>958</b>	994.4	<b>962</b>
v <sub>13</sub>	<b>a<sub>2</sub></b>	810.7	<b>784</b>	808.0	<b>781</b>
v <sub>14</sub>	<b>a<sub>2</sub></b>	381.2	<b>369</b>	380.7	<b>368</b>
v <sub>15</sub>	<b>b<sub>1</sub></b>	1007.2	<b>974</b>	1006.6	<b>973</b>
v <sub>16</sub>	<b>b<sub>1</sub></b>	933.4	<b>903</b>	935.4	<b>905</b>
v <sub>17</sub>	<b>b<sub>1</sub></b>	807.2	<b>781</b>	808.8	<b>782</b>
v <sub>18</sub>	<b>b<sub>1</sub></b>	660.9	<b>639</b>	655.7	<b>634</b>
v <sub>19</sub>	<b>b<sub>1</sub></b>	488.6	<b>472</b>	480.5	<b>465</b>
v <sub>20</sub>	<b>b<sub>1</sub></b>	194.5	<b>188</b>	187.8	<b>182</b>
v <sub>21</sub>	<b>b<sub>2</sub></b>	3204.4	<b>3099</b>	3196.3	<b>3091</b>
v <sub>22</sub>	<b>b<sub>2</sub></b>	3181.9	<b>3077</b>	3173.6	<b>3069</b>
v <sub>23</sub>	<b>b<sub>2</sub></b>	1549.2	<b>1498</b>	1547.1	<b>1496</b>
v <sub>24</sub>	<b>b<sub>2</sub></b>	1442.9	<b>1395</b>	1446.6	<b>1399</b>
v <sub>25</sub>	<b>b<sub>2</sub></b>	1344.4	<b>1300</b>	1340.4	<b>1296</b>
v <sub>26</sub>	<b>b<sub>2</sub></b>	1271.8	<b>1230</b>	1278.4	<b>1236</b>
v <sub>27</sub>	<b>b<sub>2</sub></b>	1155.7	<b>1118</b>	1164.2	<b>1126</b>
v <sub>28</sub>	<b>b<sub>2</sub></b>	1082.6	<b>1047</b>	1091.2	<b>1055</b>
v <sub>29</sub>	<b>b<sub>2</sub></b>	595.4	<b>576</b>	597.1	<b>577</b>
v <sub>30</sub>	<b>b<sub>2</sub></b>	443.3	<b>429</b>	447.1	<b>432</b>

**Table 6.2.** Calculated vibrational frequencies for phenoxy radical in the ground electronic state ( $X^2B_1$ ).

<b>Assignment</b>	<b>Sym</b>	<b>TDDFT cc-pVDZ</b>		<b>TDDFT aug-cc-pVTZ</b>	
		<b>B<sup>2</sup>A<sub>2</sub></b>	<b>x0.967</b>	<b>B<sup>2</sup>A<sub>2</sub></b>	<b>x0.967</b>
0.63v <sub>2</sub> +0.26v <sub>1</sub>	<b>a<sub>1</sub></b>	3229.8	<b>3123</b>	3220.5	<b>3114</b>
0.74v <sub>1</sub> +0.25v <sub>2</sub>	<b>a<sub>1</sub></b>	3194.1	<b>3089</b>	3187.8	<b>3083</b>
0.87v <sub>3</sub> +0.12v <sub>2</sub>	<b>a<sub>1</sub></b>	3172.1	<b>3067</b>	3166.2	<b>3062</b>
0.76v <sub>5</sub> +0.19v <sub>4</sub>	<b>a<sub>1</sub></b>	1630.2	<b>1576</b>	1586.3	<b>1534</b>
0.69v <sub>4</sub> +0.21v <sub>6</sub> +0.09v <sub>5</sub>	<b>a<sub>1</sub></b>	1581.1	<b>1529</b>	1571.9	<b>1520</b>

$0.73v_6+0.15v_5+0.11v_4$	<b>a<sub>1</sub></b>	1413.1	<b>1366</b>	1419.7	<b>1373</b>
$0.92v_7$	<b>a<sub>1</sub></b>	1165.7	<b>1127</b>	1177.5	<b>1139</b>
$0.91v_8$	<b>a<sub>1</sub></b>	1039.7	<b>1005</b>	1041.7	<b>1007</b>
$0.99v_9$	<b>a<sub>1</sub></b>	967.9	<b>936</b>	979.7	<b>947</b>
$0.99v_{10}$	<b>a<sub>1</sub></b>	813.8	<b>787</b>	816.3	<b>789</b>
$1.00v_{11}$	<b>a<sub>1</sub></b>	514.7	<b>498</b>	519.8	<b>503</b>
$0.96v_{12}$	<b>a<sub>2</sub></b>	979.0	<b>947</b>	979.9	<b>948</b>
$0.97v_{13}$	<b>a<sub>2</sub></b>	836.4	<b>809</b>	840.4	<b>813</b>
$0.99v_{14}$	<b>a<sub>2</sub></b>	335.3	<b>324</b>	331.2	<b>320</b>
$0.87v_{15}+0.12v_{16}$	<b>b<sub>1</sub></b>	984.1	<b>952</b>	996.8	<b>964</b>
$0.63v_{16}+0.27v_{17}$	<b>b<sub>1</sub></b>	862.8	<b>834</b>	866.6	<b>838</b>
$0.48v_{17}+0.29v_{18}+0.12v_{16}+0.10v_{19}$	<b>b<sub>1</sub></b>	764.5	<b>739</b>	774.1	<b>749</b>
$0.63v_{18}+0.12v_{16}+0.10v_{17}$	<b>b<sub>1</sub></b>	529.8	<b>512</b>	528.8	<b>511</b>
$0.84v_{19}+0.13v_{17}$	<b>b<sub>1</sub></b>	413.5	<b>400</b>	410.3	<b>397</b>
$0.94v_{20}$	<b>b<sub>1</sub></b>	109.2	<b>106</b>	101.1	<b>98</b>
$1.00v_{21}$	<b>b<sub>2</sub></b>	3193.2	<b>3088</b>	3187.1	<b>3082</b>
$1.00v_{22}$	<b>b<sub>2</sub></b>	3175.2	<b>3070</b>	3169.2	<b>3065</b>
$0.47v_{24}+0.31v_{23}+0.17v_{25}$	<b>b<sub>2</sub></b>	1620.6	<b>1567</b>	1620.3	<b>1567</b>
$0.60v_{23}+0.36v_{24}$	<b>b<sub>2</sub></b>	1413.1	<b>1366</b>	1439.3	<b>1392</b>
$0.74v_{25}+0.13v_{24}$	<b>b<sub>2</sub></b>	1356.4	<b>1312</b>	1366.4	<b>1321</b>
$0.98v_{26}$	<b>b<sub>2</sub></b>	1244.6	<b>1204</b>	1259.1	<b>1218</b>
$0.89v_{27}$	<b>b<sub>2</sub></b>	1164.7	<b>1126</b>	1182.2	<b>1143</b>
$0.94v_{28}$	<b>b<sub>2</sub></b>	1019.1	<b>985</b>	1020.8	<b>987</b>
$0.99v_{29}$	<b>b<sub>2</sub></b>	593.1	<b>574</b>	598.4	<b>579</b>
$0.99v_{30}$	<b>b<sub>2</sub></b>	430.1	<b>416</b>	434.1	<b>420</b>

**Table 6.3.** Calculated vibrational frequencies for phenoxy radical in the second excited electronic state ( $B^2A_2$ ).

TDDFT calculations predict the first electronic transition  $A^2B_2 \leftarrow X^2B_1$ , which is symmetry forbidden, to occur in the IR region. This involves the promotion of an electron from MO 23 to MO 25. The upper state of the second electronic transition was a doublet with  $A_2$  symmetry. This is the first optically allowed electronic transition. The transition involved the promotion of one electron from the MO 24 to MO 25. The calculated vertical excitation energy (with the aug-cc-pVTZ basis set) for  $B^2A_2 \leftarrow X^2B_1$  was 2.3484 eV (527.96 nm or  $18,940 \text{ cm}^{-1}$ ) with a weak oscillator strength ( $f=0.0048$ ). This prediction is slightly higher in energy than the observed experimental origin band.

The  $A_2$  orbital from which the electron was promoted (MO 24) can be described as a bonding  $\pi_x$  molecular orbital with population density over the  $C_2C_3$  carbons and the  $C_5C_6$  carbons. The optimized excited state geometry is compared with the ground state geometry in Table 6.1. There was little change in the C=O bond length and it still retained double bond character. The carbon-carbon bonds  $C_1C_2$ ,  $C_2C_3$ , and  $C_3C_4$  were 1.440, 1.433, and 1.385 Å respectively. The largest change in carbon-carbon bond distances was the increase in the  $C_2C_3$  bond compared to the ground electronic state. There was a large decrease in the  $C_6C_1C_2$  bond  $C_3C_4C_5$  bond angles. The calculated (and scaled) harmonic vibrational frequencies for the  $B^2A_2$  electronic state are listed in Table 6.3. The assignments are linear combinations of the ground state normal modes with

coefficients corresponding to the dominant squared elements of the Duschinsky matrix ( $J_{ik}^2$ ).

The  $B^2A_2 \leftarrow X^2B_1$  vibronic spectrum of phenoxy was calculated using the Franck-Condon principle to determine intensities of transitions between the two states. The optimized geometries and frequencies were used for the ground and excited states described above, along with the built in function in Gaussian 09 to calculate<sup>51</sup> the vibrationally-resolved electronic spectrum shown in Figure 6.3 (green trace). The scaled harmonic frequencies were used in this simulation.

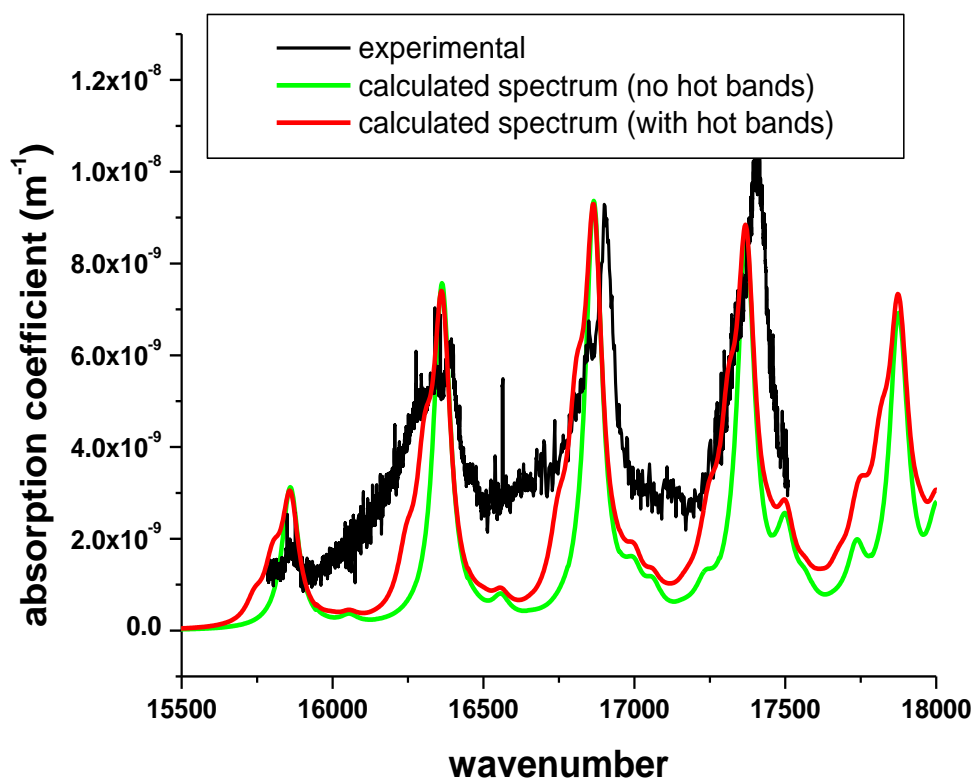


**Figure 6.3.** Visible CRD absorption spectrum of products in an expansion of electrically dissociated anisole along with calculated spectrum with (red) and without (green) hot bands. The calculated spectrum was shifted  $760 \text{ cm}^{-1}$ .

TDDFT with the aug-cc-pVTZ basis set predicted the origin of the electronic transition to be  $T_0=16620\text{ cm}^{-1}$  ( $17147\text{ cm}^{-1}$  with the cc-cVDZ basis set). Experimentally, with this assignment the origin was detected at  $15860\text{ cm}^{-1}$ , a difference of  $760\text{ cm}^{-1}$ . This difference is not beyond the typical error for this level of theory for similar molecules.<sup>47</sup> The calculated spectrum was shifted  $760\text{ cm}^{-1}$  in Figure 6.3 to compare the calculated vibrational contour with our experimental spectrum. The vibrational contour resulting from the cc-pVDZ basis set had only subtle differences. The calculated vibronic lines were broadened to account for lifetime broadening using a Lorentzian type profile with a full width half max (FWHM) of  $70\text{ cm}^{-1}$ . The simulated contour agrees well with a previous calculation published by Dierksen<sup>47</sup>.

Another alternative assignment also exists. The relative intensity of the suspected origin band at  $15860\text{ cm}^{-1}$  is much larger than observed in the experiment. If instead the origin is assigned as the peak at  $16403\text{ cm}^{-1}$  the agreement with the calculation is better. The relative intensities are a closer match, the peak positions are also in better agreement, and the origin at  $16403\text{ cm}^{-1}$  is in better agreement with the TDDFT calculation. However in this case there is not a definitive assignment for the peak at  $15860\text{ cm}^{-1}$ . The comparison of the calculated spectrum, shifted only  $217\text{ cm}^{-1}$  to match the experimental data, with the experimental data is shown in Figure 6.4 (green trace). The calculated

spectrum was shifted on the y-axis to account for background broadband absorption.

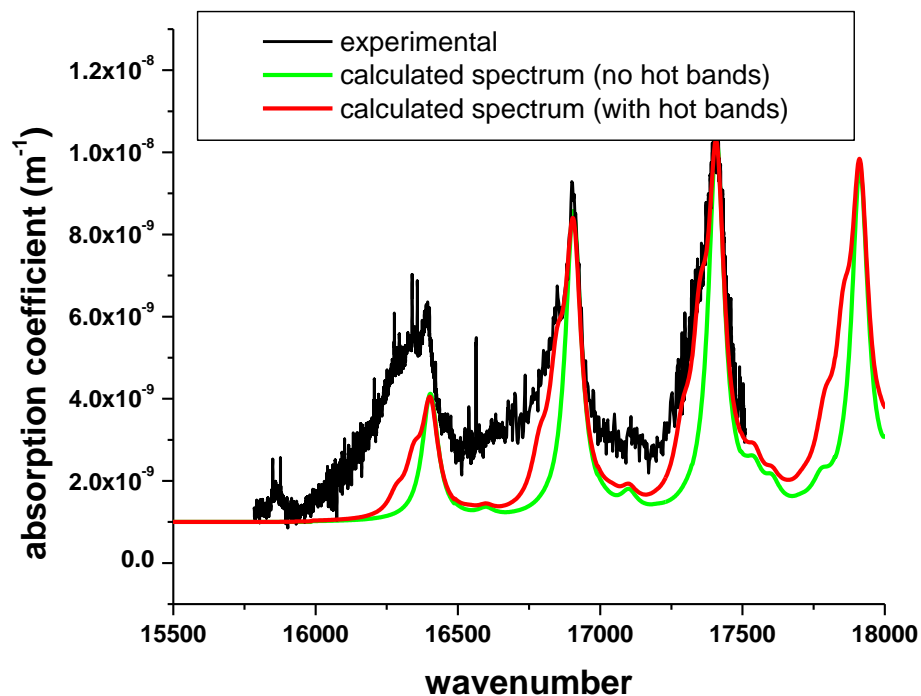


**Figure 6.4.** Visible CRD absorption spectrum of products in an expansion of electrically dissociated anisole along with calculated spectrum with (red) and without (green) hot bands. The calculated spectrum was shifted  $217 \text{ cm}^{-1}$ .

To test the influence of structure on the fit PGOPHER<sup>52</sup> was used to simulate the full rotationally resolved origin band using the rotational constants from the calculated optimized geometries ( $A''= 0.18501$ ,  $B''=0.093459$ ,  $C''=0.062093$ ,  $A'=0.19602$ ,  $B'=0.087466$ ,  $C'=0.060480$  in  $cm^{-1}$ ). The contour of the simulation including rotational splitting was nearly indistinguishable from the contour of a single broadened delta function when the Lorentzian FWHM was larger than  $20 \text{ cm}^{-1}$ . For this reason the simulated spectra reported here do not

contain rotational information but instead are composed of broadened delta functions assigned to vibronic transitions. The difference of the calculated relative intensities compared to the experimental data is then due to errors from computational approximations, hot band contributions (discussed below), and variations in the ring-down time and radical production efficiency throughout the experiments.

The intense  $516\text{ cm}^{-1}$  progression of peaks was assigned to the progression of the lowest energy  $a_1$  modes,  $\nu_{11_0}^1, \nu_{11_0}^2, \nu_{11_0}^3$ . This mode has been described as a totally symmetric (in-plane) CC-stretching/bending mode.<sup>47</sup> The blue sides of the broad simulated peaks match well with the  $70\text{ cm}^{-1}$  FWHM simulation however there appears to be shoulders about  $60\text{ cm}^{-1}$  to the red of each vibronic transition in the progression. The lowest ground state vibrational mode,  $\nu_{20}$ , was  $182\text{ cm}^{-1}$ . Therefore the shoulders cannot be attributed to the  $\nu_{11_0}^1\nu_{20_1}^0 \dots$  hot bands. Besides the difference in energy, the transition is symmetry forbidden. However, upon electronic excitation, the  $\nu_{20}$  mode is predicted to decrease by  $84\text{ cm}^{-1}$ . This could explain the bands to the red, if they were assigned to the symmetry allowed  $\nu_{11_0}^1\nu_{20_1}^1, \nu_{11_0}^2\nu_{20_1}^1, \nu_{11_0}^3\nu_{20_1}^1$  hot bands. For the best agreement, hot bands originating from  $\nu_{20_1}^1$  and  $\nu_{20_2}^2$  were added using intensities from a Boltzmann distribution at 300K and a red shift of  $60\text{ cm}^{-1}$ . The result is shown as the red traces in Figures 6.3 and 6.4. The calculated spectrum including these hot bands had better agreement with the

experimental spectrum. The peak at  $16376\text{ cm}^{-1}$  had more intense shoulder peaks because this band was acquired using the continuous expansion while the other two bands, at higher energy, were acquired using the pulsed expansion. The continuous expansion decreased the cooling efficiency resulting in a higher vibrational temperature and therefore larger shoulder peak intensities. To be sure, the peak at  $17400\text{ cm}^{-1}$  was measured using the continuous expansion. The result was much more intense shoulder peaks when compared to the pulsed valve measurement. These observations support our assignment of the shoulder peaks to these hot bands.

## 6.5. Discussion and Conclusions

By comparing the  $C_1C_2$ ,  $C_2C_3$ , and  $C_3C_4$  relative bond lengths to benzene (1.397, 1.397 and 1.397 Å) or *p*-benzoquinone (1.477, 1.322, and 1.477 Å), Chipman et al. described the phenoxy ring in its electronic ground state to be intermediate between aromatic and quinoid.<sup>41</sup> This character carries with it chemical implications especially relating to redox chemistry.<sup>53</sup> The calculated carbon ring bond lengths for the ground state (1.448, 1.371, and 1.405 Å) agree with Chipman. The ring structure for the  $B^2A_2$  electronic state (1.440, 1.433, and 1.385 Å) has reduced quinoid resemblance. The  $C_2C_3$  bond is lengthened by the removal of the electron from the  $\pi_x$  bonding orbital centralized on the  $C_2C_3$  bond to a delocalized  $\pi_x$  bond with bonding character at the  $C_3C_4C_5$  and  $C_6C_1C_2$



regions. Along with the C<sub>2</sub>C<sub>3</sub> bond shortening, this description of the electronic transition also explains the significant decrease for the C<sub>3</sub>C<sub>4</sub>C<sub>5</sub> and C<sub>6</sub>C<sub>1</sub>C<sub>2</sub> angles of 4.2 and 5.0 degrees respectively. The C=O bond retains its double bond character.

Our results cannot be compared with the isoelectronic phenylthiyl (C<sub>6</sub>H<sub>5</sub>S) radical because the experimental and theoretical work<sup>54</sup> predicts that the HOMO of phenylthiyl is localized on the S atom while for phenoxy it is delocalized over oxygen and the aromatic ring resulting in different bonding effects.

Based on the calculations reported here, the B<sup>2</sup>A<sub>2</sub> ← X<sup>2</sup>B<sub>1</sub> transition was assigned as π<sup>o</sup> ← π. This disagrees with the most recent assignments of π\* ← π.<sup>6,15</sup> The calculations support this assignment in several ways. First, the non-bonding SOMO orbital of phenyl (MO 21 in Figure 5.5) is of comparable energy to the SOMO of phenoxy (MO 25 in Figure 6.2) which is the π orbital assigned as non-bonding. TDDFT calculations also support this assignment. The one electron energy of the excited state π orbitals involved in the transition are all stabilized with respect to the isolated carbon and oxygen energies. Figure 6.5 shows the β electron energies for several molecular orbitals nearby the SOMO in the ground and excited electronic states.

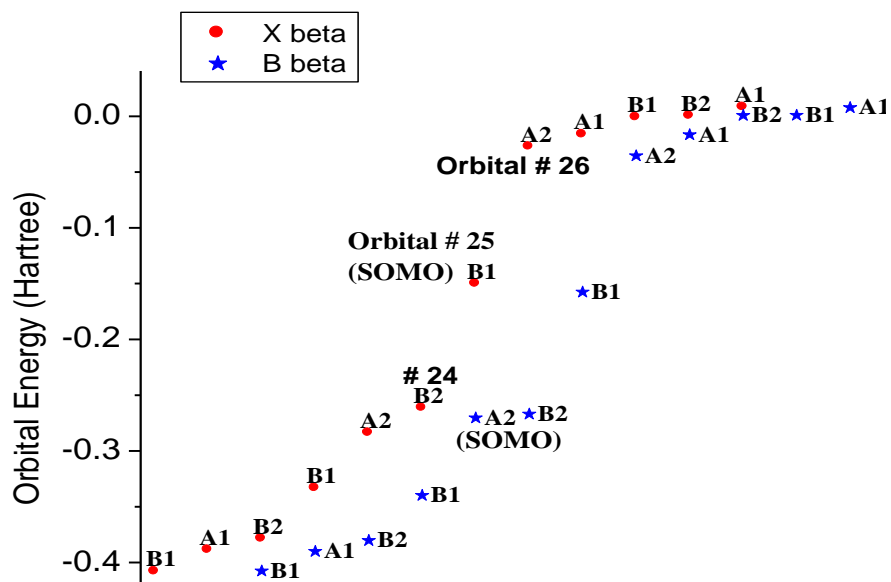


**Figure 6.5.** Calculated (TDDFT/aug-cc-pVTZ)  $\beta$  electron energies in Hartree for the ground electronic state ( $X^2B_1$ ) and second excited electronic states ( $B^2A_2$ ) of phenoxy. The orbital symmetries are labeled along with selected orbital numbers. The x-axis has no physical meaning and the orbitals are only staggered for clarity.

Orbitals 19, 22, 23, 25, 26, and 29 are all  $\pi_x$  orbitals involved in the conjugated ring and oxygen atom. Note that the orbital numbering may be different with the TDDFT than with ROHF. The majority of these orbitals, including the 25<sup>th</sup> orbital, are stabilized upon excitation. The Mulliken atomic spin density analysis of the  $X^2B_1$  and  $B^2A_2$  states also support the assignment. There is little change in spin density between the two states. This can be explained by the fact that the electron transition occurs within the same spin system - the conjugated  $\pi_x$  orbitals on the ring. This is in contrast to the  $A^2B_2$

electronic state for which Cheng's et al. calculations<sup>46</sup> predict that the spin density is almost entirely localized on the oxygen atom. They assign the  $A^2B_2 \leftarrow X^2B_1$  transition as  $\pi \leftarrow \pi$  or  $\pi^\circ \leftarrow \pi$ . The present study supports the  $\pi^\circ \leftarrow \pi$  assignment since the  $B^2A_2 \leftarrow X^2B_1$  transition involves an electron promotion to the same SOMO which they assign as  $\pi$  or  $\pi^\circ$ . MO 25 also closely resembles the highest energy doubly occupied molecular orbital of the phenyl radical, which has been assigned as a  $\pi$  bonding orbital. The final support for the assignment is that the newly doubly occupied  $\pi$  orbital shows a significant decrease for the  $C_3C_4C_5$  and  $C_6C_1C_2$  angles indicative of the bonding character for this orbital. It is this geometry change which accounts for the strong progression in our experimental spectra. The antibonding contribution at the CO region shows no change in the CO bond length.

The accuracy of the calculations reported here is supported by the agreement of the calculated spectrum with our experimental measurements. The  $516\text{ cm}^{-1}$  progression was assigned to a totally symmetric (in-plane) CC-stretching/bending  $\nu_{11}$  mode which results in a large change in the  $C_3C_4C_5$  and  $C_6C_1C_2$  angles. This stretch reflects the geometric change resulting from the  $B^2A_2 \leftarrow X^2B_1$  electronic transition. This gives a favorable Franck-Condon effect resulting in a large amplitude progression for this fundamental stretch mode.

The significant  $70\text{ cm}^{-1}$  FWHM broadening is attributed to lifetime broadening due to fast nonradiative decay from the  $B^2A_2$  electronic state. This

correlates to an excited state lifetime of 76 fs. The calculated transition oscillator strength ( $f = 0.0054$ ) corresponds to a radiative lifetime of 1.1  $\mu\text{s}$ . The fluorescence quantum yield from this state is  $7 \times 10^{-8}$ . The lifetime broadening has been observed in several previous studies<sup>6,15</sup> however the measured lifetime broadening in a jet expansion was two to three times narrower than previous reports. The larger broadening in previous reports was likely due to matrix effects. Rapid internal conversion to the  $A^2B_2$  electronic state has been suggested as the key energy transfer process.<sup>15</sup> However, dissociation of CO to produce cyclopentadienyl cannot necessarily be ignored. The thermal decomposition of phenoxy to CO and cyclopentadienyl has been measured experimentally in two separate studies<sup>55,56</sup> which both report an activation energy of 44 kcal/mol or  $15400 \text{ cm}^{-1}$  which is below the measured origin bands for both assignments. In contrast to the experimental work, computational work has consistently predicted a dissociation limit nearly 10 kcal/mol or  $3500 \text{ cm}^{-1}$  larger than the reported experimental values which would rule out the dissociation pathway. The proposed reason for this discrepancy is that the experimental measurements do not represent high-pressure values and that the use of an Arrhenius expression will underestimate the activation energy.<sup>11,57</sup> The  $B^2A_2 \leftarrow X^2B_1 \nu_{110}^1, \nu_{110}^2, \nu_{110}^3$  excitation does however bring the  $C_2$  and  $C_6$  atoms closer together which follows the proposed dissociation mechanism where the  $C_2$  and  $C_6$  atoms combine to form cyclopentadiene while ejecting CO.

## BIBLIOGRAPHY

- (1)Friderichsen, A. V.; Shin, E. J.; Evans, R. J.; Nimlos, M. R.; Dayton, D. C.; Ellison, G. B. *Fuel* **2001**, *80*, 1747.
- (2)Albert, D. R.; Davis, H. F. *J Phys Chem Lett* **2010**, *1*, 1107.
- (3)Cheng, C. W.; Witek, H.; Lee, Y. P. *J Chem Phys* **2008**, *129*.
- (4)Tonokura, K.; Ogura, T.; Koshi, M. *J Phys Chem A* **2004**, *108*, 7801.
- (5)Bayrakceken, F.; Aktas, S.; Toptan, M.; Unlugedik, A. *Spectrochim Acta A* **2003**, *59*, 135.
- (6)Radziszewski, J. G.; Gil, M.; Gorski, A.; Spanget-Larsen, J.; Waluk, J.; Mroz, B. J. *J Chem Phys* **2001**, *115*, 9733.
- (7)Friderichsen, A. V.; Radziszewski, J. G.; Nimlos, M. R.; Winter, P. R.; Dayton, D. C.; David, D. E.; Ellison, G. B. *Journal of the American Chemical Society* **2001**, *123*, 1977.
- (8)Tao, Z. N.; Li, Z. J. *Int J Chem Kinet* **1999**, *31*, 65.
- (9)Platz, J.; Nielsen, O. J.; Wallington, T. J.; Ball, J. C.; Hurley, M. D.; Straccia, A. M.; Schneider, W. F.; Sehested, J. *J Phys Chem A* **1998**, *102*, 7964.
- (10)Berho, F.; Lesclaux, R. *Chemical Physics Letters* **1997**, *279*, 289.
- (11)Liu, R. F.; Morokuma, L.; Mebel, A. M.; Liu, M. C. *J Phys Chem-US* **1996**, *100*, 9314.
- (12)Yu, T.; Mebel, A. M.; Lin, M. C. *J Phys Org Chem* **1995**, *8*, 47.
- (13)Yu, T.; Lin, M. C. *Journal of the American Chemical Society* **1994**, *116*, 9571.
- (14)Spanget-Larsen, J.; Gil, M.; Gorski, A.; Blake, D. M.; Waluk, J.; Radziszewski, J. G. *Journal of the American Chemical Society* **2001**, *123*, 11253.
- (15)Johnston, L. J.; Mathivanan, N.; Negri, F.; Siebrand, W.; Zerbetto, F. *Can J Chem* **1993**, *71*, 1655.
- (16)Kajii, Y.; Obi, K.; Nakashima, N.; Yoshihara, K. *J Chem Phys* **1987**, *87*, 5059.
- (17)Pullin, D.; Andrews, L. *Journal of Molecular Structure* **1982**, *95*, 181.
- (18)Beck, S. M.; Brus, L. E. *J Chem Phys* **1982**, *76*, 4700.
- (19)Ward, B. *Spectrochim Acta a-M* **1968**, *A 24*, 813.
- (20)Land, E. J.; Porter, G.; Strachan, E. *Transactions of the Faraday Society* **1961**, *57*, 1885.
- (21)Porter, G.; Strachan, E. *Transactions of the Faraday Society* **1958**, *54*, 1595.
- (22)Nix, M. G. D.; Devine, A. L.; Cronin, B.; Dixon, R. N.; Ashfold, M. N. R. *J Chem Phys* **2006**, *125*.
- (23)Jarvis, M. W.; Daily, J. W.; Carstensen, H. H.; Dean, A. M.; Sharma, S.; Dayton, D. C.; Robichaud, D. J.; Nimlos, M. R. *J Phys Chem A* **2011**, *115*, 428.
- (24)Scheer, A. M.; Mukarakate, C.; Robichaud, D. J.; Ellison, G. B.; Nimlos, M. R. *J Phys Chem A* **2010**, *114*, 9043.

- (25) Kim, J. B.; Yacovitch, T. I.; Hock, C.; Neumark, D. M. *Physical Chemistry Chemical Physics* **2011**, *13*, 17378.
- (26) Schuler, R. H.; Neta, P.; Zemel, H.; Fessenden, R. W. *Journal of the American Chemical Society* **1976**, *98*, 3825.
- (27) Neta, P.; Fessenden, R. W. *J Phys Chem-U*s **1974**, *78*, 523.
- (28) Porter, G.; Wright, F. J. *Transactions of the Faraday Society* **1955**, *51*, 1469.
- (29) Dixon, W. T.; Murphy, D. *J Chem Soc Farad T 2* **1976**, *72*, 1221.
- (30) Dixon, W. T.; Norman, R. O. C. *J Chem Soc* **1964**, 4850.
- (31) Stone, T. J.; Waters, W. A. *P Chem Soc London* **1962**, 253.
- (32) Stone, T. J.; Waters, W. A. *J Chem Soc* **1964**, 213.
- (33) Mukherjee, A.; Mcglashen, M. L.; Spiro, T. G. *J Phys Chem-U*s **1995**, *99*, 4912.
- (34) Tripathi, G. N. R.; Schuler, R. H. *J Chem Phys* **1984**, *81*, 113.
- (35) Tripathi, G. N. R.; Schuler, R. H. *J Phys Chem-U*s **1988**, *92*, 5129.
- (36) Johnson, C. R.; Ludwig, M.; Asher, S. A. *Journal of the American Chemical Society* **1986**, *108*, 905.
- (37) Roebber, J. L. *J Chem Phys* **1962**, *37*, 1974.
- (38) Gunion, R. F.; Gilles, M. K.; Polak, M. L.; Lineberger, W. C. *International Journal of Mass Spectrometry and Ion Processes* **1992**, *117*, 601.
- (39) Kesper, K.; Diehl, F.; Simon, J. G. G.; Specht, H.; Schweig, A. *Chemical Physics* **1991**, *153*, 511.
- (40) Richardson, J. H.; Stephenson, L. M.; Brauman, J. I. *Journal of the American Chemical Society* **1975**, *97*, 2967.
- (41) Chipman, D. M.; Liu, R. F.; Zhou, X. F.; Pulay, P. *J Chem Phys* **1994**, *100*, 5023.
- (42) Takahashi, J.; Momose, T.; Shida, T. *Bulletin of the Chemical Society of Japan* **1994**, *67*, 964.
- (43) Hirata, S.; Head-Gordon, M. *Chemical Physics Letters* **1999**, *302*, 375.
- (44) Adamo, C.; Barone, V. *Chemical Physics Letters* **1999**, *314*, 152.
- (45) Chang, H. M.; Jaffe, H. H.; Masmanidis, C. A. *J Phys Chem-U*s **1975**, *79*, 1118.
- (46) Cheng, C. W.; Lee, Y. P.; Witek, H. A. *J Phys Chem A* **2008**, *112*, 2648.
- (47) Dierksen, M.; Grimme, S. *J Chem Phys* **2004**, *120*, 3544.
- (48) Rinkevicius, Z.; Tunell, I.; Salek, P.; Vahtras, O.; Agren, H. *J Chem Phys* **2003**, *119*, 34.
- (49) Freil, K.; Park, J.; Lin, M. C.; Heaven, M. C. *Chemical Physics Letters* **2011**, *507*, 216.
- (50) Frisch, M. J. **2009**.
- (51) Bloino, J.; Biczysko, M.; Santoro, F.; Barone, V. *J Chem Theory Comput* **2010**, *6*, 1256.

- (52) C.M. Western, P., a program for simulating rotational structure, University of Bristol, 2007.
- (53) Brunmark, A.; Cadenas, E. *Free Radical Bio Med* **1989**, *7*, 435.
- (54) Lim, J. S.; Lim, I. S.; Lee, K. S.; Ahn, D. S.; Lee, Y. S.; Kim, S. K. *Angewandte Chemie-International Edition* **2006**, *45*, 6290.
- (55) Lin, C. Y.; Lin, M. C. *J Phys Chem-Us* **1986**, *90*, 425.
- (56) Frank, P.; Herzler, J.; Just, T.; Wahl, C. *Symposium (International) on Combustion* **1994**, *25*, 833.
- (57) Carstensen, H. H.; Dean, A. M. *Int J Chem Kinet* **2012**, *44*, 75.

## Chapter 7. The Phenyl Peroxy Radical

### 7.1. Introduction

The phenyl peroxy radical ( $C_6H_5O_2$ ) is known to be an important intermediate in combustion chemistry and the low temperature oxidation of benzene<sup>1-6</sup>. It is produced by the barrierless exothermic reaction of the phenyl radical with  $O_2$ . Following its production, phenyl peroxy may be stabilized by collisional relaxation or it may rearrange to form the 2-oxepinoxy radical<sup>7-9</sup>. If there is sufficient internal energy, the latter may further decompose to  $CO_2$  and the cyclopentadienyl radical. There are several other decomposition pathways at higher energies, including those that lead to the formation of the phenoxy radical ( $C_6H_5O$ )<sup>7-11</sup>. Experimental studies of the  $C_6H_5+O_2$  reaction have been conducted using normal gas phase conditions<sup>2,12,13</sup> and crossed molecular beams techniques<sup>4,10,11</sup>. This work has been accompanied by a substantial computational modeling effort<sup>5-9,14</sup>.

In several experimental studies of the reaction kinetics, the absorption spectrum in the visible range has been used to monitor the concentration of the radical<sup>2,12,13</sup>. Some of the earliest spectroscopic data for phenyl peroxy were obtained in the solution phase, using pulsed radiolysis to generate the radical<sup>15,16</sup>. A broad absorption band, with a maximum near 470 nm, was reported. Yu and Lin<sup>13</sup> then observed an absorption feature in a gas phase experiment that was attributed to phenyl peroxy. Their original intent was to study the phenyl +  $O_2$



reaction by means of a phenyl absorption band at 504.8 nm. Owing to the weakness of this transition, they used the pulsed cavity ring-down spectroscopy (CRDS) technique for these measurements. A revised monitoring strategy was adopted when it was recognized that one of the reaction products also absorbed the 504.8 nm light. A spectrum for this product, which was essentially featureless over the 495-531 nm range, was attributed to phenyl peroxy. This absorption was used by Lin and Yu<sup>13</sup>, and subsequently by other groups studying the kinetics of phenyl peroxy<sup>2,12</sup>, to monitor the production and decay of the radical. There is good circumstantial evidence linking the broad absorption near 504 nm to phenyl peroxy, but the lack of structure is problematic. First, it is difficult to know if phenyl peroxy is the only absorbing species, or if there are other reaction products that contribute. Secondly, the lack of structure precludes a rigorous species assignment.

There have been theoretical studies of the three lowest energy electronic transitions of phenyl peroxy<sup>14,16,17</sup>. Electronic structure calculations predict that the molecule is planar in the ground and the lower energy excited states, with  $C_s$  symmetry. The lowest energy transition,  $\tilde{A}^2A' - \tilde{X}^2A''$  is attributed to promotion of an electron between orbitals that are mostly localized on the peroxy moiety<sup>14,17</sup> (the singly occupied molecular orbital (SOMO) of the ground state receives the excited electron). This transition, which typically has a very small oscillator strength, is found at an energy near 7500  $\text{cm}^{-1}$  for a range of aromatic and

aliphatic peroxy radicals<sup>14,18</sup>. The next higher excited state for phenyl peroxy involves promotion of an electron from an orbital that is approximately  $p\pi$  of the phenyl ring, to the SOMO. As there are two ring  $p\pi$  orbitals that are close in energy (related to the  $e_{1g}$  orbitals of benzene), the second and third excited states (both  $A''$  symmetry) are attributed to promotions from these two orbitals (see Fig. 5 of ref. 14). These transitions have larger oscillator strengths (on the order of  $10^{-3}$  to  $10^{-2}$ ), and are thought to be responsible for the visible and near uv absorption.

There are few spectroscopic studies reported for phenyl peroxy. Yamauchi et al.<sup>19</sup> tentatively assigned the EPR spectrum and obtained a  $g$ -value typical of peroxy radicals ( $g \sim 2.014$ ). IR absorption spectra have been reported for the radical isolated in solid Argon at 10 K<sup>20</sup>. In that study, seventeen fundamental bands were identified for the normal isotope, and three other isotopic variants were characterized. Density functional theory (DFT) calculations, at the level of UB3LYP with the Dunning cc-pVTZ basis set<sup>21</sup>, yielded vibrational frequencies that were in reasonably good agreement with the measurements. The  $\tilde{A}^2A' - \tilde{X}^2A''$  transition of phenyl peroxy in the gas phase was examined by Just et al.<sup>17</sup> using CRDS. Their vibrationally resolved spectrum showed the origin ( $7497 \text{ cm}^{-1}$ ), sequence bands involving a low frequency mode ( $\approx 85 \text{ cm}^{-1}$ ), the O-O stretch modes and C-O-O bending. The intensity pattern was consistent with the model of a peroxy-centered excitation to the  $\pi^*$ -like

SOMO. Electronic structure calculations were performed to facilitate the analysis of the spectrum. Equilibrium geometries and vibrational frequencies were calculated for both the  $\tilde{A}$  and  $\tilde{X}$  states using the combination B3LYP/6-31+g(d). The scaled vibrational frequencies for the excited state were in good agreement with the observations.

Gas phase CRDS data for the higher energy transition(s) have been recorded at room temperature, with a focus on the 18850-20200  $\text{cm}^{-1}$  range<sup>2,12,13</sup>. These studies all report a structureless spectrum, and it is of obvious interest to determine the cause. Is the lack of structure due to homogeneous line broadening associated with rapid internal conversion and/or isomerization, spectral congestion, or some combination of these causes? Are there lower energy regions of the spectrum where structure can be observed? If so, the analysis of this structure might be used to further explore the validity of the assignment to the phenyl peroxy radical. The discovery of structured regions of the spectrum may also facilitate a more species specific detection of the radical in future kinetic studies.

The congestion of the phenyl peroxy spectrum may be significantly reduced by the application of jet-expansion cooling techniques. Miller and co-workers have shown that cold peroxy radicals can be produced using  $\text{O}_2$  addition reactions in an electric discharge slit expansion<sup>22-24</sup>. In the present study we used the same system as in the previous chapters to examine phenyl peroxy. A

vibrationally resolved spectrum was observed in the 17500 - 19900  $\text{cm}^{-1}$  range. The spectrum was assigned using the predictions from time-dependent density functional theory (TD-DFI) calculations.

## 7.2. Experimental

The discharge-jet, cavity ring down spectrometer used for these measurements was described in detail Chapter 3. The most significant difference for the present experiments was the use of a continuous slit expansion. The pulsed valves of the earlier design were not used due to problems with the repeatability of the gas pulses, which resulted in non-uniform discharges, intermittent arching, and problems with the deposition of soot on the discharge electrodes. Consequently, a continuous gas flow was used, with pulsed discharge production of the radicals.

High voltage jaws and grounding plates defined the slit discharge assembly. Phenolic spacers (1 mm thick) provided insulation between the electrically grounded aluminum mounting plate and the high voltage jaws. The discharge plates (80 mm in length) formed a slit with a width of 1 mm. The electrical discharge was operated at a voltage of -800 V with a pulse duration of 1 ms. These conditions produced a current of approximately 65 mA through a  $1\text{k}\Omega$  ballast resistor during the discharge.

The phenyl peroxy radical was produced by secondary reactions in the discharge and post-discharge flow. The gas mixture prior to the discharge consisted of bromobenzene vapor in a mixture of Ar and O<sub>2</sub>. It is well known that discharge excitation of bromobenzene / Ar mixtures will produce the phenyl radical. Presumably, the phenyl peroxy radical was produced in the jet by the subsequent O<sub>2</sub> addition reaction. Bromobenzene vapor was entrained by bubbling the Ar/O<sub>2</sub> carrier gas mixture through a liquid sample. The sample and gas lines were heated to 70 C to increase the partial pressure of bromobenzene. For a carrier gas source pressure of 1 atm (the typical operating condition for these experiments) we estimate that the mole fraction of bromobenzene was in the range 0.01-0.04. To help identify the reaction products resulting from the oxygen chemistry, spectra were recorded for mixtures with and without oxygen, but with all other conditions held as near to constant as could be achieved. The mole fraction of the oxygen in the gas mixture was varied to find the optimum conditions for phenyl peroxy formation. Initial experiments were performed with premixed Ar/O<sub>2</sub>. However, it was found to be easier to tune the conditions continuously by inline mixing. A needle valve was used to control the addition of O<sub>2</sub> to Ar, prior to the mixture passing through the bromobenzene. The liquid sample was replaced at regular intervals to avoid the accumulation of oxidation products.

Two sets of cavity mirrors were used for these measurements. The dielectric coatings on these mirrors provided their highest reflectivities (99.995%) at 500 and 540 nm. As the mirrors were separated by 1m, the maximum theoretical ring-down time was 66  $\mu$ s. Typically, empty cavity ring-down times of around 40  $\mu$ s were observed. The ring-down spectra of the discharge products exhibited lines from metastable excited states of Ar and the Swan bands of C<sub>2</sub>. These features were used to establish the absolute wavenumber calibrations. For the phenyl peroxy spectrum, the best compromise between signal strength and cooling was obtained with the laser beam position 7 mm away from the discharge slit.

Survey scans covering about 10 nm per sweep were acquired using a laser step size of  $\sim 0.4$  cm<sup>-1</sup> while averaging 30 ring-down decay curves per point (15 with the discharge on and 15 with the discharge off). Pairs of scans were co-added to improve the sensitivity and ensure reproducibility. Shorter ranges of interest, such as the origin band region, were acquired using a smaller laser step size of  $\sim 0.04$  cm<sup>-1</sup> while averaging 30 ring-down time measurements per point. Five scans were co-added to reduce the noise.

### 7.3. Experimental Results

The experimental conditions were first optimized by observing the spectrum of the phenyl radical by discharging Ar/C<sub>6</sub>H<sub>5</sub>Br mixtures. Broadband

absorption and/or scattering losses were present across the entire range of the spectrum. The ring-down time also changed with wavelength due to changes in mirror reflectivity.

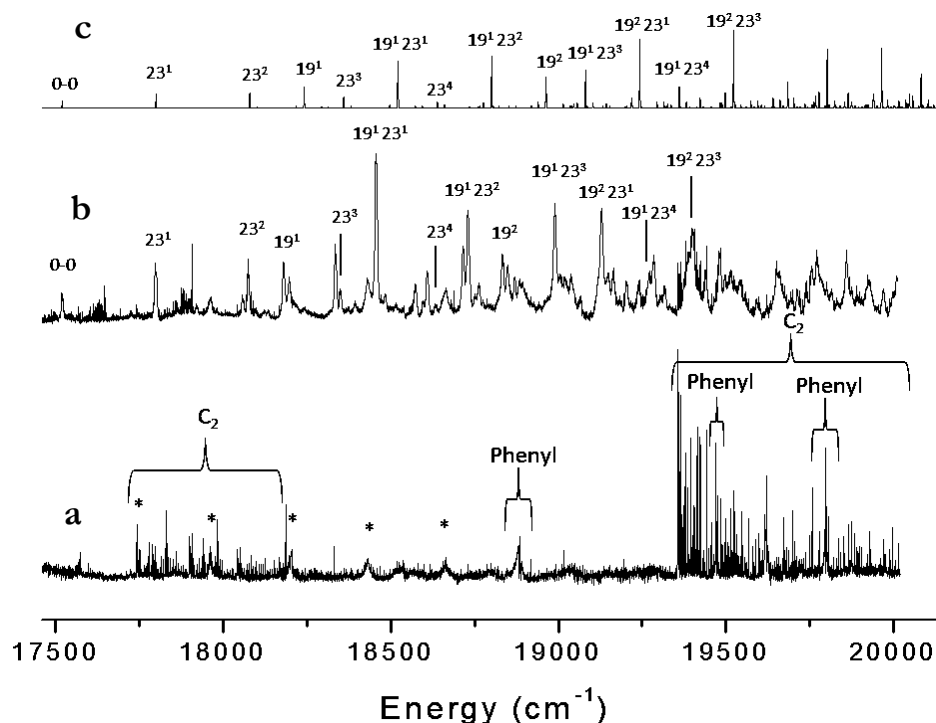


**Figure 7.1.** CRDS absorption spectra of the products in an expansion of electrically dissociated bromobenzene **(a)** without O<sub>2</sub> and **(b)** with O<sub>2</sub> compared to **(c)** a spectrum for phenyl peroxy predicted using molecular properties from a TDDFT/aug-cc-pVTZ calculation.

Trace a in Fig. 7.1 shows a typical spectrum for the Ar/C<sub>6</sub>H<sub>5</sub>Br mixtures. The bands of phenyl, C<sub>2</sub> and the atomic lines of Ar were the dominant features. There was also a progression of bands with a spacing of about 235 cm<sup>-1</sup> (marked with asterisks in Fig. 7.1), for which the carrier has not yet been identified. In addition to the structured features, there was a continuous background that

increased approximately linearly from  $8.1 \times 10^{-9} \text{ m}^{-1}$  at  $17650 \text{ cm}^{-1}$  to  $3.6 \times 10^{-8} \text{ m}^{-1}$  at  $20000 \text{ cm}^{-1}$ . This background has been subtracted from the traces a and b of Fig 7.1.

After observing the Ar/C<sub>6</sub>H<sub>5</sub>Br discharge products, O<sub>2</sub> was added to the carrier flow and the concentration was increased until the phenyl radical absorption was below the noise level. Premixed gases with 1% and 10% O<sub>2</sub> in Ar were used to test the concentration necessary to observe new features. It was found that >10% O<sub>2</sub> was needed to deplete the phenyl absorption and produce the new spectral features. At 10% O<sub>2</sub> the phenyl absorption was reduced by 50%, but new features were not observed. However, further addition of O<sub>2</sub>, accomplished using inline mixing, resulted in the complete consumption of phenyl and the appearance of many new spectral features. As can be seen in Fig. 7.1b, the reaction with oxygen removed the C<sub>2</sub> and phenyl absorption bands, but the unidentified features with a spacing of  $235 \text{ cm}^{-1}$  remained. We have assigned the dominant bands in Fig. 7.1b to a single carrier, on the basis of their common response to changes in the oxygen content and expansion conditions. Scanning to energies below  $17500 \text{ cm}^{-1}$  revealed known bands of the phenoxy radical<sup>13</sup>, but no other features of the dominant new spectrum. Hence, we assign the feature at  $17519 \text{ cm}^{-1}$  as an origin band. The band centers for the more intense new features of Fig. 7.1b are listed in Table 7.1. After correction for the baseline signal, the most intense band of the new spectrum ( $18463 \text{ cm}^{-1}$ ) had an



<b>Band</b>	<b>Band Center</b>	<b>G(v)</b>	<b><math>\Delta E</math></b>	<b><math>\Delta E</math> scaled</b>
0 <sup>0</sup>	17519	0	0	0
23 <sup>1</sup>	17798	279	289.3	279.8
22 <sup>1</sup>	17920	401	432.2	417.9
20 <sup>1</sup>	18057	538	601.3	581.5
23 <sup>2</sup>	18074	555	578.6	559.5
19 <sup>1</sup>	18180	661	746.2	721.6
22 <sup>1</sup> 23 <sup>1</sup>	18196	678	721.5	697.7
20 <sup>1</sup> 23 <sup>1</sup>	18335	816	890.5	861.1
23 <sup>3</sup>	18349	830	867.8	839.2
19 <sup>1</sup> 23 <sup>1</sup>	18456	937	1035.4	1001.3
22 <sup>1</sup> 23 <sup>2</sup>	18483	964	1010.8	977.4
19 <sup>1</sup> 22 <sup>1</sup>	18573	1054	1178.4	1139.5
20 <sup>2</sup>	18596	1078	1202.5	1162.8
20 <sup>1</sup> 23 <sup>2</sup>	18608	1090	1179.8	1140.9
23 <sup>4</sup>	18633	1115	1157.1	1118.9
19 <sup>1</sup> 20 <sup>1</sup>	18715	1196	1347.4	1303.0
19 <sup>1</sup> 23 <sup>2</sup>	18730	1211	1324.7	1281.0
22 <sup>1</sup> 23 <sup>3</sup>	18752	1234	1300.0	1257.1
12 <sup>1</sup>	18762	1243	1288.7	1246.2
19 <sup>2</sup>	18833	1314	1492.3	1443.1
19 <sup>1</sup> 22 <sup>1</sup> 23 <sup>1</sup>	18848	1329	1467.6	1419.2
20 <sup>2</sup> 23 <sup>1</sup>	18869	1351	1491.8	1442.6
20 <sup>1</sup> 23 <sup>3</sup>	18883	1365	1469.1	1420.6
19 <sup>1</sup> 23 <sup>3</sup>	18989	1471	1614.0	1560.7
19 <sup>1</sup> 20 <sup>1</sup> 23 <sup>1</sup>	19004	1486	1636.7	1582.7

$20^1 22^1 23^2$	19019	1501	1612.0	1558.8
$12^1 23^1$	19038	1520	1578.0	1525.9
$19^2 23^1$	19128	1610	1781.6	1722.8
$19^1 22^1 23^2$	19148	1629	1756.9	1698.9
$12^1 22^1$	19163	1645	1720.9	1664.1
$19^1 20^2$	19203	1684	1948.7	1884.4
$12^1 20^1$	19240	1721	1889.9	1827.6
$19^1 23^4$	19271	1752	1903.3	1840.5
$19^1 20^1 23^2$	19284	1765	1926.0	1862.4
$12^1 23^2$	19316	1797	1867.3	1805.6

**Table 7.1.** List of measured band positions and vibrational energies ( $G(v)$ ) compared with scaled harmonic vibrational frequencies ( $\Delta E$ ) from theoretical calculations ( $\text{cm}^{-1}$  units).

absorption coefficient of  $\alpha=4.2 \times 10^{-8} \text{ m}^{-1}$ . Regular vibrational progressions were easily recognized in the lower energy range. The harmonic vibrational constants defined by these progressions are given in Table 7.2.

Band progression	$\omega_e$
$23^v$	$278.0 \pm .6$
$20^v$	$539.0 \pm .6$
$19^v$	$657.0 \pm 2.3$
$22^1 23^v$	$278.0 \pm 4.6$
$20^1 23^v$	$275.5 \pm .3$
$19^1 23^v$	$270.5 \pm 2.7$

**Table 7.2.** Harmonic Vibrational Constants for the  $\tilde{B}^2A''$  state derived from the experimental data.

The sharper molecular features of Fig. 7.1b exhibited widths of approximately  $5\text{-}10\text{ cm}^{-1}$  (FWHM) in the low resolution survey scan. To learn more about the rotational structure, and/or the homogeneous line broadening, the  $17519\text{ cm}^{-1}$  band was recorded using a step size of  $0.04\text{ cm}^{-1}$ . The result from this scan, shown in Fig. 7.2, was an unresolved contour. However, this feature was not entirely without structure, and the characteristic P- and R- branch maxima of a parallel transition could be discerned.

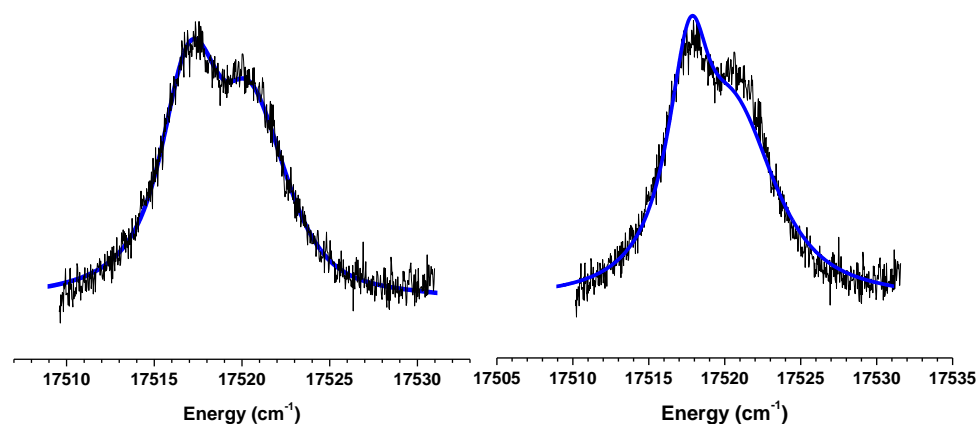


**Figure 7.2.** Rotational contour of the phenyl peroxy  $\tilde{B}^2A'' - \tilde{X}^2A''$  origin band. This figure shows two copies of the experimental data (traces with noise) accompanied by computer simulations. The left-hand side shows the best fit simulation based on the molecular constants from the TD-DFT/aug-cc-pVDZ calculations. These were  $A'' = 0.172045$ ,  $B'' = 0.053640$ ,  $C'' = 0.040903$ ,  $A' = 0.162784$ ,  $B' = 0.055228$ ,  $C' = 0.0412371\text{ cm}^{-1}$ ,  $\mu_a = 0.827$  and  $\mu_b = 0.371\text{ D}$ . The simulation on the right used the constants from the TD-DFT/aug-cc-pVTZ calculations. These were  $A'' = 0.17415$ ,  $B'' = 0.05045$ ,  $C'' = 0.04125$ ,  $A' = 0.16449$ ,  $B' = 0.05564$ ,  $C' = 0.04115\text{ cm}^{-1}$ ,  $\mu_a = 0.838$  and  $\mu_b = 0.385\text{ D}$ .

#### 7.4. Theoretical calculations

Theoretical predictions of the visible band systems of phenyl peroxy were carried out to assist with the spectral assignment. All calculations were performed using the Gaussian 09 suite of computational chemistry programs<sup>25</sup>. The ground state equilibrium structure and harmonic vibrational frequencies were calculated using the UB3LYP hybrid DFT method with Dunning's aug-cc-pVDZ and aug-cc-pVTZ basis sets<sup>21</sup>. Tight convergence criteria were used for the geometry optimizations. In agreement with earlier studies<sup>14,17</sup>, the peroxy  $p\pi$  orbital was found to be prominent in the SOMO of the  $\tilde{X}^2A''$  ground state. This orbital is shown in Fig. 7.3. Bond lengths and bond angles are listed in Table 7.3, while Fig. 7.4a shows the equilibrium structure from the B3LYP/ aug-cc-pVTZ calculation. The O=O bond length of 1.321 Å is close to known lengths for other peroxy radicals. The CO bond was 1.398 Å which is comparable to the single bond C-O in methanol (1.427 Å). All of the CC bonds were close to 1.40 Å - representative of a benzene ring. The rotational constants were predicted to be  $A''=0.17415$ ,  $B''=0.05045$  and  $C''=0.04125$  cm<sup>-1</sup>. Ground state vibrational frequencies, scaled by the recommended value of 0.967<sup>26</sup>, are listed in Table 7.4. These were in good agreement with the results from the matrix isolation study of the IR spectrum<sup>20</sup>.

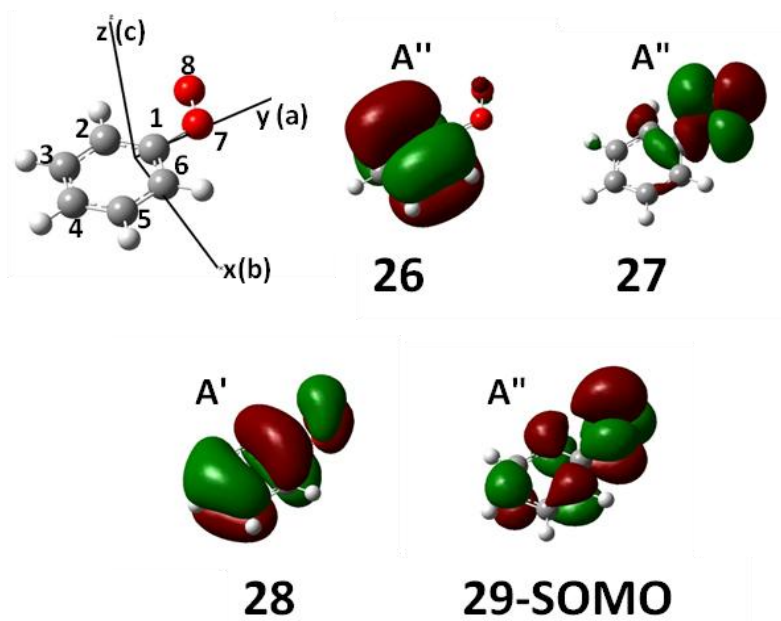


**Figure 7.3.** Molecular orbitals involved in the first three electronic transitions of phenyl peroxy calculated at the B3LYP/aug-cc-pVTZ level for  $\tilde{X}^2A''$ . Plots were generated with an isodensity value of 0.02 a.u.

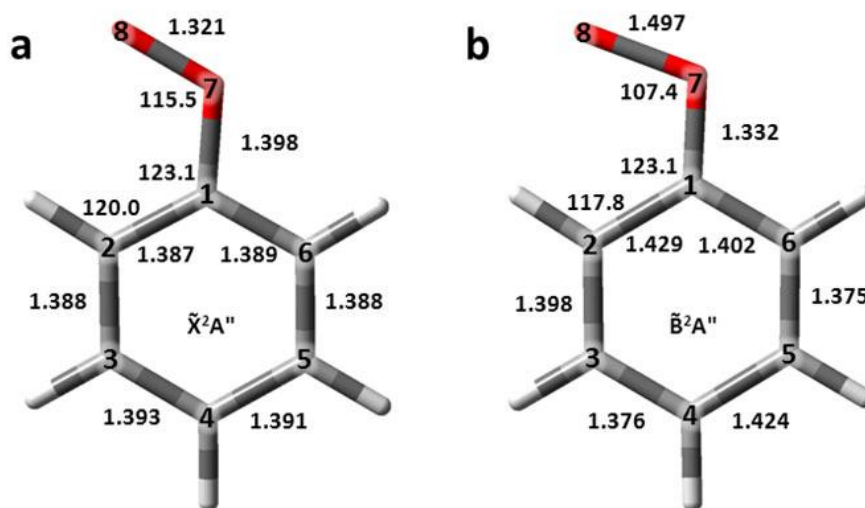


**Figure 7.4.** Equilibrium bond lengths and bond angles for the phenyl peroxy radical calculated at the B3LYP/aug-cc-pVTZ level for (a)  $X^2A''$  and (b) by TDDFT/aug-cc-pVTZ for  $B^2A''$ .

Level	B3LYP	TDDFT	TDDFT	TDDFT
Basis Set	aug-cc-pVDZ	aug-cc-pVDZ	aug-cc-pVDZ	aug-cc-pVDZ
Electronic				
State	$\tilde{X}^2A''$	$\tilde{A}^2A'$	$\tilde{B}^2A''$	$\tilde{C}^2A''$
r OO	1.321	1.372	1.492	1.456
r CO	1.403	1.382	1.340	1.340
r C <sub>1</sub> C <sub>6</sub>	1.397	1.401	1.407	1.427
r C <sub>6</sub> C <sub>5</sub>	1.396	1.393	1.385	1.432
r C <sub>5</sub> C <sub>4</sub>	1.400	1.402	1.432	1.379
r C <sub>4</sub> C <sub>3</sub>	1.401	1.397	1.383	1.412
r C <sub>3</sub> C <sub>2</sub>	1.397	1.399	1.408	1.433
r C <sub>2</sub> C <sub>1</sub>	1.395	1.397	1.437	1.387
r C <sub>6</sub> H <sub>6</sub>	1.089	1.089	1.089	1.090
r C <sub>5</sub> H <sub>5</sub>	1.090	1.090	1.091	1.090
r C <sub>4</sub> H <sub>4</sub>	1.090	1.090	1.089	1.088
r C <sub>3</sub> H <sub>3</sub>	1.090	1.090	1.090	1.091
r C <sub>2</sub> H <sub>2</sub>	1.087	1.088	1.084	1.086
a O <sub>8</sub> O <sub>7</sub> C <sub>1</sub>	115.3	114.2	107.2	110.5
a O <sub>7</sub> C <sub>1</sub> C <sub>2</sub>	123.1	122.9	122.9	125.2
a C <sub>2</sub> C <sub>1</sub> C <sub>6</sub>	122.6	122.0	120.2	117.6
a C <sub>1</sub> C <sub>6</sub> C <sub>5</sub>	118.5	118.5	119.0	121.7
a C <sub>6</sub> C <sub>5</sub> C <sub>4</sub>	120.2	120.7	121.7	120.7
a C <sub>5</sub> C <sub>4</sub> C <sub>3</sub>	120.0	119.6	119.2	117.4
a C <sub>4</sub> C <sub>3</sub> C <sub>2</sub>	120.8	120.9	120.7	122.8
a C <sub>3</sub> C <sub>2</sub> C <sub>1</sub>	117.9	118.3	119.3	119.8
a C <sub>1</sub> C <sub>6</sub> H <sub>6</sub>	119.7	119.8	119.4	118.5
a C <sub>4</sub> C <sub>5</sub> H <sub>5</sub>	120.2	120.1	119.1	120.9
a C <sub>1</sub> C <sub>2</sub> H <sub>2</sub>	120.0	120.5	117.8	118.7
a C <sub>4</sub> C <sub>3</sub> H <sub>3</sub>	119.9	120.1	120.4	119.4
a C <sub>5</sub> C <sub>4</sub> H <sub>4</sub>	120.0	120.2	119.6	121.9

Level	B3LYP	TDDFT	TDDFT	TDDFT
Basis Set	aug-cc-pVTZ	aug-cc-pVTZ	aug-cc-pVTZ	aug-cc-pVTZ
Electronic State	$\tilde{X}^2A''$	$\tilde{A}^2A'$	$\tilde{B}^2A''$	$\tilde{C}^2A''$
r OO	1.321	1.371	1.497	1.456
r CO	1.398	1.377	1.332	1.333
r C <sub>1</sub> C <sub>6</sub>	1.389	1.393	1.402	1.418
r C <sub>6</sub> C <sub>5</sub>	1.388	1.385	1.375	1.426
r C <sub>5</sub> C <sub>4</sub>	1.391	1.394	1.424	1.370
r C <sub>4</sub> C <sub>3</sub>	1.393	1.389	1.376	1.403
r C <sub>3</sub> C <sub>2</sub>	1.388	1.391	1.398	1.427
r C <sub>2</sub> C <sub>1</sub>	1.387	1.390	1.429	1.379
r C <sub>6</sub> H <sub>6</sub>	1.081	1.080	1.080	1.081
r C <sub>5</sub> H <sub>5</sub>	1.081	1.081	1.081	1.081
r C <sub>4</sub> H <sub>4</sub>	1.081	1.081	1.080	1.079
r C <sub>3</sub> H <sub>3</sub>	1.081	1.081	1.081	1.082
r C <sub>2</sub> H <sub>2</sub>	1.078	1.079	1.074	1.077
a O <sub>8</sub> O <sub>7</sub> C <sub>1</sub>	115.5	114.5	107.4	110.8
a O <sub>7</sub> C <sub>1</sub> C <sub>2</sub>	123.1	122.9	123.1	125.3
a C <sub>2</sub> C <sub>1</sub> C <sub>6</sub>	122.4	121.8	120.0	117.3
a C <sub>1</sub> C <sub>6</sub> C <sub>5</sub>	118.6	118.6	119.1	121.9
a C <sub>6</sub> C <sub>5</sub> C <sub>4</sub>	120.1	120.7	121.6	120.7
a C <sub>5</sub> C <sub>4</sub> C <sub>3</sub>	120.0	119.6	119.3	117.3
a C <sub>4</sub> C <sub>3</sub> C <sub>2</sub>	120.7	120.8	120.7	122.8
a C <sub>3</sub> C <sub>2</sub> C <sub>1</sub>	118.1	118.4	119.4	120.0
a C <sub>1</sub> C <sub>6</sub> H <sub>6</sub>	119.6	119.7	119.2	118.4
a C <sub>4</sub> C <sub>5</sub> H <sub>5</sub>	120.2	120.1	119.1	120.9
a C <sub>1</sub> C <sub>2</sub> H <sub>2</sub>	120.0	120.4	117.8	118.6
a C <sub>4</sub> C <sub>3</sub> H <sub>3</sub>	119.9	120.1	120.4	119.5
a C <sub>5</sub> C <sub>4</sub> H <sub>4</sub>	120.0	120.2	119.6	121.9

**Table 7.3.** Complete list of bond lengths and bond angles for the phenyl peroxy radical calculated at the B3LYP/aug-cc-pVDZ level (first table) and B3LYP/aug-cc-pVTZ (second table) for  $\tilde{X}^2A''$ , and by TD-DFT for the excited electronic states.

Excited state properties were predicted using time-dependent density functional theory (TD-DFT) with the basis sets noted above. The calculations considered eight excited states and were separately optimized for the first, second and third excited states. Equilibrium structures and vibrational frequencies were obtained. The bond lengths and bond angles for the  $\tilde{A}^2A'$ ,  $\tilde{B}^2A''$ , and  $\tilde{C}^2A''$  states are given in Table 7.3. Fig. 7.4b shows the equilibrium structure for the second excited state ( $\tilde{B}^2A''$ ). At the ground state equilibrium geometry the calculations yielded vertical transition energies of  $9345 \text{ cm}^{-1}$   $\tilde{A}^2A' - \tilde{X}^2A''$ ,  $22696 \text{ cm}^{-1}$   $\tilde{B}^2A'' - \tilde{X}^2A''$  and  $24917 \text{ cm}^{-1}$   $\tilde{C}^2A'' - \tilde{X}^2A''$ . The oscillator strengths were  $<10^{-4}$ , 0.059 and 0.022, respectively. These transitions involve the promotion of an electron from molecular orbitals 26, 27, or 28 (c.f., Fig. 7.3) to the SOMO. Orbital 27 has been described as being antibonding along the R-O bond, and nonbonding between the oxygen atoms. Orbitals 26 and 28 resemble the two  $e_{1g}$  degenerate HOMO's of benzene.

Scaled vibrational frequencies for the  $\tilde{B}^2A''$  state are listed in Table 7.4, while the frequencies for the  $\tilde{A}^2A'$  and  $\tilde{C}^2A''$  states are given in Table 7.5. Note that the mode labels for the excited states are given as linear combinations of the ground state normal modes with coefficients corresponding to the leading squared elements of the Duschinsky matrix ( $|J_{ik}^2|$ )<sup>26</sup>.

The vibrationally-resolved electronic spectra for the first three electronic transitions of phenyl peroxy were predicted using the Franck-Condon



approximation, as implemented in Gaussian 09. This model considers transitions arising from only the zero-point level of the ground state. The scaled vibrational frequencies were used. The calculated oscillator strengths and adiabatic transition energies ( $T_e$  and  $T_0$ ) are given in Table 7.6.

$\tilde{X}^2A''$				$\tilde{B}^2A''$			
mode	sym	$\omega$	exp.	mode assignment	sym	$\omega$	exp
v <sub>1</sub>	a'	3120	3119	0.99v <sub>1</sub> ...	a'	3157	
v <sub>2</sub>	a'	3096	3189	0.96v <sub>2</sub> ...	a'	3101	
v <sub>3</sub>	a'	3088	3089	0.97v <sub>3</sub> ...	a'	3095	
v <sub>4</sub>	a'	3078	3071	0.85v <sub>4</sub> +0.14v <sub>5</sub> ...	a'	3080	
v <sub>5</sub>	a'	3069		0.84v <sub>5</sub> +0.13v <sub>4</sub> ...	a'	3072	
v <sub>6</sub>	a'	1586		0.67v <sub>7</sub> ...	a'	1623	
v <sub>7</sub>	a'	1566		0.53v <sub>9</sub> +0.31v <sub>6</sub> ...	a'	1480	
v <sub>8</sub>	a'	1461	1481	0.66v <sub>8</sub> +0.25v <sub>6</sub> ...	a'	1448	
v <sub>9</sub>	a'	1447	1464	0.17v <sub>11</sub> +0.35v <sub>9</sub> +0.19v <sub>6</sub>	a'	1396	
v <sub>10</sub>	a'	1303	1313	0.68v <sub>10</sub> ...	a'	1333	
v <sub>11</sub>	a'	1300		0.66v <sub>11</sub> ...	a'	1274	
v <sub>12</sub>	a'	1161		0.47v <sub>15</sub> +0.22v <sub>10</sub> ...	a'	1246	1243
v <sub>13</sub>	a'	1143	1123	0.79v <sub>13</sub> ...	a'	1150	
v <sub>14</sub>	a'	1131		0.14v <sub>16</sub> +0.18v <sub>15</sub> +0.49v <sub>12</sub>	a'	1104	
v <sub>15</sub>	a'	1088		0.75v <sub>16</sub> +0.15v <sub>12</sub> ...	a'	1038	
v <sub>16</sub>	a'	1060	1123	0.28v <sub>16</sub> +0.59v <sub>17</sub> ...	a'	976	
v <sub>17</sub>	a'	986	1019	0.68v <sub>18</sub> +0.28v <sub>17</sub> ...	a'	962	
v <sub>18</sub>	a'	820		0.76v <sub>19</sub> +0.14v <sub>14</sub> ...	a'	794	
v <sub>19</sub>	a'	750	793	0.12v <sub>20</sub> +0.17v <sub>19</sub> +0.58v <sub>14</sub>	a'	721	661
v <sub>20</sub>	a'	606	615	0.80v <sub>21</sub> +17v <sub>20</sub> ...	a'	581	538
v <sub>21</sub>	a'	600	607	.17v <sub>21</sub> +0.66v <sub>20</sub> ...	a'	493	
v <sub>22</sub>	a'	432		0.93v <sub>22</sub> ...	a'	418	401
v <sub>23</sub>	a'	257		0.95v <sub>23</sub> ...	a'	280	279
v <sub>24</sub>	a''	1005		0.94v <sub>24</sub> ...	a''	963	

$\nu_{25}$	$a''$	981		$0.92\nu_{25} \dots$	$a''$	959
$\nu_{26}$	$a''$	962	905	$0.93\nu_{26} \dots$	$a''$	871
$\nu_{27}$	$a''$	906		$0.92\nu_{27} \dots$	$a''$	806
$\nu_{28}$	$a''$	780	752	$0.98\nu_{28} \dots$	$a''$	736
$\nu_{29}$	$a''$	673	679	$0.87\nu_{29} \dots$	$a''$	672
$\nu_{30}$	$a''$	479	481	$0.88\nu_{30} \dots$	$a''$	461
$\nu_{31}$	$a''$	407		$0.94\nu_{31} \dots$	$a''$	390
$\nu_{32}$	$a''$	228		$0.20\nu_{33}+0.78\nu_{32} \dots$	$a''$	173
$\nu_{33}$	$a''$	88		$0.77\nu_{33}+0.20\nu_{32} \dots$	$a''$	111

**Table 7.4.** Calculated and scaled normal mode frequencies ( $\text{cm}^{-1}$ ) for the phenyl peroxy radical in the  $\tilde{X}^2A''$  and  $\tilde{B}^2A''$  electronic states compared with experimental vibrational intervals. The ground state experimental values were reported by Mardyukov and Sander<sup>20</sup>. The calculations are for the aug-cc-pVTZ basis set.

$\tilde{A}^2A'$			
mode assignment	sym	$\omega$	exp.
$1.00\nu_1 \dots$	$a'$	3206	
$0.97\nu_3 \dots$	$a'$	3202	
$1.00\nu_2 \dots$	$a'$	3195	
$1.00\nu_4 \dots$	$a'$	3181	
$0.92\nu_5 \dots$	$a'$	3173	
$1.00\nu_6 \dots$	$a'$	1631	
$0.22\nu_8+0.69\nu_7 \dots$	$a'$	1621	
$0.76\nu_8+0.24\nu_7 \dots$	$a'$	1513	
$1.00\nu_9 \dots$	$a'$	1493	
$0.99\nu_{10} \dots$	$a'$	1356	
$0.94\nu_{11} \dots$	$a'$	1334	900
$0.97\nu_{12} \dots$	$a'$	1209	
$0.95\nu_{13} \dots$	$a'$	1182	944
$0.90\nu_{14} \dots$	$a'$	1171	
$0.94\nu_{15} \dots$	$a'$	1101	
$0.18\nu_{20}+0.79\nu_{16} \dots$	$a'$	1046	
$0.52\nu_{20}+0.17\nu_{17}+0.18\nu_{16} \dots$	$a'$	1033	
$0.13\nu_{20}+0.81\nu_{17} \dots$	$a'$	1012	

0.91v <sub>18</sub> ...	a'	797	
0.12v <sub>21</sub> +0.79v <sub>18</sub> ...	a'	627	
0.75v <sub>21</sub> ...	a'	563	
0.91v <sub>22</sub> ...	a'	432	
0.93v <sub>23</sub> ...	a'	229	213
0.95v <sub>24</sub> ...	a''	1004	
0.95v <sub>25</sub> ...	a''	982	
0.96v <sub>26</sub> ...	a''	905	
0.20v <sub>28</sub> +0.80v <sub>27</sub> ...	a''	831	
0.80v <sub>28</sub> +0.20v <sub>27</sub> ...	a''	766	
0.98v <sub>29</sub> ...	a''	698	
0.98v <sub>30</sub> ...	a''	508	
0.93v <sub>31</sub> ...	a''	418	
0.89v <sub>32</sub> ...	a''	226	
0.88v <sub>33</sub> ...	a''	97	53

---

$\tilde{C}^2A''$			
mode assignment	sym	$\omega$	exp.
0.97v <sub>1</sub> ...	a'	3147	N/A
0.90v <sub>2</sub> ...	a'	3117	
0.99v <sub>3</sub> ...	a'	3096	
0.93v <sub>4</sub> ...	a'	3084	
0.21v <sub>10</sub> +0.56v <sub>9</sub> ...	a'	3077	
0.94v <sub>5</sub> ...	a'	3013	
0.93v <sub>6</sub> ...	a'	1616	
0.96v <sub>7</sub> ...	a'	1509	
0.90v <sub>8</sub> ...	a'	1389	
0.65v <sub>10</sub> +0.27v <sub>9</sub> ...	a'	1354	
0.86v <sub>11</sub> ...	a'	1317	
0.77v <sub>12</sub> ...	a'	1291	
0.78v <sub>13</sub> ...	a'	1168	
0.65v <sub>20</sub> ...	a'	1152	
0.91v <sub>15</sub> ...	a'	1031	
0.98v <sub>14</sub> ...	a'	980	
0.16v <sub>17</sub> +0.69v <sub>16</sub> ...	a'	964	
0.52v <sub>18</sub> +0.24v <sub>17</sub> +0.21v <sub>16</sub> ...	a'	956	
0.35v <sub>18</sub> +0.57v <sub>17</sub> ...	a'	812	

0.85v <sub>20</sub> ...	a'	574
0.30v <sub>22</sub> +0.49v <sub>19</sub> ...	a'	449
0.21v <sub>24</sub> +0.42v <sub>23</sub> +0.20v <sub>19</sub> ...	a'	405
0.32v <sub>24</sub> +0.36v <sub>22</sub> ...	a'	262
0.32v <sub>24</sub> +0.50v <sub>23</sub> ...	a''	949
0.88v <sub>25</sub> ...	a''	875
0.83v <sub>26</sub> ...	a''	859
0.31v <sub>28</sub> +0.64v <sub>27</sub> ...	a''	854
0.43v <sub>28</sub> +0.21v <sub>27</sub> ...	a''	709
0.16v <sub>31</sub> +0.81v <sub>29</sub> ...	a''	633
0.86v <sub>30</sub> ...	a''	429
0.75v <sub>32</sub> +0.12v <sub>31</sub> ...	a''	332
0.20v <sub>32</sub> +0.54v <sub>31</sub> +0.12v <sub>29</sub> ...	a''	170
0.86v <sub>33</sub> ...	a''	65

**Table 7.5.** Calculated and scaled normal mode frequencies for phenyl peroxy radical (TD-DFT/aug-cc-pVTZ) in the  $\tilde{A}^2A'$  and  $\tilde{C}^2A''$  electronic states compared with experimental term values, G(v'). The  $\tilde{A}^2A'$  experimental values were reported by Just et al. (Chem. Phys. Lett. 2006, 417, 378-82).

Transition	Oscillator Strength (f)*	Vertical Excitation Energy (cm <sup>-1</sup> )*	TD-DFT		exp.** T <sub>00</sub> (cm <sup>-1</sup> )
			T <sub>e</sub> (cm <sup>-1</sup> )*	T <sub>00</sub> (cm <sup>-1</sup> )*	
$\tilde{A}^2A' - \tilde{X}^2A''$	0.0/0.0	9314/9345	8900/8938	8743/8787	7497
$\tilde{B}^2A'' - \tilde{X}^2A''$	0.0561/0.0587	22486/22696	17572/17580	17204/17222	17518
$\tilde{C}^2A'' - \tilde{X}^2A''$	0.0228/0.0220	24614/24917	20516/20686	21056/21189	

**Table 7.6.** Oscillator strength (f), vertical excitation energy, adiabatic excitation energy (T<sub>e</sub>), and electronic transition origin (T<sub>00</sub>) for the first three electronic transition of phenyl peroxy calculated using TD-DFT with the aug-cc-pVDZ and aug-cc-pVTZ basis sets.

\* Calculated values listed using basis sets aug-cc-pVDZ/aug-cc-pVTZ

\*\*Experimental values are listed for comparison (T<sub>00</sub> for  $\tilde{A}^2A' - \tilde{X}^2A''$  taken from Ref. 17).

## 7.5. Discussion

The calculated spectrum for the  $\tilde{A}^2A' - \tilde{X}^2A''$  transition is compared with the experimental data of Just et al.<sup>17</sup> in Fig. 7.5. For this exercise the origin band was shifted down by  $1290\text{ cm}^{-1}$  to match the experiment. With this correction, the vibronic intensity pattern is in moderately good agreement with the data for transitions from the zero-point level.

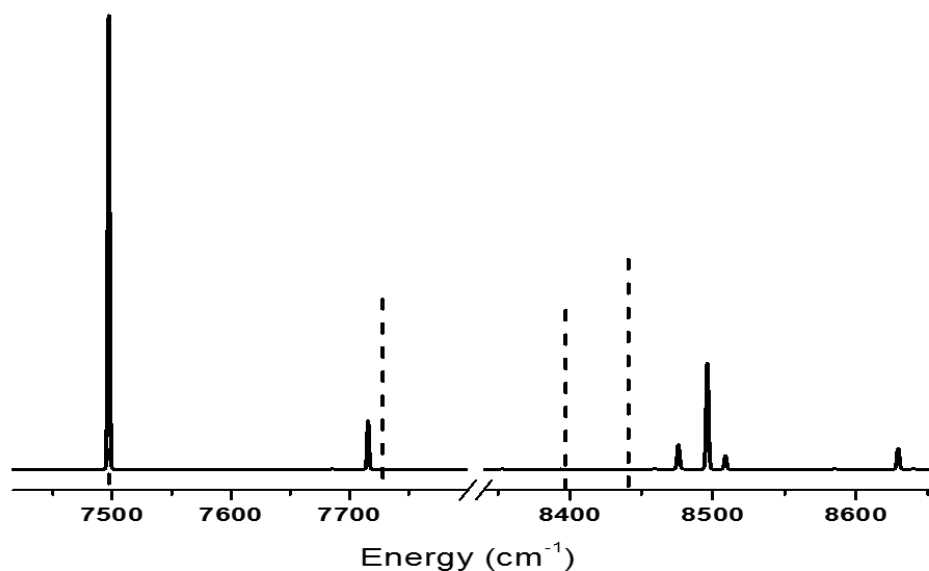


**Figure 7.5.** Calculated (TD-DFT/aug-cc-pVTZ) vibrationally-resolved electronic spectrum for the  $A^2A' - X^2A''$  transition of phenyl peroxy (solid trace) compared to the experimental (dashed) line positions and estimated relative intensities from Reference 17. The break is where experimental data was not available.

As expected<sup>14,17</sup>, significant geometry changes for the  $\tilde{A}^2A' - \tilde{X}^2A''$  transition were localized at the peroxy group. There was an increase in the O-O bond length and slight decreases in the C-O bond length and O-O-C bond angle.

These same geometric changes were also predicted for the  $\tilde{B}^2A'' - \tilde{X}^2A''$  transition, but to a larger extent (c.f., Fig. 7.4). In addition, there were significant changes in the carbon ring. The ring geometry in the excited state resembled a quinone while the ground electronic state resembled benzene. The largest change in bond angles for this transition were the eight degree decrease of the  $O_8-O_7-C_1$  bond angle, the two degree decrease of the  $C_2-C_1-C_6$  angle, and the two degree decrease of the  $C_1-C_2-H_2$  angle. In the ground state the atoms  $O_8-O_7-C_1-C_2-H_2$  were arranged with angles resembling a six-member ring. The geometry of these atoms in the  $\tilde{B}^2A''$  state resembled a five-member ring. This is explained by the interaction between  $O_8$  and  $C_2$  indicated by the SOMO, which becomes stronger when the orbital is doubly occupied in the excited state.

The calculated vibronic structure for the  $\tilde{B}^2A'' - \tilde{X}^2A''$  transition is shown as trace c in Fig. 7.1. For comparison with the experimental data, the origin of the calculated spectrum has been shifted up by  $296\text{ cm}^{-1}$ . The level of agreement between the new spectrum and the simulation strongly supports the assignment to phenyl peroxy. Excited state vibrational intervals from the spectrum are compared with calculated frequencies in Table 7.4. As Gaussian 09 uses harmonic frequencies, it is no surprise to find that the level of agreement decreases with increasing vibrational excitation. All of the optically active vibrational modes are of  $a'$  symmetry. The two most intense progressions are associated with vibrational modes 23 and 19. These can be approximately

described as the C-O-O bend and the O-O stretch. Progressions with weaker intensities were associated with modes 22, 20, and 12. The displacement vectors for these Franck-Condon favored modes are shown in Fig. 7.6. All have significant displacements relating to O-O stretching or in-plane bending within the O<sub>8</sub>-O<sub>7</sub>-C<sub>1</sub>-C<sub>2</sub>-H<sub>2</sub> group.

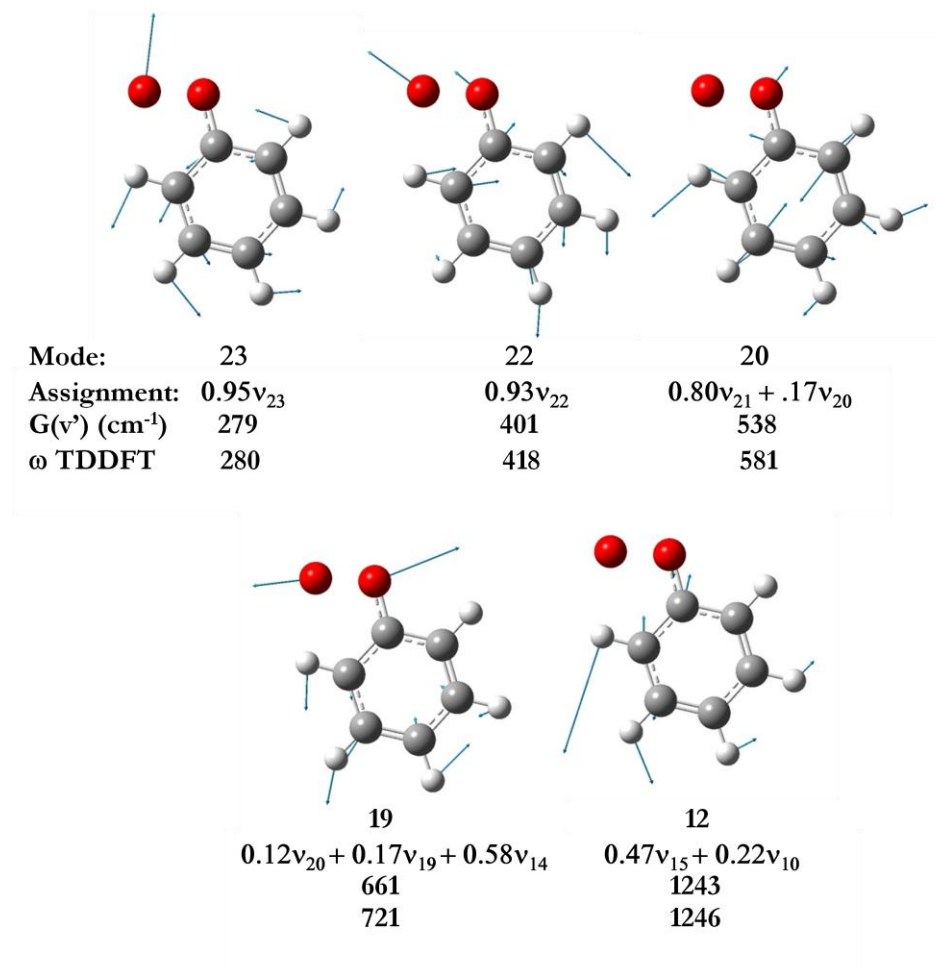


**Figure 7.6.** Excited state normal modes responsible for the observed progressions in the  $\tilde{B}^2A''$ - $\tilde{X}^2A''$  vibronic spectrum of phenyl peroxy. The experimental term values are compared with the harmonic vibrational frequencies calculated by TD-DFT/aug-cc-pVTZ.

Similar geometric changes were predicted for the  $\tilde{C}^2A'' - \tilde{X}^2A''$  transition. Again there was an increase in the O-O bond length, and decreases in the CO bond length, O-O-C angle,  $C_2-C_1-C_6$  angle (c.f., Table 7.3). Theoretical simulation of the  $\tilde{C}^2A'' - \tilde{X}^2A''$  transition produces a prominent origin band at  $21056 \text{ cm}^{-1}$ , followed by progressions of the O-O stretch and O-O-C bend. In contrast to the behavior of the  $\tilde{B}^2A'' - \tilde{X}^2A''$  transition, the vibronic intensity envelope decreases for bands above the origin (see Fig. 7.7 below).

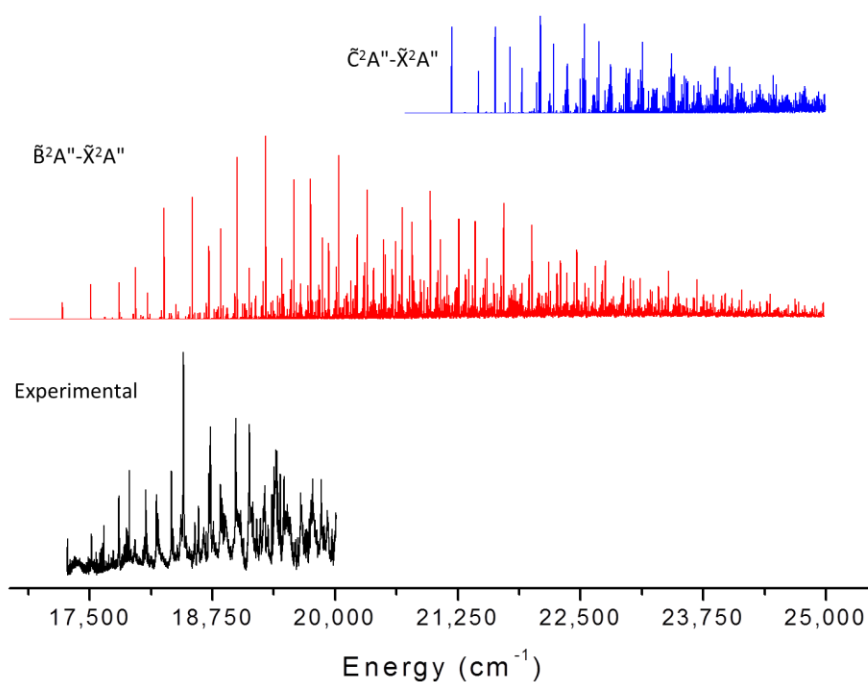


**Figure 7.7.** Calculated vibrationaly-resolved electronic spectra for the  $\tilde{B}^2A'' - \tilde{X}^2A''$  and  $\tilde{C}^2A'' - \tilde{X}^2A''$  transitions of phenyl peroxy (with aug-cc-pVTZ basis set) compared to the experimental results.



The TD-DFT calculations favored assignment of the dominant spectral features of Fig. 7.1b to the  $\tilde{B}^2A'' - \tilde{X}^2A''$  transition of phenyl peroxy. As a further test of the correspondence between the observed and calculated results, the predicted molecular constants were used to simulate the rotational contour of the origin band. The program PGOPHER<sup>27</sup> was used to simulate and fit the contour. In this process the centrifugal distortion and spin-rotation constants were set to zero. The rotational constants and transition moment projections were fixed. For comparison with the experimental contour, the band origin, rotational temperature and Lorentzian linewidth were treated as variable parameters. The results from both the double-zeta and triple-zeta basis sets were used. The smooth curves in Fig. 7.2 show the best fit contours, and the molecular constants are given in the figure caption. Note that the fit for the DZ constants is better than that for TZ, mostly due to the relative changes in the rotational constants on excitation (more influential than the slight difference in the transition moment projections). The analysis based on the DZ rotational constants yielded a band origin of 17519  $\text{cm}^{-1}$ , a rotational temperature of 34 K and a homogeneous linewidth of 2.2  $\text{cm}^{-1}$ . The last parameter shows that the resolution of the contour was limited by lifetime broadening.

Rotational contour modeling was also carried out using the molecular constants for the  $\tilde{C}^2A'' - \tilde{X}^2A''$  transition, which included transition dipole moment projections of  $\mu_a=0.513$  and  $\mu_b=0.460$  D. This ratio of projections

consistently produced contours where the relative intensities of the P- and R-branch were reversed relative to the experimental spectrum.

The assignment of Fig. 7.1b provided by the theoretical model indicated that the spectrum is dominated by transitions from the zero-point level. In contrast, the room temperature spectrum of the  $\tilde{A}^2A' - \tilde{X}^2A''$  transition reported by Just et al.<sup>17</sup> included hot bands, resulting in repeated patterns of sequence bands where successive members were separated by just  $30\text{ cm}^{-1}$ . These were attributed to population of a ground state vibrational mode ( $\nu_{33}$ ) that had a frequency of about  $85\text{ cm}^{-1}$ . For the present measurements, if the vibrational temperature for the low frequency modes was close to the rotational temperature, the lowest energy vibrationally excited state would have a fractional population of just 3%. Hence, the absence of obvious hot bands was reasonable.

If it is accepted that the broad absorption feature previously reported<sup>2,12,13</sup> in the  $18850\text{-}20200\text{ cm}^{-1}$  range does belong to phenyl peroxy, then the results from this study may be used to account for the lack of structure. This energy region of Fig. 7.1b is quite congested, despite the simplification resulting from jet cooling. The features appear to be broader at these energies, occurring in clumps that are suggestive of the mixing of bright and dark states. For the room temperature spectrum we anticipate a considerable increase in congestion resulting from hot band transitions. Typically, the rates of non-radiative decay processes increase with vibronic excitation, so the homogeneous linewidths will

be in excess of  $2\text{ cm}^{-1}$ . Add to this the broadening of the rotational contours produced by the greater range of rotational levels populated, and it is quite plausible that the combined effect will be a nearly continuous spectrum.

There are no reports of room temperature gas phase CRDS measurements for phenyl peroxy in the region  $17500 - 18100\text{ cm}^{-1}$ . In future experiments it will be of interest to see if vibrationally resolved data can be obtained for the lower energy bands. If so, this will provide a more species specific method for observing phenyl peroxy in kinetic studies. The conventional wisdom is that phenyl peroxy would be a poor candidate for detection by laser induced fluorescence, and this is confirmed for the  $\tilde{B}^2A'' - \tilde{X}^2A''$  transition. The linewidth of the origin band indicates a non-radiative decay rate of  $4 \times 10^{11}\text{ s}^{-1}$ , which would result in a fluorescence quantum yield on the order of  $3 \times 10^{-5}$ .

## BIBLIOGRAPHY

- (1) Glassman, I.; Yetter, R. A. *Combustion, Fourth Edition*; Academic Press, 2008.
- (2) Tanaka, K.; Ando, M.; Sakamoto, Y.; Tonokura, K. *Int. J. Chem. Kinet.* **2012**, *44*, 41.
- (3) Kirk, B. B.; Harman, D. G.; Kenttaemaa, H. I.; Trevitt, A. J.; Blanksby, S. J. *Physical Chemistry Chemical Physics* **2012**, *14*, 16719.
- (4) Parker, D. S. N.; Zhang, F.; Kaiser, R. I. *Journal of Physical Chemistry A* **2011**, *115*, 11515.
- (5) Sebbar, N.; Bockhorn, H.; Bozzelli, J. *Int. J. Chem. Kinet.* **2008**, *40*, 583.
- (6) da Silva, G.; Bozzelli, J. W. *J. Phys. Chem. A* **2008**, *112*, 3566.
- (7) Mebel, A. M.; Lin, M. C. *Journal of the American Chemical Society* **1994**, *116*, 9577.
- (8) Merle, J. K.; Hadad, C. M. *J. Phys. Chem. A* **2004**, *108*, 8419.
- (9) Tokmakov, I. V.; Kim, G.-S.; Kislov, V. V.; Mebel, A. M.; Lin, M. C. *J. Phys. Chem. A* **2005**, *109*, 6114.

- (10) Albert, D. R.; Davis, H. F. *Journal of Physical Chemistry Letters* **2010**, *1*, 1107.
- (11) Gu, X.; Zhang, F.; Kaiser, R. I. *Chemical Physics Letters* **2007**, *448*, 7.
- (12) Tonokura, K.; Norikane, Y.; Koshi, M.; Nakano, Y.; Nakamichi, S.; Goto, M.; Hashimoto, S.; Kawasaki, M.; Andersen, M. P. S.; Hurley, M. D.; Wallington, T. J. *J. Phys. Chem. A* **2002**, *106*, 5908.
- (13) Yu, T.; Lin, M. C. *Journal of the American Chemical Society* **1994**, *116*, 9571.
- (14) Weisman, J. L.; Head-Gordon, M. *Journal of the American Chemical Society* **2001**, *123*, 11686.
- (15) Alfassi, Z. B.; Khaikin, G. I.; Neta, P. *J. Phys. Chem.* **1995**, *99*, 265.
- (16) Krauss, M.; Osman, R. *J. Phys. Chem.* **1995**, *99*, 11387.
- (17) Just, G. M. P.; Sharp, E. N.; Zalyubovsky, S. J.; Miller, T. A. *Chem. Phys. Lett.* **2006**, *417*, 378.
- (18) Sharp, E. N.; Rupper, P.; Miller, T. A. *Phys. Chem. Chem. Phys. FIELD Full Journal Title:Physical Chemistry Chemical Physics* **2008**, *10*, 3955.
- (19) Yamauchi, S.; Hirota, N.; Takahara, S.; Misawa, H.; Sawabe, K.; Sakuragi, H.; Tokumaru, K. *Journal of the American Chemical Society* **1989**, *111*, 4402.
- (20) Mardyukov, A.; Sander, W. *Chemistry--A European Journal* **2009**, *15*, 1462.
- (21) Dunning, T. H., Jr. *J. Chem. Phys.* **1989**, *90*, 1007.
- (22) Chen, M.-W.; Just, G. M. P.; Codd, T.; Miller, T. A. *J. Chem. Phys.* **2011**, *135*, 184304/1.
- (23) Just, G. M. P.; Rupper, P.; Miller, T. A.; Meerts, W. L. *Physical Chemistry Chemical Physics* **2010**, *12*, 4773.
- (24) Just, G. M. P.; Rupper, P.; Miller, T. A.; Meerts, W. L. *J. Chem. Phys.* **2009**, *131*, 184303/1.
- (25) Frish, M. J.; Gaussian Inc.: Wallingford, CT.
- (26) Bloino, J.; Biczysko, M.; Crescenzi, O.; Barone, V. *J. Chem. Phys.* **2008**, *128*, 244105.
- (27) Western, C. M.; University of Bristol: Bristol, 2007.

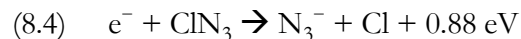
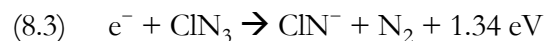
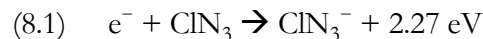
*Section 2*CHLORINE AZIDE – ELECTRON ATTACHMENT AND REACTIONS  
WITH IONS AT THE AIR FORCE RESEARCH LABORATORY**Chapter 8. Electron Attachment to Chlorine Azide****8.1. Introduction**

Since its first synthesis in 1908,<sup>1</sup> there have been relatively few studies addressing the structure and chemistry of  $\text{ClN}_3$  and none regarding electron attachment. Frierson et al.<sup>2</sup> attributes the reluctance to study the azide to “the extremely explosive character of the compound, which in undiluted condition usually detonates violently whatever the temperature, without apparent provocation.” It is precisely the energy content that makes azides interesting and potentially useful. Furthermore, molecules such as  $\text{ClN}_3$  may be stepping stones toward the synthesis of higher-order azides.<sup>3,4</sup>

Despite the risk associated with studying the compound, there have been several studies concerning the explosive decomposition and other chemical reactions involving  $\text{ClN}_3$ .<sup>2,5</sup> Spectroscopic studies have refuted the originally<sup>6</sup> supposed cyclic  $\text{N}_3$  ligand and confirmed a slightly bent  $\text{N}_3$  structure.<sup>7</sup> More recent work has been focused on the photodissociation dynamics<sup>8-11</sup> of  $\text{ClN}_3$  and in particular, the question of the existence of a cyclic  $\text{N}_3$  photolysis product.<sup>3</sup>

$\text{ClN}_3$  has been of interest in lasing media for a high power all gas iodine laser.<sup>12-14</sup> An all gas laser would be more versatile and robust than the chemical oxygen iodine laser (COIL).<sup>15</sup> The COIL operates by  $\text{O}_2(a^1\Delta_g)$  pumping ground state  $\text{I}(^2\text{P}_{3/2})$  to the  $\text{I}(^2\text{P}_{1/2})$  level so that a population inversion exists and a 1315 nm stimulated radiation results.  $\text{ClN}(a^1\Delta)$ , which can be generated efficiently from gas phase reactions, can replace isovalent  $\text{O}_2(a^1\Delta_g)$  in the lasing scheme. This replacement would eliminate the need for the inconvenient liquid precursors which are used for  $\text{O}_2(a^1\Delta_g)$  production. The photolysis of  $\text{ClN}_3$  is an established source of  $\text{ClN}(a^1\Delta)$ , and this method of generation was used in the first demonstration of a  $\text{ClN}(a^1\Delta)/\text{I}$  transfer laser.<sup>12</sup> The performance of the  $\text{ClN}(a^1\Delta)$  pumped iodine laser can be optimized by developing our understanding of the chemical mechanisms and kinetics involved in the lasing media. As the chemistry of the photolysis-driven laser system is simpler than that of the chemically driven version, it is the preferred prototype for detailed investigations. Understanding the chemistry of the  $\text{ClN}$  precursor  $\text{ClN}_3$ , including its reaction with free electrons, is an essential first step in the process of analyzing and optimizing the performance of the photolysis laser.

Exothermic channels for electron attachment to  $\text{ClN}_3$  are:



An attachment reaction yielding  $\text{ClN}_2^-$  (which consists of  $\text{N}_2$  electrostatically coupled to  $\text{Cl}^-$  with a bond energy of 0.06 eV) is technically exothermic, but is not shown above because this channel will surely show up in the experiment in the form given by Eq. 8.2b. Reaction 8.2 is interesting because the exothermicity is sufficiently large that the neutral product could include the high-energy form of  $\text{N}_3$  (possibly cyclic  $\text{N}_3$ ) which has been calculated to lie 1.31 eV above the linear, ground state of  $\text{N}_3$ .<sup>4,16</sup> The energies given in Eqs. 8.1 - 8.4 are those calculated using the G4 compound method<sup>17</sup> at 0 K, carried out using the Gaussian-09W program,<sup>18</sup> with the exception of the 1.31 eV energy difference between linear and cyclic  $\text{N}_3$ .<sup>4,16</sup> The G4 prescription, which includes empirical corrections based on accurate experimental energies, approximates a coupled cluster calculation with a large basis set. Neutral and anion geometries were optimized at the B3LYP/6-31G(2df) level of theory<sup>19-23</sup>

and zero-point energies calculated from scaled harmonic frequencies.<sup>17</sup> Reaction enthalpies calculated at 298 K are greater than the 0 K values by less than 35 meV, including the enthalpy of the electron. Neutral products were not detected in the present work.

## 8.2. Experimental

The electron attachment rate constant of  $\text{ClN}_3$  was measured with a flowing afterglow Langmuir probe (FALP) at the Air Force Research Laboratory (AFRL). The reaction products were observed by mass spectrometry immediately following the reaction flow tube. The FALP at AFRL is well established and has been described in previous literature.<sup>24,25</sup> The experiment is described here with significant experimental parameters.

The experimental setup is shown in Figure 8.1.  $\text{ClN}_3$  in He was added halfway along the length of the flow tube through four glass inlet needles evenly spaced within the tube. Upstream of the  $\text{ClN}_3$  inlet, a fast flow of He gas was passed through a 10 - 20 W microwave discharge cavity in 2.5 cm glass tubing. The resulting afterglow was carried into a 7.3 cm (ID) glass flow tube. A small amount of Ar ( $\sim 2\%$ ) was added downstream from the cavity to obtain a thermalized electron- $\text{He}^+$ ,  $\text{Ar}^+$  plasma as a source with 95% of the cations being  $\text{Ar}^+$ . The discharge produced electron densities in the range of  $10^8$ - $10^9$   $\text{cm}^{-3}$  which is small enough to minimize electron-ion recombination. A moveable



Langmuir probe<sup>26</sup> was used to monitor the electron density from 10 cm upstream of the  $\text{ClN}_3$  inlet to 40 cm downstream. The current through the Langmuir probe's 25  $\mu\text{m}$  diameter, 51mm long tungsten wire was measured as a function of applied voltage.

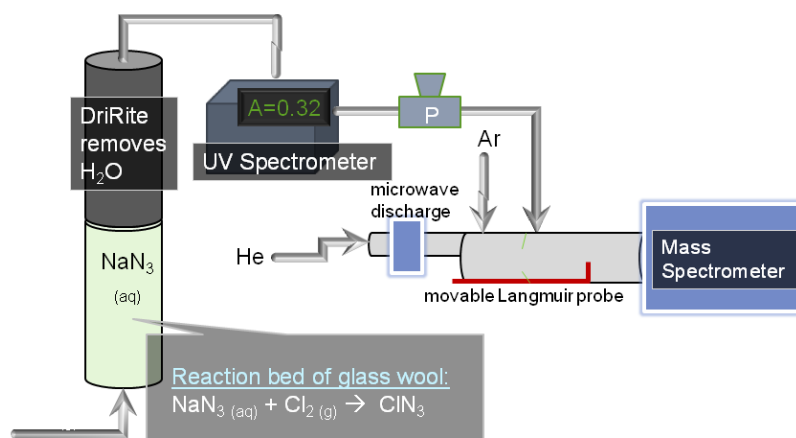


**Figure 8.1.** Experimental setup. Chlorine azide was produced in the packed bed reactor (left). The absorption from  $\text{ClN}_3$  was measured with the UV spectrometer. The  $\text{ClN}_3$  was then sent to the FALP apparatus. Product ions were detected with a mass spectrometer.

Prior to the electron-attachment measurements, the flow velocity was measured by pulsing the discharge and measuring the time it took for the perturbation to travel a known distance down the flow tube. Flow velocities near  $10^4$  cm/s were typical with a flow tube pressure of 1 Torr.

The  $\text{ClN}_3$  inlet was added at 60 sccm which provided sufficient reactant concentration ( $>10^{10}$  molecules/ $\text{cm}^3$ ) to ensure pseudo-first order kinetics. Electron densities along the flow tube axis were first obtained in absence of  $\text{ClN}_3$

to obtain the ambipolar diffusion rate  $v_D$  and then with  $\text{ClN}_3$  added. The concentration of  $\text{ClN}_3$  was adjusted so that the electron density decay was mostly due to electron attachment. The electron density data as a function of time  $n_e(t)$  were fit to solutions of the rate equations describing attachment and diffusion downstream of the reactant inlet ( $t = 0$ )<sup>24,27</sup>

$$n_e(t) = v_a(0) [v_a \exp(-v_a t) - v_D \exp(-v_D t)] / (v_a - v_D) \quad (8.5)$$

to obtain the apparent rate constant  $k_a' = v_a / [\text{ClN}_3]$ . This required an accurate measurement of  $[\text{ClN}_3]$  which is described below.

The  $\text{ClN}_3$  production apparatus has been used previously by Henshaw<sup>28</sup> et al. and the Heaven group.  $\text{ClN}_3$  was synthesized by passing 1%  $\text{Cl}_2$  (Sigma-Aldrich Inc. St Louis MO, USA) in He (Middlesex Gasses & Technologies, Inc. Everett MA) through a 50 cm<sup>3</sup> tubular glass reaction chamber packed full with  $\text{NaN}_3$  laced glass wool. The reactor was prepared by sprinkling 5 g of  $\text{NaN}_3$  (99.99+% Sigma-Aldrich Inc. St Louis MO, USA) uniformly on both sides of a 0.5 cm x 5 cm x 20 cm bed of glass wool, spraying with 2 mL of distilled  $\text{H}_2\text{O}$  (Market Basket Inc.), rolling tight and stuffing the glass wool cylinder into the reaction chamber which was cooled to 0 C. The  $\text{ClN}_3$  product was then passed through 50 mL of Drierite (W.A. Hammond Drierite Co. Ltd.) to remove evaporated  $\text{H}_2\text{O}$ .

Absorption measurements through a 7.0 cm Pyrex cell containing the flowing product were made using a Perkin–Elmer Lambda 10 UV–Vis spectrometer. A UV spectrum from 190–300 nm confirmed the presence of  $\text{ClN}_3$  by comparing the absorption data with previously reported spectra<sup>28</sup>. The absorbance spectrum is shown in Figure 8.2 (solid line) along with the  $\text{ClN}_3$  spectrum reported by Henshaw et al. (dashed line).

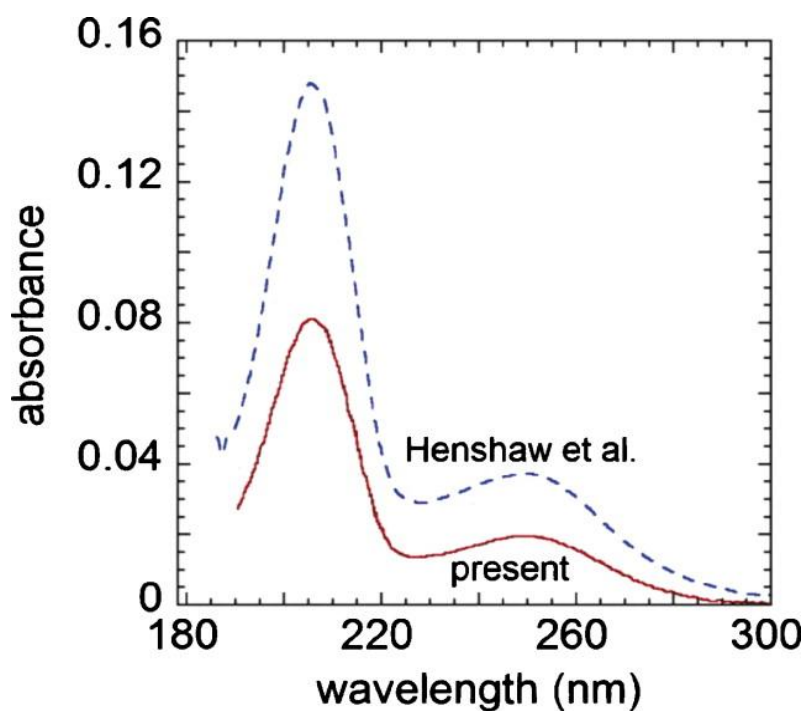


**Figure 8.2.** An example of a UV absorption spectrum of  $\text{ClN}_3$  (solid line) juxtaposed with the cross section data from Henshaw et al. (Ref. 28) plotted as absorbance using the same path length (7 cm) and pressure (26.5 Torr) as in the present experiment. The difference in the peak heights at 205 nm implies that the sample used was 54.8%  $\text{ClN}_3$  (the remainder being unreacted  $\text{Cl}_2$ ).

Throughout the experiments the concentration of  $\text{ClN}_3$  was monitored by measuring the absorption at  $\lambda_{\text{max}} = 204.5 \text{ nm}$  and using the Beer-Lambert law with  $(\sigma_{\text{max}} = 5.8 \times 10^{-18} \text{ cm}^2)^{28}$  to calculate the absolute concentration. Reaction yields varied from 50% to 100%.

Since the attachment rate constant for  $\text{Cl}_2$  is much smaller than for  $\text{ClN}_3$ ,  $k_a'$  for the  $\text{ClN}_3/\text{Cl}_2$  mixture consisting of a fraction  $f$  of  $\text{ClN}_3$  is given by

$$k_a' = f k_a + (1 - f) k_{\text{Cl}_2} \quad (8.6)$$

where  $k_{\text{Cl}_2}$  is the known attachment rate constant for  $\text{Cl}_2$  ( $1.65 \times 10^{-9} \text{ cm}^3 \text{ s}^{-1}$  at 298 K and  $2.20 \times 10^{-9} \text{ cm}^3 \text{ s}^{-1}$  at 400 K)<sup>29</sup> and  $k_a$  is the electron attachment rate constant for  $\text{ClN}_3$ . For the measurements reported here:  $f=0.548$ ,  $k_a = 1.83k_a' - 1.36 \times 10^{-9} \text{ cm}^3 \text{ s}^{-1}$  (at 298 K) or  $k_a = 1.83k_a' - 1.82 \times 10^{-9} \text{ cm}^3 \text{ s}^{-1}$  (at 400 K). FALP experiments were not carried out at temperatures higher than 400 K because of possible thermal decomposition.

### 8.3. Results and Discussion

Attachment data obtained at 298 K are shown in Figure 8.3. The diffusion rate ( $352 \text{ s}^{-1}$ ) was obtained in absence of reactant. The attachment data were fit assuming that the reactant ( $7.52 \times 10^{10} \text{ cm}^{-3}$ ) was entirely  $\text{ClN}_3$ , giving an

apparent attachment rate constant of  $k_a' = 2.0 \times 10^{-8} \text{ cm}^3 \text{ s}^{-1}$ . Correction for incomplete conversion of  $\text{Cl}_2$  to  $\text{ClN}_3$  in the synthesis yields  $k_a = 3.5 \times 10^{-8} \text{ cm}^3 \text{ s}^{-1}$ .

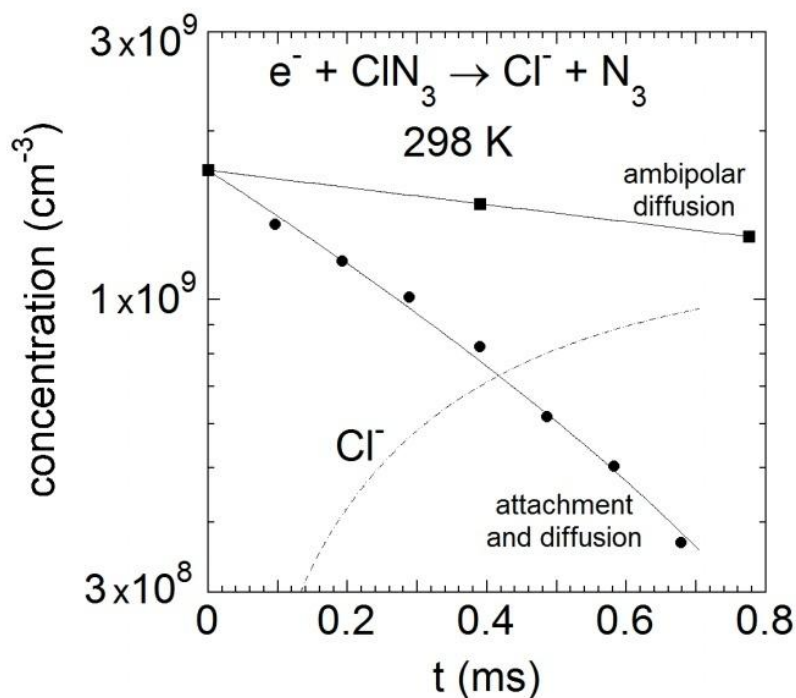


**Figure 8.3.** Electron density data obtained for electron attachment to  $\text{ClN}_3$  in  $3.25 \times 10^{16} \text{ cm}^{-3}$  He (2% Ar) carrier gas.

Rate constants for electron attachment to  $\text{ClN}_3$  were measured at 298 and 400 K. At 298 K, the apparent rate constants  $k_a'$  were measured to be 2.03 and  $2.00 \times 10^{-8} \text{ cm}^3 \text{ s}^{-1}$ . Taking the average value and correcting for the fractions of  $\text{ClN}_3$  and  $\text{Cl}_2$  in the reactant gives  $k_a(\text{ClN}_3) = 3.5 \times 10^{-8} \text{ cm}^3 \text{ s}^{-1}$ , estimated accurate to  $\pm 35\%$ . At 400 K, the raw measurements were 2.60 and  $2.53 \times 10^{-8}$

$\text{cm}^3 \text{s}^{-1}$ . Taking the average value and correcting for the fractions of  $\text{ClN}_3$  and  $\text{Cl}_2$  in the reactant gives  $k_a(\text{ClN}_3) = 4.5 \times 10^{-8} \text{ cm}^3 \text{ s}^{-1}$ , estimated accurate to  $\pm 35\%$ . An Arrhenius plot of these data showed an activation energy of  $24 \pm 10 \text{ meV}$  where the uncertainty was based on 10% relative error between the 298 and 400 K points. The collisional rate constant was  $2.93 \times 10^{-7} \text{ cm}^3 \text{ s}^{-1}$  according to the formula of Dashevskaya et al.,<sup>30</sup> implying that the attachment occurs upon every eight collisions on average at 298 K. The measured activation energy was not sufficiently accurate for an Arrhenius extrapolation to infinite temperature to obtain an experimental estimate of the collisional rate constant for  $\text{ClN}_3$ . Arrhenius behavior in dissociative electron attachment has been studied theoretically by Fabrikant and Hotop.<sup>31</sup> Arrhenius behavior extrapolating to collisional rate constants has been noted for halogenated methanes<sup>32</sup> and halogenated hydrocarbons.<sup>33</sup> However, many exceptions to such regular behavior have been noted.<sup>34,35</sup>

The most exothermic dissociative attachment channel, yielding  $\text{Cl}^-$  ion product, was the dominant reaction channel observed in the present experiments at 298 and 400 K. Minor anion species in the mass spectra will be discussed below. Observation of the parent anion as a direct product of attachment was deemed unlikely at the outset because small molecules tend not to possess soft vibrational modes needed to trap the incoming electron via intramolecular vibrational redistribution. It is energetically possible for the  $\text{Cl}^-$  channel to be

accompanied by cyclic  $N_3$  but we have no diagnostic on the neutral products of attachment. If the neutral product was cyclic  $N_3$  [Eq. (8.2c)] that channel becomes the least exothermic one (0.51 eV exothermic). If the  $N_3$  product was in fact  $N+N_2$  [Eq. (8.2b)] the exothermicity would be reduced only slightly to 1.55 eV.

Aside from  $Cl^-$ , weak anion signals of  $N_3^-$ ,  $ClN^-$ ,  $Cl_2^-$ , and  $(ClN_3)Cl^-$  were found as shown in Figure 8.4. Impurities (e.g.,  $HN_3$ ) and secondary ion-molecule reactions [being obvious in the cases of  $(ClN_3)Cl^-$  and  $Cl_2^-$ ] may be the source of these peaks since the largest of these weak signals ( $ClN^-$ ) was only 0.6% of the  $Cl^-$  intensity. Therefore, the intensities can be viewed as upper limits to the minor channels, i.e.,  $ClN^-$  and  $N_3^-$  are less than 0.6% and 0.25% of the products of electron attachment at 298 K. According to the formulas given earlier to account for the presence of  $Cl_2$  in the reactant, 4% of the  $Cl^-$  ion signal is due to electron attachment to  $Cl_2$ . Normally, the reactant concentration could be varied to pin down the source of the minor ion signals but doing so was too difficult with the  $ClN_3$  reactant.

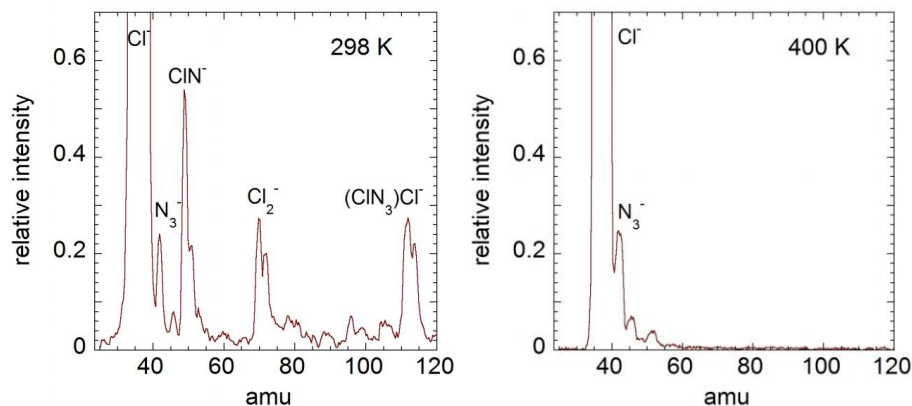


**Figure 8.4.** Electron attachment anion spectra at 298 K and 400 K. The  $\text{Cl}^-$  peak ( $>99\%$  of the total ion signal) is off scale to allow the minor peaks to be seen. The small mass peak to the right of  $\text{N}_3^-$  is  $\text{NO}_2^-$ , a common impurity in afterglows. Another small peak clearly observed at 400 K was assigned to  $\text{ClO}^-$ .

At 400 K, the anion mass spectrum was much simpler. Looking only at the 298 K spectrum, it was tempting to believe that  $\text{ClN}^-$  may have been a product of attachment to  $\text{ClN}_3$  since this is the second most exothermic channel. However, its almost complete absence at 400 K makes it likely that it is due to an impurity related to the several variables in the  $\text{ClN}_3$  synthesis. The channel yielding the  $\text{N}_3^- + \text{Cl}$  product [Eq. (8.4)] differs only in the location of the charge from the main  $\text{Cl}^- + \text{N}_3$  channel [Eq. (8.2)]. The large  $\text{Cl}^-$  to  $\text{N}_3^-$  ratio is a result of the large difference in electron affinities of Cl and  $\text{N}_3$ . The large ratio may give an indication that  $\text{N}_3$  is formed [Eq. (8.2)] in the linear configuration since the exothermicity would otherwise favor the  $\text{N}_3^-$  and  $\text{ClN}^-$  channels [Eqs. (8.3,8.4)].



Positive-ion mass spectra were monitored to determine if the Drierite was sufficiently removing H<sub>2</sub>O from the reactant flow. The dominant cation in the upstream afterglow was Ar<sup>+</sup> with some He<sup>+</sup>. Other positive ions in the mass spectra were produced from reaction of Ar<sup>+</sup> with Cl<sub>2</sub>, ClN<sub>3</sub>, and H<sub>2</sub>O flowing from the ClN<sub>3</sub> synthesis vessel. One example will suffice (Figure. 8.5). In this case, the H<sub>2</sub>O<sup>+</sup> and ClN<sup>+</sup> signals were each 30%–40% of the Ar<sup>+</sup> intensity. Note that the mass spectrum was obtained after a 4.5 ms reaction time while the electron attachment data (Figure. 8.3) were obtained over the first 0.7 ms. Thus, the ion products from reaction with Ar<sup>+</sup> are ~ 15 times weaker in the electron attachment reaction zone so that electron-ion recombination accounts for little (≤ 1%) of the electron density decay.

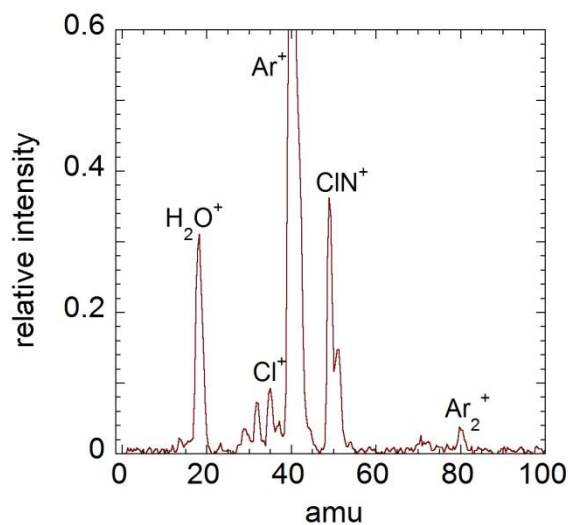


**Figure 8.5.** Positive ion spectrum obtained at 400 K from reaction of Ar<sup>+</sup> (~5% He<sup>+</sup>) with the Cl<sub>2</sub>, ClN<sub>3</sub>, and H<sub>2</sub>O flowing from the ClN<sub>3</sub> synthesis vessel, after 4.5 ms reaction time.

#### 8.4. Conclusions

A FALP apparatus was used to study electron attachment to chlorine azide,  $\text{ClN}_3$ , at 298 and 400 K in a He buffer gas at a concentration of  $3.2 \times 10^{16} \text{ cm}^{-3}$ . Only  $\text{Cl}^-$  ion product is attributed to the attachment reaction at these temperatures. Electron attachment rates were measured to be  $3.5 \times 10^{-8}$  and  $4.5 \times 10^{-8} \text{ cm}^3 \text{ s}^{-1}$  at 298 K and 400 K, respectively, with an estimated 35% accuracy. An Arrhenius plot of these data, with an estimated 10% relative uncertainty, yields an activation energy for the attachment reaction of  $24 \pm 10 \text{ meV}$ .

- (1) Raschig, F. *Ber Dtsch Chem Ges* **1908**, *41*, 4194.
- (2) Frierson, W. J.; Kronrad, J.; Browne, A. W. *Journal of the American Chemical Society* **1943**, *65*, 1696.
- (3) Samartzis, P. C.; Wodtke, A. M. *Phys. Chem. Chem. Phys.* **2007**, *9*, 3054.
- (4) Bittererova, M.; Ostmark, H.; Brinck, T. J. *Chem. Phys.* **2002**, *116*, 9740.
- (5) Dehnicke, K. *Angewandte Chemie, International Edition in English* **1967**, *6*, 240.
- (6) Curtius, T. *Ber Dtsch Chem Ges* **1890**, *23*, 3023.
- (7) Douglas, A. E.; Jones, W. J. *Can. J. Phys.* **1965**, *43*, 2216.
- (8) Hansen, N.; Wodtke, A. M. *J. Phys. Chem. A* **2003**, *107*, 10608.
- (9) Hansen, N.; Wodtke, A. M.; Goncher, S. J.; Robinson, J. C.; Sveum, N. E.; Neumark, D. M. *J Chem Phys* **2005**, *123*, 104305.
- (10) Goncher, S. J.; Sveum, N. E.; Moore, D. T.; Bartlett, N. D.; Neumark, D. M. *The Journal of Chemical Physics* **2006**, *125*, 224304.
- (11) Quinto-Hernandez, A.; Lee, Y.-Y.; Huang, T.-P.; Pan, W.-C.; Lin, J. J.-M.; Bobadova-Parvanova, P.; Morokuma, K.; Samartzis, P. C.; Wodtke, A. M. *Int. J. Mass Spectrom.* **2007**, *265*, 261.
- (12) Ray, A. J.; Coombe, R. D. *J. Phys. Chem.* **1995**, *99*, 7849.
- (13) Henshaw, T. L.; Manke, G. C., II; Madden, T. J.; Berman, M. R.; Hager, G. D. *Chem. Phys. Lett.* **2000**, *325*, 537.
- (14) Masuda, T.; Nakamura, T.; Endo, M. *Chem. Phys. Lett.* **2010**, *485*, 296.
- (15) McDermott, W. E.; Pchelkin, N. R.; Benard, D. J.; Bousek, R. R. *Appl. Phys. Lett.* **1978**, *32*, 469.
- (16) Zhang, P.; Morokuma, K.; Wodtke, A. M. *J Chem Phys* **2005**, *122*.
- (17) Curtiss, L. A.; Redfern, P. C.; Raghavachari, K. *J Chem Phys* **2007**, *126*.
- (18) Frisch, M. J. **2009**.
- (19) Becke, A. D. *J. Chem. Phys.* **1993**, *98*, 5648.
- (20) Becke, A. D. *J Chem Phys* **1992**, *97*, 9173.
- (21) Becke, A. D. *J Chem Phys* **1992**, *96*, 2155.
- (22) Lee, C. T.; Yang, W. T.; Parr, R. G. *Phys Rev B* **1988**, *37*, 785.
- (23) Dunning, T. H. *J Chem Phys* **1989**, *90*, 1007.
- (24) Smith, D.; Spanel, P. *Advances in Atomic, Molecular, and Optical Physics* **1994**, *32*, 307.
- (25) Miller, T. M.; Miller, A. E. S.; Paulson, J. F.; Liu, X. F. *J Chem Phys* **1994**, *100*, 8841.
- (26) Langmuir, I.; Mott-Smith, H. M. *General Electric Review* **1924**, *27*, 449.
- (27) Miller, T. M. *Advances in Atomic, Molecular, and Optical Physics* **2005**, *51*, 299.
- (28) Henshaw, T. L.; Herrera, S. D.; Haggquist, G. W.; Schlie, L. A. *J. Phys. Chem. A* **1997**, *101*, 4048.
- (29) Friedman, J. F.; Miller, T. M.; Schaffer, L. C.; Viggiano, A. A.; Fabrikant, I. I. *Physical Review A* **2009**, *79*.

- (30) Dashevskaya, E. I.; Litvin, I.; Nikitin, E. E.; Troe, J. *Physical chemistry chemical physics : PCCP* **2008**, *10*, 1270.
- (31) Fabrikant, I. I.; Hotop, H. *J Chem Phys* **2008**, *128*.
- (32) Miller, T. M.; Friedman, J. F.; Schaffer, L. C.; Viggiano, A. A. *J Chem Phys* **2009**, *131*.
- (33) Kopyra, J.; Wnorowska, J.; Forys, M.; Szamrej, I. *Int. J. Mass Spectrom.* **2010**, *291*, 13.
- (34) Miller, T. M.; Viggiano, A. A.; Dolbier, W. R., Jr.; Sergeeva, T. A.; Friedman, J. F. *J. Phys. Chem. A* **2007**, *111*, 1024.
- (35) Van Doren, J. M.; Miller, T. M.; Viggiano, A. A.; Spanel, P.; Smith, D.; Bopp, J. C.; Troe, J. *J Chem Phys* **2008**, *128*.

## Chapter 9. Reactions of Positive and Negative Ions with $\text{ClN}_3$ at 300K

### 9.1. Introduction

This chapter reports the second part of the reactivity studies of chlorine azide conducted at the Air Force Research Laboratory. The applications of  $\text{ClN}_3$ , as mentioned in section 8.1, were the motivation for the  $\text{ClN}_3$  reactivity studies. Despite its various applications, no studies of the reactivity of  $\text{ClN}_3$  with ions have been reported. However, the ionization potential of  $\text{ClN}_3$  has been determined by photoionization. Quinto-Hernandez et al. reported the adiabatic ionization energy of  $961 \pm 2$  kJ/mol ( $9.97 \pm 0.02$  eV) for  $\text{ClN}_3$ .<sup>1</sup> A detailed study of the  $\text{ClN}_3 + e^-$  reaction was presented in Chapter 8.

This chapter reports the reactivity of  $\text{ClN}_3$  with 17 negative ions and 18 positive ions at 300K. A wide variety of ion reactants was chosen so that reaction trends and thermochemistry could be determined. A major goal of the study was to determine upper and lower limits for the electron affinity, proton affinity, and ionization energy. Since unreacted  $\text{Cl}_2$  was present in the system, it was also necessary to study the reactivity of the ions with  $\text{Cl}_2$ . G3 and G3B3 calculations were completed to complement the experimental results.

## 9.2. Experimental

Ion chemistry with  $\text{ClN}_3$  was studied using the well established selected ion flow tube (SIFT)<sup>2</sup> at the Air Force Research Laboratory (AFRL). This experiment as shown in Figure 9.1 is analogous to the FALP experiment (Figure 8.1) however the reactant with  $\text{ClN}_3$  was a selected ion as opposed to an electron. A specific ion was produced by flowing a precursor ( $\sim 10\%$  in a noble gas) into the source inlet across an ion source composed of a tungsten filament. Mass selection of the specific ion was possible with a quadrupole placed upstream from the reaction drift tube. After ion selection the ions were injected into the flow tube via a venturi inlet using a He buffer gas.

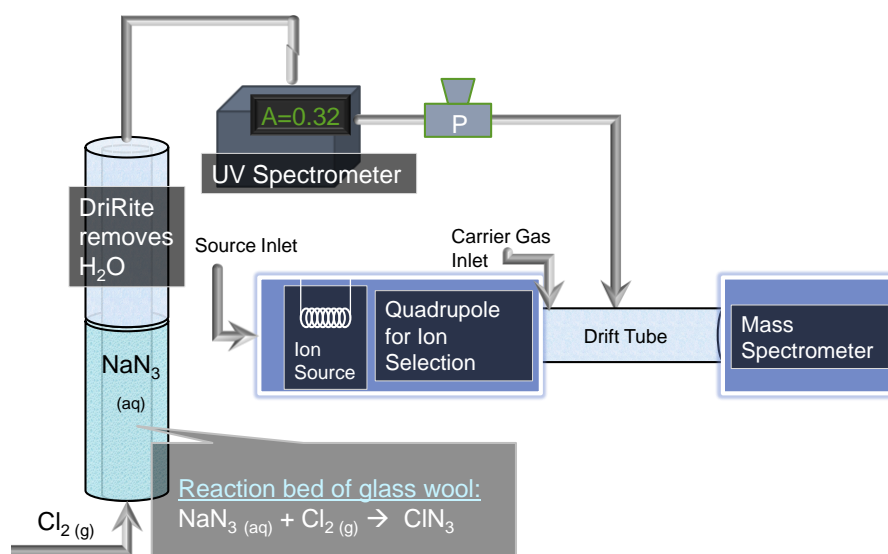


**Figure 9.1.** Schematic diagram of the selected ion flow tube (SIFT) with the inline synthesis of  $\text{ClN}_3$ .

The  $\text{ClN}_3$  in He was injected halfway along the middle of the flow tube, 59.0 cm upstream from the sampling orifice. The depletion of the reactant ion and products of the reaction were monitored by quadrupole mass spectrometry at various rates of natural reactant flow.

The  $\text{ClN}_3$  was produced in-line with the flow tube and the concentration was monitored by UV absorption, as described in Section 8.2, to ensure that the neutral concentration was much larger than the ion concentration. In this way pseudo-first-order kinetics was assumed and the rate constants were determined from the slope of the log of reactant ion concentration vs. neutral product concentration. The neutral product concentration was varied by adjusting the neutral reagent flow rate. A second quadrupole mass spectrometer was used to identify ion products. Branching ratios were determined by plotting product fractions as a function of  $[\text{ClN}_3]$  and extrapolating to zero thereby eliminating effects from secondary chemistry. Typical errors in rate constant measurements were 20% for the SIFT however the additional error from the absolute concentration measurement of  $\text{ClN}_3$  by absorption increases the total error to nearly 50%.

Reactions yields for  $\text{ClN}_3$  production ranged from 40-100% with typical yields  $> 80\%$ . Unreacted  $\text{Cl}_2$  and  $\text{H}_2\text{O}$  reactants were inevitably introduced into the flow tube. To account for this complication the reaction rate constants and

branching ratios were also measured for the reaction of  $\text{Cl}_2$  and  $\text{H}_2\text{O}$  with various ions.

The following precursors were used to create the reactant ions listed below. For negative ions:  $\text{O}_2$  for  $\text{O}_2^-$  and  $\text{O}^-$ ;  $\text{CO}_2$  for  $\text{CO}_3^-$ ;  $\text{N}_2\text{O}_4$  for  $\text{NO}_2^-$  and  $\text{NO}_3^-$ ;  $\text{Cl}_2$  for  $\text{Cl}_2^-$  and  $\text{Cl}^-$ ;  $\text{SF}_6$  for  $\text{SF}_6^-$ ,  $\text{SF}_5^-$ , and  $\text{F}^-$ ;  $\text{H}_2\text{O}$  for  $\text{OH}^-$ ;  $\text{CH}_3\text{CN}$  for  $\text{CN}^-$ ;  $\text{CBrF}_3$  for  $\text{Br}^-$ ;  $\text{C}_2\text{H}_5\text{I}$  for  $\text{I}^-$ ; and  $\text{CH}_3\text{OH}$  for  $\text{CH}_3\text{O}^-$ .  $\text{NH}_2^-$  was produced by allowing  $\text{O}^-$  to react with  $\text{NH}_3$ . For positive ions:  $\text{O}_2$  for  $\text{O}_2^+$  and  $\text{O}^+$ ;  $\text{H}_2\text{O}$  for  $\text{H}_3\text{O}^+$ ;  $\text{NO}_2$  for  $\text{NO}_2^+$ ;  $\text{CH}_3\text{OH}$  for  $\text{CH}_3\text{OH}_2^+$  and  $\text{CH}_3^+$ ;  $\text{CO}$  for  $\text{C}^+$  and  $\text{CO}^+$ ;  $\text{Ar}$  for  $\text{Ar}^+$ ;  $\text{N}_2$  for  $\text{N}_2^+$  and  $\text{N}^+$ ;  $\text{SF}_6$  for  $\text{SF}_5^+$  and  $\text{SF}_3^+$ ;  $\text{SO}_2$  (with or without  $\text{H}_2\text{O}$ ) for  $\text{HSO}_2^+$  and  $\text{SO}^+$ ; and  $\text{CS}_2$  for  $\text{CS}_2^+$ .

Electronic structure calculations were carried out using the Gaussian 03 program package<sup>3</sup>. Optimized geometries and energies for molecules and transition states were calculated at the B3LYP/6-311+G(d) level for reaction coordinate diagrams. Calculations to determine the ionization energy, proton affinity, and electron affinity were carried out using G3 theory<sup>4</sup>.

### 9.3. Results: $\text{ClN}_3$ + Negative Ions

An example of a typical semilogarithmic plot of reactant and product ion counts vs.  $[\text{ClN}_3]$  is shown in Figure 9.2. This example shows the decay of  $\text{F}^-$  due to its reaction with  $\text{ClN}_3$ . Also shown is the increase of  $\text{Cl}^-$  and  $\text{N}_3^-$  product as  $[\text{ClN}_3]$  increases.  $\text{N}_3^-$  decreased at larger densities because it also reacted with



$\text{ClN}_3$ . The percent decay of the primary reactant ion varied between 20 – 80% depending on the reactant. The semilogarithmic decays were observed to be linear for every observed reaction as expected for pseudo-first-order reactions.

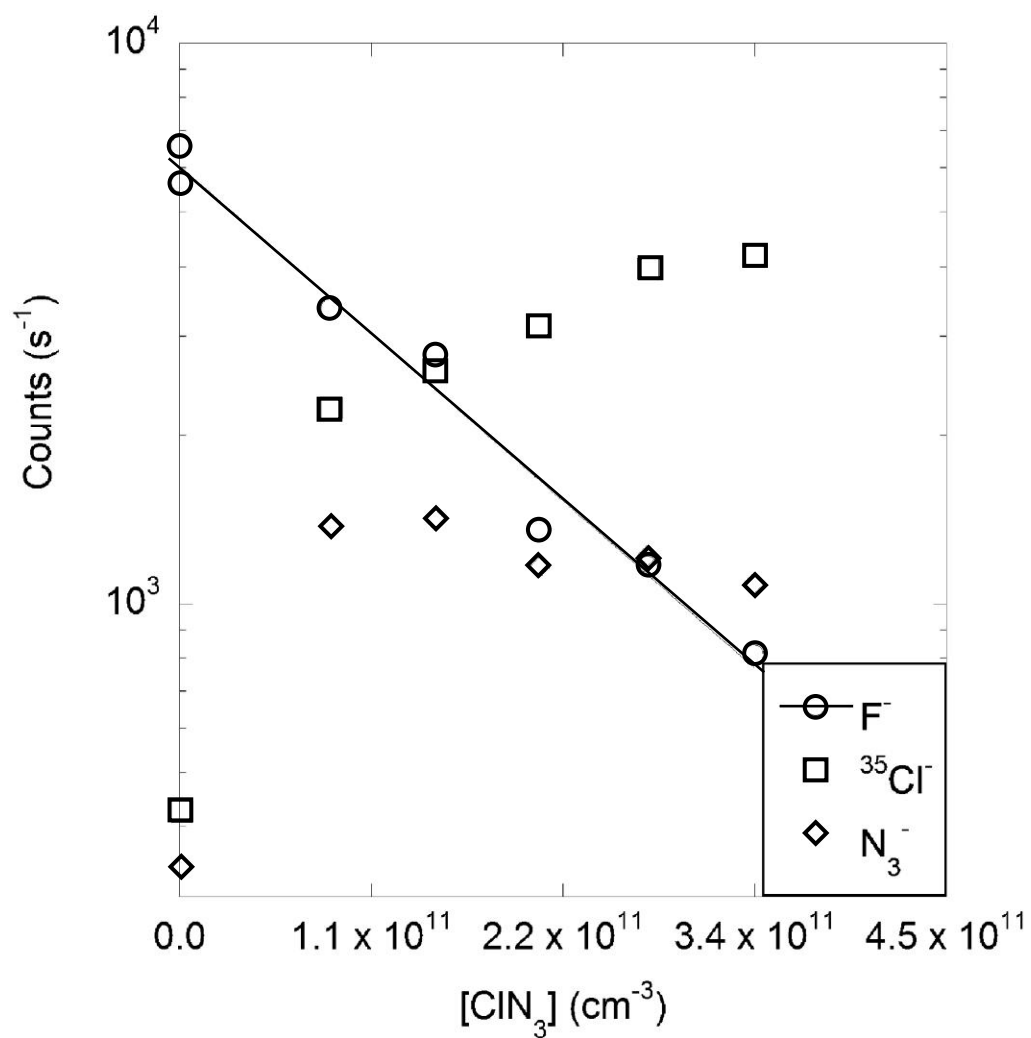


**Figure 9.2.** Semilogarithmic plot of fluoride ion reacting with chlorine azide. The line through the  $\text{F}^-$  data is a least-squares fit.

### 9.3.1. Negative Ions + Cl<sub>2</sub>

Reaction rate constants, reaction efficiencies (Eff = measured rate constant / collision rate constant), reaction enthalpies ( $\Delta H_{\text{rxn}}$ ), and product ion branching ratios were measured for the reaction of various ions with Cl<sub>2</sub> and listed in Table 9.1. The electron binding energies (eBE) were taken from the NIST Chemistry Webbook<sup>5</sup>. As mentioned above, these measurements were necessary to account for unreacted Cl<sub>2</sub> which introduced competing reactions with the ion reactant in the ion + ClN<sub>3</sub> studies.

A reaction was observed with all but one ion (SF<sub>5</sub><sup>-</sup>). Cl<sup>-</sup> and Cl<sub>2</sub><sup>-</sup> were often the main ion products. Cl<sup>-</sup> was a product in all but one of the reactions. However, the Cl<sup>-</sup> product was not useful to account for the Cl<sub>2</sub> background in ClN<sub>3</sub> experiments because Cl<sup>-</sup> was a possible ion product in ion + ClN<sub>3</sub> reactions. Cl<sub>2</sub><sup>-</sup>, which was a product in many of the reactions in Table 9.1 was more useful since it could not be a product of any of the ion + ClN<sub>3</sub> reactions.

O<sub>2</sub><sup>-</sup>, O<sup>-</sup>, NO<sub>2</sub><sup>-</sup>, SF<sub>6</sub><sup>-</sup>, OH<sup>-</sup>, NH<sub>2</sub><sup>-</sup>, and CH<sub>3</sub>O<sup>-</sup> all have electron binding energies that are lower than Cl<sub>2</sub> (2.4 eV). As a result, Cl<sub>2</sub><sup>-</sup> was an ion product of their reaction with Cl<sub>2</sub>. For these ions, the measured rate constants and branching fractions were used to subtract the unreacted Cl<sub>2</sub> contribution in the ClN<sub>3</sub> reactions.

Reaction	eBE (eV)	Rate Constant	Eff	Ionic Products	Hypothesized		$\Delta H_{\text{rxn}}$
					Neutral Products	Branching Ratio	
$\text{O}_2^- + \text{Cl}_2$	0.448	11.8	1.10	$\text{Cl}^-$	$\text{ClO}_2$	0.67	-80
				$\text{Cl}_2^-$	$\text{O}_2$	0.33	-188
$\text{O}^- + \text{Cl}_2$	1.461112	17.3	1.24	$\text{Cl}^-$	$\text{ClO}$	0.06	-234
				$\text{ClO}^-$	$\text{Cl}$	0.11	-95
				$\text{Cl}_2^-$	$\text{O}$	0.83	-91
$\text{NO}_2^- + \text{Cl}_2$	2.273	7.87	0.83	$\text{Cl}^-$	$\text{NO}_2\text{Cl}$	0.09	7
				$\text{Cl}_2^-$	$\text{NO}_2$	0.91	-15
$\text{SF}_6^- + \text{Cl}_2$	1.2	0.945	0.13	$\text{Cl}_2^-$	$\text{SF}_6$	1	-132
$\text{SF}_5^- + \text{Cl}_2$	3.8		0.00	N/R			
$\text{F}^- + \text{Cl}_2$	3.4012	7.87	0.61	$\text{Cl}^-$	$\text{FCl}$		-43
$\text{OH}^- + \text{Cl}_2$	1.8277	12.7	0.91	$\text{Cl}^-$	$\text{HClO}$	0.18	-163
				$\text{ClO}^-$	$\text{HCl}$	0.03	-61
				$\text{Cl}_2^-$	$\text{OH}$	0.79	-54
$\text{CN}^- + \text{Cl}_2$	3.862	0.126	0.01	$\text{Cl}^-$	$\text{ClCN}$		-162
$\text{NH}_2^- + \text{Cl}_2$	0.771	1.34	0.10	$\text{Cl}^-$	$\text{NH}_2\text{Cl}$	0.14	
				$\text{Cl}_2^-$	$\text{NH}_2$	0.86	-152
$\text{N}_3^- + \text{Cl}_2$	2.68	0.0346	0.00	$\text{Cl}^-$	$\text{ClN}_3$	1	-250
$\text{Br}^- + \text{Cl}_2$	3.363538	0.268	0.03	$\text{Cl}^-$	$\text{BrCl}$	1	-14
$\text{I}^- + \text{Cl}_2$	3.059036	0.496	0.07	$\text{Cl}^-$	$\text{ICl}$	1	-365
$\text{CH}_3\text{O}^- + \text{Cl}_2$	1.572	0.945	0.09	$\text{Cl}^-$	$\text{CH}_2\text{O} + \text{HCl}$	0.59	-296
				$\text{Cl}_2^-$	$\text{CH}_3\text{O}$	0.41	-76

**Table 9.1.** Reaction rate constant ( $10^{-10} \text{ cm}^3 \text{ molecule}^{-1} \text{ s}^{-1}$ ), product ion branching ratios, and reaction enthalpies ( $\text{kJ mol}^{-1}$ ) of negative ions with  $\text{Cl}_2$

The remaining ions (besides  $\text{SF}_5^-$  which did not react) produced exclusively  $\text{Cl}^-$  as an ion product. The lack of  $\text{Cl}_2^-$  in these reactions did not allow for a direct correction for the unreacted  $\text{Cl}_2$ . However a reaction that did form  $\text{Cl}_2^-$  was run immediately before or after the  $\text{ClN}_3$  study so that the necessary corrections could be made. The  $\text{Cl}_2^-$  count was never larger than 10% of the major product and the corrections mainly affected the branching ratio for the minor channels.

### 9.3.2. Negative Ions + $\text{ClN}_3$

Reaction rate constants, reaction efficiencies, reaction enthalpies ( $\Delta H_{\text{rxn}}$ ), and product ion branching ratios were measured for the reaction of various ions with  $\text{ClN}_3$  and are listed in Table 9.2. The reaction rate for  $^{17}\text{Cl}^-$  was corrected for the natural abundance of  $^{35}\text{Cl}^-$  in  $\text{ClN}_3$ . Asterisks mark the  $\Delta H_{\text{rxn}}$  values which were estimated from electronic structure calculations. Reactions with  $\text{O}^-$ ,  $\text{O}_2^-$ ,  $\text{NO}_2^-$ ,  $\text{OH}^-$ , and  $\text{CH}_3\text{O}^-$  produced trace amounts of  $\text{Cl}_2^-$  as a result of  $\text{Cl}_2$  contamination and the rate constants and branching ratios were corrected accordingly.

Reaction	EA (eV)	Rate Constant	Eff	Hypothesized		Branching Ratio	$\Delta H_{\text{rxn}}$
				Ionic Products	Neutral Products		
$\text{O}_2^- + \text{ClN}_3$	0.448	11.4	0.88	$\text{Cl}^-$	$\text{N}_3 + \text{O}_2$	0.80	-110
					$\text{N}_2 + \text{NO}_2$		-534
				$\text{N}_3^-$	$\text{Cl} + \text{O}_2$	0.09	-20
				$\text{ClO}_2^-$	$\text{N}_3$	0.01	+92
				$\text{ClN}_3^-$	$\text{O}_2$	0.11	-170*
$\text{O}^- + \text{ClN}_3$	1.461112	16.4	0.96	$\text{Cl}^-$	$\text{N}_3 + \text{O}$	0.65	-12
					$\text{N}_2 + \text{NO}$		-628
				$\text{N}_3^-$	$\text{ClO}$	0.11	-191
				$\text{ClO}^-$		0.09	-152
				$\text{ClN}_3^-$		0.15	-80*
$\text{CO}_3^- + \text{ClN}_3$	3.26	NR	0.00				
$\text{NO}_2^- + \text{ClN}_3$	2.273	10.4	0.90	$\text{Cl}^-$	$2 \text{NO} + \text{O}_2$	0.31	-46
				$\text{N}_3^-$	$\text{NO}_2\text{Cl}$	0.06	+10
				$\text{ClN}_3^-$	$\text{NO}_2$	0.63	+9
$\text{NO}_3^- + \text{ClN}_3$	3.937	NR	0.00				
$^{37}\text{Cl}^- + ^{35}\text{ClN}_3$	3.6144	3.1	0.25	$^{35}\text{Cl}^-$	$^{37}\text{ClN}_3$	1.0	0
$\text{SF}_6^- + \text{ClN}_3$	1.20	2.42	0.28	$\text{FN}_3^-$	$\text{SF}_5\text{Cl}$	0.34	+175
				$\text{SF}_5^-$	$\text{ClF} + \text{N}_3$	0.66	+72
$\text{SF}_5^- + \text{ClN}_3$	3.8	0.390	0.04	$\text{FN}_3^-$	$\text{SF}_4\text{Cl}$	0.66	+366
				$\text{SF}_4\text{N}_3^-$	$\text{FCl}$	0.34	+119
$\text{F}^- + \text{ClN}_3$	3.4012	8.98	0.57	$\text{Cl}^-$	$\text{FN}_3$	0.64	-63*
				$\text{N}_3^-$	$\text{FCl}$	0.36	-62*
$\text{OH}^- + \text{ClN}_3$	1.8277	13.0	0.80	$\text{Cl}^-$	$\text{N}_2 + \text{HNO}$	0.67	-372
				$\text{ClO}^-$	$\text{HN}_3$	0.12	-69
				$\text{ClN}_3^-$	$\text{OH}$	0.12	-36*
				$\text{Cl}^-(\text{ClN}_3)$		0.09	
$\text{CN}^- + \text{ClN}_3$	3.862	9.30	0.66	$\text{Cl}^-$	$\text{N}_2 + \text{CNN}$	0.41	-67

				$\text{N}_3^-$	ClCN	0.59	-120
$\text{NH}_2^- + \text{ClN}_3$	0.771	1.72	0.10	$\text{Cl}^-$	$2 \text{N}_2 + \text{H}_2$	1.0	-721
					$\text{N}_3 + \text{NH}_2$		-74
$\text{N}_3^- + \text{ClN}_3$	2.68	0.0969	0.01	$\text{Cl}^-$	$3 \text{N}_2$	1.0	-808
$\text{Br}^- + \text{ClN}_3$	3.363538	0.0824	0.01	$\text{Cl}^-$	$\text{BrN}_3$	1.0	+3*
$\text{I}^- + \text{ClN}_3$	3.059036	0.574	0.06	$\text{Cl}^-$	$\text{IN}_3$	0.83	-13*
				$\text{N}_3^-$	ICI	0.17	(+21) -59*
$\text{CH}_3\text{O}^- + \text{ClN}_3$	1.572	1.64	0.12	$\text{Cl}^-$	$\text{CH}_3\text{O} + \text{N}_3$	0.75	-67
					$\text{N}_2 + \text{NO} + \text{CH}_3$		-255
				$\text{N}_3^-$	$\text{CH}_3\text{OCl}$	0.15	-187
				$\text{ClO}^-$	$\text{CH}_3\text{N}_3$	0.10	-67
$\text{Cl}_2^- + \text{ClN}_3$		2.61	0.26	$\text{Cl}_3^-$	$\text{N}_3$	1.0	-362

**Table 9.2.** Reaction rate constant ( $10^{-10} \text{ cm}^3 \text{ molecule}^{-1} \text{ s}^{-1}$ ), product ion branching ratios, and reaction enthalpies ( $\text{kJ mol}^{-1}$ ) of negative ions with  $\text{ClN}_3$ .

Reactions of  $\text{ClN}_3$  with  $\text{O}_2^-$ ,  $\text{O}^-$ ,  $\text{NO}_2^-$ ,  $\text{F}^-$ ,  $\text{CN}^-$  produced both  $\text{Cl}^-$  and  $\text{N}_3^-$  with efficiencies  $> 50\%$ .  $\text{I}^-$  and  $\text{CH}_3^-$  reacted to form the same product ions but with only 12 and 6% efficiencies respectively. In general, the relative exothermicities of the two channels were reflected in the branching ratios.  $\text{Cl}^-$  and  $\text{N}_3^-$  account for at least 75% of the total product ions in these reactions with  $\text{Cl}^-$  dominating in most cases.

Charge transfer dominated in the reaction with  $\text{NO}_2^-$  and was also an observed mechanism in reactions with  $\text{O}_2^-$ ,  $\text{O}^-$ , and  $\text{OH}^-$ . Particular attention

was paid to the production of the  $\text{ClN}_3^-$  product. This product was of interest to bracket the electron affinity of  $\text{ClN}_3$ . The  $\text{ClN}_3^-$  product was produced for reactions where the electron affinity of the ion reactant was smaller than that of  $\text{ClN}_3$ . If the electron affinity of the ion reactant was larger than that of  $\text{ClN}_3$ , the  $\text{ClN}_3^-$  product would not be observed. Based on the observed results listed in Table 9.2 the electron affinity of  $\text{ClN}_3$  must lie between that of  $\text{NO}_2$  and  $\text{N}_3$ , estimating  $\text{EA} = 2.48 \pm 0.2$  eV.

Isotope exchange of Cl was studied by injecting  $^{37}\text{Cl}^-$  to react with  $\text{ClN}_3$ . Exchange was found to occur in  $\sim 25\%$  of collisions. The natural abundance of  $^{35}\text{Cl}$  in the  $\text{ClN}_3$  reactant was accounted for.  $\text{N}_3^-$ ,  $\text{Br}^-$ , and  $\text{I}^-$  produced exclusively  $\text{Cl}^-$  but at low efficiency. Reactions of  $\text{SF}_6^-$  and  $\text{SF}_5^-$  were interesting as they produced exotic and unexpected ions ( $\text{FN}_3^-$  and  $\text{SF}_4\text{N}_3^-$ ). The oxygen-containing ion reactants all reacted with  $\text{ClN}_3$  to produce minor oxygen-containing products.

#### 9.4. Discussion: $\text{ClN}_3$ + Negative Ions

One of the goals of the present study was to determine the electron affinity of  $\text{ClN}_3$ . G3B3 calculations were completed and predicted the electron affinity to be  $2.32 \pm 0.1$  eV. G3B3 is a variant of the G3 theory in which

structures and zero point vibrational energies were calculated at the B3LYP/6-31G(d) level of theory instead of MP2/6-31G(d).<sup>6-8</sup> The experimental value of  $EA = 2.48 \pm 0.2$  eV is in good agreement with the calculated value. There is a possibility that  $ClN_3^-$  was created in an exothermic reaction and dissociated. However complete dissociation was unlikely. Partial dissociation would result in an underestimation of  $ClN_3^-$  and an overestimation of  $Cl^-$  branching fractions.

The reaction rate constants and branching ratios for  $Cl_2$  with  $O_2^-$ ,  $O^-$ ,  $NO_2^-$ ,  $SF_6^-$ , and  $F^-$  have been reported previously and are within the error bars of our measured values.<sup>9-12</sup> Reaction mechanisms were inferred from previous experimental studies and computational efforts.

The reaction coordinate for the reaction of  $F^-$  with  $ClN_3$  has been reported.<sup>13</sup> The computational results showed that  $Cl^-$  was produced in the reaction via a nearly barrierless syn attack on the terminal N of  $ClN_3$ . A distinct barrier was calculated for the attack of  $F^-$  on the chlorine atom resulting in the formation of  $ClF$  and  $N_3^-$ . All of the reactions in this study were expected to occur in a similar manner.

The results from this study offer some clues to the mechanistic details. For the isotope exchange reaction, if a long-lived complex was made for every collision, and efficiency of 50% would be expected. The lower efficiency in this



study (25%) implies that either the complex was not formed efficiently or that there was a barrier to the product formation. The low efficiency of the  $\text{Br}^-$  and  $\text{I}^-$  reactions to produce  $\text{Cl}^-$  was due to the low exothermicities. The  $\text{N}_3^-$  reaction was probably slow because the formation of four products ( $3 \text{N}_2 + \text{Cl}^-$ ) is generally not efficient.

The reactions of  $\text{ClN}_3$  with  $\text{SF}_6^-$  and  $\text{SF}_5^-$  produced never before observed product ions,  $\text{FN}_3^-$  and  $\text{SF}_4\text{N}_3^-$ .  $\text{FN}_3^-$  was formed in both reactions likely through a syn attack on the terminal nitrogen and elimination of  $\text{SF}_{x-1}\text{Cl}$ . The production of  $\text{SF}_4\text{N}_3^-$  and  $\text{SF}_5^-$  likely occurs through the same mechanism.

Computational work was completed to address the mechanisms of the oxygen-containing reactions.<sup>13</sup> The transfer of the chlorine atom to  $\text{O}^-$  was believed to occur as a barrierless process. From there,  $\text{ClO}^-$  may dissociate or electron back transfer would produce  $\text{ClO}$  and  $\text{N}_3^-$ . However, in this study  $\text{Cl}^-$  was the major product. Further computational work predicted that  $\text{ClO}^-$  further reacts with  $\text{N}_3$ . In this case the oxygen attacks the terminal nitrogen, resulting in the formation of  $\text{Cl}^-$  and  $\text{NNNO}$ , which is unstable and decomposes to form  $\text{N}_2$  and  $\text{NO}$ .

### 9.5. Results: $\text{ClN}_3$ + Positive Ions

As with the reactions of  $\text{ClN}_3$  with negative ions, the reaction of positive ions with  $\text{Cl}_2$  were also examined to account for unreacted  $\text{Cl}_2$  from the  $\text{ClN}_3$  synthesis. Computational work was completed to complement the experimental results.

Reactions of  $\text{Cl}_2$  with  $\text{O}_2^+$ ,  $\text{H}_3\text{O}^+$ ,  $\text{Ar}^+$ ,  $\text{C}^+$ ,  $\text{CO}^+$ ,  $\text{N}^+$ ,  $\text{N}_2^+$ ,  $\text{SF}_5^+$ , and  $\text{SF}_3^+$  were observed. Reactions with contaminant  $\text{H}_2\text{O}$  were observed with  $\text{O}_2^+$ ,  $\text{CH}_3\text{OH}_2^+$ ,  $\text{C}^+$ , and  $\text{O}^+$ . Reactant rate constants and branching ratios for the reactions with these ions with  $\text{ClN}_3$  were corrected. Semi-logarithmic decays were observed in all cases. Decay of the primary ion was  $\sim 20\%$  for the slowest reactions and  $\sim 80\%$  for faster reactions.

The reactivity of  $\text{ClN}_3$  with 18 positive ions was investigated, allowing for general reaction trends and thermochemistry to be determined. The rate constants, ion products with branching ratios, and efficiencies for these reactions are listed in Tables 9.3 and 9.4. Accurate branching ratios could not be determined for some reactions due to the effects from  $\text{ClN}_3$  reactant impurities. In those cases only major products are identified and rate constants are reported as upper limits.

Of particular interest were reactions that allowed for the ionization potential and proton affinity of  $\text{ClN}_3$  to be determined. The reactions that were

Reaction	Ionization energy (eV)*	Rate constant ( $10^{-10} \text{ cm}^3 \text{ s}^{-1}$ )	Eff	Ionic products	Branching ratio
$\text{Ar}^+ + \text{ClN}_3$	15.76	<20	<1	$\text{NCl}^+$ $\text{Cl}^+$ $\text{N}_3^+$	Major
$\text{N}_2^+ + \text{ClN}_3$	15.58	<20	<1	$\text{NCl}^+$ $\text{Cl}^+$ $\text{ClN}_2^+$	Major
$\text{N}^+ + \text{ClN}_3$	14.53	17	0.9	$\text{NCl}^+$ $\text{N}_3^+$ $\text{Cl}^+$ $\text{ClN}_2^+$	0.7 0.2 0.1 Trace
$\text{CO}^+ + \text{ClN}_3$	14	<10	<0.8	$\text{Cl}^+$ $\text{N}_3^+$ $\text{CCl}^+$ $\text{ClN}_2^+$	Major
$\text{O}^+ + \text{ClN}_3$	13.6	<40	<1	$\text{N}_3^+$ $\text{NCl}^+$	Major
$\text{SO}_2^+ + \text{ClN}_3$	12.35	5.6	0.5	$\text{SOCl}^+$ $\text{NCl}^+$ $\text{Cl}^+$	Trace 0.8 0.2
$\text{O}_2^+ + \text{ClN}_3$	12.07	15	1	$\text{NCl}^+$	
$\text{C}^+ + \text{ClN}_3$	11.2	<20	<1	$\text{NCl}^+$	Major
$\text{SO}^+ + \text{ClN}_3$	10.29	8.1	0.6	$\text{SOCl}^+$ $\text{SON}_3^+$ $\text{SONCl}^+$ $\text{SN}^+$ $\text{ClN}_2^+$ $\text{NCl}^+$	0.2 0.2 0.3 0.2 Trace 0.1
$\text{CS}_2^+ + \text{ClN}_3$	10.073	6.8	0.6	$\text{CSCl}^+$ $\text{CS}_2\text{N}^+$	0.3 0.7
$\text{CH}_3^+ + \text{ClN}_3$	9.84	27	1	$\text{CNH}_2^+$ $\text{HN}_3^+$	0.9 0.1
$\text{SF}_5^+ + \text{ClN}_3$	9.6	0.13	0.01	$\text{NCl}^+$ $\text{SF}_5\text{ClN}^+$	Major
$\text{NO}_2^+ + \text{ClN}_3$	9.586	N/R	<0.001		
$\text{NO}^+ + \text{ClN}_3$	9.264	N/R	<0.001		
$\text{SF}_3^+ + \text{ClN}_3$	8.18	0.001	0.001	$\text{SF}_2\text{Cl}^+$	

**Table 9.3.** Reaction rate constants, reaction efficiencies (Eff), and product ion branching distributions measured at 300 K for reactions used to determine the ionization energy of  $\text{ClN}_3$ .

\* The ionization energy listed is the ionization energy for the neutral of the corresponding ion reactant.

Reaction	Proton binding energy (kJ mol <sup>-1</sup> )	Rate constant (10 <sup>-10</sup> cm <sup>3</sup> s <sup>-1</sup> )	Eff	Ionic products	Branching ratio
CH <sub>3</sub> OH <sub>2</sub> <sup>+</sup> + ClN <sub>3</sub>	754	0.21	0.01	HN <sub>3</sub> <sup>+</sup>	
H <sub>3</sub> O <sup>+</sup> + ClN <sub>3</sub>	691	1.3	0.08	NCI <sup>+</sup>	0.5
				HN <sub>3</sub> <sup>+</sup>	0.5
HSO <sub>2</sub> <sup>+</sup> + ClN <sub>3</sub>	672	4.2	0.35	HClN <sub>3</sub> <sup>+</sup>	0.1
				NCI <sup>+</sup>	0.8
				Cl <sup>+</sup>	0.1

**Table 9.4.** Reaction rate constants, reaction efficiencies (Eff), and product ion branching distributions measured at 300 K for reactions used to determine the electron affinity of ClN<sub>3</sub>.

used to bracket the ionization potential are listed in Table 9.3 along with the ionization energy for the corresponding neutral of the reactant ion. A charge-exchange reaction would imply that the ionization energy of ClN<sub>3</sub> must be lower than the listed ionization energy. Unfortunately, ClN<sub>3</sub><sup>+</sup> was not observed as a product of any reaction so an upper limit to the ionization energy could not be determined. This is consistent with a previously reported observation<sup>14</sup> that ClN<sub>3</sub> dissociates upon ionization. NO<sup>+</sup> and NO<sub>2</sub><sup>+</sup> were found not to react with ClN<sub>3</sub> signifying that the IE of ClN<sub>3</sub> is greater than the IE of either NO or NO<sub>2</sub>. The IE is therefore > 930 kJ mol<sup>-1</sup>(>9.6 eV).

The reactions that were used to bracket the proton affinity of ClN<sub>3</sub> are listed in Table 9.4 along with the proton binding energy for the corresponding ion. Proton transfer occurred if the proton affinity of ClN<sub>3</sub> was greater than the proton binding energy of the ion. Rapid, moderately efficient (35%), non-

dissociative proton transfer was observed in the reaction with  $\text{HSO}_2^+$ , indicating the  $\text{PA}(\text{ClN}_3) > 672 \text{ kJ mol}^{-1}$ .  $\text{HClN}_3^+$  was not observed in reactions of  $\text{ClN}_3$  with  $\text{H}_3\text{O}^+$  or  $\text{CH}_3\text{OH}_2^+$  but the proton transfer dissociation transfer product,  $\text{HN}_3^+$  was observed. This product was present at a low but significant efficiency (8%) for the reaction with  $\text{H}_3\text{O}^+$ . Although  $\text{HN}_3^+$  was observed in the reaction with  $\text{CH}_3\text{OH}_2^+$  the efficiency was too low (1%) to be sure it is an exothermic reaction. The proton affinity of  $\text{ClN}_3$  was then bracketed between the proton binding energies of  $\text{CH}_3\text{OH}_2^+$  and  $\text{HSO}_2^+$  at  $713 \pm 41 \text{ kJ mol}^{-1}$ .

The high energy content of  $\text{ClN}_3$  makes a wide variety of ion products accessible. Reactions were more efficient if the corresponding neutral of the reactant ion had a large ionization energy. Many different ion products were observed and often a single reaction would result in several products.  $\text{ClN}^+$ ,  $\text{Cl}^+$ ,  $\text{N}_3^+$ , and  $\text{ClN}_2^+$  were common ion products. The dissociative charge-transfer product  $\text{NCl}^+$  was produced in fourteen of the sixteen cations that did react.  $\text{Cl}^+$  and  $\text{N}_3^+$  were products of reactions with listed ionization energies greater than 12.2 eV. Few oxygen containing ion products were observed yet sulfur containing ion products were produced efficiently.

## 9.6. Discussion: $\text{ClN}_3$ + Positive Ions

The lack of  $\text{ClN}_3^+$  and the observation of both  $\text{NCl}^+$  and  $\text{Cl}^+$  dissociative products confirmed that  $\text{ClN}_3^+$  is weakly bound and dissociates easily upon ionization of  $\text{ClN}_3$ .<sup>14</sup> The bracketing study to determine the ionization energy gave an upper limit of 9.2 eV which is consistent with a previous estimate of 9.97 eV.<sup>1</sup>

G3 calculations gave three stable structures of  $\text{HCIN}_3^+$ .<sup>15</sup> The proton could have attached to Cl (PA = 587 kJ mol<sup>-1</sup>), the N closest to the chlorine atom (PA = 637 kJ mol<sup>-1</sup>), or the N furthest from the Cl atom (PA = 703 kJ mol<sup>-1</sup>), but not to the central N. The experimentally bracketed PA of  $713 \pm 41$  kJ mol<sup>-1</sup> suggested that the proton attached to the terminal N. Note that the proton transfer reaction observed with  $\text{HSO}_2^+$  required the PA to be  $> 672$  kJ mol<sup>-1</sup>.

Only generalizations were able to be made about reaction trends due to complications from competing reactions of the reactant ion with  $\text{Cl}_2$  and  $\text{H}_2\text{O}$  from the  $\text{ClN}_3$  reactor. A wide variety of product ions were observed but the dissociative products  $\text{Cl}^+$  and  $\text{NCl}^+$  were often abundant. Incorporation of oxygen into the product ions was not as prevalent when compared to negative ion reactions. In contrast, reactions with isovalent sulfur-containing ions, with the exception of  $\text{HSO}_2^+$ , formed product ions containing sulfur. These sulfur containing product ions also incorporate either chlorine or nitrogen. If the

production mechanism for these ions involves direct attachment, then the ions interact with neutral  $\text{ClN}_3$  at several sites. G3 computations of the neutral species predict the Mulliken charges on the chlorine atom and the first and third nitrogen atoms to be negative, giving at least two likely places of attack for the positive ion.

## BIBLIOGRAPHY

- (1)Quinto-Hernandez, A.; Lee, Y. Y.; Huang, T. P.; Pan, W. C.; Lin, J. J. M.; Bobadova-Parvanova, P.; Morokuma, K.; Samartzis, P. C.; Wodtke, A. M. *International Journal of Mass Spectrometry* 2007, 265, 261.
- (2)Viggiano, A. A.; Morris, R. A.; Dale, F.; Paulson, J. F.; Giles, K.; Smith, D.; Su, T. *J Chem Phys* 1990, 93, 1149.
- (3)Frisch, M. J.; Trucks, G. W.; Schlegel, H. B.; Scuseria, G. E.; Robb, M. A.; Cheeseman, J. R.; Montgomery, J. A.; Vreven, T.; Kudin, K. N.; Burant, J. C.; Millam, J. M.; Iyengar, S. S.; Tomasi, J.; Barone, V.; Mennucci, B.; Cossi, M.; Scalmani, G.; Rega, N.; Petersson, G. A.; Nakatsuji, H.; Hada, M.; Ehara, M.; Toyota, K.; Fukuda, R.; Hasegawa, J.; Ishida, M.; Nakajima, T.; Honda, Y.; Kitao, O.; Nakai, H.; Klene, M.; Li, X.; Knox, J. E.; Hratchian, H. P.; Cross, J. B.; Bakken, V.; Adamo, C.; Jaramillo, J.; Gomperts, R.; Stratmann, R. E.; Yazyev, O.; Austin, A. J.; Cammi, R.; Pomelli, C.; Ochterski, J. W.; Ayala, P. Y.; Morokuma, K.; Voth, G. A.; Salvador, P.; Dannenberg, J. J.; Zakrzewski, V. G.; Dapprich, S.; Daniels, A. D.; Strain, M. C.; Farkas, O.; Malick, D. K.; Rabuck, A. D.; Raghavachari, K.; Foresman, J. B.; Ortiz, J. V.; Cui, Q.; Baboul, A. G.; Clifford, S.; Cioslowski, J.; Stefanov, B. B.; Liu, G.; Liashenko, A.; Piskorz, P.; Komaromi, I.; Martin, R. L.; Fox, D. J.; Keith, T.; Laham, A.; Peng, C. Y.; Nanayakkara, A.; Challacombe, M.; Gill, P. M. W.; Johnson, B.; Chen, W.; Wong, M. W.; Gonzalez, C.; Pople, J. A. 2003.
- (4)Curtiss, L. A.; Raghavachari, K.; Redfern, P. C.; Rassolov, V.; Pople, J. A. *J Chem Phys* 1998, 109, 7764.
- (5)P.J. Linstrom and W.G. Mallard, E., NIST Chemistry WebBook, NIST Standard Reference Database Number 69, National Institute of Standards and Technology, Gaithersburg MD, 20899, <http://webbook.nist.gov>, (retrieved January 14, 2013).
- (6)Mayer, P. M.; Parkinson, C. J.; Smith, D. M.; Radom, L. *J Chem Phys* 1998, 108, 604.
- (7)Baboul, A. G.; Curtiss, L. A.; Redfern, P. C.; Raghavachari, K. *J Chem Phys* 1999, 110, 7650.
- (8)Montgomery, J. A.; Frisch, M. J.; Ochterski, J. W.; Petersson, G. A. *J Chem Phys* 1999, 110, 2822.
- (9)Streit, G. E. *J Phys Chem-Us* 1982, 86, 2321.
- (10)Streit, G. E. *J Chem Phys* 1982, 77, 826.
- (11)Babcock, L. M.; Streit, G. E. *J Chem Phys* 1982, 76, 2407.
- (12)Dunkin, D. B.; Fehsenfeld, F.; Ferguson, E. E. *Chemical Physics Letters* 1972, 15, 257.
- (13)Eyert, N.; Freil, K.; Heaven, M. C.; Viggiano, A. A. *J Phys Chem A* 2010, 114, 6832.



(14) Hansen, N.; Wodtke, A. M.; Komissarov, A. V.; Morokuma, K.; Heaven, M. C. *J. Chem. Phys.* 2003, *118*, 10485.

(15) Eyet, N.; Freel, K.; Heaven, M. C.; Viggiano, A. A. *International Journal of Mass Spectrometry* 2011, *303*, 220.

*Section 3*

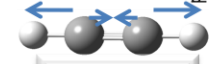
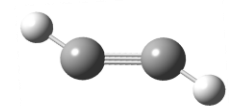
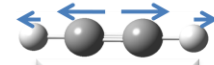
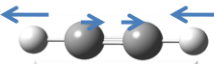
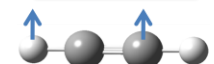
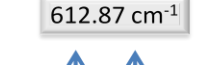
## ROVIBRATIONAL ENERGY TRANSFER IN ACETYLENE

**Chapter 10. Rotational and Vibrational Energy Transfer From the First Overtone Stretch (10100)<sup>00</sup> of Acetylene****10.1. Introduction**

Acetylene has recently been demonstrated as medium for a potential high quality, scalable, molecular gas phase laser near 3  $\mu\text{m}$ .<sup>1</sup> Acetylene is an ideal candidate for this type of laser because it is pumped using 1.5  $\mu\text{m}$  radiation from readily available diode and fiber laser systems. It is anticipated that multiple lower quality fiber lasers would be coupled to pump the acetylene molecular laser producing a high powered, high quality beam with high efficiency.

The vibrational modes, energies, and symmetries of acetylene in the  $X\Sigma_g^+$  state are shown in the first column of Table 10.1. In this section, as with convention, the vibrational state of interest is labeled  $(\nu_1, \nu_2, \nu_3, \nu_4^{l_4}, \nu_5^{l_5})^l$  where  $\nu_n$  represents the vibrational modes in Table 10.1,  $l_4$  and  $l_5$  are the vibrational angular momentum quantum numbers for the doubly degenerate  $\nu_4$  and  $\nu_5$  modes, and  $l$  is the total vibrational angular momentum quantum number ( $l_4 + l_5$ ).  $l$  may be omitted when its value is zero. For the acetylene laser demonstration<sup>1</sup>, the (10100) vibrational level was populated by pumping with an optical parametric

oscillator (OPO) laser at 1.5  $\mu\text{m}$ . Lasing was observed near 3  $\mu\text{m}$  indicating a loss of a single C-H stretch.

<u>Ground State <math>X \Sigma_g^+</math> (<math>D_{\infty h}</math>)</u>	<u>First Excited State <math>A^1 A_u</math> (<math>C_{2h}</math>)</u>
$v''_1$  $\Sigma_g^+$ 3372.85 $\text{cm}^{-1}$	
$v''_2$  $\Sigma_g^+$ 1974.32 $\text{cm}^{-1}$	$v'_1$ CH sym str $a_g$ 2880.5 $\text{cm}^{-1}$
$v''_3$  $\Sigma_u^+$ 3288.39 $\text{cm}^{-1}$	$v'_2$ CC stretch $a_g$ 1386.9 $\text{cm}^{-1}$
$v''_4$  $\Pi_g$ 612.87 $\text{cm}^{-1}$	$v'_3$ trans bend $a_g$ 1047.55 $\text{cm}^{-1}$
$v''_5$  $\Pi_u$ 730.33 $\text{cm}^{-1}$	$v'_4$ torsion $a_u$ 764.91 $\text{cm}^{-1}$
	$v'_5$ CH anti str $b_u$ 2857.41 $\text{cm}^{-1}$
	$v'_6$ cis bend $b_u$ 768.26 $\text{cm}^{-1}$

**Table 10.1.** The vibrational modes, energies, and symmetries of acetylene in the  $X\Sigma_g^+$  and  $A^1A_u$  electronic states. Data were acquired from References 2-5.

Acetylene has been thoroughly studied because it is easily obtainable, exists as a gas at room temperature, and is a relatively simple molecule with rich rovibrational energy levels. Among the thousands of publications involving spectroscopy and energy transfer in acetylene, only the few pertaining to this study will be listed here. A more detailed review of the spectroscopy and energetics of acetylene has been published by Orr<sup>6</sup>. Watson<sup>2</sup> et al. and Herman<sup>5</sup> et al. have published detailed data on the ground electronic state of acetylene as listed in Table 10.1. These modes can be observed by IR ( $u$  symmetry modes)

and Raman ( $g$  symmetry modes) spectroscopy or by double resonance techniques.  $g$ -symmetry modes near (10100) have also been observed using IR by absorption from the thermally populated low lying  $\nu_5$  level.<sup>7</sup> Overtone and combination bands have been observed above 15000  $\text{cm}^{-1}$  where acetylene is dissociated to vinylidene ( $\text{H}_2\text{C}=\text{C}$ ):<sup>8</sup> At high energies, spectra become congested and rovibrational eigenstates are perturbed by anharmonic mixing, l-resonance effects, and Coriolis coupling.<sup>9</sup> At this point the normal-mode description is no longer valid and the eigenstates must be described by polyad models.

Acetylene was the first molecule to show a large change in geometry upon excitation to a higher electronic state.<sup>6</sup> Acetylene is linear in its ground state but trans-bent planar in its first excited  $A^1A_u$  state. The symmetry is changed from  $D_{\infty h}$  in the ground state to  $C_{2h}$  in the  $A^1A_u$  state. The vibrational modes, energies, and symmetries of acetylene in the  $A^1A_u$  state are shown in the second column of Table 10.1. The change in electronic symmetry from  $g$  to  $u$  allows direct absorption or laser induced fluorescence (LIF) measurements from the ground vibrational level in  $X\Sigma_g^+$  to levels in  $A^1A_u$  with  $g$  vibrational symmetry.<sup>2,4,10,11</sup> The  $u$ -symmetry levels in  $A^1A_u$  have been observed by double resonance techniques.<sup>3,12</sup>

Double resonance spectroscopy (described below) has also been used to study collision-induced rotational and vibrational energy transfer in acetylene and is reviewed by Orr.<sup>6</sup> Several rotational energy transfer (RET) studies have

quantified the state-to-state rotational energy transfer kinetics within various vibrational levels in acetylene.<sup>13-18</sup> Vibrational energy transfer (VET) studies identified vibrational levels populated by transfer from the pumped intermediate rovibrational level and the kinetics of this transfer was investigated.<sup>19-24</sup> More specifically related to this work, the kinetics studies by Tobiason and Crim measured the rate constants of the total population removal from various J states in the (10100) vibrational manifold of the ground electronic state.<sup>25</sup> Although the total removal kinetics from this state have been studied, the state-to-state RET and vibrational relaxation pathways from have not been addressed.

In this study time resolved double resonance (IR pump, UV probe) spectroscopy was used to study the collision-induced energy transfers from the vibrational manifold responsible for the previously mentioned lasing in acetylene. After pumping a specific rotational state in (10100), nearby rovibrational states that were populated by rotational and vibrational energy transfer were identified. Furthermore, we measured energy transfer rate constants for the identified transitions.

## 10.2. Experimental

### 10.2.1. Double Resonance Spectroscopy

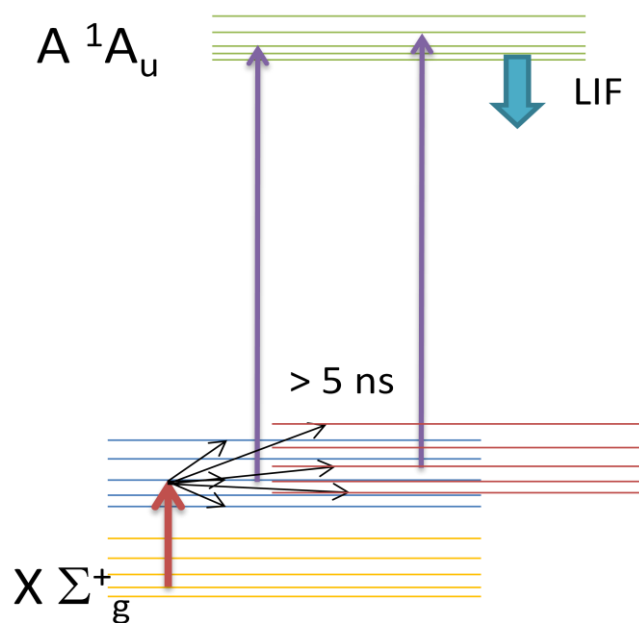


**Figure 10.1.** Eigenstates involved in IR-UV double resonance experiment includes the initially populated ground state (bottom), intermediate pumped state (next higher), collisionally transferred state (next higher), and electronically excited state (highest).

Figure 10.1 shows the rovibronic states involved in the double resonance experiment. The color groups the vibrational manifold and each horizontal line represents a specific rovibrational state. The bottom three vibrational manifolds are in the  $X \Sigma_g^+$  electronic state and the green level (top) represents a vibrational manifold in the  $A^1A_u$  electronic state. First, population was transferred (by IR radiation in this experiment) from a specific ground rovibrational state ( $J''$ ) to a single rovibrational state in the intermediate vibrational level ( $J$ ), referred to as

pumping. After some time, or immediately after pumping, an intermediate state population was observed by laser induced fluorescence, referred to as probing ( $J \rightarrow J'$ ).

There were three typical types of experiments that were done with this scheme involving three variable parameters: the pump wavelength, the probe wavelength, and the time delay between the pump and probe. In the case of a variable time delay, both the pump and probe energies were set in resonance with specific rovibrational transitions. After some time delay to allow for energy transfer, the probe beam was used to observe either the same or a nearby rovibrational state by LIF. Kinetic information was measured for energy transfer processes by recording the time delay vs. LIF intensity.

The second type of experiment was the pump wavelength scan. In this experiment the pump-probe time delay was fixed, the probe wavelength was fixed to induce fluorescence from a specific intermediate rovibrational state, and the pump wavelength was scanned while observing the LIF. If the pump-probe delay was zero, fluorescence was observed only when the pump wavelength was in resonance with the states being probed. If there was some time delay between the pump and probe lasers to allow for RET or VET, then fluorescence was observed when the pump wavelength was in resonance with the states involved in this energy transfer. The fluorescence intensity was proportional to the population in the probed state.

The third type of experiment was the probe wavelength scan. In this experiment the pump-probe time delay was fixed, the pump wavelength was fixed to populate a specific intermediate rovibrational state, and the probe wavelength was scanned while observing the LIF. If the pump-probe delay was zero, fluorescence was observed only when the probe wavelength was in resonance with an allowed transition from the pumped intermediate state. As the delay was increased, peaks arose that corresponded to the states being populated by collisional energy transfer while the peaks assigned to the initially populated state decreased.

In general, the time delay scan gave the best kinetic information. The pump wavelength scan was used to identify which states had energy transfer pathways *to* the probed state. The probe wavelength scan was used to identify energy transfer pathways *from* the pumped state.

### 10.2.2. *Experimental Setup*

The experimental setup is illustrated in Figure 10.2. A small vacuum chamber was evacuated to 1 mTorr using a standard mechanical pump with a dry ice trap to keep pump oil vapors from diffusing into the chamber. Extended from the sides of the chamber were two 0.45 m copper tubes with 1.5 inch diameters. Quartz windows were attached at the ends of the tubes. Within the tubes were bellows constructed of black painted washers with diameters



converging to about 1.0 cm openings designed to reduce light scatter within the chamber. Acetylene flowed from the ends of the extensions to the center of the chamber at 1 mL/s. This was slow enough for laminar flow and negligible convection effects. The pressure was kept constant near 100 mTorr by two flow control valves. The pressure was measured using a Baratron pressure gauge (MKS Model 622A11TAE).

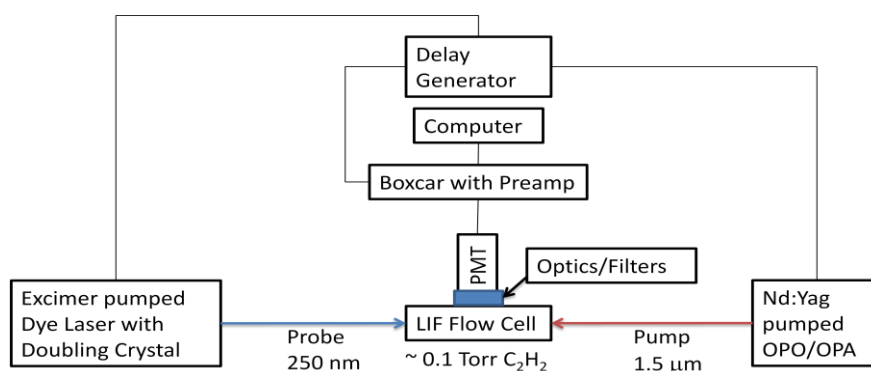


**Figure 10.2.** Experimental setup for IR pump, UV probe double resonance spectroscopy.

An optical parametric oscillator / optical parametric amplifier (OPO/OPA) (LaserVision) laser pumped by a Nd:YAG laser at 1.064 μm provided the pump beam near 1.5 μm. The probe beam was produced by an excimer pumped dye laser (Lambda Physik) frequency doubled to 250 nm. The OPO/OPA produced up to 8 mJ/pulse with a 10 ns pulse duration and 1.3 cm<sup>-1</sup> bandwidth (FWHM). The UV laser had approximately a 10 ns pulse duration and varied from 20 – 200 μJ/pulse. The pulse length of the lasers were short

relative to the timescale of the energy transfer (hundreds of nanoseconds). Both the IR and UV lasers were focused to the center of the chamber, through the quartz windows, so that the IR laser at 0.5 mm was  $5/8$  the size of the UV laser. This insured that after hundreds of nanoseconds very few pumped molecules could diffuse outside the UV beam path. The pump and probe beams entered the chamber from opposite ends and the laser power of both lasers were monitored using a photodiode or a photo multiplier tube (PMT). If the laser power changed more than 10% during a single experiment the data was discarded. The pump-probe time delay was set using a delay generator (SRS, DG 535), which was controlled using a Lab View program.

The LIF was detected by a PMT through the wall of the chamber which was composed of a silica window. The PMT was mounted perpendicular to the pump-probe beams and was located behind filters and optics used to focus the beam intersection into the PMT. The optics and filters reduced background scattered light and increased the sensitivity at least tenfold. The signal from the PMT was integrated with a boxcar and stored on a computer using the Labview program. In some cases the integration began 30-50 ns after the peak fluorescence to reduce the scatter contribution.

### 10.3. Results and Analysis

#### 10.3.1. Absorption Spectrum of Acetylene

The pump laser was calibrated based on  $X\Sigma_g^+(00000) \rightarrow (10100)$  absorption. Figure 10.3 shows the absorption spectrum. Acetylene contains two hydrogen atoms with nuclear spin-1/2 (fermions), and carbon has zero spin. Molecules in even  $J''$  states have symmetric rotational wavefunctions and those in odd  $J''$  states have antisymmetric rotational wavefunctions. To satisfy the Pauli principle, the nuclear spin functions must have opposite symmetry (the electronic and vibrational wavefunctions are symmetric upon exchange of the hydrogens). The symmetrized forms of the nuclear wavefunctions include three symmetric and one antisymmetric form. Therefore, the degeneracy of odd  $J''$  and even  $J''$  states of acetylene are 3 and 1 respectively as observed in the absorption spectrum.

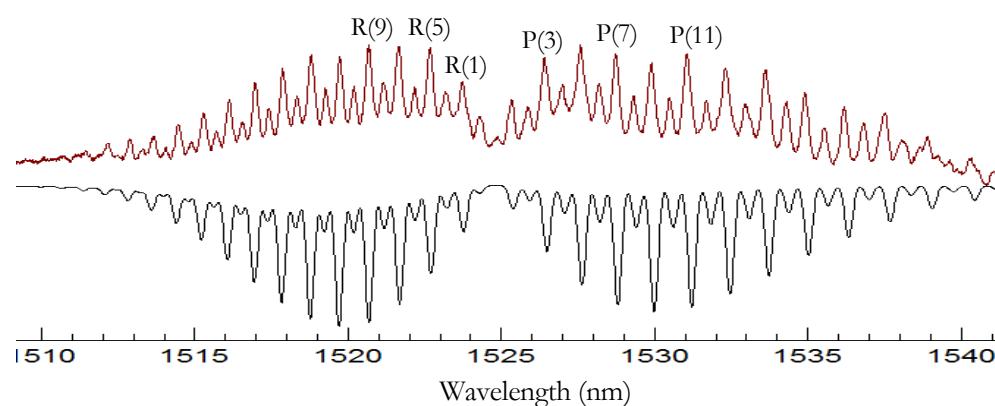


**Figure 10.3.** Absorption spectrum of the  $X\Sigma_g^+(00000) \rightarrow (10100)$  transition of acetylene by IR absorption. Experimental data is plotted above to be compared with the PGOPHER simulation below.

### 10.3.2. Probe Scan Results and Analysis

As explained in the experimental section, the probe scan was used to identify energy transfer pathways *from* the pumped state (10100). Once the pump laser was set in resonance with a vibrational transition, i.e. one of the peaks in Figure 10.3, the probe laser was scanned and LIF was observed using the A(001010)-X(10100) band and recorded as a function of probe laser wavelength. This experiment was repeated for various delay times between the pump and probe lasers.

Figure 10.4 compares UV probe scans at 15 ns delay and 220 ns delay after pumping to  $J = 6, 8, 10, 12, \text{ or } 14$ . The bottom spectrum is a calculated spectrum using constants provided by Tobbiason<sup>14</sup> et al. and simulated using PGOPHER software. The simulation predicts what would be observed if all of the even  $J$  states were pumped simultaneously. In the short time delay experimental spectra (top five), peaks were observed only for transitions from the initially pumped state. After 220 ns (bottom five spectra), rotational energy transfer occurred and peaks appeared for transitions from neighboring  $J$  states. After correcting for laser power, the intensity of the peak was directly proportional to the population in that particular intermediate state. Collisional energy transfer was faster to closely lying  $J$  states than to  $J$  states further in energy. This energy transfer will be quantified later.

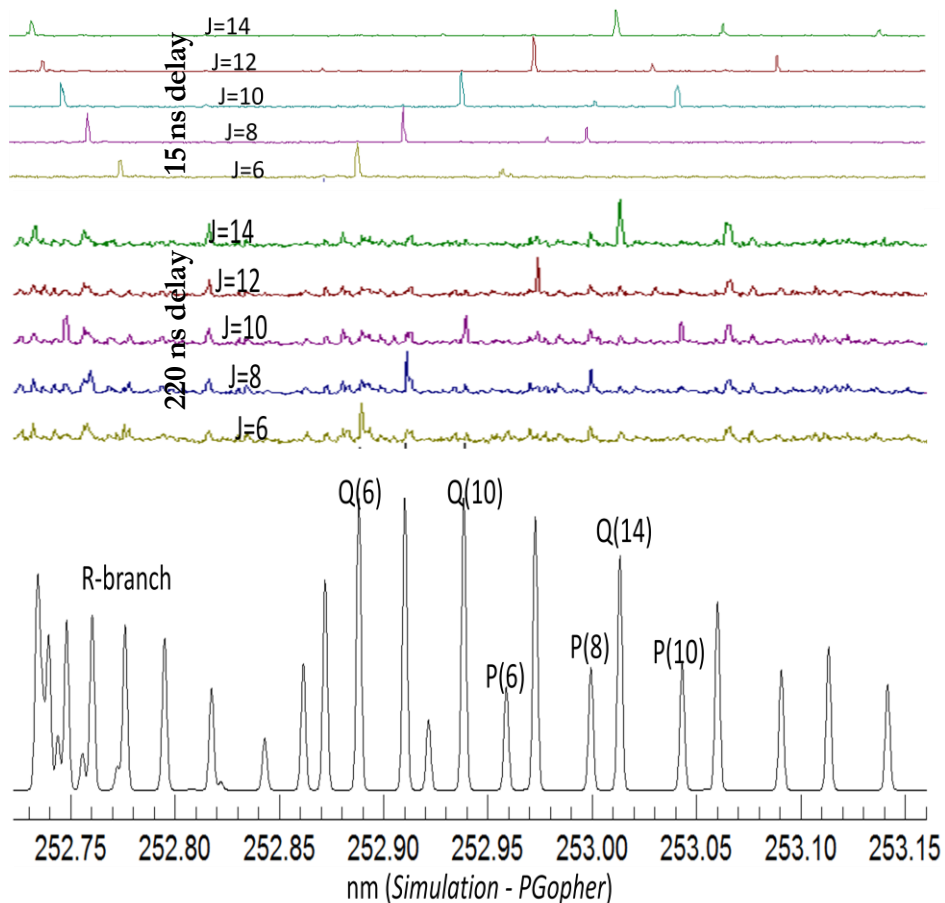


**Figure 10.4.** Probe wavelength scans of the (10100) vibrational level 15 ns and 220 ns after pumping  $J=6,8,10,12$  or 14. The top spectra are the experimental spectra while the bottom simulation gives a reference for peak positions.

Another important artifact in these spectra was the presence of “quasi-continuous” absorption along the entire spectrum which was not assigned necessarily to the (10100) state. These convoluted peaks could not be assigned due to the congestion of the spectra.

There was evidence that VET occurred and these peaks may be due to fluorescence that originated from rotational levels in a different vibrational

manifold nearby the intermediate pumped level. High intensity fluorescence was detected in shorter wavelength UV probe scans. Figure 10.5 shows the probe scan spectrum acquired to the blue of our initially pumped state. The large peaks stick out above the lower intensity background fluorescence. The large peaks

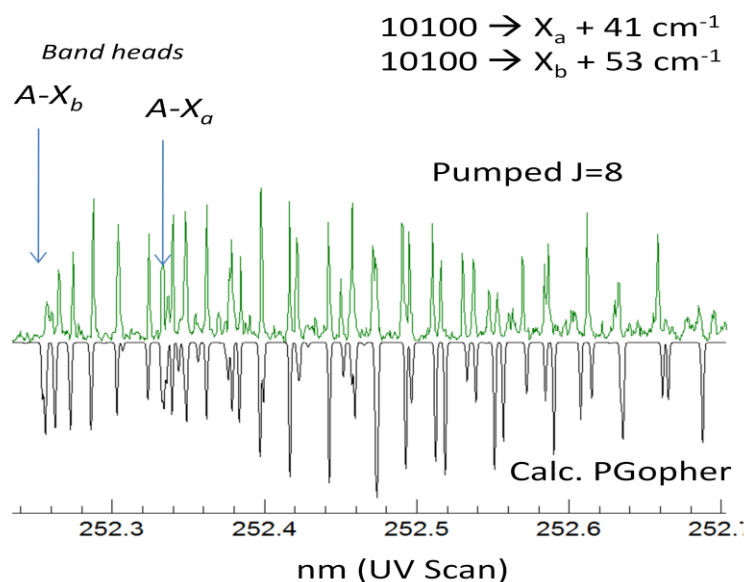


**Figure 10.5.** UV scan about  $50\text{ cm}^{-1}$  to the blue of the (10100) manifold with 200 ns delay and pumping the (10100)  $J=8$  state. The top is the experimental spectrum and the bottom is a PGOPHER simulation of the two assigned transitions.

After a tedious search through possible transitions, the spectrum was assigned to two nearby vibrational manifolds with transitions  $X\Sigma_g^+(00200) \rightarrow A^1A_u(101000)$  and  $X\Sigma_g^+(11020) \rightarrow A^1A_u(101000)$ . The two band heads are labeled in Figure 10.5. The two intermediate states are mixed to form a diad composed of the symmetric and antisymmetric linear combinations

of the 00200 and 11020 normal modes. These states lie about 41 and 53  $\text{cm}^{-1}$  below the initially pumped (10100) state. Below the spectrum is a simulation based on molecular constants from Herman et al. and Merer et al.<sup>4,5</sup> It turns out that this simulation is composed of odd J levels. So by pumping to even J and observing odd  $\Delta J$  VET it is necessary to go from *u* to *g* vibrational symmetry to conserve nuclear spin symmetry. If odd J were pumped an entirely different spectrum was observed and could be assigned according to opposite symmetry. A quantitative analysis of this VET was not possible because Franck-Condon factors were not known for these states and could not be measured easily because the states are symmetry forbidden for IR absorption.

### 10.3.3. Pump Scan Results and Analysis

The pump scan was used to identify energy transfer pathways *from* the pumped state of interest. Pump scan experiments were completed at various time delays for (10100)  $J = 0, 2, 4, 6, 8, 10, 12,$  and 14. Figure 10.6 shows an example of a typical results from these experiments. The UV laser was set to induce fluorescence from the (10100)  $J = 8$  level. The IR pump laser was then scanned to acquire a spectrum which identified the intermediate states that are connected (directly or by energy transfer) to the probed intermediate state. Experiments with various time delays were completed as shown in Figure 10.6. A simulated IR absorption spectrum is plotted below the experimental data for assignment. At very short delay (50 ns), only the  $J = 8$  peaks was observed.

These largest peaks indicate the total population present shortly after excitation of the (10100)  $J=8$  intermediate level by pumping R(7) or P(9). Energy transfer from other nearby  $J$  states was observed at longer delays. After correcting for laser power, the intensity of the peak for neighboring  $J$  states corresponds to the energy transfer kinetics. Quantitative measurements will be discussed in more detail later.

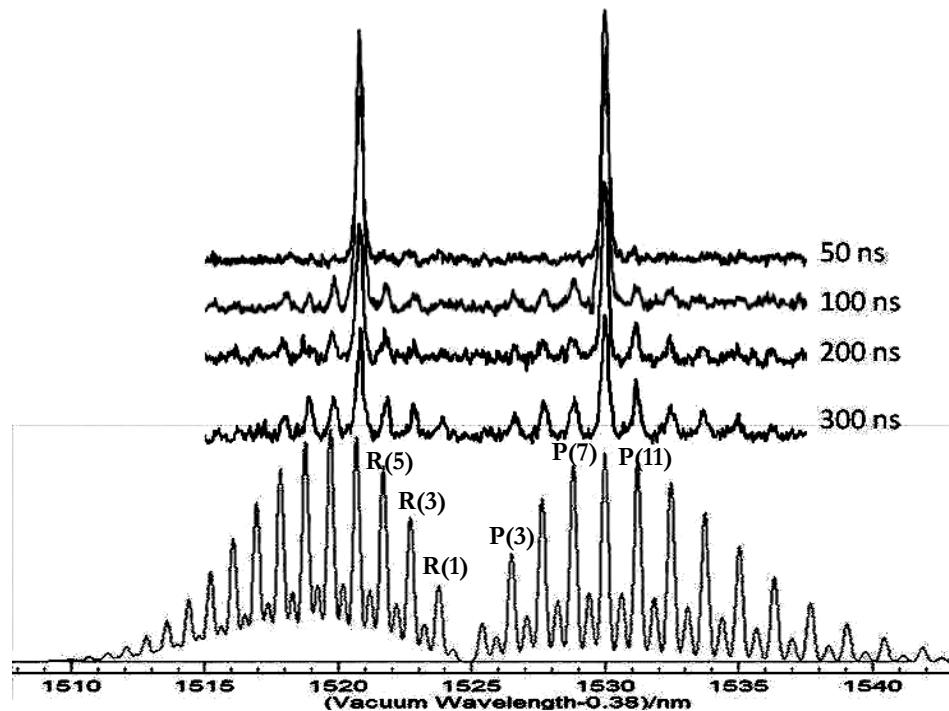


**Figure 10.6.** Pump wavelength scan of the (10100) vibrational level 50, 100, 200, and 300 ns prior to probing the  $J=8$  level. The y-axis is LIF intensity and the x-axis is the pump wavelength



The pump scan was also beneficial for detecting coincidental resonance. In some cases, such as an R-branch bandhead or P/Q branch overlap (see simulation in Figure 10.4), the UV probe may have been set at a wavelength that would produce LIF from more than one intermediate J state. Setting the probe laser and scanning the IR pump laser, at very short delay, helped to identify exactly what intermediate state were observed. This care was necessary for all double-resonance measurements.

Finally, the pump scan experiment was used for detecting VET. As observed with the probe scan experiment, VET was observed between the (00200/11020) diad and the (10100) initially pumped state. The diad has  $g$  symmetry so it cannot be populated from the  $g$  ground state because the transition is symmetry forbidden. However, because the probe scan experiment allowed the assignment of the double resonance (00200/11020) spectrum we could set the UV probe laser at resonance with the  $X\Sigma_g^+(11020) - A^1A_u(101000)$  transition and scan the pump laser allowing for VET to occur prior to detection. Figure 10.7 is an example of this experiment with a 70 ns delay between the pump and probe laser while detecting J=5 of the (11020) manifold. The population has a nearly Boltzmann distribution which indicates a small J dependence on the VET. However, the deviation from the Boltzmann distribution is apparent in the taller P(6) and R(4) lines indicating slight

conservation of J in VET. A quantitative analysis of these energy transfer processes will be discussed in a later section.

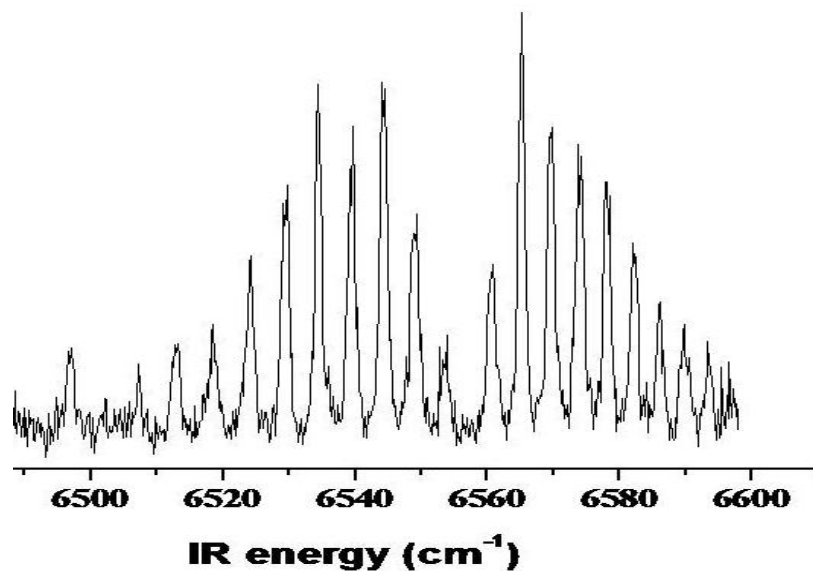


**Figure 10.7.** Pump scan near (10100) region while observing the (11020) J=5 state by UV-LIF with a 70 ns delay between the pump and probe laser.

#### *10.3.4. Time Delay Scan Results and Analysis*

The third type of experiment, the time delay scan, more accurately measured the kinetics of the energy transfer processes described above. This experiment was carried out in two different ways. Figure 10.8 gives the results of the following experiments:

1. Total removal rate kinetic measurements were made by pumping and probing the same rovibrational level and varying the time delay between the pump and probe.

2. RET kinetic measurements were made by pumping a single (10100) rovibrational level and probing a different nearby (10100) rovibrational level using the A(001010)-X(10100) band.

In the total removal measurements (Figure 10.8, J=0) the sharp rise shows the initial LIF produced when the pump and probe laser fire simultaneously. The rise time of the initial peak was  $< 20$  ns. After initial excitation, the population decreases exponentially. A secondary rise from background fluorescence was also observed making the trace a summation of the fluorescence from the two processes. Not all vibrational manifolds exhibited this phenomenon. For example, the (01120) J=0 state showed no background contribution.

The RET traces were also complicated by the background fluorescence. Figure 10.8 shows the RET traces for various even J states after pumping J=0 (10100). In most cases the background fluorescence accounted for the majority of the signal in the trace. Fortunately, the RET was faster than the rise of the background and therefore the beginning of the trace had a significant portion due to RET and the two processes were separated mathematically. The results from these experiments shows the RET was more efficient for smaller  $\Delta J$ .

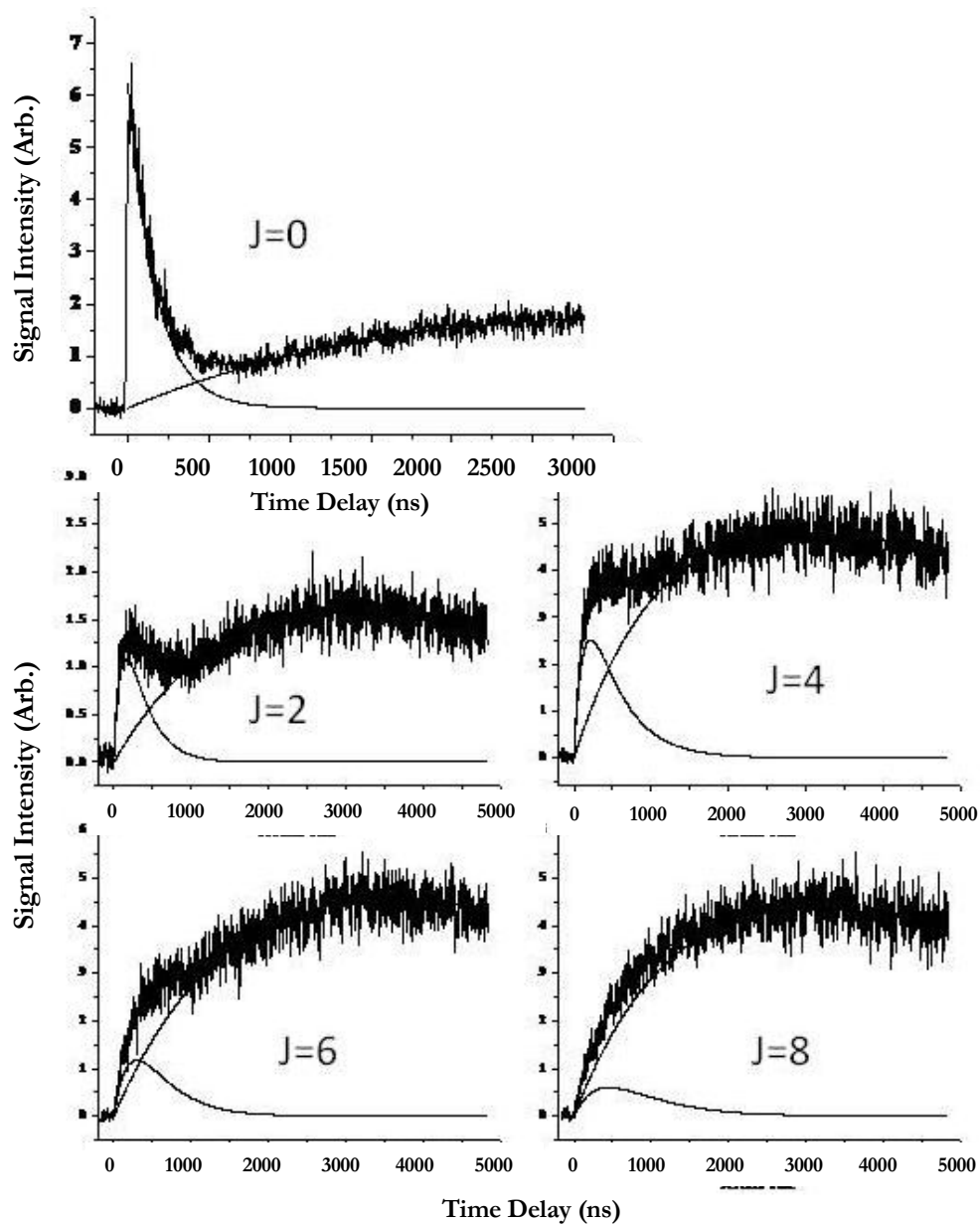


**Figure 10.8.** Time delay scans pumping various  $J$  states in the (10100) manifold while observing the (10100)  $J=0$  state. The data is accompanied by a fit for the LIF from RET as well as background fluorescence.

### 10.3.5. Quantitative Analysis of Energy Transfer

Total removal rate constants were measured for  $J = 0, 2, 4, 6, 8, 10, 12$  in the  $X\Sigma_g^+$  (10100) vibronic state and they are listed in Table 10.2. They were on the order of  $10^{-9}$  cm<sup>3</sup>/s and did not vary with respect to  $J$  except for  $J=0$  which was almost 50% faster. Origin was used to fit the data using a least squares fitting procedure with the formula:

$$I(t) = Ae^{-k_1t} + B(e^{-k_2t} - e^{-k_3t}) \quad (10.1)$$

where  $I(t)$  was the LIF intensity at time  $t$ ,  $A$  was the weighting coefficient for the exponential decay of LIF due to excitation from the probed (10100) rovibrational state with a decay constant  $k_1$ , and  $B$  was the weighting coefficient for the exponential rise and decay of LIF due to background with rise and decay constants  $k_2$  and  $k_3$ . Figure 10.8 gives an example of the data collected with the best fits. The total removal rate constant is therefore related to the rate  $k_1$  by

$$K_{totJ} = \frac{k_1}{P} \quad (10.2)$$

where  $P$  is the experimental pressure of acetylene at the point of measurement.  $K_{totJ}$  then represents the total removal of population from the pumped rovibrational state by all removal processes.

Rotational state $J_i$	Rate Constant (present study)	Rate Constant (Utz et al.) <sup>24</sup>	Pressure broadening <sup>24,26</sup>	$\sum_{f \neq i} k_{i,f}$ (PEGL)
0	18.0±0.79			16.9
2	12.8±0.96			12.9
4	12.6±0.45			12.0
6	12.8±1.15		10.4	11.3
8	12.3±0.71	9.2 ± 1.3	9.5 ± 0.4	10.6
10	12.3±1.37	8.5 ± 1.3	9.9 ± 0.4	9.9
12	12.7±1.02	9.0 ± 0.7	9.8 ± 0.4	9.2
14		9.5 ± 1.2	9.2 ± 0.6	
16		8.8 ± 1.6	9.5 ± 0.4	
18		7.1 ± 1.1	7.5 ± 0.6	
20		8.5 ± 1.5	6.8 ± 1.2	
22		6.9 ± 1.3	7.4 ± 1.2	

**Table 10.2.** Total removal rate constants for some rotational  $J$  states in  $C_2H_2$   $X\Sigma_g^+$  (10100) in units of  $10^{-10} \text{ cm}^3 \text{ s}^{-1}$ . The measurements at  $T=295\text{K}$  are given in the 2<sup>nd</sup> column. Given in the 3<sup>rd</sup> column are rate constants measured by Utz et al.<sup>24</sup> using IR-UV double resonance technique. The 4<sup>th</sup> column lists rates deduced by Utz et al.<sup>24</sup> from pressure broadening data.<sup>26</sup> Also listed in the last column are values deduced from our state-to-state RET rate measurements and rebuilt from PEGL fitting reflecting the RET contribution to the total removal rate.

The state-to-state rotational energy transfer constants  $k_{if}$  were determined for the  $X\Sigma_g^+$  (10100) vibronic state where  $i$  and  $j$  are the rotational quantum numbers for the initial and final states involved in the RET. As explained previously, the state to state rate transfer can be described as a function of the intensities of the lines in the pump scan experiment. More specifically, for

first order kinetics and assuming single collision conditions existed, the state-to-state rate constants  $k_{i,f}$  can be extracted using the relationship:

$$k_{i,f}(t) = \frac{1}{Nt} \cdot \frac{I_f(t)}{I_i(0)} \cdot \frac{S_i}{S_f} \quad (10.3)$$

In the pump scan experiment at time  $t$ ,  $N$  is the number density (pressure),  $I_f(t)$  is the intensity of the peak attributed to RET, and  $I_i(0)$  is the peak intensity of the initially pumped state at time zero.  $\frac{S_i}{S_f}$  normalizes the peak intensities to their room temperature Boltzmann population.

This procedure for determining  $k_{i,f}$  from the experimental data is demonstrated here by an example. In this example the state-to-state RET constants  $k_{i0}(t)$  are desired. These constants represent the kinetics of RET from  $J=2,4,6,8\dots$  to  $J=0$  in the  $X\Sigma_g^+$  (10100) state. First a pump scan experiment was completed with a delay of 100 ns, observing the  $J=0$  rovibrational state by UV-LIF. From the results (analogous to Figure 10.6) it was tempting to measure the intensity of each peak  $I_f$  compared with  $I_i(0)$  and use equation 10.3 to solve for  $k_{i0}$ .

However examination of the time scan data (Figure 10.8) indicated that the intensity of the peaks in the pump scan experiment was not completely from RET. Figure 10.8 shows examples where a large portion of the intensity is due to background. The time scan data was then fit to the following equation:

$$I(t) = A(e^{-k_2 t} - e^{-k_3 t}) + B(e^{-k_4 t} - e^{-k_5 t}) \quad (10.4)$$

where  $I(t)$  is the LIF intensity at time  $t$ , and  $A$  is the weighting coefficient for the exponential rise and decay of LIF due to background with rise and decay constants  $k_2$  and  $k_3$ .  $B$  is the weighting coefficient for the exponential rise and decay of LIF due to RET where  $k_4$  is the  $J_i \rightarrow J_f$  transfer rate and  $k_5$  is the total removal rate of  $J_f$ . This method determined what fraction of the LIF was attributed to the background at any time. The background portion could then be subtracted out leaving only LIF from RET. The remaining LIF intensity was then used in equation 10.3 to solve for  $k_{i0}$ . Table 10.3 lists the measured rate constants with standard errors for various RET measurements. The rates were on the order of  $10^{-11}$  -  $10^{-10}$  cm<sup>3</sup>/s.



$\frac{J_i}{J_f}$	0	2	4	6	8	10	12	$\sum_{f \neq i} k_{i,f}$
0	0	6.6(1.0) 6.8	4.6(1.1) 4.1	2.2(0.8) 2.6	1.4(0.5) 1.6	1.0(0.7) 0.9	0.6(0.2) 0.5	16.5(1.9) 16.9
2	1.4(0.2) 1.4	0	5.5(0.8) 4.9	2.3(0.6) 2.9	1.6(0.7) 1.7	1.5(0.5) 1.0	0.7(0.4) 0.5	12.8(1.4) 12.9
4	0.6(0.1) 0.51	3.3(0.5) 2.9	0	3.93	2.2	1.2	0.6	12.0
6	0.22(0.08) 0.24	1.1(0.3) 1.4	3.1	0	3.3	1.7	0.9	11.3
8	0.13(0.05) 0.14	0.66 (0.31 ) 0.75	1.6	3.0	0	2.8	1.3	10.6
10	0.09(0.07) 0.08	0.66(0.21) 0.43	0.9	1.5	2.8	0	2.4	9.93
12	0.06 (0.01) 0.05	0.31(018) 0.25	0.5	0.9	1.5	2.7	0	9.19
PEGL Fitting parameters : $K_0 = 11.83 \pm 1.58$ ( $\cdot 10^{-10} \text{cm}^3 \text{s}^{-1}$ ) $\alpha = 2.05 \pm 0.52$ $\beta = 0.27 \pm 0.07$								

**Table 10.3.** State-to-state RET rate constants  $k_{i,f}$  in units of  $10^{-10} \text{cm}^3 \text{s}^{-1}$ . The top values in each row are the directly measured rate constants as described in the paper. The numbers in parenthesis are standard deviations for the measurements. The lower values in each row are rate constants rebuilt from the parameters used to fit the PEGL to the experimental data. The PEGL fitting parameters are listed in the bottom row. The last column lists the summation of the PEGL predicted rates in each row.

### 10.3.6. Scaling Law

The number of RET rate constants determined in this study were not sufficient to describe all of the processes that would be of importance for relaxation to a thermal distribution at room temperature. Consequently, the measured rate constants were fit to empirical fitting laws to extrapolate values for

to complete the rate constant matrices. There are several scaling laws which attempt to model collisional RET kinetics based on the energy spacing of the states involved in the transfer. Many of these models were developed from experimental data in diatomic molecules and have been applied to polyatomic molecules.<sup>25,27-30</sup> The power exponential gap law (PEGL) was chosen to fit our data because it was a better fit to our experimental data than other scaling laws. It was likely a better fit because it has a larger number of variable parameters than the other models. The PEGL has the following form:

$$k_{if} = K \cdot \left[ \frac{|E_f - E_i|}{B\nu} \right]^\beta \cdot \exp \left[ -\alpha \cdot \frac{|E_f - E_i|}{k_B \cdot T} \right] \quad (10.5)$$

where  $|E_f - E_i|$  is the energy difference between the RET states,  $B\nu$  is the molecular rotational constant for vibrational state  $\nu$ ,  $k_B \cdot T$  is the Boltzmann energy at temperature  $T$ , and  $K$ ,  $\beta$ , and  $\alpha$  are fitting parameters. This method was used for exothermic transfer. The principle of detailed balance was utilized to determine endothermic transfer rate constants:

$$k_{fi} = k_{if} \cdot \frac{2J_i + 1}{2J_f + 1} \cdot \exp \left( \frac{E_f - E_i}{k_B \cdot T} \right) \quad (10.6)$$

The experimental data was fit using equation 10.5 to obtain fitting parameters  $K$ ,  $\beta$ , and  $\alpha$ . These parameters were then used, along with equation 10.6, to calculate values for each RET rate constant matrix element, i.e. the state-to-state RET rate constants. The interpolated and extrapolated values are included below the experimental values in Table 10.3.

### 10.3.7. *Vibrational Energy Transfer*

The only conclusive VET pathways observed was  $(10100) \rightarrow (00200/11020)$ . The background fluorescence may have been attributed to other VET pathways but this was not conclusive as the absorption was too congested to be assigned. As stated previously, a quantitative analysis of this transfer was not possible. However, an upper limit was applied to the VET by considering RET. The last column of Table 10.2 lists the summation of RET constants for each J state. This accounts for approximately 90% of the total removal rate from each state. Therefore, the upper limit of VET was 10%.

## 10.4. Discussion and Conclusions

Experiments were conducted pumping from odd J" because the 3:1 population ratio gave greater sensitivity. The same experiments could be conducted for even J". For the probe scan experiments we observed  $\Delta K \neq \pm 1$  transitions along with the stronger  $\Delta K = 0$  transitions. This is a result of axis switching which relaxes the  $\Delta K = \pm 1$  selection rule and has been observed previously for acetylene.<sup>25</sup>

The "quasi-continuous" background in these experiments (see Figure 10.4) caused considerable difficulty and added many assumptions to our analysis. The background was termed "quasi-continuous" because of the label that Payne et al.<sup>31</sup> termed their similar observation during double resonance studies of the

$X\Sigma_g^+$  (10300) state of acetylene. The background they observed was considerably more continuous absorption than the spiky background in Figure 10.4. This can be explained by the higher density of states in the (10300) region which leads to more possible low intensity fluorescence transitions related to VET.

The possibility that the background was a result of energy transfer to nearby vibrational states (as theorized by Payne et al.) may be strengthened due to the fact that we were able to assign an intense feature within the background to VET (see Figure 10.5). The assignment of the intense band involved the transition to the  $A^1A_u$  (101000) state has been shown to have a large transition strength.<sup>2</sup> This might explain why this particular band towers above others and is not necessarily related to a larger population in that state. Furthermore, in low energy vibrational manifolds (01000) the continuous background has not been observed in double resonance studies.<sup>16</sup> Assignments of the background might be possible with a higher resolution pump source.

The IR scans, in combination with the time delay scans to remove background effects, gave reasonable state-to-state RET constants. The constants are similar in value to other rates obtained for other vibrational states.<sup>14-18,23</sup> The measured total removal rates were slightly faster than those obtained by Utz<sup>24</sup> et al. This is due to the care that was taken in removing the background contribution. When the decays were fit without removing the background values were obtained that were the same as theirs. In fact the removal of the

background increased our values by 40%. Utz et al. did not observe the background rise probably because they had less sensitivity and it may have been hidden in the noise.

The study concluded that the transfer occurred could be accurately modeled by the exponential or power gap scaling laws. Also, the RET accounted for about 90% of the total removal. As the density of vibrational states increases, thermodynamics predicts that VET might also increase. This was true to some extent as (00300) had 30% VET<sup>23</sup>, (10100) had 10% VET, and (01000) had 0% VET<sup>16</sup>. But in addition, energy transfer was also dependent on state mixing and preference to transfer within nearby levels with the same diad or polyad<sup>20</sup>. In our case, the VET observed was within the same polyad [2 10 0].

Further research from the Heaven group<sup>32</sup> found that transfer from (10100) into (1101<sup>1</sup>1<sup>-1</sup>) accounted for 3% of total removal owing to its small energy difference. Other transitions involved small percentages (< 0.5%) into (0203<sup>1</sup>1<sup>-1</sup>) and (0112<sup>0</sup>0). Due to the forbidden symmetry, it was not possible to conclude the portion of transfer to (00200)/(11020). The results from this work were recently used in models for developing hollow-core optical fiber gas lasers.<sup>33</sup>

- (1) Nampoothiri, A. V. V.; Ratanavis, A.; Campbell, N.; Rudolph, W. *Opt Express* **2010**, *18*, 1946.
- (2) Watson, J. K. G.; Herman, M.; Vancraen, J. C.; Colin, R. *J Mol Spectrosc* **1982**, *95*, 101.
- (3) Tobiason, J. D.; Utz, A. L.; Crim, F. F. *J Chem Phys* **1993**, *99*, 928.
- (4) Merer, A. J.; Yamakita, N.; Tsuchiya, S.; Stanton, J. F.; Duan, Z. C.; Field, R. W. *Mol Phys* **2003**, *101*, 663.
- (5) Herman, M.; Campargue, A.; El Idrissi, M. I.; Vander Auwera, J. *J Phys Chem Ref Data* **2003**, *32*, 921.
- (6) Orr, B. J. *Int Rev Phys Chem* **2006**, *25*, 655.
- (7) Keppler, K. A.; Mellau, G. C.; Klee, S.; Winnewisser, B. P.; Winnewisser, M.; Pliva, J.; Rao, K. N. *J Mol Spectrosc* **1996**, *175*, 411.
- (8) Srivastava, H. K.; Conjusteau, A.; Mabuchi, H.; Callegari, A.; Lehmann, K. K.; Scoles, G.; Silva, M. L.; Field, R. W. *J Chem Phys* **2000**, *113*, 7376.
- (9) Herman, M.; Lievin, J.; Vander Auwera, J.; Campargue, A. *Adv Chem Phys* **1999**, *108*, 1.
- (10) Vancraen, J. C.; Herman, M.; Colin, R.; Watson, J. K. G. *J Mol Spectrosc* **1986**, *119*, 137.
- (11) Vancraen, J. C.; Herman, M.; Colin, R.; Watson, J. K. G. *J Mol Spectrosc* **1985**, *111*, 185.
- (12) Utz, A. L.; Tobiason, J. D.; Carrasquillo, E.; Sanders, L. J.; Crim, F. F. *J Chem Phys* **1993**, *98*, 2742.
- (13) Domenech, J. L.; Martinez, R. Z.; Ramos, A.; Bermejo, D. *J Chem Phys* **2010**, *132*.
- (14) Tobiason, J. D.; Utz, A. L.; Crim, F. F. *J Chem Phys* **1992**, *97*, 7437.
- (15) Frost, M. J. *J Chem Phys* **1993**, *98*, 8572.
- (16) Dopheide, R.; Cronrath, W.; Zacharias, H. *J Chem Phys* **1994**, *101*, 5804.
- (17) Chadwick, B. L.; Milce, A. P.; Orr, B. J. *Can J Phys* **1994**, *72*, 939.
- (18) Carrasquillo, E.; Utz, A. L.; Crim, F. F. *J Chem Phys* **1988**, *88*, 5976.
- (19) Henton, S.; Islam, M.; Smith, I. W. M. *J Chem Soc Faraday T* **1998**, *94*, 3207.
- (20) Frost, M. J.; Smith, I. W. M. *J Phys Chem-US* **1995**, *99*, 1094.
- (21) Tobiason, J. D.; Utz, A. L.; Crim, F. F. *J Chem Phys* **1994**, *101*, 1108.
- (22) Chadwick, B. L.; Milce, A. P.; Orr, B. J. *J Chem Phys* **1993**, *175*, 113.
- (23) Tobiason, J. D.; Utz, A. L.; Crim, F. F. *Laser Techniques for State-Selected and State-to-State Chemistry* **1993**, 1858, 317.
- (24) Utz, A. L.; Tobiason, J. D.; Carrasquillo, E.; Fritz, M. D.; Crim, F. F. *J Chem Phys* **1992**, *97*, 389.
- (25) Tobiason, J. D. *Laser double-resonance studies of electronic spectroscopy and state-resolved collisional relaxation in highly vibrationally excited acetylene*, 1992.

- (26) Varanasi, P.; Bangaru, B. R. P. *J. Quant. Spectrosc. Radiat. Transfer* **1975**, *15*, 267.
- (27) Hostutler, D. A.; Smith, T. C.; Hager, G. D.; McBane, G. C.; Heaven, M. C. *J. Chem Phys* **2004**, *120*, 7483.
- (28) Looney, J. P.; Rosasco, G. J.; Rahn, L. A.; Hurst, W. S.; Hahn, J. W. *Chem Phys Lett* **1989**, *161*, 232.
- (29) Sanctuary, B. C. *Chem Phys Lett* **1979**, *62*, 378.
- (30) Steinfeld, J. I.; Ruttenberg, P.; Millot, G.; Fanjoux, G.; Lavorel, B. *J Phys Chem-Us* **1991**, *95*, 9638.
- (31) Payne, M. A.; Milce, A. P.; Frost, M. J.; Orr, B. J. *Chem Phys Lett* **2000**, *324*, 48.
- (32) Han, J. *This data was calculated by Jiande Han after I switched to the CRDS experiment.* **2011**.
- (33) Nampoothiri, A. V. V.; Jones, A. M.; Fourcade-Dutin, C.; Mao, C.; Dadashzadeh, N.; Baumgart, B.; Wang, Y. Y.; Alharbi, M.; Bradley, T.; Campbell, N.; Benabid, F.; Washburn, B. R.; Corwin, K. L.; Rudolph, W. *Opt. Mater. Express* **2012**, *2*, 948.